eman ta zabal zazu

Universidad del País Vasco

Euskal Herriko Unibertsitatea

POLYIMIDES FOR PIEZOELECTRIC MATERIALS, MAGNETOELECTRIC NANOCOMPOSITES AND BATTERY SEPARATORS: SYNTHESIS AND CHARACTERIZATION

Memoria para optar al Grado de Doctor por la Universidad del País Vasco (UPV/EHU) presentada por

Alberto Maceiras Martínez

Leioa, Junio 2016

(cc)2016 ALBERTO MACEIRAS MARTINEZ (cc by-nc-sa 4.0)

AGRADECIMIENTOS

Durante los últimos años he estado rodeado por personas que me han apoyado en este viaje. Nunca hubiese sido capaz de acabar esta tesis sin su guía, ayuda o, aún más importante, sin su paciencia conmigo. Ahora es tiempo de acabar este periodo de mi vida, pero no sin antes de daros las gracias a todos.

Primeramente me gustaría agradecer a la Universidad del País Vasco / Euskal Herriko Unibertsitatea (UPV/EHU) por el apoyo económico recibido para la realización de mi doctorado (Convocatoria de Ayuda para la Formación de Personal Investigador). Asímismo quiero agradecer el apoyo técnico y humano de los servicios SGIker (UPV/EHU, MICINN, GV/EJ, FEDER y FSE)

Me gustaría expresar mi gratitud a mi director, Luis Manuel León, y a mi co-directora, María San Sebastián, por proporcionarme las condiciones necesarias para desarrollar mi investigación. Desearía especialmente dar las gracias a Luis por darme la oportunidad de trabajar en su grupo de investigación. Nunca olvidaré todas las cosas que has hecho por mí. Estoy agradecido por tu paciencia, cariño, confianza y amistad.

También me gustaría reconocer el trabajo incansable de Matilde, ha sido verdadero placer trabajar contigo, todos sabemos lo mucho que el grupo tiene que agradecerte. Tampoco puedo olvidar a los profesores del grupo recientemente retirados, Fernando Mijangos y Maite Garay, por el cariño y las palabras amables que siempre me han brindado; ahora os toca disfrutar de la bien merecida jubilación.

A Jose Luis Vilas darle las gracias por haberme permitido trabajar con él desde que me dirigió el proyecto de Máster, y desearle toda la suerte del mundo como jefe de grupo. A las nuevas profesoras del laboratorio, Leyre Pérez, Amaia Saracibar y Leire Ruiz, os deseo el mayor de los éxitos en vuestra carrera. Al Dr. José Manuel Laza, uno de los pilares indispensables del grupo, simplemente gracias por tus consejos y por todas las cosas que he aprendido contigo.

Ahora quisiera agradecer a mis compañeros de laboratorio (Postdoc, doctorandos, técnicos de laboratorio, alumnos de máster y de grado) que han pasado por el

laboratorio en estos años y que sin duda me han hecho la vida más feliz y divertida. Por mi parte, espero haberos ayudado en todo lo posible y haber contribuido al buen ambiente. Sois muchos, así que si me olvido de alguno de vosotros os pido disculpas.

A los "minions" del labo: Alain, Veronica, Nerea G., Janire, Maitane, Mari Paz, Sara, Aitor, María, Paula, Garazi, Mireia, Estela, Christian, Eva, Maru, Nerea A., Ane. ¡Gracias, colegas! En especial a Ander, gracias por esas simulaciones; espero que hayas disfrutado trabajando conmigo.

Alazne, gracias por ser siempre tan dulce y simpática con todos. A Nuria, en estos años te he visto crecer mucho y en el futuro espero seguir viéndolo. A Míriam, espero que en este tiempo te lo hayas pasado tan bien conmigo como yo me lo he pasado contigo. A Erlantz, gran investigador y persona, espero poder trabajar algún día contigo y discutir juntos como se merece. A Mikel, tranquilo que no me olvido de nombrarte, algún día montaremos un spin-off utópico juntos, no te preocupes. Y por último a David, empezamos esta aventura juntos y también la terminaremos juntos, pero aunque esta etapa se termine otras nuevas vendrán, no te libras tan fácil de mí.

Quiero expresar mi gratitud al Profesor Senentxu Lanceros-Mendez por darme la oportunidad de trabajar durante varios meses en su grupo de investigación (Electroactive Smart Materials Group) en la Universidade do Minho, Braga, Portugal. Asimismo, quiero dar las gracias a todos los miembros de su grupo por su inestimable ayuda, por su valía profesional y, sobre todo, por la amistad que siempre me han demostrado. Muito obrigado.

Quiero agradecer al Basque Center for Materials, Applications and Nanostructures (BCmaterials) por permitirme usar sus instalaciones y equipamientos. Al Grupo de Magnetismo y Materiales Magnéticos del Departamento de Electricidad y Electrónica de la UPV/EHU, en especial al profesor Jon Gutierrez y a Andoni Lasheras, por toda su ayuda y colaboración siempre que lo he necesitado. A la profesora Aintzane Goñi del Departamento de Química Inorgánica de la UPV/EHU deseo agradecerle toda la ayuda prestada con el estudio y caracterización de los separadores de baterías.

Bueno, también agradecer al resto de amigos de dentro y fuera de la universidad por todos los momentos que hemos compartido.

Para finalizar quiero dar las gracias a mi familia. Os debo todo.

A mi familia

“*La ciencia no sabe de países, porque el conocimiento le pertenece a la humanidad y es la antorcha que ilumina el mundo. La ciencia es el alma de la prosperidad de las naciones y la fuente de todo progreso*.”

Louis Pasteur (1822 – 1895)

“*Cree a aquellos que buscan la verdad. Duda de los que la encuentran.*”

André Gide (1869 – 1951)

ABSTRACT

A series of nitrile containing polyimide polymers and copolymers were synthesized, and subsequently poled by corona poling in order to provide them piezoelectric behavior. The corona poling conditions were optimized for our samples, and d_{33} coefficients showed thermal stability and over time. Moreover, the influence in the piezoelectric properties of the repeating unit with two nitrile groups was studied, observing that a progressive increase in the content of the component with two nitrile groups (2CN) in the film improves the piezoelectric response. High thermal stability of polymer films was demonstrated by means of DSC and TGA, allowing their use at temperatures higher than 100ºC.

Dielectric properties of the samples were determined by dielectric spectroscopy to understand the dielectric behaviour of the polyimide films. The contribution of nitrile groups in the dielectric relaxations and the types of polarization involved were analyzed.

The use of polyimides in magnetoelectric (ME) nanocomposites was demonstrated for the first time. Magnetoelectric voltage coefficient was measured in a 0–3 nanocomposite film, prepared via in-situ polymerization method, using spherical cobalt ferrite nanoparticles ($CoFe_2O_4$) as fillers and an amorphous copolyimide, as matrix.

Different polyimide fibers were prepared by electrospinning, characterized and tested as separators for Li-ion batteries. It was the first approach in the development of gel polymer separators based in nitrile containing polyimides.

RESUMEN

Se ha sintetizado una serie de poliimidas y copoliimidas que contienen grupos nitrilo en su estructura, y posteriormente han sido polarizadas por corona con objeto de dotarlas de comportamiento piezoeléctrico. Las condiciones de la polarización por corona han sido optimizadas para las muestras estudiadas, mostrando los coeficientes d_{33} una buena estabilidad térmica y a lo largo del tiempo. Además, se ha estudiado la influencia en la piezoelectricidad de la unidad repetitiva con dos grupos nitrilo, observando que un incremento progresivo del contenido en el componente con dos grupos nitrilo (2CN) aumenta la respuesta piezoeléctrica. Los films poliméricos han demostrado alta estabilidad térmica mediante DSC y TGA, demostrando su uso a temperaturas superiores a 100ºC.

Las propiedades dieléctricas de las muestras han sido determinadas mediante espectroscopia dieléctrica para comprender el comportamiento dieléctrico de los films de poliimida. Se ha analizado la contribución de los grupos nitrilo en las relajaciones dieléctricas y en los tipos de polarización que se ven implicados.

El uso de poliimidas en nanocomposites magnetoeléctricos (ME) ha sido demostrado por primera vez en esta Memoria. Se ha medido el coeficiente magnetoeléctrico en un film de nanocomposite, preparado mediante un método de polimerización in-situ, usando nanopartículas esféricas de ferrita de cobalto ($CoFe_2O_4$) como inclusión y una copoliimida amorfa, como matriz.

Se han preparado diferentes fibras de poliimida mediante electrospinning (electrohilado), han sido caracterizadas y testadas como separadores para baterías de ion Litio. Ha sido la primera aproximación en el desarrollo de separadores de polímero gel basados en poliimidas que contienen grupos nitrilo.

TABLE OF CONTENTS

Chapter 1. Introduction 1

1.1. Smart materials 2

1.2. Piezoelectric materials 6

1.2.1. Discovery and main events 6

1.2.2. Definitions and general concepts 12

1.2.3. Types of piezoelectric materials 33

A. Ceramics 33

B. Polymer piezoelectric materials 38

1.2.4. General objectives and work plan 56

1.3. References 60

Chapter 2. Materials, experimental techniques and apparatus 69

2.1. Materials 70

2.2. Experimental techniques and apparatus 71

2.2.1. Broadband dielectric spectroscopy 71

2.2.2. Differential scanning calorimetry (DSC) 73

2.2.3. Digital temperature controller 74

2.2.4. Electrochemical impedance spectroscopy 75

2.2.5. Fourier transform infrared spectroscopy (FTIR) 76

2.2.6. Galvanostatic cycling 77

2.2.7. High voltage source 78

2.2.8. Magnetron sputtering 79

2.2.9. Scanning Electron Microscopy (SEM) 80

2.2.10. Syringe pump 82

2.2.11. Lock-in amplifier 83

2.2.12. Thermogravimetric analysis (TG) 85

2.2.13 Vibrating sample magnetometer (VSM) 86

2.2.14. Wide range d_{33}-meter 88

Chapter 3. Synthesis, corona poling and characterization 91

3.1. Introduction 92

3.1.1. Poling 94

A. Contact poling 97

B. Corona Poling 97

3.1.2. Conservation of electrets 100
3.1.3. Charge formation in electrets 100

3.2. Experimental and results *103*
3.2.1. Synthesis 103
3.2.2. Films preparation and thermal imidization 105
3.2.3. Optimization of Corona poling conditions 106
3.2.4. Influence of the comonomer with two cyano groups 111
3.2.5. Thermal characterization 113

3.3. Conclusions *119*

3.4. References *120*

Chapter 4. Dielectric spectroscopy study 125

4.1. Introduction *126*
4.1.1. Definitions and terms 129
4.1.2. Electric polarization 134
A. Mechanisms of electric polarization 139
4.1.3. Macroscopic and microscopic interaction with the electric field 146
4.1.4. Dielectric loss and relaxation 151

4.2. Experimental *160*

4.3. Results and discussion *161*
4.3.1. Overall dielectric response 161
A. Temperature dependence 161
B. Frequency dependence 168
4.3.2. Overall conductivity 171
4.3.3. Electric modulus formalism 178

4.4. Conclusions *184*

4.5. References *185*

Chapter 5. Polyimide based magnetoelectric nanocomposites 189

5.1. Introduction *190*
5.1.1. Polymer nanocomposites 191
A. Polyimide nanocomposites 195
5.1.2. Magnetoelectric effect 197
A. Types of ME composites 205
B. Enhanced ME effects at resonance 208

C. Magnetoelectric Effect in polymer composites 212

5.2. Experimental *216*

5.2.1. Synthesis and fabrication of polyimide based ME nanocomposites 216

5.2.2. Characterization of nanocomposites 219

A. Thermal and morphological characterization 220

B. Magnetic and piezoelectric characterization 220

C. Magnetoelectric effect measurement 220

5.2. Results and discussion *222*

5.2.1. Thermal and morphological characterization 222

5.2.3. Magnetoelectric effect measurement 231

5.3. Conclusions *232*

5.4. References *233*

Chapter 6. Electrospun polyimide for polymer membranes in Li-ion battery applications 241

6.1. Introduction *242*

6.1.1. Battery parts 244

6.1.2. Characteristics of rechargeable batteries 247

A. Impedance spectroscopy 249

B. Uptake, porosity, tortuosity and Ionic conductivity 255

C. Capacity and C-rate 258

6.1.3. Parts of Li-ion batteries 262

A. Cathode material 264

B. Anode material 268

C. Electrolyte 271

D. Separator 273

6.1.4. Polyimide membranes 278

6.1.5. Electrospinning 281

6.2. Experimental details *287*

6.2.1. Synthesis and electrospun membranes fabrication 287

A. Synthesis of polyimides 287

B. Electrospinning process optimization 289

C. Electrospinning setup in the optimum conditions 290

6.2.2. Characterization of membranes 293

A. Electrolyte solution and uptake 293

B. Porosity 293

C. Cell preparation and electrochemical measurements 294

6.3. Results and discussion *296*
6.3.1. Morphology, infrared and thermal properties 296
6.3.2. Electrical properties 302
6.3.3. Battery performance 305
6.4. Conclusions *310*
6.5. References *311*
Chapter 7. Conclusions and final considerations 321
Curriculum vitae & contributions 325

Chapter 1.

Introduction

In this chapter the main concepts, terms and phenomena in the field of piezoelectric materials will appear. In addition of the main events in history that have influenced the development of this field, the classification of piezoelectric materials and their most common examples will be detailed. Finally, a summary about polyimides, the type of polymer of this thesis, will be shown.

1.1. SMART MATERIALS

Smart materials are a general name for a wide group of different materials with very different characteristics. They have in common that one or more of their properties might be significantly modified under controlled conditions [1].

Although widely discussed, there is no universally accepted definition of exactly what "Smart" or "Intelligent" materials are [2]. Smartness is a typical feature of systems that are able to adaptively interact with the environment. Indeed, some systems are able to respond or modify themselves on the basis of the information or stimuli they get from surrounding environment.

In general the term "Smart" refers to a kind of materials that, in response to a deliberately imposed external stimulus or to changes in their surrounding conditions, are able to reversibly modify one or more of their functional or structural properties. In that way, they can receive, transmit, or process a stimulus and respond by producing a controlled and specific signal or response, because they have the ability to change their physical properties in a specific manner in response to specific stimulus input [3].

The external stimuli causing the smart response of the materials could be of various kinds: physical (temperature, light, electric or magnetic fields, etc.), chemical (pH, analyte concentrations in air, water, biological fluids), and mechanical (stress, strain), and they are summarized in Table 1.1. It is intended that the process is fully reversible: a Smart Material is capable of returning to its initial state as soon as the external stimulus is removed.

As it can be seen in Table 1.1 there are many examples of Smart Materials. Their classification can be approached from the point of view of their chemical nature, or even in some cases the source of the smart behavior could lie in the micro- or nanostructure of the materials, rather than being intrinsically ascribed to the material itself. They can be categorized into three different levels: a) single-phase materials, b) composite materials, and c) smart structures. But, since this Thesis is mainly focused on polymers, it will be centered only in Smart Polymers [4,5].

Table 1.1. Comprehensive table of Smart Materials classified according to their basic physical/chemical effects. The columns represent the type of stimulus applied to the material, and the rows the type of response appearing.

Response / *Stimulus*	**Electrical**	**Magnetic**	**Optical**	**Thermal**	**Mechanical**	**Chemical**
Electrical		Magneto-electronics, spin-electronics, spintronics	Electro-chromic, electro-luminescent, electro-optic, piezo-chromic, Kerr Effect, Pockel Effect	Thermo-electric (Peltier)	Piezo-electric, electro-strictive, electro-rheological, electro-kinetic	Electrolysis, electro-chemical, bio-electric, electro-migration
Magnetic	Magneto-electronics, spin-electronics, spintronics, Hall Effect		Magneto-optic, piezo-chromic	Magneto-thermal	Magneto-strictive, magneto-rheological	Nuclear-magnetic-resonance, magneto-chemical
Optical	Photo-conductive	Opto-magnetic	Optical bi-stability	Photo-thermic	Opto-mechanical, photo-acoustic	Photo-chemical, photosynthesis, photo-catalyst
Thermal		Curie point	Thermo-cromic,		Shape-memory	
Mechanical	Piezoelectric, electrostrictive	Magnetostrictive,			Rheopexic, auxetic, shear-thinning, dilatants, non-Newtonian, pseudo-plastic	
Chemical		Magneto-chemical	Colour-change, litmus, luminiscence	Exothermic, endothermic		Catalysis

Among Smart Polymers, there are also many examples, and in several of them, the research group "Laboratorio de Química Macromolecular" has years of experience, both in articles and in thesis. For instance, there are shape memory polymers (SMPs) [6–8] that change their physical shape returning to a preset one in response to temperature variations, making them useful for actuation [8–10].

Conducting polymers [11–13] gained considerable attention due to many attractive features: tenability of physical properties, flexibility, stimuli-responsiveness, etc. Among the different classes of inherently conductive polymers that have been explored during the past two decades, conjugated polymers are the most interesting.

Micro- and nanopatterning of polymers is nowadays available with relatively inexpensive techniques such as hot embossing and imprinting, or also exploiting self-assembling procedures and supramolecular arrangement of organic molecules [14,15]. In this way, novel "soft" nanofabrication processes, very different from more common lithographic techniques, are exploited for the production of nanostructured organic materials. In addition, post-modification of polymer surfaces, aiming at including specific functionalities on existing surfaces to, e.g., induce change in wettability properties or alter biomolecular functions, is quite easily achieved by chemical modifications [16]. Moreover, the deposition of thin layers of polymers is easily prepared with techniques such as spin coating that are faster and cheaper than those required for deposition of thin layers of inorganic counterparts, very often performed under high-vacuum conditions or with the use of special equipments.

Other examples are the micro or nanostructured block copolymers that change their surface properties from hydrophilic to hydrophobic (and/or vice versa) in response to changes in temperature [15,17], or some classes of cross-linked polymers that are able to self-heal their own mechanical damages by self-restoring chemical bonds [18,19].

Responsive polymer gels [20,21], with their responsiveness to thermal or chemical stimuli, represent another class of smart materials with wide applications. A polymer gel can be in general described as a soft, wet, elastic material where a network of cross-linked polymer chains encloses some fluid. In addition, there exist smart hydrogels that are able to swell/deswell in response to change in pH and are widely applied in drug delivery systems [22,23] or chemoresponsive polymer nanocomposites [24] that are able to change their stiffness in presence of a chemical regulator mimicking the architecture of some echinoderms, etc.

And finally, the subject of this work, piezoelectric materials, are the materials of choice for all the applications in which electro-mechanical transduction is needed (Table 1.2), and represent one of the most valuable classes of materials in the modern world [25,26].

Table 1.2. Major applications of piezoelectricity.

Communications and control	**Industrial**	**Health and consumer**	**Newer applications**
Cellular radio	Transducers	Transducers	Smart Structures
Television	Sensors	Sensors	High Displacement Transducers
Automotive radar	Actuators	Actuators	Mixed-effect Devices
	Pumps	Pumps	
-Signal Processing	Motors	Motors	-Microelectromechanical (MEMS) devices
-Frequency control and timing			-Microoptomechanical (MOMS) devices
-Correlators	-Ultrasonic cleaning	-Noninvasive medical diagnostics	-Biomimetic devices
-Convolvers	-Sonar	-Hyperthermia	-Composite and functionally graded devices
-Filters	-Nondestructive evaluation (NDE)	-Lithotripsy	-Rainbow devices
Delay lines	-Liquid level sensors	-Subcutaneous medication	-Acousto-photonic-electronic devices
-Oscillators	-Vibration damping	-Wristwatches	
	-High temperature sensors	-Camera focusing/steadying	
	Material properties determination	-Computer timing/printing/modems	
	-Chemical/biological sensors	-Ignition of gases (“spark pump”)	

1.2. PIEZOELECTRIC MATERIALS

1.2.1. DISCOVERY AND MAIN EVENTS

Piezoelectric materials are the dielectric materials that are able to transducer mechanical deformations in electrical potentials and vice versa. The word *piezoelectricity* means electricity resulting from pressure. It is derived from the Greek *piezo* or *piezein* (πιέζειν), which means to squeeze or press, and *electric* or *electron* (ήλεκτρον), which stands for amber, an ancient source of electric charge [27].

The history of piezoelectricity elapses in parallel with the history of ferroelectricity and pyroelectricity, which they are intimately connected concepts but different. So it is necessary a detailed explanation in order to avoid misunderstandings.

Pyroelectricity is defined as the appearance of electrostatic charges upon variation of temperature. Although the term was first coined by Sir David Brewster in 1824, the phenomenon was observed by the Greeks more than 24 centuries ago. The philosopher Theophrastus wrote that "lyngourion" (most likely the mineral tourmaline) had the property of attracting straws and bits of wood. This property must have had something to do with the heating/cooling of the mineral in question. For two millennia the peculiar properties of tourmaline were more a part of mythology than of science.

Two thousand years after, tourmaline's unusual physical properties were reintroduced to Europe through a book written by Johann Georg Schmidt. He described the experiences of Dutch gem cutters with tourmaline in a fire, because it had the property of not only attracting the ashes from the warm or burning coals, as the magnet does iron, but also repelling them again.

In 1717 the chemist and physician Louis Lemery wrote the first scientific paper about pyroelectricity in a journal. The naturalist Carl von Linné (Linnaeus) was the first to relate the pyroelectric property of tourmaline to electricity; he called the mineral *lapis electricus*-electric stone. Experiments on tourmaline during the 18^{th} century by Franz Ulrich Theodor Aepinus, Johann Karl Wilcke, Benjamin Wilson, Joseph Priestley, John

Canton, and Torben Bergman made major contributions to the rapidly developing field of electrostatics.

In 1824 David Brewster, was the first author to use the term "pyroelectricity". One of the materials he studied was the Rochelle salt. John Mothée Gaugain made the first precise measurements of pyroelectric charges in 1859. William Thomson (Lord Kelvin) published the first major theoretical treatment of pyroelectricity in 1878. Jacques and Pierre Curie also proposed that the electrical effects due to non-uniform heating of quartz crystals might have been caused by pressure, a speculation that led to their discover of piezoelectricity. W. Voigt established a school of crystallography, thermodynamics and crystal physics. During the latter part of the 19^{th} century and the early decades of the 20^{th} century, seven Nobel laureates – Wilhelm Röntgen, Pierre Curie, Gabriel Lippman, Heike Kammerlingh Onnes, Erwin Schrödinger, Archer J. P. Martin, and Max Born – published papers on pyroelectricity. In 1938 was published a paper that initiated the great growth that continues in the field today, for the first time it was proposed that tourmaline crystals could be used as IR sensors in spectroscopy. Since then many experiments were conducted on pyroelectric IR detectors during and immediately after World War II.

The piezoelectricity effect was first demonstrated in 1880 by the brothers Jacques and Pierre (Figure 1.1) Curie in single crystals of quartz and later was reported in other materials such as Rochelle salt, tourmaline, and topaz (Figure 1.2). Piezoelectricity appears in certain solid dielectric materials, such as crystals, some ceramics, and biological matter such as bone, DNA and various proteins and polymers. It is a reversible effect that consists of two different processes, the internal generation of electrical charge resulting from an applied mechanical force (direct piezoelectric effect) and also the internal generation of a mechanical strain resulting from an applied electrical field (reverse piezoelectric effect).

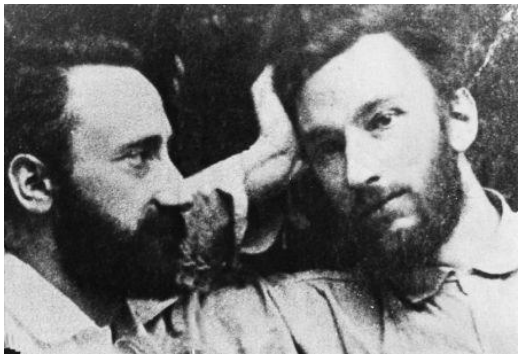

Figure 1.1. Jacques (Left) and Pierre Curie (Right).

In a similar way, the history of the discovery of ferroelectricity (electrically switchable spontaneous polarization) extends as far back as the mid-1600s when Rochelle salt (sodium potassium tartrate tetrahydrate) was first prepared by Elie Seignette in La Rochelle, France, for medical purposes. However, its pyroelectric (thermo-polar) properties were not discovered until approximately 200 years later, other half century until its piezoelectric properties were uncovered, and finally another 40 years for ferroelectricity. This last property was hypothetical but yet unproved at the turn of the 20th century, because it was first discovered by Joseph Vasalek in 1921. Rochelle salt was a popular material in these initial studies, because it was readily available and easily grown as large single crystals of excellent optical quality, but its water solubility eventually led to its disuse in later years.

a) b) c) d)

Figure 1.2. a) crystal of quartz, b) Rochelle salt, c) tourmaline and d) topaz.

As it was said before, piezoelectricity, pyroelectricity and ferroelectricity are related phenomena. In Figure 1.3 can be observed that a dielectric material can experiment one, two, the three effects or none of them, i.e. every ferroelectric material is piezoelectric

and pyroelectric, but not every piezoelectric material is necessarily ferroelectric and pyroelectric.

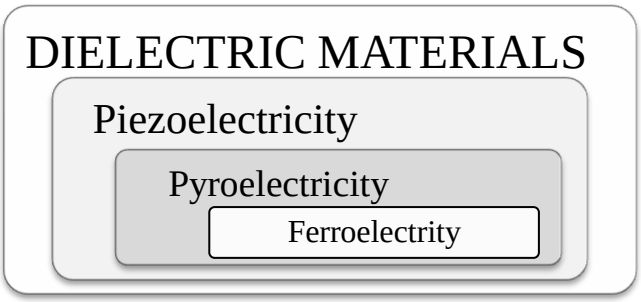

Figure 1.3. Dielectric materials and subgroups.

The connection between macroscopic piezoelectric phenomena and the structure of the dielectric materials was first demonstrated by Pierre and Jacques Curie [28]. They asserted that there was a one-to-one correspondence between the electrical effects of temperature change and mechanical stress in a given crystal, and that they had used this correspondence not only to pick the crystals for the experiment, but also to determine the cuts of those crystals. To them, their demonstration was a confirmation of predictions which followed naturally from their understanding of the microscopic crystallographic origins of pyroelectricity (i.e., from certain crystal asymmetries).

The Curie brothers did not, however, predict that crystals exhibiting the direct piezoelectric effect (electricity from applied stress) would also exhibit the converse piezoelectric effect (stress in response to applied electric field). This property was mathematically deduced by Lippmann in 1881. The Curies immediately confirmed the existence of the "converse effect".

At this point in time, the core of piezoelectric applications science was established: the identification of piezoelectric crystals on the basis of asymmetric crystal structure, the reversible exchange of electrical and mechanical energy.

In the following 25 years much more work was done to grow into a versatile and complete framework which defined completely the 20 natural crystal classes in which piezoelectric effects occur, and defined all 18 possible macroscopic piezoelectric

coefficients using appropriate tensorial analysis. In 1910 Voigt's general theory was published, and it became the standard reference work embodying the understanding which had been reached. But piezoelectricity was obscure, the mathematics required to understand it was complicated, and no publicly visible applications had been found for any of the piezoelectric crystals.

The first serious applications work on piezoelectric devices took place during World War I. In 1917, P. Langevin began to perfect an ultrasonic submarine detector. Their transducer was a mosaic of thin quartz crystals glued between two steel plates (the composite having a resonant frequency of about 50 KHz), mounted in a housing suitable for submersion.

The success of sonar stimulated intense development activity on all kinds of piezoelectric devices, both resonating and non-resonating. In fact, after World War I, most of the classic piezoelectric applications with which we are now familiar (microphones, accelerometers, ultrasonic transducers, bender element actuators, phonograph pick-ups, signal filters, etc.) were conceived and put into practice; but taking into account that the materials available in that time were very limited.

During World War II research groups working on improved capacitor materials discovered that certain ceramic materials (prepared by sintering metallic oxide powders) exhibited dielectric constants up to 100 times higher than common cut crystals. The discovery of easily manufactured piezoelectric ceramics with astonishing performance characteristics naturally touched off a revival of intense research and development into piezoelectric devices.

From the second half of the 20^{th} century until now new kinds of materials are being developed. On the one hand, inorganic pyroelectric, piezoelectric and ferroelectric effects of materials flourished principally by the development of the barium titanate family of piezoceramics and later the lead zirconate titanate family, achieving desired properties such as dielectric constant, stiffness, piezoelectric coupling coefficients, ease of poling, etc. There are examples such as, the research and development of transparent electrooptic lead lanthanum zirconate titanate (PLZT) ceramics the late 1960s, ferroelectric composites of the late 1970s, lead magnesium niobate (PMN) relaxor

ceramics and the use of sol-gel techniques for the preparation of ferroelectric films in the 1980s, the strain-amplified actuator of the early 1990s, relaxor single-crystal materials in 1997 or lead-free piezoceramics since the 2000s [29,30].

On the other hand, there were important advances in piezoelectrics from other materials with completely different nature, i.e. organic molecules and polymers. Since the 1950s, piezoelectricity was investigated in polymers of biological origin (such as cellulose and collagen) as well as synthetic optically active polymers (such as polyamides and polylactic acids). After the discovery of piezoelectricity in poled polyvinylidene fluoride (PVDF) in 1969 [31], the piezoelectricity was investigated in a number of polymers.

There are three main different categories that can be considered piezoelectric: bulk piezoelectric polymers, piezocomposites and voided charged polymers [32]. In the first category, bulk polymers, these are solid polymer films that have piezoelectric mechanism through their molecular structure and its arrangement. From this type, common examples are PVDF and its copolymers, copolymers of vinylcyanide and vinylacetate, nylons and certain polyimides. The second type is the piezoelectric composite polymer. These are polymer structures with integrated piezoelectric ceramics from which the piezoelectric effect is generated, which make use of the mechanical flexibility of polymers and the high electromechanical coupling of the piezoelectric ceramics. The third category is the voided charged polymer, a completely different type of piezoelectric than the first two categories. This is a polymer film in which gas voids are introduced and surfaces are charged in a way to form internal dipoles. The polarization of these dipoles changes with the applied stress on the polymer film, i.e. it has piezoelectric response.

In conclusion, a polymer exhibiting transducer characteristics has special advantages over the ceramic because of the more flexible and less brittle nature of polymers. Also, many polymers are biocompatible and can be used in biological applications. All of these advances contributed to establishing an entirely new method of piezoelectric device development - namely, tailoring a material to a specific application.

1.2.2. DEFINITIONS AND GENERAL CONCEPTS

Prior to advance in developing the Thesis it is necessary to explain in detail some important concepts or parameters that they need to be well defined for a full understanding.

—Dielectric materials

A dielectric material is an electrical insulator that can be polarized by an applied electric field. When it is placed in an electric field, electric charges do not flow through the material as they do in a conductor, but only slightly shift from their average equilibrium positions causing dielectric polarization, i.e. when are subjected to an external electric field undergo change in dimension, due to the displacements of positive and negative charges within the material. Because of dielectric polarization, positive charges are displaced toward the field and negative charges shift in the opposite direction. This creates an internal electric field that reduces the overall field within the dielectric itself. If a dielectric is composed of weakly bonded molecules, those molecules not only become polarized, but also reorient so that their symmetry axis aligns to the field [26].

The change in dimension can be very small or quite important, depending on the type of material (crystal, ceramic, polymer or biological). In crystals is very important the crystal class to which the dielectric belongs, because piezoelectricity in inorganic materials basically depends on crystal lattice structure, and lack of a center of symmetry in the unit crystal cell is the necessary requirement for a material to show piezoelectricity in any form (pyroelectricity and ferroelectricity). Thus among the total 32 crystal classes, 11 are centrosymmetric (possess a centre of symmetry or inversion centre) and 21 are noncentrosymmetric (do not have a centre of symmetry) [33].

When a dielectric material having a center of symmetry is subjected to an external electric field, because of symmetry (center of inversion), the movement of cations and anions are such that the extension and contraction are canceled between neighboring springs (chemical bonds) and the net strain in the crystal is ideally zero. But the chemical bonds are not perfectly harmonic and, due to the anharmonicity of the bonds,

there will be second-order effects resulting in a small net deformation of the lattice. The deformation in this case is proportional to the square of the electric field. That is, the deformation is independent of the direction of the applied electric field. This effect is called electrostrictive effect. The anharmonic effect exists in all dielectrics, and so it can be said that all dielectrics are electrostrictive.

When a dielectric material belonging to a noncentrosymmetric class (except the octahedral class) is subjected to an external electric field, there will be asymmetric movement of the neighbouring ions, resulting in significant deformation of the crystal and the deformation is directly proportional to the applied electric field. These materials exhibit an electrostrictive effect due to the anharmonicity of the bonds, but it is marked by the more significant asymmetric displacement. The materials are called piezoelectric materials. The classification of dielectric materials based on their response to external stimuli is shown in Figure 1.4.

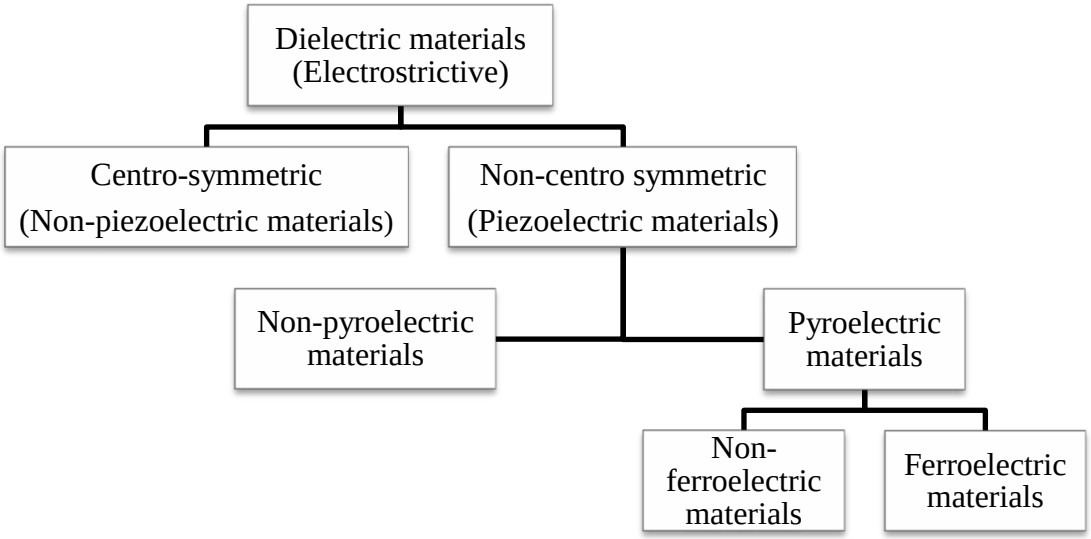

Figure 1.4. Classification of dielectric materials.

About dielectric materials there are some concepts of interest [33] for understanding piezoelectricity and for dielectric spectroscopy, a technique that it will be used in Chapter 4.

—Electric dipole moment (p)

The *electric dipole moment* shown in Figure 1.5 is a measure of the separation of positive and negative electrical charges in a system of electric charges, that is, a measure of the charge system's overall polarity and the atom or the molecule possesses an electric dipole moment given by:

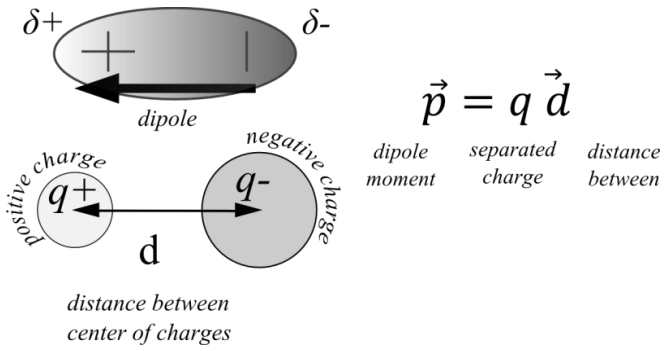

Figure 1.5. Scheme of the electric dipole moment.

where q is the charge, and d is the separation between the positive and negative charge centres. P is a vector, the direction of the vector is from the negative charge to the positive charge, and its unit is C·m (coulomb meter), but also can be expressed in a non-SI metric unit, the Debye (D), 1 D $\approx 3.33564\times10^{-30}$ C·m.

—Nonpolar and polar dielectric materials

Dielectrics materials can be classified as polar and nonpolar. In nonpolar dielectric materials, normally the atoms do not possess an electric dipole moment as the centres of positive and negative charges coincide. Examples of nonpolar dielectrics are benzene, oxygen, methane, nitrogen, etc. In these cases when they are subject to an external electric field, the centres of positive and negative charges get separated and thus dipole moments are induced. Once the electric field is removed the induced dipole moments disappear.

In polar dielectric materials the situation is different, each atom or molecule possesses a dipole moment as the centres of positive and negative charges do not coincide. Typical examples of polar dielectrics are water, HCl, alcohol, NH_3, etc. Most of the ceramics

and polymers are from this category. When an external electric field is applied to these materials, the electric dipoles tend to orient themselves in the direction of the field.

—Electric Polarization (P)

Electric polarization (polarization density or polarization, P) is the vector field that expresses the density of permanent or induced electric dipole moments in a dielectric material. It is defined as the total dipole moment per unit volume and is given by:

$$\vec{P} = \frac{\sum_i \overrightarrow{p_i}}{V} \tag{1.1}$$

where V is the volume of the material. The unit of P is $C \cdot m^{-2}$ (coulomb·meter^{-2}), and it is sometimes called the *surface charge density.* P is a vector normal to the surface of the material.

A polar dielectric material consists of a large number of atoms or molecules each possessing an electric dipole moment. The total or the net dipole moment of the dielectric material is the vector sum of all the individual dipole moments given by:

$$\sum_i \overrightarrow{p_i} \tag{1.2}$$

Normally, in a polar dielectric, the individual electric dipoles are all randomly oriented and so the net polarization is zero. When an electric field is applied, the individual dipoles tend to orient themselves in the direction of the electric field and the material develops a finite polarization (Figure 1.6). The polarization increases with an increasing electric field and attains saturation when all the dipole moments are oriented in the direction of the field.

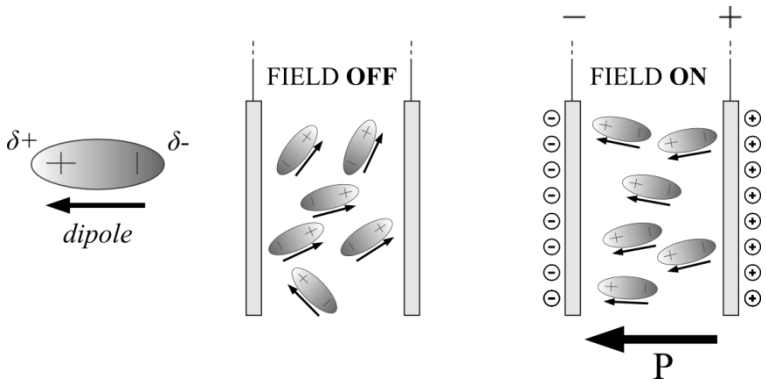

Figure 1.6. Representation of the electric polarization.

—Dielectric Displacement or Flux Density (D), Dielectric Constant (ε_r), and Electric Susceptibility (χ)

In a dielectric material the presence of an electric field (E) develops a finite polarization (P, induced polarization in nonpolar materials and orientation polarization in polar materials). The electric flux density (D) developed inside the material due to the external field (E) is given by:

$$\vec{D} = \varepsilon_0 \vec{E} + \vec{P} = \varepsilon \vec{E} = \varepsilon_0 \varepsilon_r \vec{E} \tag{1.3}$$

where ε_0 is the permittivity of free space ($8.854 \cdot 10^{-12}$ F·m^{-1}) and ε_r is the relative permittivity or dielectric constant of the dielectric material. The unit of D is C·m^{-2}.

The dielectric constant is also defined by the ratio:

$$\varepsilon_r = \frac{D}{\varepsilon_0 E} \tag{1.4}$$

ε_r is a unitless quantity and is always greater than 1.

The polarization (P) is directly related to the applied electric field by the relation:

$$\vec{P} = \varepsilon_0 \chi \vec{E} \tag{1.5}$$

Where χ is called the electric susceptibility of the material. From the equations we get the relation between the dielectric constant and the electric susceptibility as:

$$\varepsilon_r = 1 + \chi \tag{1.6}$$

—Spontaneous Polarization (P_S)

The spontaneous polarization is electric polarization that a substance possesses in the absence of an external electric field. Pyroelectric and ferroelectric materials exhibit spontaneous polarization. In pyroelectric materials, the spontaneous polarization is not observed normally as the surface charges get compensated by the free charges in the surroundings. But the spontaneous polarization decreases when the material is heated, and so the change in polarization on heating can be observed. In ferroelectric materials, the direction of spontaneous polarization can be changed by applying an external electric field.

—Electrostrictive Effect

Electrostriction is a property of all dielectric materials, and is caused by the presence of randomly aligned electrical domains within the material. Application of an external electric field polarizes the material. This process involves the orientation of the dipoles that results in deformation of the material. The strain x is related to the polarization P by:

$$x = QP^2 \tag{1.7}$$

where Q is the *electrostrictive coefficient.* Noting that for materials with high dielectric constant $P \gg \varepsilon_0 E$, we can write:

$$x = QD^2 = Q\varepsilon^2 E^2 \tag{1.8}$$

The previous equation describes the electrostrictive effect in which the resulting strain is proportional to the square of the electric field. Thus, the strain generated is independent of the polarity of the applied field.

—Piezoelectric Effect

In inorganic piezoelectric crystalline materials, when they are subjected to an external electric field, there will be asymmetric displacements of anions and cations that cause considerable net deformation of the crystal. In piezoelectric materials, the relationship between induced charges per unit area and the applied stress is linear and reversible.The resulting strain is directly proportional to the applied electric field unlike electrostrictive materials in which the strain is proportional to E^2. The strain in a piezoelectric material is extensive or compressive, depending on the polarity of the applied field. This effect is called the *indirect piezoelectric effect* or *motor action.*

The direct and indirect piezoelectric effects are illustrated in Figure 1.7 and 1.8. The direct piezoelectric effect is seen as a voltage produced when the material is under tension or compression stress. Each of these two types of stress generate opposite polarity voltages in the materials. Thus, the deformation of the material brings the polarized dipoles closer into line, so that the positive and negative ends come closer together. As this happens the electric dipoles have a cumulative effect and a potential difference is set up over the whole crystal. The potential difference set up causes a positive charge at one end and a negative charge at the other end of the material.

The inverted effect is also reciprocal and occurs by exactly the opposite mechanism, when a potential difference is applied across and causes it to deform. An electric potential difference (voltage) is placed across the material and at great enough voltage the electric field within the material will then create a large enough force on the dipoles to move them into alignment in order to lower the energy of the system. The voltage needed to cause this effect is greater than the potential used for the initial poling process. This effect is also impermanent - there is an elastic relaxation to the original shape when the potential difference is removed, whereas a poled material remains poled even when the field is removed. That is, when an external voltage is applied to the material, the material gets extended if the polarity of the voltage is the same as that of the field applied during poling and, when the voltage is applied in the reverse direction, the material gets compressed (Figure 1.8).

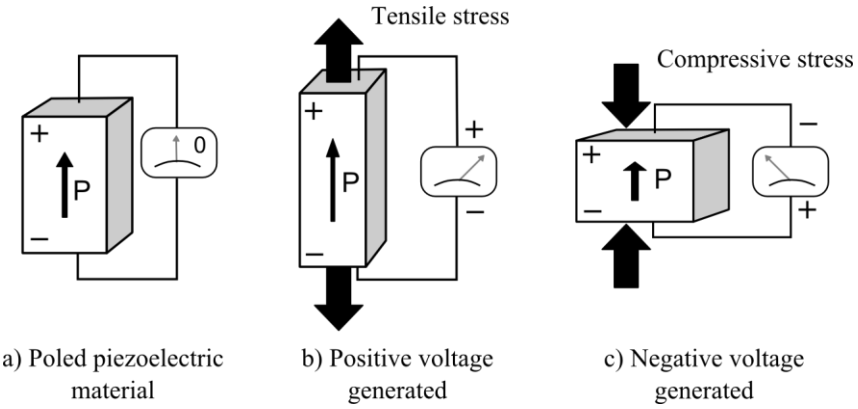

Figure 1.7. Direct piezoelectric effect: a) Poled piezoelectric material. b) When tensile stress is applied to the material, the material develops voltage across its face with the same polarity as the poling voltage. c) When a compressive stress is applied to the material, the material develops voltage with polarity opposite to that of the poling voltage.

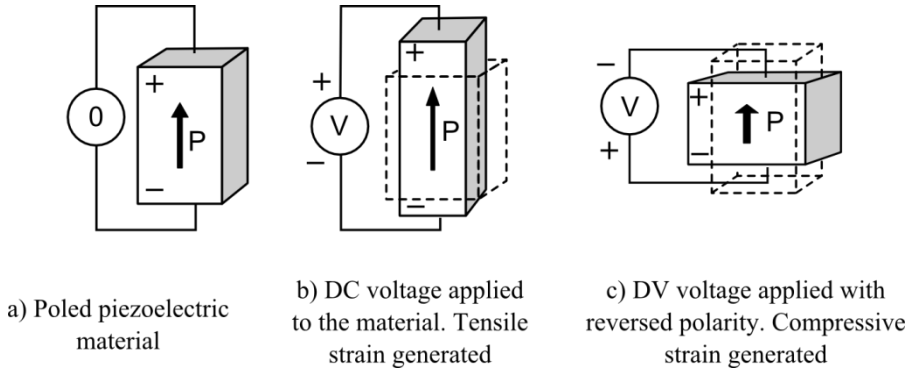

Figure 1.8. Indirect piezoelectric effect: a) Poled piezoelectric material. b) When a DC field is applied with the same polarity as the poling field, the material develops tensile strain. c) When a DC field is applied in the reverse direction, the material develops compressive strain.

—Pyroelectric Effect

Pyroelectricity (from the Greek *pyr*, fire, and electricity) is the ability of certain materials to generate a temporary voltage when they are heated or cooled [34]. Pyroelectric materials exhibit spontaneous polarization (dipole moment per unit volume of the material), but their polarization cannot be reoriented by application of external

electric fields. Normally, in these materials, the spontaneous polarization cannot be observed as the surface charges get compensated by free charges in the surroundings. But when the material is heated, the spontaneous polarization decreases and this change in polarization can be measured, which it is very useful for sensors to detect infrared radiation.

The pyroelectric effect is described by the equation:

$$dP_S = -p\, dT \tag{1.9}$$

where dT is the change in temperature, and dP_S is the corresponding change in the spontaneous polarization. p is the pyroelectric coefficient ($C \cdot m^{-2} \cdot K^{-1}$). The negative sign indicates that the spontaneous polarization decreases with increasing temperature. Since temperature is a scalar and polarization is a vector, the pyroelectric coefficient is a vector.

To understand the nature of the pyroelectric effect, consider an example: a thin, parallel-sided sample of material, cut so that its crystallographic symmetry axis is perpendicular to the flat surfaces. The unit cells of pyroelectric materials have a dipole moment. The dipoles are packed so that the components of the dipole moment in each unit cell add up in the direction normal to the flat surfaces. Always nonzero in a pyroelectric material, P_S, exists in the absence of an applied electric field and is equivalent to a layer of bound charge on each flat surface of the sample.

Nearby free charges such as electrons or ions will be attracted to the sample. Imagine that conductive electrodes are then attached to the surfaces and connected through an ammeter having a low internal resistance. If the temperature of the sample is constant, then so is P_S and no current flows through the circuit. But an increase in temperature causes the net dipole moment and, consequently, the spontaneous polarization to decrease. Then the quantity of bound charge decreases, and a current flow in the circuit (the pyroelectric current) results from the redistribution of free charges to compensate for the change in bound charge. That is, when a pyroelectric material with an intrinsic dipole moment (Figure 1.9a) is fashioned into a circuit with electrodes attached on each surface (Figure 1.9b), there is an increase in temperature prompts the spontaneous

polarization P_S to decrease as the dipole moments, on average, diminish in magnitude. The horizontal tilting of the dipoles (Figure 1.9c) signifies the effect. A current flows to compensate for the change in bound charge that accumulates on the crystal edges.

But if the sample had been cooled instead of heated, the current's sign would be reversed. Remembering that the pyroelectric effect is only observable during the period in which the temperature changes, and that in an open circuit, the free charges would simply remain on the electrodes and a voltage could be measured.

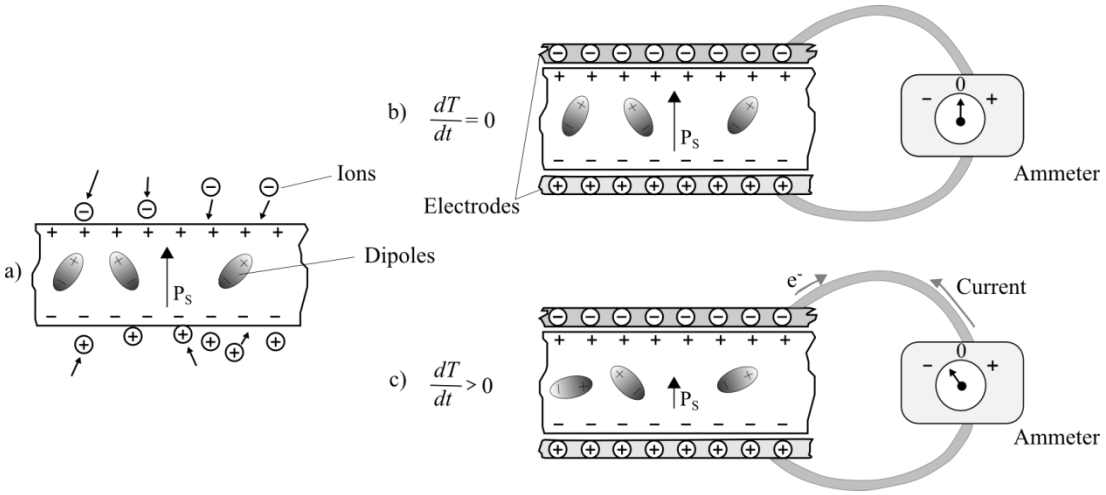

Figure 1.9. Representation of the pyroelectric effect.

—Ferroelectric materials

Ferroelectricity is a term used in analogy to ferromagnetism, in which a material exhibits a permanent magnetic moment. Ferroelectric materials are a subclass of pyroelectric materials, which are again a subclass of piezoelectric materials. Thus, ferroelectric materials exhibit both piezoelectric and pyroelectric properties. They exhibit spontaneous polarization such as pyroelectrics, but they have the characteristic property of *reversible polarization*. That is, the spontaneous polarization can be reversed by applying an external electric field. Ferroelectrics are characterized by the following properties:

Ferroelectric hysteresis	Spontaneous polarization	Reversible polarization	Ferroelectric transition temperature

In a ferroelectric material, the polarization P as a function of the applied electric field E is nonlinear, and is related with the existence of domains. Ferroelectric domain is defined as a small microscopic region in the material within which all the electric dipoles are oriented in the same direction due to a strong short-range interaction caused by internal electric fields. A ferroelectric material consists of a large number of domains with each domain having a specific polarization direction. Normally, the domains are randomly oriented, and so the net polarization of the material is zero in the absence of an external electric field (E). When an external electrical field is applied, the domains tend to get oriented in the direction of the applied field. That is, the domains that are in the direction of the external field grow in size at the expense of the other domains. As the external field is increased, more and more domains get oriented in the direction and ultimately the material ideally consists of a single domain (Figure 1.10).

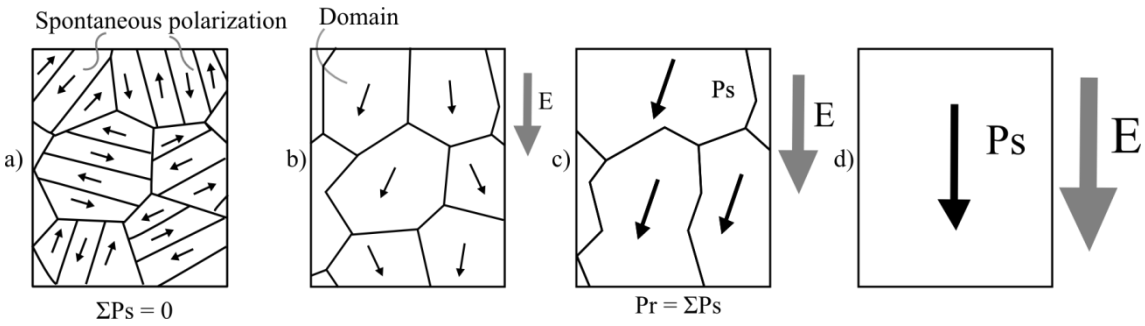

Figure 1.10. Behavior of ferroelectric materials in the presence of electric fields.

Hysteresis is the dependence of the output of a system not only on its current input, but also on its history of past inputs. The dependence arises because the history affects the value of an internal state. The variation of polarization with an applied electric field in a ferroelectric material is shown in Figure 1.11.

Initially, when the applied field is zero, the ferroelectric domains are all randomly oriented and so the polarization is zero (point O). As the field is increased, the domains

get oriented in the direction of the field, and the polarization increases linearly in the beginning. This is shown by the portion of the curve OA. As the field is further increased, more and more domains get oriented, the curve becomes nonlinear, and ultimately when all the domains get oriented, the polarization attains the maximum value (point C). The polarization at this point is called *saturation polarization* (P_S). If the electric field is now reduced gradually, the polarization decreases but the curve is not retraced. The decrease in polarization is rather slow; that is, the polarization lags behind the electric field. When the field is reduced to zero, there remains a finite polarization called the *remnant polarization* (P_R). In order to make the remnant polarization disappear, an electric field in the reverse direction has to be applied. At an electric field of $-E_C$ called the *coercitive field*, the polarization becomes zero (at point E). If the field is further increased in the reverse direction beyond E_C, the domains get oriented in the direction of the field and the polarization increases with increasing field (in the new reversed direction). The polarization attains the maximum value, saturation polarization ($-P_S$) in the reverse direction (at F). If the field is now again reduced back to zero, the curve traces the path GH and there will be a remnant polarization $-P_R$ (at G). If the field is increased from zero in the positive direction, the remnant polarization disappear when the field is $+E_C$. Further increase in the field will close the loop. The closed loop is called the *hysteresis curve*.

Ferroelectric material loses its spontaneous polarization beyond a certain temperature. This temperature is called the *ferroelectric transition temperature.* At this temperature, the material is said to undergo a transition from ferroelectric phase to a paraelectric phase.

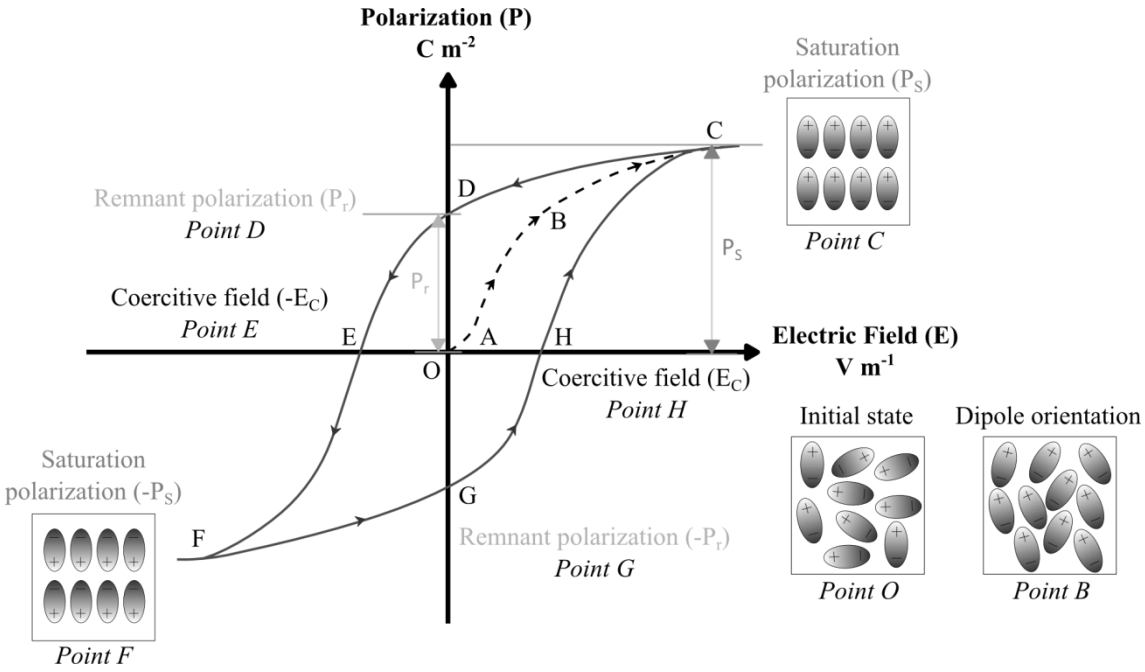

Figure 1.11. Hysteresis curve of a ferroelectric material.

—Poling

Piezoelectric materials need to be poled. Poling is the process of generating net remnant polarization in the material by applying sufficiently high electric field. When a high electric field is applied to a piezoelectric material, the dipoles orient themselves in the direction of that field. The material in this state possesses maximum polarization. If the material is maintained at a high temperature (close to the transition temperature) while the electric field is applied, the orientation of the dipoles is better facilitated.

Note: There will be further explanations in Chapter 3. Poling is one of the most important parts in piezoelectric materials, because it is the critical element in being able to utilize the piezoelectric effect, without poling, the material is not piezoelectric.

—Piezoelectric coefficients

Previously it was said that two effects are operative in piezoelectric materials. In the direct piezoelectric effect (designated as a generator), the input is mechanical energy and the output is electrical energy, whereas in the indirect effect (designated as a motor) is just the contrary, the input is electrical energy and the output is mechanical energy. Mechanical input can be in the form of external stress (X) or strain (x). Electrical output is in the form of surface charge density (D or P), electric field (E), or voltage (V) (Figure 1.12).

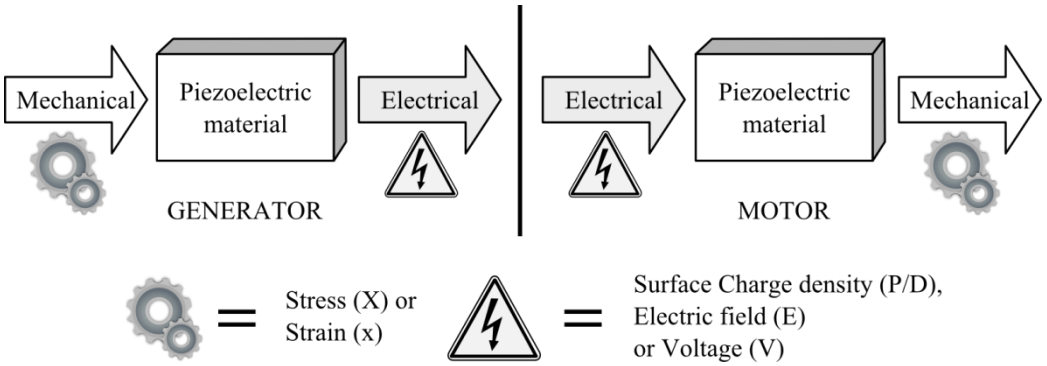

Figure 1.12. Direct (Left) and indirect (Right) piezoelectric effect.

The basic equations that describe these two effects in regard to electric and elastic properties are:

$$D = dX + \varepsilon^X E \qquad \text{(generator)} \qquad (1.10)$$

$$x = s^E X + dE \qquad \text{(motor)} \qquad (1.11)$$

where D is the dielectric displacement (consider it equal to polarization), X the stress, E the electric field, s the material compliance (inverse of modulus of elasticity), and ε the dielectric constant (permittivity). The superscripts indicate a quantity held constant: in the case of ε^X, the stress is held constant, which means that the piezoelectric element is mechanically unconstrained, and, in the case of s^E, the electric field is held constant, which means the electrodes on the element are shorted together.

The parameters that describe the sensitivity of a piezoelectric material are the piezoelectric coefficients that relate the input and output parameters. The piezoelectric effect is a transient effect, which means that the observed parameter is not an absolute value but it is the change in the parameter. In the direct piezoelectric effect, a change in strain δx (or in stress δX) causes a change in the polarization δD (or a change in the electric field δE). In the indirect piezoelectric effect, a change in the applied field δE (or polarization δD) causes a change in the strain δx (or stress δX).

The various piezoelectric coefficients can be defined by the following partial derivatives summarized in Table 1.3, with their definitions and units.

Table 1.3. Piezoelectric Coefficients, definitions and units.

Piezoelectric Coefficient	**Definition**	**Unit**	**Indirect Piezoelectric Coefficient**	**Definition**	**Unit**
$d = \left(\frac{\partial D}{\partial X}\right)_E$	$\frac{polarization}{stress}$	C·N^{-1}	$d^* = \left(\frac{\partial x}{\partial E}\right)_X$	$\frac{strain}{electric\ field}$	m·V^{-1}
$g = -\left(\frac{\partial E}{\partial X}\right)_D$	$\frac{electric\ field}{stress}$	V·m·N^{-1}	$g^* = \left(\frac{\partial x}{\partial D}\right)_X$	$\frac{strain}{polarization}$	m^2·C^{-1}
$e = \left(\frac{\partial D}{\partial x}\right)_E$	$\frac{polarization}{strain}$	C·m^{-2}	$e^* = -\left(\frac{\partial X}{\partial E}\right)_X$	$\frac{stress}{electric\ field}$	N·V^{-1}·m^{-1}
$h = -\left(\frac{\partial E}{\partial x}\right)_D$	$\frac{electric\ field}{strain}$	V·m^{-1}	$h^* = -\left(\frac{\partial X}{\partial D}\right)_X$	$\frac{stress}{polarization}$	N·C^{-1}

Piezoelectric coefficients, elastic constants, and permittivity are all tensors as they relate vectors and tensors. Since the piezoelectric coupling is described by a linear relationship between the first-rank tensor or vector (D or E) and the second-rank tensor (X), the corresponding coupling coefficients d_{kji} (also called charge piezoelectric coefficients)

form a third-rank tensor. Hence, the piezoelectric equations may be written in the following form (i, j, k = 1, 2, 3):

$$S_{ij} = d_{kij}E_k \tag{1.12}$$

$$D_k = d_{kij}X_{ij} \tag{1.13}$$

where the Einstein's summation rule for repeated indices is implied. Both direct and converse piezoelectric effects are frequently expressed using the reduced matrix notation d_{km}, where k denotes the component of electric displacement D or field E in the Cartesian reference frame (x_1, x_2, x_3), and the index $m = 1,\ldots,6$ is used to define the mechanical stress or strain. In this case, $m = 1$, 2, and 3 correspond to the normal stresses along the x_1, x_2, and x_3 axes, respectively, whereas $m = 4$, 5, and 6 denote the stress X_{23}, X_{13}, and X_{12}.

The system of coordinates is the right-handed Cartesian coordinate system. The *X*-, *Y*-, and *Z*-axes are represented by *1*, *2*, and *3*, respectively, and the rotations about the *X*-, *Y*-, and *Z*-axes are represented by *4*, *5*, and *6* as shown in Figure 1.13.

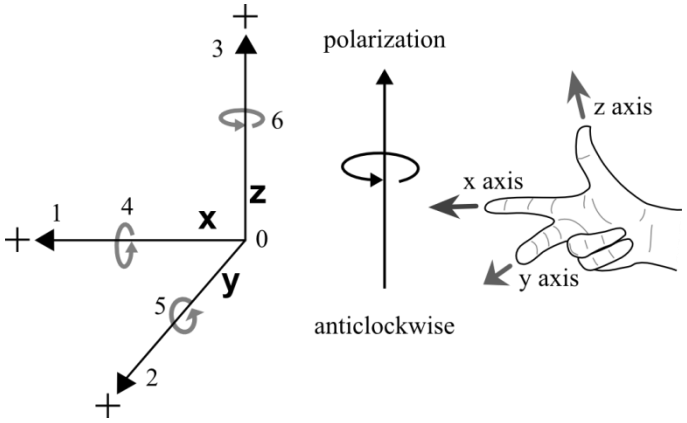

Figure 1.13. Right-handed Cartesian coordinate system. Directions 1, 2, and 3 represent the axes X, Y, and Z, respectively, and 4, 5, and 6 represent rotations (anticlockwise) about the three axes X, Y, and Z.

For example, with the piezoelectric coefficient (d), considering the direct piezoelectric effect that relates the polarization (D) and the stress (X):

$$D = dX \tag{1.14}$$

It may be written in the matrix form, where the piezoelectric coefficient d is represented as a 3 x 6 matrix:

$$\begin{pmatrix} D_1 \\ D_2 \\ D_3 \end{pmatrix} = \begin{pmatrix} d_{11} & d_{12} & d_{13} & d_{14} & d_{15} & d_{16} \\ d_{21} & d_{22} & d_{23} & d_{24} & d_{25} & d_{26} \\ d_{31} & d_{32} & d_{33} & d_{34} & d_{35} & d_{36} \end{pmatrix} \begin{pmatrix} X_1 \\ X_2 \\ X_3 \\ X_4 \\ X_5 \\ X_6 \end{pmatrix} \tag{1.15}$$

But the piezoelectric tensor of polymers is described by only five piezoelectric coefficients: transverse piezoelectric coefficients (d_{31} and d_{32}), the longitudinal piezoelectric coefficient (d_{33}) and the shear coefficients (d_{15} and d_{24}):

$$d = \begin{pmatrix} 0 & 0 & 0 & 0 & d_{15} & 0 \\ 0 & 0 & 0 & d_{24} & 0 & 0 \\ d_{31} & d_{32} & d_{33} & 0 & 0 & 0 \end{pmatrix} \tag{1.16}$$

Similarly, in the indirect piezoelectric effect, the equation that relates the electric field E with the stress X is written in the matrix form as:

$$\begin{pmatrix} X_1 \\ X_2 \\ X_3 \\ X_4 \\ X_5 \\ X_6 \end{pmatrix} = \begin{pmatrix} e_{11} & e_{12} & e_{13} \\ e_{21} & e_{22} & e_{23} \\ e_{31} & e_{32} & e_{33} \\ e_{41} & e_{42} & e_{43} \\ e_{51} & e_{52} & e_{53} \\ e_{61} & e_{62} & e_{63} \end{pmatrix} \begin{pmatrix} E_1 \\ E_2 \\ E_3 \end{pmatrix} \tag{1.17}$$

Thus, in the indirect piezoelectric effect, the piezoelectric coefficient e is represented as a 6 x 3 matrix.

—Interpretation of Piezoelectric Coefficients d_{33} and d_{31}

Previously it was said that the piezoelectric d coefficient has the units of coulombs. Newton^{-1} or meters. volt^{-1}. There are other piezoelectric coefficients that are defined in different ways such as the piezoelectric stress coefficient, e, the piezoelectric voltage coefficient, g, and the inverse piezoelectric strain coefficient, h. They are all related and can be derived from one another but I will restrict only to the d coefficient.

In most of the piezoelectric materials, there are only 3 or 4 piezoelectric coefficient elements and the rest of the elements are zero in the (3 x 6) tensor. The two popular and common elements in most piezoelectric materials are d_{33} and d_{31}.

The d_{33} mode, also called the longitudinal mode (Figure 1.14, Left), is the induced polarization per unit applied stress in direction 3. Alternatively it is the induced strain per unit electric field in direction 3. The coefficient relates D and X by the relation:

$$D_3 = d_{33} X_3 \tag{1.18}$$

The d_{31} coefficient, or the transverse mode (Figure 1.14, Right), is the induced polarization in direction 3 per unit stress applied in direction 1. Alternatively it is the mechanical strain induced in the material in direction 1 per unit electric field applied in direction 3. The coefficient relates D and X by the relation:

$$D_3 = d_{31} X_1 \tag{1.19}$$

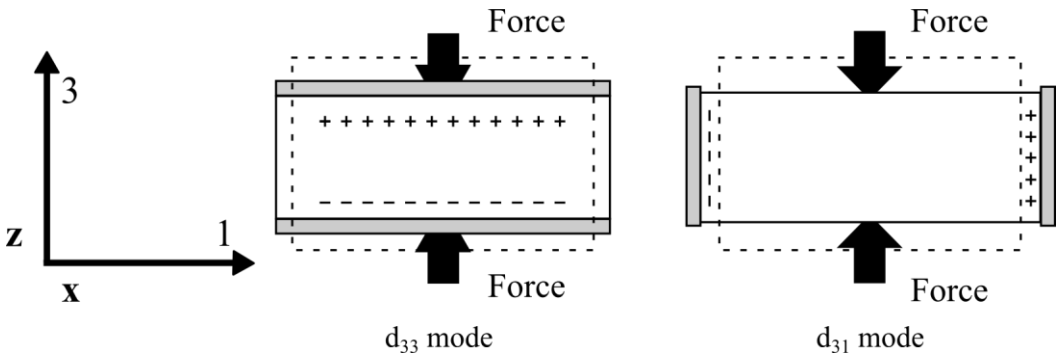

Figure 1.14. The piezoelectric transduction modes. d_{33} (Left) and d_{31} (Right).

Similarly, the rest of direct and indirect piezoelectric coefficients can be interpreted, as they were the coefficients d_{33} and d_{31}.

—Dielectric Parameter: Permittivity

The permittivity (or dielectric constant) is defined as the dielectric displacement per unit electric field. The first subscript gives the direction of the dielectric displacement, the second gives the direction of the electric field.

The permittivity (ε), relates the vectors D and E, and so it is a second-rank tensor:

$$D_i = \varepsilon_{ij} E_j \tag{1.20}$$

The subscripts *i* and *j* each take values 1, 2, and 3. The tensor form of the equation is:

$$\begin{bmatrix} D_1 \\ D_2 \\ D_3 \end{bmatrix} = \begin{bmatrix} \varepsilon_{11} & \varepsilon_{12} & \varepsilon_{13} \\ \varepsilon_{21} & \varepsilon_{22} & \varepsilon_{23} \\ \varepsilon_{31} & \varepsilon_{32} & \varepsilon_{33} \end{bmatrix} \begin{bmatrix} E_1 \\ E_2 \\ E_3 \end{bmatrix} \tag{1.21}$$

Thus, the permittivity is a 3 x 3 tensor.

—Piezoelectric Coupling Coefficient (k)

Piezoelectric coupling is a numerical measure of the efficiency of a piezoelectric material as a transducer. It quantifies the ability of the piezoelectric material to convert one form of mechanical or electrical energy to the form electrical or mechanical. It is defined by:

$$k^2 = \frac{(Piezoelectric\ energy\ density\ stored\ in\ the\ material)^2}{Electrical\ energy\ density\ \times\ Mechanical\ energy\ density} \tag{1.22}$$

The coupling coefficient is the ratio of useable energy delivered by the piezoelectric element to the total energy taken up by the element. *k* values depend on the design of the device and the direction of the applied stimulus and the measured response.

The coupling coefficient can be written with subscripts just like piezoelectric constants to denote the direction of the external stimulus and the direction of measurement.

—Dynamic Behavior of a Piezoelectric Material

When exposed to an AC electric field, a piezoelectric element changes dimensions cyclically, at the cycling frequency of the field. The frequency at which the ceramic element vibrates most readily, and most efficiently converts the electrical energy input into mechanical energy, is the *resonance frequency.*

For the analysis of the dynamic behavior of a vibrating piezoelectric material, an equivalent electrical circuit is used (Figure 1.15).

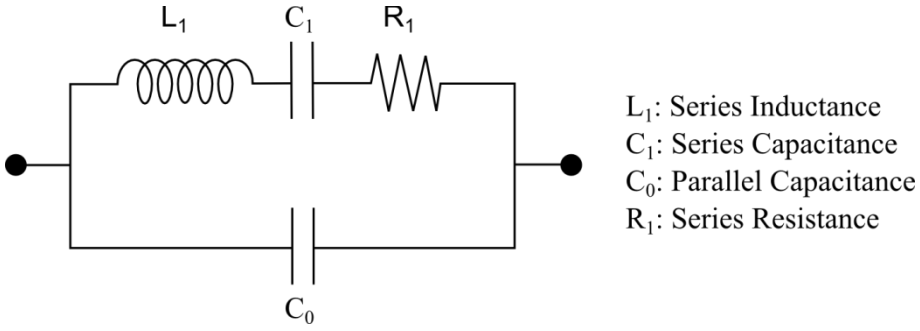

Figure 1.15. Equivalent circuit of transducer.

The impedance of the vibrating system is a function of frequency. The variation of the impedance as a function of frequency for such a system is shown in Figure 1.16. The impedance shows a minimum and a maximum as shown in the figure. The frequency at which the impedance is minimum is called the *resonance frequency*, and the frequency at which the impedance is a maximum is called the *antiresonance frequency.*

At the resonance frequency (f_m), the piezoelectric system vibrates with maximum amplitude. Resonance frequency obtained from the equivalent circuit near the resonance frequency and anti-resonance frequency can be expressed by the following equations:

$$f_m = f_s = \frac{1}{2\pi}\sqrt{\frac{1}{LC}} \tag{1.23}$$

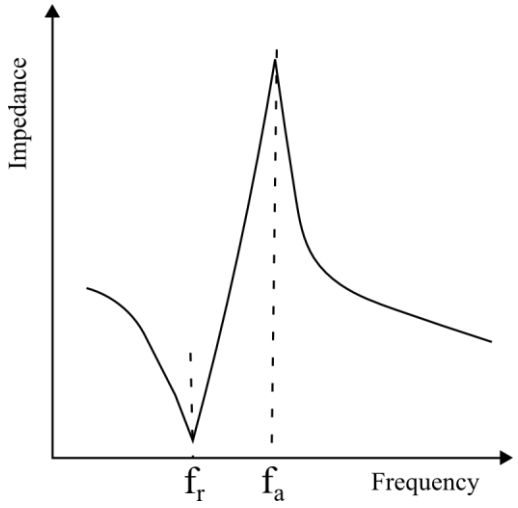

Figure 1.16. Frequency response of a piezoelectric element.

The antiresonance frequency (f_a) is equal to the parallel resonance frequency (f_p) of the equivalent electrical circuit, assuming that the resistance due to mechanical loss is zero.

$$f_a = f_p = \frac{1}{2\pi}\sqrt{\frac{C + C_0}{LCC_0}} \tag{1.24}$$

Resonance and antiresonance frequencies can be experimentally measured for a piezoelectric element. The values of f_r and f_a can be used to evaluate the electromechanical coupling coefficient k. The relation between coupling coefficient and the frequencies f_r and f_a depends on the shape of the piezoelectric element.

1.2.3. TYPES OF PIEZOELECTRIC MATERIALS

A. CERAMICS

Since the discovery of piezoelectricity in 1880 and the ferroelectricity in 1921, in single-crystal materials and its subsequent extension into the realm of polycrystalline ceramic (barium titanate, $BaTiO_3$) during the early to mid-1940s, there has been a continuous succession of new materials and technology developments that have led to a significant number of industrial and commercial applications, ranging from high-dielectric-constant capacitors to piezoelectric transducers or positive temperature coefficient devices [35]. Since that time, ferroelectric ceramics based on two systems, barium titanate and lead zirconate titanate, have dominated the field.

These ceramic materials proved to be very interesting when in 1945 was discovered that an external electric field could orient the domains within the material, thus producing a ceramic material that acted very similar to a single crystal possessing both ferroelectric and piezoelectric properties. This electrical aligning, or poling process, was identified as the key to turning an inert ceramic into an electromechanically active material with a multitude of industrial commercial uses. This was a very important discovery, since without poling that ceramics could not be piezoelectrically active, because the randomly oriented crystallites would, on the whole, cancel out each other.

In general, the fundamental steps that were critical to the understanding of ferroelectricity and piezoelectricity in ceramics were the discovery of the unusually high dielectric constant which is due to its ferroelectric (permanent internal dipole moment) nature, thus ushering in a new class of ferroelectric (the simple oxygen octahedral ABO_3 group), and the discovery of the electrical poling process that aligns the internal dipoles of the crystallites (domains) within the ceramic and causes it to act very similar to a single crystal.

An understanding of the concept of piezoelectricity in inorganic solids begins with an understanding of the internal structure of the material; for purposes here, consider a single crystallite. This crystallite has a definite chemical composition and, hence, is

made up of ions (atoms with positive or negative charge) that are constrained to occupy positions in a specific repeating relationship to each other, thus building up the structure or lattice of the crystal. The smallest repeating unit of the lattice is called the unit cell, and the specific symmetry possessed by the unit cell determines whether it is possible for piezoelectricity to exist in the crystal. Furthermore, the symmetry of a crystal's internal structure is reflected in the symmetry of its external properties (Neumann's principle).

The elements of symmetry that are utilized by crystallographers to define symmetry about a point in space, e.g., the central point of a unit cell, are (1) a center of symmetry, (2) axes of rotation, (3) mirror planes, and (4) combinations of these. All crystals can be divided into 32 different classes or point groups utilizing these symmetry elements, as shown in Figure 1.17. These 32 point groups are subdivisions of seven basic crystal systems that are, in order of ascending symmetry, triclinic, monoclinic, orthorhombic, tetragonal, rhombohedral (trigonal), hexagonal, and cubic. Of the 32 point groups, 21 classes are noncentrosymmetric (a necessary condition for piezoelectricity to exist in ceramics) and 20 of these are piezoelectric. One class, although lacking a center of symmetry, is not piezoelectric because of other combined symmetry elements. A lack of a center of symmetry is all-important for the presence of piezoelectricity when one considers that a homogeneous stress is centrosymmetric and cannot produce an unsymmetric result, such as vector-quantity-like polarization, unless the material lacks a center of symmetry, whereby a net movement of the positive and negative ions with respect to each other (as a result of the stress) produces electric dipoles, i.e., polarization. Furthermore, for those materials that are piezoelectric but not ferroelectric (i.e., they do not possess spontaneous polarization), the stress itself is the only means by which the dipoles are generated. For piezoelectricity, the effect is linear and reversible, and the magnitude of the polarization is dependent on the magnitude of the stress and the sign of the charge produced is dependent on the type of stress (tensile or compressive).

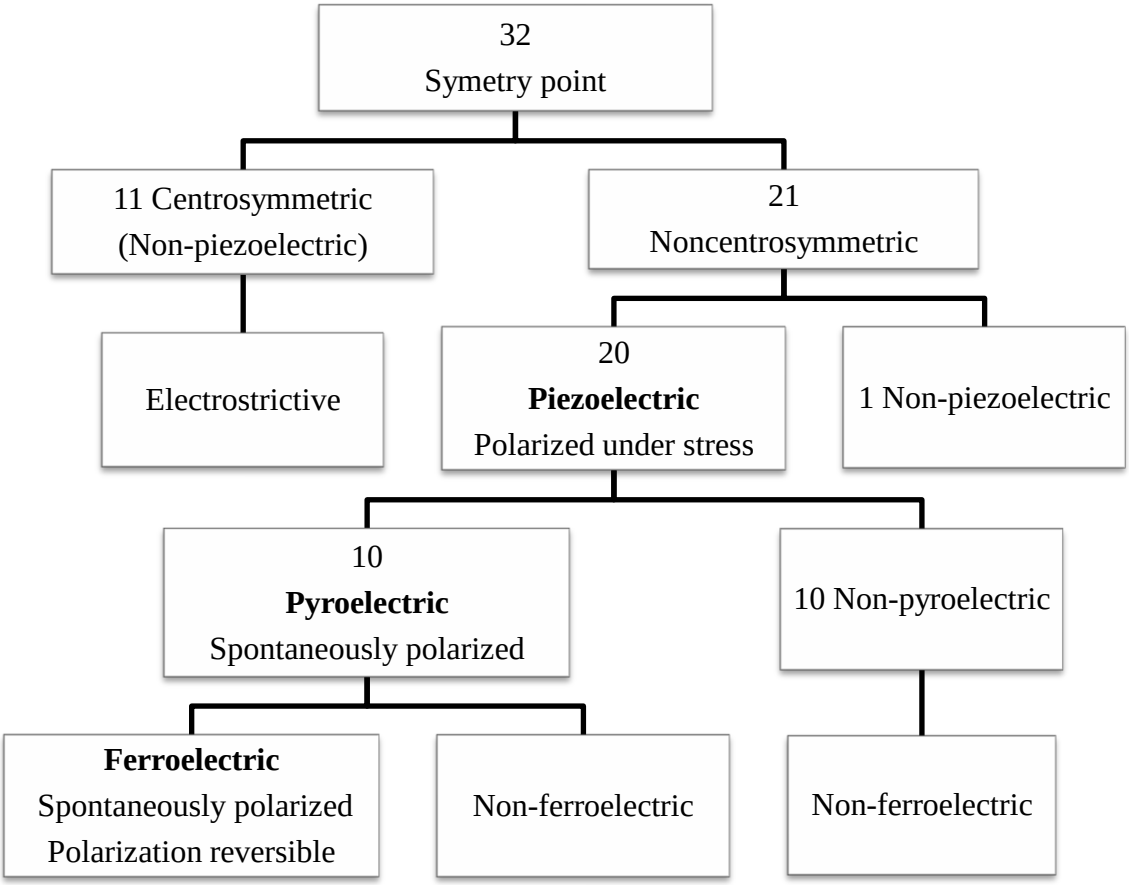

Figure 1.17. Grouping of crystal classes according to their piezoelectric, pyroelectric, ferroelectric and electrostrictive properties.

Four types of ceramic ferroelectrics are given in Figure 1.18, as subcategories of the general group of ferroelectric materials, with typical examples representing the type based on its unit cell structure: the tungsten-bronze group, the oxygen octahedral group, the pyrochlore group, and the bismuth layer-structure group. Of these, the second group (ABO_3 perovskite type) is by far the most important category, economically. The families of compositions listed: barium titanate ($BaTiO_3$), lead zirconium titanate ($Pb(Zr_{1-x}Ti_x)O_3$) or PZT), perovskite lead lanthanum zirconate titanate (PLZT), lead titanate (PT), lead magnesium niobate (PMN), and sodium potassium niobate ($(Na,K)NbO_3$, represent the majority of the ferroelectric ceramics manufactured in the world today. These ceramics show values of piezoelectric coefficient d_{33} of 150 up to 700 $pC \cdot N^{-1}$ approximately, depending on the type and processing conditions.

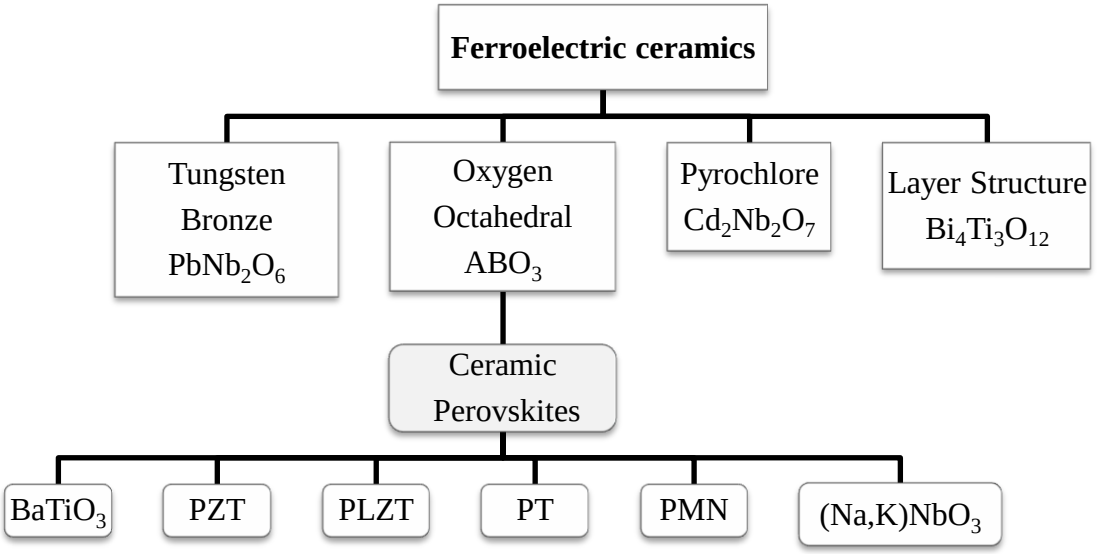

Figure 1.18. Classes of ferroelectric ceramics.

A typical ABO_3 unit-cell structure is give in Figure 1.19. For example, the PLZT unit cell consists of a corner-linked network of oxygen octahedra with Zr^{4+} and Ti^{4+} ions occupying sites (B sites) within the octahedral cage and the Pb^{2+} and La^{3+} ions situated in the interstices (a sites) created by the linked octahedra. As a result of the different valency between Pb^{2+} and La^{3+}, some of the A sites and B sites are vacant (referred to as vacancies) to maintain electrical neutrality in the structure.

When an electric field is applied to this unit cell, the Ti^{4+} or Zr^{4+} ion moves to a new position along the direction of the applied field. Because the crystallite and, hence, the unit cell is randomly oriented and the ions are constrained to move only along certain crystallographic directions of the unit cell, it is most often the case that an individual ionic movement only closely approximates an alignment with the electric field. However, when this ionic movement does occur, it leads to a macroscopic change in the dimensions of the unit cell and the ceramic as a whole. The dimensional change can be as large as a few tenths of a percent elongation in the direction of the field and approximately one-half that amount in the other two orthogonal directions. The original random orientation of the domain polarization vectors can be restored by heating the material above its Curie temperature (T_C). This process is known as thermal depoling.

Also shown in Figure 1.19 is the reversibility of the polarization caused by the displacement of the central Ti^{4+} or Zr^{4+} ion. Displacement is illustrated here as occurring along the **c** axis in a tetragonal structure, although it should be understood that it can also occur along the orthogonal *a* or *b* axes as well. The views of "polarization up" and "polarization down" (representing 180º polarization reversal) show two of the six possible permanent polarization positions.

When many of these unit cells, which are adjacent to each other, switch in like manner, this is referred to as domain reorientation or switching. The homogeneous areas of the material with the same polarization orientation are referred to as domains, with domain walls existing between areas of unlike polarization orientation. There exists in tetragonal materials both 90º (strain-producing domains on switching) and 180º a domain remaining as nonstrain producing. Macroscopic charges occur in the dimensions of the material when strain-producing domains are switched.

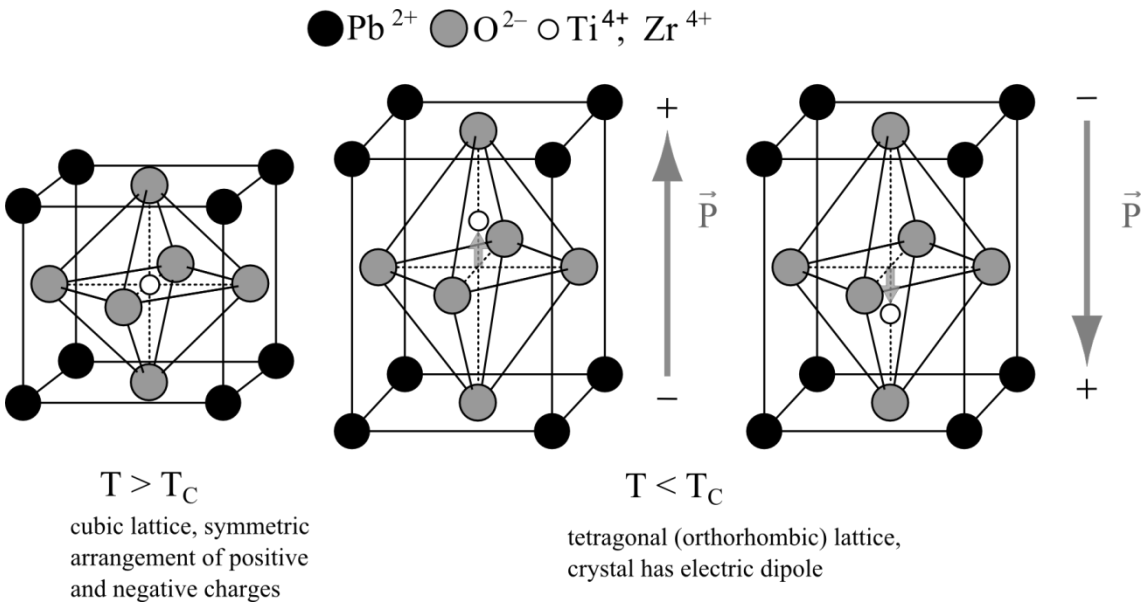

Figure 1.19. Perovskite ABO_3 unit cell for PZT or PLZT, illustrating 180º polarization reversal for two of the six possible polarization states produced by displacement of the central cation in the tetragonal plane.

In conclusion, since the last century ferroelectric and piezoelectric ceramics are being used in capacitors, sensors, actuators and acoustic applications owing to their high

elastic modulus, high dielectric constants, and low dielectric and elastic losses. But they also have important drawbacks. For instance, high mass density, fragility, low strains, which are important limitations in certain applications where weight and mechanical properties are key factors, like in the aerospace industry.

B. POLYMER PIEZOELECTRIC MATERIALS

The use of polymer piezoelectric materials is certainly desirable, because they have special advantages over ceramics. They are flexible, mechanically more stable, and can be obtained in the form of large-area thin films. Other advantages of polymers are that they can be easily manufactured at much lower temperatures and can be formed more easily into different shapes. These properties make them attractive for piezoelectric applications, although the few known piezoelectric polymers have much lower piezoelectric coefficients compared to ceramic piezoelectrics. They have limited applications as actuators but are widely used as sensors.

The properties of polymers are so different in comparison to inorganics that they are qualified to fill areas where ceramics are incapable of performing effectively. Polymers as sensors and actuators offer the advantage of processing flexibility because they are tough, lightweight, readily manufactured into large areas, and can be cut and formed into complex shapes. Other notable features of polymers are high strength, high impact resistance, low dielectric constant, low elastic stiffness, and low density, which result in a high voltage sensitivity (excellent sensor characteristic), and low acoustic and mechanical impedance (crucial for medical and underwater applications). Polymers also typically possess a high dielectric breakdown and high operating field strength. In addition, they offer the ability to pattern electrodes on the film surface, and pole only selected regions [36].

Although, the science and technology of piezoelectric polymers has been dominated by the family of the ferroelectric polymer polyvinylidene fluoride (PVDF) [25], there are other types and families. In general, there are divided in three main categories: bulk polymers, piezoelectric composite polymers and voided charged polymers. In fact, the

origin of the piezoelectric response in polymers ranges from dipole density piezoelectricity in ferroelectric polymers to intrinsic like piezoelectricity in ferroelectrets, passing through multifunctional polymer ceramic nanocomposites (Figure 1.20). Polymer piezoelectric polymers show very different values of piezoelectric coefficient d_{33}, from 0.2–30 for bulk piezoelectric polymers, to 100–2000 pC·N^{-1}, for composites and voided charged polymers, depending on the type and processing conditions.

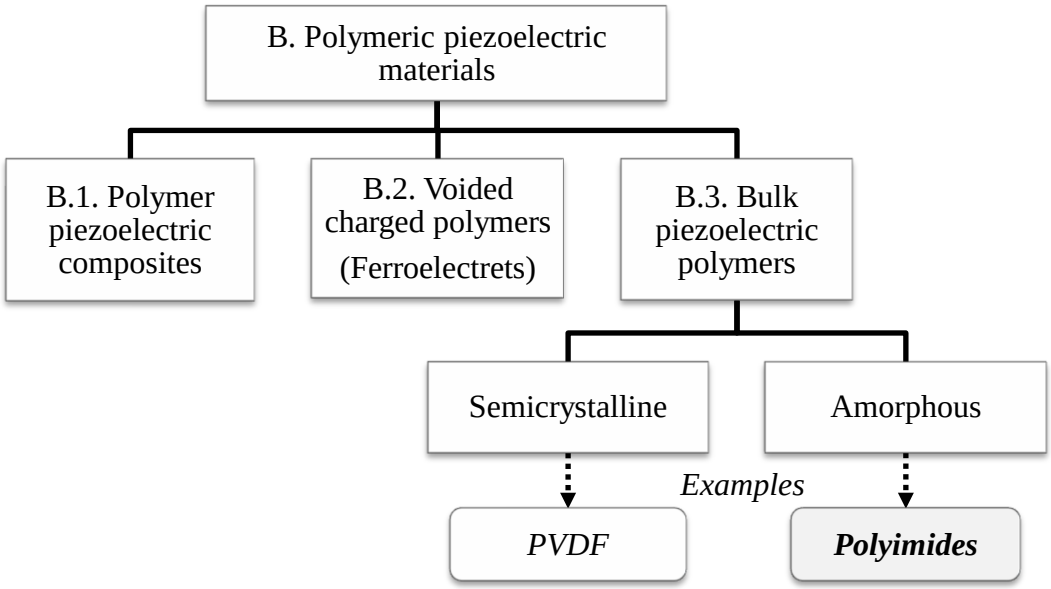

Figure 1.20. Classification of piezoelectric polymers.

Probably the first study of the piezoelectric effect in an organic material was in 1924, about the piezo-electrification in ebonite, glass, sealing wax, rubber, celluloid, and hard paraffin. Later, in 1941, piezoelectricity and pyroelectricity was found in bundles of wool or human hair, studies that were continued by Bazhenov and Konstantinova in 1950 and by Eiichi Fukada in 1955. Fukada and Yasuda found piezoelectricy in bone in 1957 [37,38]. These effects were also detected in tendon and in many kinds of biological polymers, polysaccharide, proteins and DNA and synthetic polymers including polypeptides and optically active polymers. But the discovery of a strong piezoelectric effect in polymers, significantly large to be of interest for technical applications, dates back to the pioneering work of Kawai on poly(vinylidene fluoride)

poled films in 1969, followed by the finding of pyroelectricity in the same polymer two years later by Bergman, Nakamura and Wada [39]. Since then, the field has been dominated by polymers from the PVDF family, especially the copolymers of vinylidene fluoride and the trifluoroethylene P(VDF-TrFE). Nonetheless, there are other possibilities, starting with bulk piezoelectric polymers, semi-crystalline or amorphous. But also, voided charged polymers (ferroelectrets or piezoelectrets), which they were first discovered by Gerhard Sessler in the early 1960s, or nanocomposites based on non-piezoelectric polymers and piezoelectric ceramics in the 1970s [25,31,40–43].

B.1. POLYMER PIEZOELECTRIC COMPOSITES

Piezoelectric polymer composites, also called piezocomposites, are the polymer materials with embedded inorganic piezoelectric materials, where the polymer is assumed to be not electromechanically active. That is, a composite with a non-piezoelectric polymer matrix material [44,45]. The purpose of mixing piezoelectric ceramics with polymers is to combine the advantages of both materials, which include the mechanical flexibility of polymers and the higher coupling factor.

Arrangement of ceramic/polymer composites can have many different combinations to improve their properties. There are important connectivity patterns in diphasic solids, ranging from a 0-0 unconnected checkerboard pattern to a 3-3 pattern in which both phases are three dimensionally self-connected. The notation 0-3, 2-2, 1-3, etc. is used to describe the structure of a two-phase composite, where each number denotes the connectivity of each phase. For instance, a 0-3 particulate composite is composed of single-phase particles (denoted by 0) embedded in a matrix of another phase (denoted by 3), as shown in Figure 1.21. The common connectivity schemes examined so far include 0-3 particulate films, 2-2 horizontal heterostructures, and 1-3 vertical heterostructures. Most of the work has been limited to the connectivities which are easier to form, namely ceramic particle filled polymer (0-3), unidirectional laminates of ceramic fiber (1-3), laminated sheets of ceramic and polymer (2-2), porous ceramic (3-0), drilled ceramic (3-1 and 3-2), and ceramic/polymer networks (3-3) [46].

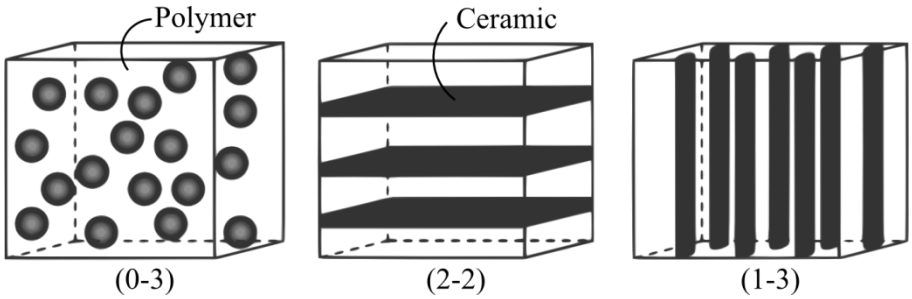

Figure 1.21. Schematic illustration of three bulk composites with three common connectivity schemes: a) 0-3 particulate composite, b) 2-2 laminate composite, and c) 1-3 fiber/rod composite.

B.2. VOIDED CHARGED POLYMERS OR FERROELECTRETS

Voided charged polymers (cellular polymers or ferroelectrets) are cellular structures consisting of gas-filled voids, surrounded by a polymer matrix, for instance, polypropylene (PP), polyethylene terephthalate (PET) or polytetrafluoroethylene (PTFE) [47,48]. In this kind of materials the concept of piezoelectricity consists basically in the effect produced when a large electric field is applied across the film, gas molecules in the voids get ionized and opposite charges are accelerated and implanted on each side of the voids. Positive and negative charges are stored separately on the internal gas/polymer interfaces facing each other, and form a permanent dipole moment. Those embeded dipoles respond externally to an applied electrical field or mechanical force similar to piezoelectric material. Instead of ion displacement in a crystalline structure of a regular piezoelectric material, the combination of the internal dipole moment and the anisotropic cellular polymer matrix is the cause of the piezoelectric effect.

For application as ferroelectrets, the electrically charged polymer foams should be metallized with electrodes on both outer surfaces. The internal stored charges generate compensating charges in the electrodes, in order to compensate the electric field in the voids. If the polymer foam is compressed by a mechanical stress, the height of the cellular voids is decreased due to the lower elastic modulus of gas compared to the polymer bulk. The distance between the positive and negative charges, i.e. the dipole moment, and therefore the amount of compensating charges, is decreased. If he

electrodes are short-circuited, a current is generated. Ferroelectrets exhibits permanent orientation of the inner dipoles and a hysteresis in response to an outer electric field, by which the orientation of the direction of the dipoles can be reversed (Figure 1.22).

The piezoelectric response of ferroelectrets is very attractive, but there still exist important challenges, such as the lifetime of the trapped charges and the thermal stability. There are factors related to the voids and the polymer material. The density and shape of the voids affects the distribution of the final formed dipoles. Also, the type and pressure of gas inside the voids affects the amount of ionization occurring during the poling process. These factors affect the value of the piezoelectric coefficient and its stability. For example, for ferroelectrets made of polypropylene (PP), although show a strong piezoelectric response, its maximum service temperature is in the range between 60 and 80ºC, depending on the preparation. Progress in the field is rapid, and the current challenge is to develop materials with a stable piezoelectric response above 100ºC.

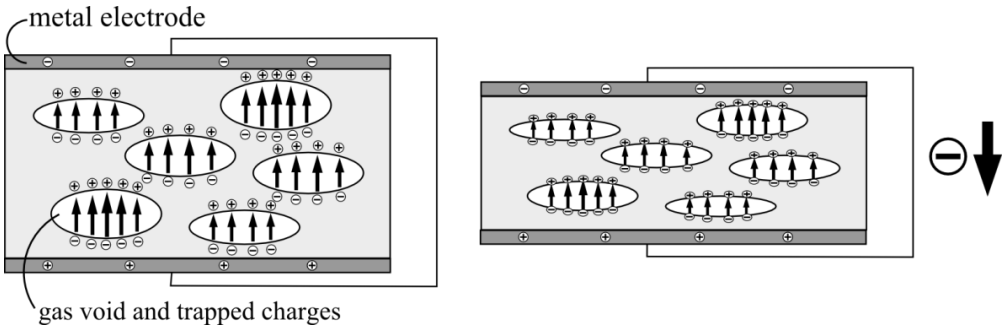

Figure 1.22. Scheme of a ferroelectret with metal electrodes on both sides (Left). Change of dipole moment due to thickness compression in a flow of charge (Right).

B.3. BULK PIEZOELECTRIC MATERIALS: SEMICRYSTALLINE AND AMORPHOUS POLYMERS

It is important the comprehension of the origin of piezoelectric and ferroelectric phenomena in bulk polymers, to present the state-of-the-art in them and emerging

material systems that exhibit promising properties to discuss modeling approaches and applications of piezoelectric polymers [49].

Bulk piezoelectric materials are the polymers that have piezoelectric effect due to the molecular structure of the polymer and its orientation. There are two types of bulk polymers that have different operating principles: semicrystalline polymers and amorphous polymers. In these two types, there are structural requirements that must exist for being piezoelectric regardless of morphology. These elements are: a) the presence of permanent molecular dipoles, b) the ability to orient or align the molecular dipoles, c) the capacity to sustain this dipoles alignment once it is achieved, and d) the ability of the material to undergo large strains when mechanically stressed.

- **SEMICRYSTALLINE PIEZOELECTRIC POLYMERS**

Semicrystalline polymers in principle operate similar to piezoelectric inorganic materials, but the bulk of a semicrystalline polymer is not a single crystal structure, they are randomly oriented microscopic crystals distributed within an amorphous bulk (Figure 1.23). It is necessary to render them piezoelectric, and for that semicrystalline polymers must have a polar crystalline phase. The morphology of such polymers consists of crystallites dispersed within amorphous regions. The amorphous region has a glass transition temperature that dictates the mechanical properties of the polymer while the crystallites have a melting temperature that dictates the upper limit of the use temperature. The degree of crystallinity present in such polymers depends on their method of preparation and thermal history. Most semicrystalline polymers have several polymorphic phases, some of which may be polar. Mechanical orientation, thermal annealing and high voltage treatment have all been shown to be effective in inducing crystalline phase transformations. Thus, to get an effective piezoelectric response out in them, it is compulsory the ability to reorient these crystallites and keep them in the preferable orientation, which is done by the poling.

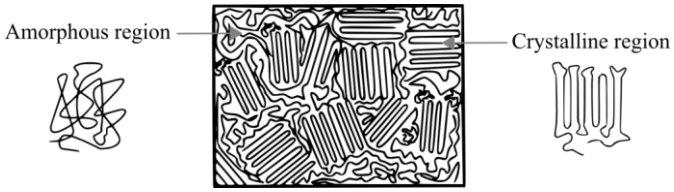

Figure 1.23. Amorphous and crystalline parts of a semicrystalline polymer.

There are numerous numbers of papers on the research of piezoelectricity, pyroelectricity and ferroelectricity in semicrystalline polar polymers [36,40,50–52]. In particular, PVDF and its copolymers have been studied most extensively [53–55]. These semicrystalline fluoropolymers represent the state of the art in piezoelectric polymers, but there are others with semi-crystalline structure. For example, odd-numbered nylons (Nylon-7 or Nylon-11), the next most widely investigated semicrystalline piezoelectric polymers, have excellent piezoelectric properties at high temperatures but have not yet been used in practical applications, because of among other reasons their tendency to absorb water [56]. Other semicrystalline polymers include polyureas (polyurea-9), liquid crystalline polymers, biopolymers (polylactic acid (PLLA) and poly(lactic-co-glycolic acid) (PLGA)) and Parylene-C© (trade name for a variety of poly(p-xylylene) polymer) (Figure 1.24).

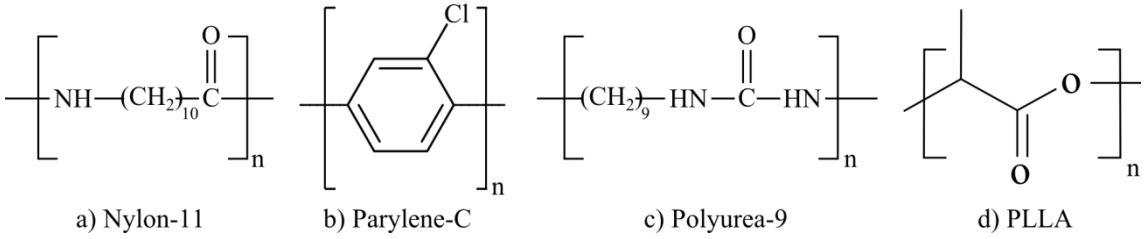

Figure 1.24. Molecular structure of some bulk semicrystalline piezoelectric polymers.

—Polyvinylidene fluoride (PVDF)

Polyvinylidene fluoride (PVDF) is the best known and most used piezoelectric polymer, because it has the highest piezoelectric, pyroelectric and ferroelectric properties, added to its excellent chemical resistance and mechanical properties, allowing an important

variety of technological applications [53,57,58]. PVDF characteristics and properties have been exhaustively studied and established, due to the material's relevance. The spatially symmetrical disposition of the hydrogen and fluorine atoms along the polymer chain gives rise to unique polarity effects that influence the electromechanical response, solubility, dielectric properties, crystal morphology and yield an unusually high dielectric constant. The dielectric constant of PVDF is greater than most polymers. The amorphous phase in PVDF has a glass transition that is well below room temperature (-35ºC), hence the material is quite flexible and readily strained at room temperature. PVDF crystalline percentage depends on thermal and processing history and can have 5 crystal phases, of which the most investigated are α, β and γ-phases (Figure 1.25). The β phase is the one with the highest dipole moment per unit cell ($8 \cdot 10^{-30}$ C·m) when compared to the other two phases. The α and ε phases are non-polar due to antiparallel packing of the dipoles within the unit cell. Since the β and γ phases are the most electrically active phases, their proportion within the material is important depending on the application. Different strategies have been developed to obtain the electroactive phases of PVDF, mainly focusing on the development of specific processing procedures and the inclusion of fillers. The most stable and non-polar α phase can be transformed into the polar β phase and into the polar δ phase. In fact, the β-phase can be obtained by mechanical stretching of the α-phase, from melt under specific conditions such as high pressure, external electric field and ultra-fast cooling; from solution crystallization at temperatures below 70ºC or by the addition of nucleating fillers such as $BaTiO_3$, clays, hydrated ionic salt or nanoparticles.

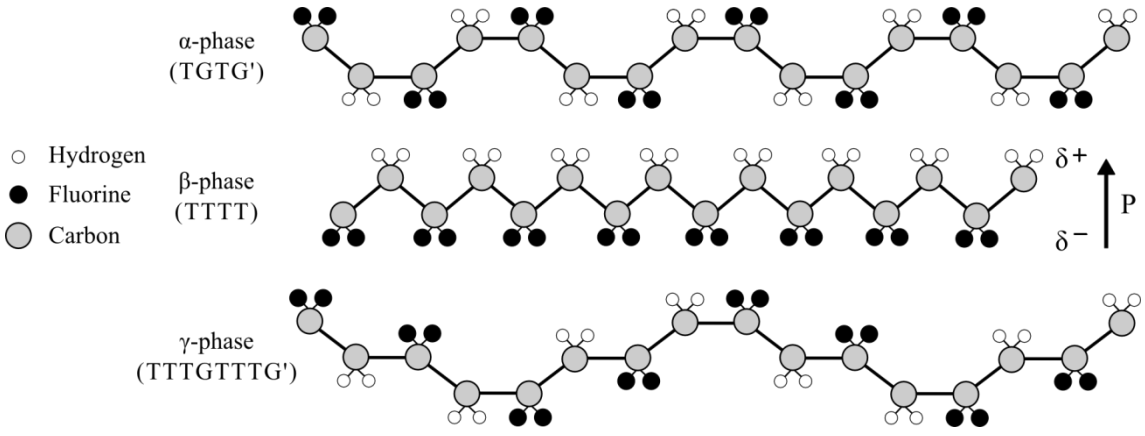

Figure 1.25. Schematic representation of the chain conformation for the α, β and γ phases of PVDF.

As it can be observed, in the β-phase the hydrogen atoms (H), which have a net positive charge and the fluorine atoms (F), which have a net negative charge end up on opposite sides of the backbone, which creates a pole direction (P).

With the aim to improve the PVDF properties and to adapt it to the increasing technological demands, different copolymers have been developed (Figure 1.26) [53]. One of the most studied copolymer is the poly(vinylidene fluoride-trifluoroethylene), P(VDF-TrFE). Other examples are the poly(vinylidene fluoride-co-hexafluoropropene), P(VDF-HFP), consisting of the incorporation of the amorphous phase of hexafluoropropylene on the PVDF homopolymer, or the poly(vinylidene fluoride-chlorotrifluoroethylene) copolymer [59], P(VDF-CTFE), which results from the modification of the PVDF by the introduction of chloride trifluoride ethylene (CTFE) on the polymer chain and, finally, the terpolymer poly(vinylidene fluoride-trifluoroethylene-chlorofluoroethylene), P(VDF-TrFE-CFE), that comprises vinylidene fluoride (VDF), trifluoroethylene (TrFE), and 1,1-chlorofluoroethylene (CFE) or chlorotrifluoroethylene (CTFE), i.e. by the introduction of CTFE in PVDF-TrFE with different percentage of CTFE [60,61].

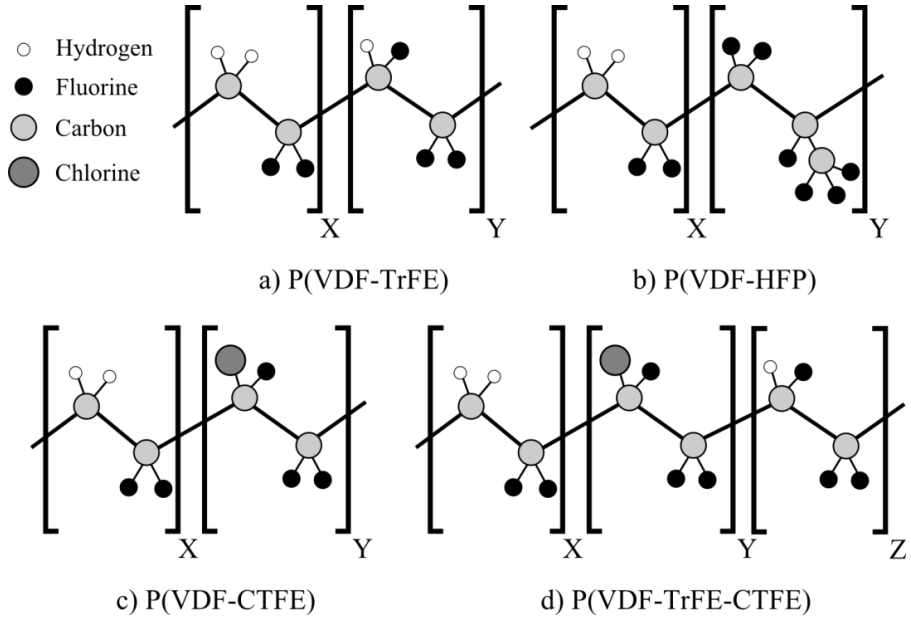

Figure 1.26. Schematic representation of the: a) P(VDF-TrFE), b) P(VDF-HFP), c) P(VDF-CTFE) and d) P(VDF-TrFE-CTFE repeat units.

PVDF and its copolymers [39] apart from the typical applications as sensors and actuators, can be used in energy harvesting [62], in vibration control, ultrasonic transducers [63], batteries [64], filters [65], magnetoelectric sensors [66,67] or in the biological field [68]. In general their processing is in film form, but polymers with other forms, such as nanofibers by electrospinning [69] are also possible.

The only important drawback of PVDF is its relative low thermal stability of the piezoelectric effect, limited to below 100ºC, which is the Curie temperature (T_C) of the material [70]. This is so, because in piezoelectric semi-crystalline polymers the amorphous region dictates the mechanical properties of the polymer while the crystallites have a melting temperature (T_m) that dictates the upper limit of the use temperature (Curie temperature). Therefore, there is an important interest in the industry to develop bulk piezoelectric polymers for temperatures above 100ºC.

- **AMORPHOUS PIEZOELECTRIC POLYMERS**

The piezoelectric effect can be found in a polymer that does not have long range order, i.e. non-crystalline, if its molecular structure contains molecular dipoles. The piezoelectricity in amorphous polymers differs from that in semi-crystalline polymers and inorganic crystals in that the polarization does not takes place in a state of thermal equilibrium but rather a quasi-stable state due to the freezing-in of molecular dipoles. The result is a pyroelectric and piezoelectric material due to the frozen-in dipolar orientation [71–74].

In an amorphous piezoelectric polymer one of the most important parameters is the glass transition temperature (T_g, temperature below which the material exhibits glass-like characteristics, and above which it has rubber-like properties), because that temperature dictates its maximum operating temperature and defines the poling process conditions (Figure 1.27). Orientation polarization of molecular dipoles is responsible for piezoelectricity in amorphous polymers. It is induced, by applying an electric field (E_p) at an elevated temperature $(T_p \geq T_g)$, where the molecular chains are sufficiently mobile and allow dipole alignment with the electric field, i.e. by the poling process. As

poling is done at a temperature a few degrees greater than the glass transition temperature of the polymer, these dipoles can be effectively aligned with the applied electric field. After cooling, these dipoles are not in the same thermal equilibrium state as their counterparts in semi-crystalline polymers. Then, partial retention of this orientation is achieved by lowering the temperature below T_g in the presence of E_p, resulting in a piezoelectric-like effect. The remnant polarization (P_r) is directly proportional to E_p and the piezoelectric response. The procedure used to prepare a piezoelectric amorphous polymer may result in both oriented dipoles and space or real charge injection. The real charges are usually concentrated near the surface of the polymer, and they are introduced due to the presence of the electrodes.

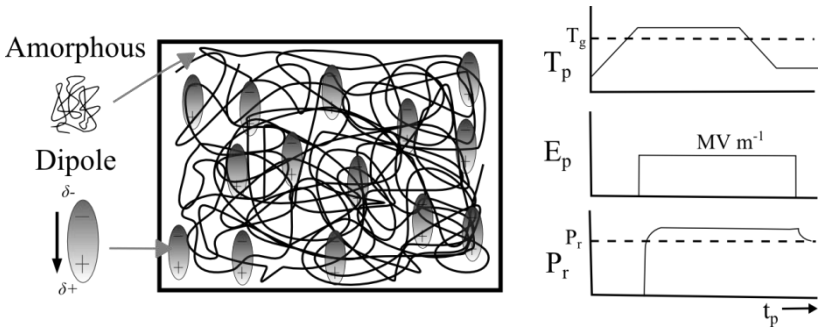

Figure 1.27. Schematic diagram of amorphous dipolar polymers (Left). Poling profile for an amorphous polymer (Right).

The origins of the dielectric contribution to the piezoelectric response of amorphous polymers is related with the potential energy (U) of a dipole μ at an angle θ with the applied electric field, $U = \mu \cdot E \cdot \cos\theta$. Using statistical mechanics and assuming a Boltzman´s distribution of the dipole energies, the mean projection of the dipole moment, $< \mu_\varepsilon >$, in the direction of the applied electric field is obtained.

$$\frac{< \mu >}{\mu} = \coth\frac{\mu E_p}{kT} - \frac{kT}{\mu E} \tag{1.25}$$

This is the Langevin equation which describes the degree of polarization in a sample when an electric field (E) is applied at temperature T. Experimentally, a poling temperature near the T_g is used to maximize dipole motion and the maximum electric

field which may be applied is determined by the dielectric breakdown strength of the polymer. For amorphous polymers, $\mu E_p/kT$ is much less than the unity, which places these systems well within the linear region of the Langevin function. The remnant polarization (P_r) is the polarization during poling minus the electronic and atomic polarization that relax at room temperature once the field (E_p) is removed. The following linear equation for the remnant polarization results when the Classius Mossotti equation is used to relate the dielectric constant to the dipole moment [75]:

$$P_r = \Delta\varepsilon\ \varepsilon_0\ E_p \tag{1.26}$$

The remnant polarization and hence piezoelectric response of a material is determined by $\Delta\varepsilon$, making it a practical criterion to use when designing piezoelectric amorphous polymers. The dielectric relaxation strength, $\Delta\varepsilon$ may be the result of either free or cooperative dipoles motion. Dielectric theory yields a mathematical approach for examining the dielectric relaxation due to free rotation of the dipoles, $\Delta\varepsilon$.

Optimal dipole alignment requires of an important study of the relationship between relaxation times, poling temperatures and poling fields. In this way obtaining a large dielectric relaxation strength and an important piezoelectric response needs the ability to incorporate highly polar groups at high concentrations and cooperative dipole motion. In theory, the higher the electric field, the better the dipole alignment is, but the value of the electric field is limited, because of the dielectric breakdown of the polymeric material. Poling times need to be of the order of the relaxation times of the polymer at the poling temperature.

The number of examples of amorphous piezoelectric polymers is much more limited than that for semi-crystalline systems. This is in part because no amorphous piezoelectric polymers have exhibited responses high enough to attract commercial interest. In the last decades, various amorphous piezoelectric polymers with a high dipolar moment in the repetitive units have been studied since they have pyro- and piezoelectric properties. Much of the work is in the area of nitrile substituted polymers including polyacrylonitrile (PAN) [76], poly(vinylidene cyanide-vinylacetate) (PVDCN/VAc) [77,78], polyphenylethernitrile (PPEN) [79], poly(1-

bicyclobutanecarbonitrile) and aromatic polyimides, but also it has been found weak piezoelectric activity in polyvinyl acetate (PVAc) and polyvinyl chloride (PVC) [80]. Figure 1.28 shows molecular structures of some of the most common amorphous piezoelectric polymers.

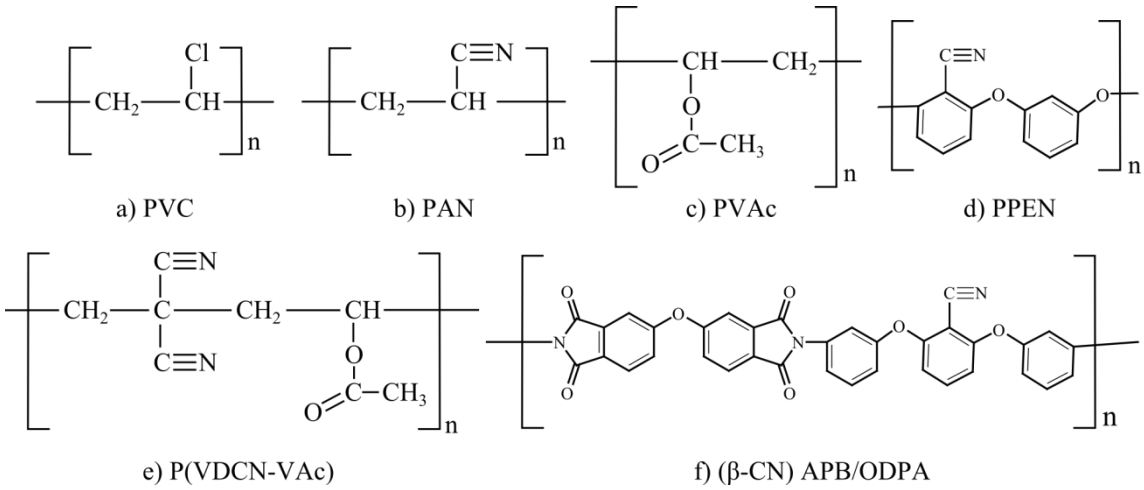

Figure 1.28. Molecular structure of some bulk amorphous piezoelectric polymers.

—Polyimides

The most promising of these materials are the aromatic polyimides, especially for high temperature applications, above 100ºC. They have lately received large interest, due to their excellent thermal, mechanical, and dielectric properties, and because of their piezoelectric properties can be improved by adding pendant highly polar groups in the chain (–CN, $–CF_3$, $–SO_2$...). In this thesis the –CN dipolar groups was chosen as pendant group and the N-phenylphthalyimide as group incorporated in the chain. Particularly, the 4,4′ oxydiphthalic anhydride (ODPA) dianhydride and bis-aminophenoxybenzene (APB) diamine based polyimide and copolyimides, (β-CN) APB–ODPA, were studied. Although investigation in piezoelectric polyimides is relatively recent [73,74,81,82] and few in number, it has a promising future. For instance, a new type of diamine, the 1,3-bis-2-cyano-3-(3-

aminophenoxy)phenoxybenzene [83,84], was developed which is the precursor of its corresponding polyimide, a polyimide with two cyano groups (poly 2CN) [85].

Polyimides (PI) are a group of polymers formed by the imide group shown in Figure 1.29. They are divided into two groups according to their chemical structure [86–88]. The first one, with a linear structure where the atoms of the imide group are part of a linear chain, and the second one where they are part of a heterocyclic unit in the polymer chain. But only the second group (aromatic polyimides) have attracted attention in the field of high temperature resistant polymers, because of their characteristic very strong heat and chemical resistance derived from their rigid polymer structures, highly symmetrical, highly polar groups and strong intermolecular interactions. This attraction is not only due to the desirable combination of their properties, but also to their synthetic potential readiness for specific applications. PI's are high performance polymers which exhibit many useful properties such as high transition temperatures, excellent dimensional stability, low dielectric constants, and outstanding thermal and thermo-oxidative stability. Therefore, they are considered as versatile polymers with an almost unlimited spectrum of applications as specialty polymers for advanced technologies in the aerospace, electrical and microelectronic industries, in applications such as high-temperature insulators [89,90] and dielectrics, coatings [91,92], adhesives [93], membranes [94,95], matrices for high-performance composites [96] and optoelectronic devices [97,98].

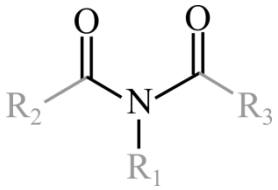

Figure 1.29. Structure of an imide group.

The properties of polyimides can be significantly modified by changes in the structure of the dianhydride and diamine [99,100]. For example, the dilution of the imide content by the insertion of orto- or meta-phenylene segments into the diamines can reduced the glass transition temperature (T_g). In addition, the attachment of pendant groups on the

backbone may lead to decrease or increase their glass transition temperature, depending on the structure of pendant groups. For example, flexible pendant groups reduce the glass transition of the polymer by reducing the frictional interaction between the chains. Polymers containing aromatic structure have higher T_g than polymers having aliphatic structure. Also, highly dipolar bridging groups such as carbonyl and sulphonyl have higher T_g than non-polar groups [101,102].

Strong interactions in polyimides are originated from intra- and interchain charge transfer complex (CTC) formation and electronic polarization, supported by the strong electron acceptor characteristics of imides and the electron donor characteristics of amine segments [103,104]. PI's are considered charge transfer complexes formed by two types of monomers, a donor and an acceptor [105]. An electron donor is a chemical entity that donates electrons to another compound. The donor (diamine) has plenty of electrons to go around because of its nitrogen groups. By contrast, the electron acceptor (anhydride) accepts electrons transferred to it from another compound, i.e. the carbonyl groups attract away its electron density. The donor support the acceptor, in fact, the donor lends some of its electrons to the acceptor, holding them tightly together (Figure 1.30).

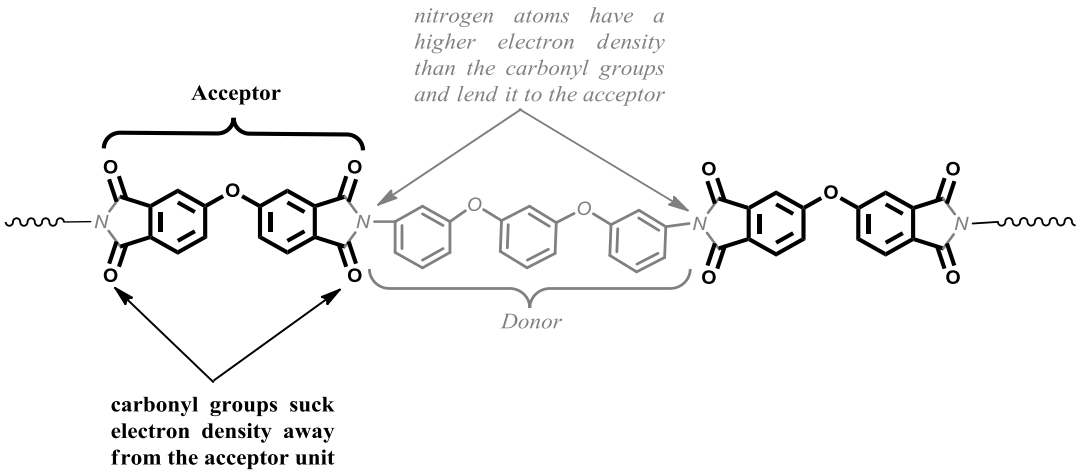

Figure 1.30. Scheme representing the acceptor and donor part of a polyimide.

Charge transfer structure in the polyimides also controls their absorption, photoreactivity and photoconductivity, which make them very promising materials, because polymers with photonic and optic properties are increasingly needed [106]. Among them, those with thermostability up to 300ºC or more is required for manufacturing reliable devices. CTC is also responsible of the colour in polymides, in collaboration with other possible origins such as chromophoric units, impurities from starting materials or side reaction products [104,107]. PIs have strong absorbance in the visible region of the UV-visible spectra and are pale yellow or deep reddish yellow because of their highly conjugate aromatic structures and/or the inter-molecular CTC formation. A lowering of the CTC generally between alternating electron-donor (diamine) and electron-acceptor (dianhydride) moieties affords polyimide with lighter colour [108]. With respect to the fluorescence, its efficiency will be decreased and gradually displace to red, the greater are such interactions, i.e. when greater is the donor and acceptor behavior of the diamine and dianhydride, respectively.

Their chemistry consists on a large variety of monomers and several methodologies available for synthesis. The first procedure in polyimide synthesis, and the most common, is a two-step polymerization process. The initial mechanism involves a nucleophilic substitution reaction of the carbonyl group of the dianhydride with the amino group of the diamine, at ambient conditions in a dipolar aprotic solvent, such as N,N-dimethylacetamide (DMAc) or N-methylpyrrolidinone (NMP) to yield an intermediary poly(amic acid) (PAA), which is a soluble polymer precursor followed by a later thermal cyclodehydration into the final polyimide (Figure 1.31) [109–112].

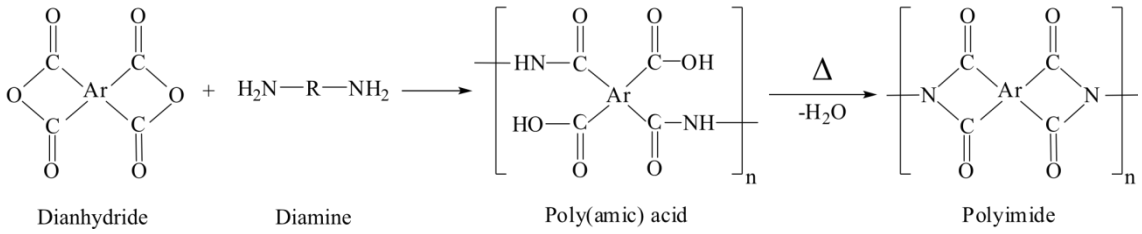

Figure 1.31. Scheme of the two-step method for polyimide synthesis.

The nucleophilic substitution reaction depends upon the electrophilicity of the carbonyl of the dianhydride and the nucleophilicity of the amino group of the diamine, where the electrophilicity is estimated in terms of electron affinity (E_a) and the nucleophilicity in ionization energy (IE). Therefore, increasing artificially the diamines nucleophilicity can be considered a recommendable method in some instances, particularly for less reactive diamines [113–115].

The second procedure, it is called one-step polycondensation method. This technique is employed for the synthesis of polyimides which are being soluble in organic solvents at polymerization temperatures [101,116,117]. The process involves heating a stoichiometric mixture of monomers in a high boiling solvent or in a mixture of solvents at 180-220ºC. The imidization proceeds rapidly at these temperatures and the water generated due to the reaction is distilled off continuously as an azeotrope mixture along with the solvent. The most common used solvents are nitrobenzene, m-cresol, and dipolar aprotic amide solvents. The high temperature solution polymerization is often performed in the presence of catalysts. An acidic catalyst such as benzoic acid is added to promote the formation of trans-isoimide and later a basic catalyst such as isoquinoline to convert it into a polyimide (Figure 1.32). This synthetic route is very useful, but it has a drawback, its very high polymerization temperature. Hence, an alternative at ambient conditions was desired, through increasing the polymerization reactivity, for instance, by means of condensation of silylated diamines.

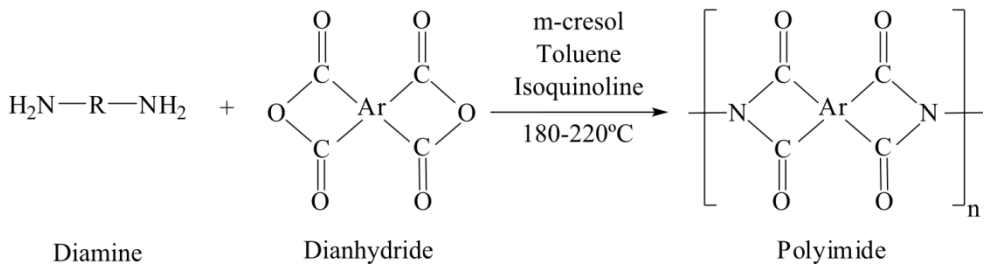

Figure 1.32. Scheme of the one step polymerization method at high temperature.

Silylated diamines have demonstrated since they were first reported by Oishi et al. [118,119] that they are more nucleophilic reactants than the normal diamines. By this method, a poly(amic trimethyl silyl ester) is produced in the first step which can be converted into polyimide via chemical imidization, which is promoted by acetic anhydride in combination with organic bases, such as pyridine or triethylamine acting as activating agents [113,115] (Figure 1.33). That method has an important disadvantage, regarding water sensitivity and rigorous control of the reaction conditions, but can be avoided with the use of in situ silylated diamines, by adding trimethylchlorosilane (TMSCl) or other silylating agents to the diamine solutions before adding the electrophilic monomer [114]. The TMSCl avoid that small amounts of water could destroy the moisture-sensitive dianhydrides and the experimental procedure is much easier.

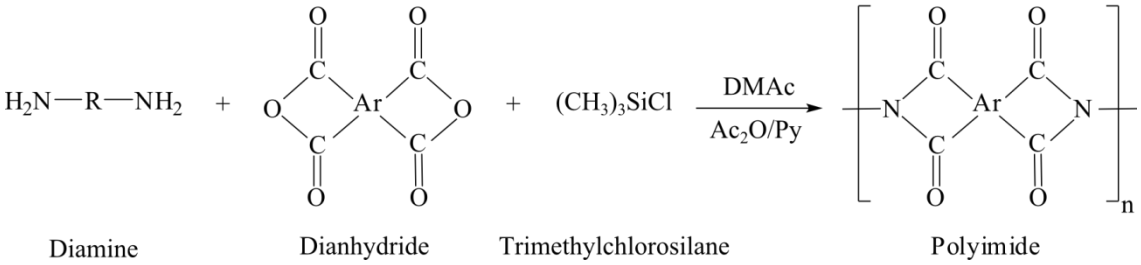

Figure 1.33. Scheme of the in situ silylation polycondensation method.

Initially, polyimides found application in a rather restricted number of technologies as films, but the advances in addition polymerization and in polymer processing have widened the range of properties and application possibilities to a great extent. Thus, polymers with other forms, such as nanofibers are interesting for some applications. Nanofibers can be processed by a number of techniques such as template synthesis, drawing, self-assembly, phase separation, and electrospinning [120]. Among these techniques, electrospinning is of great interest because of its great potential for industrial-scale processing and repeatability in control of fiber dimension [121]. The combination of the polyimides high performance and the facility of electrospinning can give birth to a series of multi-functionalizated PI materials with hierarchical constructions.

1.2.4. GENERAL OBJECTIVES AND WORK PLAN

Nowadays, there are various piezoelectric polymers, such as the polyvinylidene fluoride (PVDF) exhibiting high piezoelectric response, but they have limited use as they normally lose its piezoelectric properties near 100ºC. In the Macromolecular Chemistry Research Group (LABQUIMAC) we demonstrated in previous works that amorphous polyimides are polymers that present piezoelectricity at temperatures higher than 100ºC. The studied polyimides showed in their structure the cyano group (in two different positions) which is primarily responsible for their piezoelectric capacity. On the one hand, polyimides have being used in the industry for their great dielectric, thermal stability, chemical and radiation resistance. The characteristic properties of polyimides result from the rigid polymeric structures, highly symmetrical polar groups, and strong intermolecular interactions. The strong interactions originate from intra- and interchain charge transfer complex (CTC) formation and electronic polarization, hence the photophysical properties of these materials were studied.

On the other hand, polyimides usually suffer from poor solubility in organic solvents and non-melting characteristics. Therefore, in our group significant efforts have been focused on improving their processability and solubility through the design of new monomers (diamines and dianhydrides). Different polyimide structures via copolymerization and different polymer properties by employing different synthetic methods have been studied. Three types of synthesis have been employed up to the moment, and their processes optimized and explained in previous works.

The first synthesis procedure, and the most common, is a two-step polymerization process, also called thermal imidization method. The other two types are based in chemical imidization. One of them, is called the one-step polycondensation method. The process involves heating a stoichiometric mixture of monomers in a high boiling mixture of m-cresol and toluene at 180-220ºC, in the presence of isoquinoline as catalyst. The imidization proceeds rapidly at these temperatures and the water generated

due to the reaction is distilled off continuously as an azeotrope mixture along with the solvent.

The third method involved the use of in situ silylated diamines, by adding trimethylchlorosilane (TMSCl) or other silylating agents to the diamine solutions before adding the dianhydride. The reason of using silylated diamines is that they are more nucleophilic reactants than the normal diamines, and so the reactivity and the achieved molecular weight are increased. By this method, chemical imidization is promoted by acetic anhydride in combination with organic bases, such as pyridine or triethylamine acting as activating agents.

Once the synthetic methods were optimized, in this thesis the main objectives will be devoted to study possible future applications.

The first application is as sensor materials using the piezoelectric capacity of our polyimides. According to that, poling process (simultaneous application of heat and electric field) is required to convert them into electrets, which are solid dielectric materials that have quasi-permanent electric charge or dipole polarization. Therefore, chapter 3 of this memory will be devoted to the optimization of corona poling conditions, analysis of the influence of the polymer composition in the piezoelectricity, study of the thermal stability and characterization of the piezoelectric effect by measuring the piezoelectric coefficient d_{33}.

During poling several types of electrical polarization such as electronic polarization, atomic or ionic polarization, dipolar polarization, spontaneous polarization and interface or space charge polarization can occur. In order to study them and other phenomena observed in the polyimides, the technique of dielectric spectroscopy will be employed in chapter 4. Due to the fact that dielectric phenomena are frequency and temperature dependant, the dielectric permittivity spectrum over a wide range of frequencies at different temperatures was measured. Experimental data by dielectric spectroscopy are regarded as complex electrical impedance and expressed in terms of the resistance and capacitance. However, there are other expressions that are used depending on the information you want to share. The intensive complex dielectric quantities of dielectric

permittivity, electrical modulus and electrical conductivity are immediately derivable from complex electrical impedance.

Other possible application, analyzed in chapter 5, is the use of polyimides as the piezoelectric element and cobalt ferrite nanoparticles as magnetostrictive phase in magnetoelectric (ME) composites for applications at high temperature (superior to 100ºC). ME composites made by combining piezoelectric and magnetic substances together employing different shapes and connectivities have attracted interest, especially ME multilayer and ceramic composite materials. Nonetheless, ceramic composites are fragile, difficult to shape and miniaturize. Polymer matrix can overcome those problems; most of them are based on poly(vinylidene fluoride) and its copolymers, but those do not meet the requirement of working under extreme conditions such as high temperatures. For this reason, polyimides are very interesting for such application. The magnetoelectric effect will be measured in polyimides for the first time in this thesis.

The last application studied is as gel polymer electrolyte (GPE) membrane separators, because new materials and concepts are necessary for the development and commercialization of the next generation rechargeable battery devices. A separator is a porous membrane that absorbs and retain the required amount of liquid electrolyte, provide channels for ions during electrochemical reactions and physically isolates the cathode and anode frome electrical contact to avoid short circuit. Apart from the traditional separators used in commercial batteries, there are other types, with advantages and disadvantages. Conventional polyolefin microporous membranes (Celgard©) are usually used as separators. However, low porosity (about 40%), poor thermal stability and large difference of polarity between the highly polar liquid electrolyte and the nonpolar polyolefin separator lead to high cell resistance, low rate capability and even internal short circuits of Li-ion batteries, which restrict their electrochemical performance. Given the low cost and ease in the construction of microstructures, electrospinning is an interesting and useful technique that produces continuous fibers with diameters in the range of nanometers to a few microns. The advantages of polyimide polymer in comparison with other polymers are that exhibit higher thermal stability and chemical resistance. Hence, due to the characteristics of our polyimides good performances are expected as gel polymer electrolyte (GPE)

membranes. So chapter 6 will be devoted to study the suitability and battery performance of polyimide membranes prepared by electrospinning.

Finally, chapter 7 will be destined to resume the general conclusions of the thesis. Since the corresponding conclusions will be explained in each chapter, in this section only the general considerations will be outlined.

1.3. REFERENCES

[1] Kamila S. Introduction, classification and applications of smart materials: An overview. Am J Appl Sci 2013;10:876.

[2] Ciofani G, Menciassi A. Piezoelectric nanomaterials for biomedical applications. Berlin: Springer; 2012.

[3] Bogue R. Smart materials: a review of capabilities and applications. Assem Autom 2014;34:16–22.

[4] Kumar A, Srivastava A, Galaev IY, Mattiasson B. Smart polymers: physical forms and bioengineering applications. Prog Polym Sci 2007;32:1205–37.

[5] Galaev I. "Smart" polymers and what they could do in biotechnology and medicine. Trends Biotechnol 1999;17:335–40.

[6] Liu Y, Du H, Liu L, Leng J. Shape memory polymers and their composites in aerospace applications: a review. Smart Mater Struct 2014;23:023001.

[7] Wu X, Huang W, Zhao Y, Ding Z, Tang C, Zhang J. Mechanisms of the shape memory effect in polymeric materials. Polymers (Basel) 2013;5:1169–202.

[8] García-Huete N, Laza JM, Cuevas JM, Gonzalo B, Vilas JL, León LM. Shape memory effect for recovering surface damages on polymer substrates. J Polym Res 2014;21:481.

[9] García-Huete N, Laza JM, Cuevas JM, Vilas JL, Bilbao E, León LM. Study of the effect of gamma irradiation on a commercial polycyclooctene I. Thermal and mechanical properties. Radiat Phys Chem 2014;102:108–16.

[10] Cuevas Zarraga JM. Desarrollo y caracterización de la capacidad de memoria de forma en polímeros semicristalinos. University of the Basque Country (UPV/EHU), 2011.

[11] Luo S-C. Conducting polymers as biointerfaces and biomaterials: a perspective for a special issue of polymer reviews. Polym Rev 2013;53:303–10.

[12] Ruiz J, Gonzalo B, Laza JM, León LM, Moreno MI, Vilas JL, et al. Synthesis and characterization of new thiophene-derived polymers. Adv Polym Technol 2014;33:n/a – n/a.

[13] Ruiz J, Gonzalo B, Dios JR, Laza JM, Vilas JL, León LM. Improving the processability of conductive polymers: The case of polyaniline. Adv Polym Technol 2013;32:E180–8.

[14] Martín-Fabiani I, Siegel J, Riedel S, Boneberg J, Ezquerra TA, Nogales A. Nanostructuring thin polymer films with optical near fields. ACS Appl Mater Interfaces 2013;5:11402–8.

[15] Kaholek M, Lee W-K, Ahn S-J, Ma H, Caster KC, LaMattina B, et al. Stimulus-responsive poly(N -isopropylacrylamide) brushes and nanopatterns prepared by surface-initiated polymerization. Chem Mater 2004;16:3688–96.

[16] Clodt JI, Filiz V, Rangou S, Buhr K, Abetz C, Höche D, et al. Double stimuli-

responsive isoporous membranes via post-modification of pH-sensitive self-assembled diblock copolymer membranes. Adv Funct Mater 2013;23:731–8.

[17] Ruiz-Rubio L, Marin JR, Patrocinio D, Laza JM, Rodríguez M, Garay MT. Associative and segregative phase behaviour in mixtures of poly(N-tert-butylacrylamide) and poly(N,N-diethylacrylamide) with poly(4-vinylphenol): effect of solvent and concentration. Colloid Polym Sci 2013;291:2495–502.

[18] Döhler D, Zare P, Binder WH. Hyperbranched polyisobutylenes for self-healing polymers. Polym Chem 2014;5:992.

[19] Telitel S, Amamoto Y, Poly J, Morlet-Savary F, Soppera O, Lalevée J, et al. Introduction of self-healing properties into covalent polymer networks via the photodissociation of alkoxyamine junctions. Polym Chem 2014;5:921.

[20] Pham TTH, Wang J, Werten MWT, Snijkers F, de Wolf FA, Cohen Stuart MA, et al. Multi-responsive physical gels formed by a biosynthetic asymmetric triblock protein polymer and a polyanion. Soft Matter 2013;9:8923.

[21] Gandhi A, Paul A, Sen SO, Sen KK. Studies on thermoresponsive polymers: phase behaviour, drug delivery and biomedical applications. Asian J Pharm Sci 2015;10:99–107.

[22] Li P, Huang L, Lin Y, Shen L, Chen Q, Shi W. Printable temperature-responsive hybrid hydrogels with photoluminescent carbon nanodots. Nanotechnology 2014;25:055603.

[23] Koetting MC, Peters JT, Steichen SD, Peppas NA. Stimulus-responsive hydrogels: theory, modern advances, and applications. Mater Sci Eng R Reports 2015;93:1–49.

[24] Capadona JR, Shanmuganathan K, Tyler DJ, Rowan SJ, Weder C. Stimuli-responsive polymer nanocomposites inspired by the sea cucumber dermis. Science 2008;319:1370–4.

[25] Heywang W, Lubitz K, Wersing W. Piezoelectricity: Evolution and future of a technology. vol. 14. Springer Science & Business Media; 2008.

[26] Vijaya MS. Piezoelectric materials and devices: Applications in engineering and medical sciences. 2013th ed. Boca Raton: CRC Press. Taylor & Francis Group; 2012.

[27] Schwartz MM. Encyclopedia of smart materials. Hoboken, NJ, USA: John Wiley & Sons, Inc.; 2002.

[28] Katzir S. The beginnings of piezoelectricity: a study in mundane physics. Springer Science & Business Media; 2006.

[29] Uchino K, editor. Advanced piezoelectric materials: Science and technology. Oxford: Elsevier; 2010.

[30] Saito Y, Takao H, Tani T, Nonoyama T, Takatori K, Homma T, et al. Lead-free piezoceramics. Nature 2004;432:84–7.

[31] Fukada E. History and recent progress in piezoelectric polymers. IEEE Trans Ultrason Ferroelectr Freq Control 2000;47:1277–90.

[32] Ramadan KS, Sameoto D, Evoy S. A review of piezoelectric polymers as functional materials for electromechanical transducers. Smart Mater Struct 2014;23:033001 (26 pp.) – 033001 (26 pp.).

[33] Yang J. An introduction to the theory of piezoelectricity. Springer Science & Business Media; 2005.

[34] Lang SB. Pyroelectricity: From ancient curiosity to modern imaging tool. Phys Today 2005;58:31–6.

[35] Haertling GH. Ferroelectric ceramics: History and technology. J Am Ceram Soc 1999;82:797–818.

[36] Lang SB, Muensit S. Review of some lesser-known applications of piezoelectric and pyroelectric polymers. Appl Phys A 2006;85:125–34.

[37] Fukada E. Piezoelectric properties of organic polymers. Ann N Y Acad Sci 1974;238:7–25.

[38] Fukada E, Ueda H, Rinaldi R. Piezoelectric and related properties of hydrated collagen. Biophys J 1976;16:911–8.

[39] Kawai H. The piezoelectricity of poly (vinylidene fluoride). Japanese J Appl Phys 8 1969;8:975–6.

[40] Fukada E. Recent developments of polar piezoelectric polymers. IEEE Trans Dielectr Electr Insul 2006;13:1110–9.

[41] Bauer S, Lang SB. Pyroelectric polymer electrets. IEEE Trans Dielectr Electr Insul 1996;3:647–76.

[42] Huang Z-M, Zhang Y-Z, Kotaki M, Ramakrishna S. A review on polymer nanofibers by electrospinning and their applications in nanocomposites. Compos Sci Technol 2003;63:2223–53.

[43] Jain A, K. J. P, Sharma AK, Jain A, P.N R. Dielectric and piezoelectric properties of PVDF/PZT composites: a review. Polym Eng Sci 2015;55:1589–616.

[44] Savakus HP, Klicker KA, Newnham RE. PZT-epoxy piezoelectric transducers: A simplified fabrication procedure. Mater Res Bull 1981;16:677–80.

[45] Rittenmyer K, Shrout T, Schulze WA, Newnham RE. Piezoelectric 3–3 composites. Ferroelectrics 1982;41:189–95.

[46] Newnham RE, Skinner DP, Cross LE. Connectivity and piezoelectric-pyroelectric composites. Mater Res Bull 1978;13:525–36.

[47] Fang P. Preparation and investigation of polymer-foam films and polymer-layer systems for ferroelectrets. University of Postdam, 2010.

[48] Bauer S. Piezo-, pyro- and ferroelectrets: soft transducer materials for electromechanical energy conversion. IEEE Trans Dielectr Electr Insul 2006;13:953–62.

[49] Harrison JS, Ounaies Z. Piezoelectric polymers; NASA/Cr 2001-21142. ICASE Report No. 2001-43. John Wiley & Sons, Inc.; 2002.

[50] Furukawa T. Piezoelectricity and pyroelectricity in polymers. IEEE Trans Electr

Insul 1989;24:375–94.

[51] Scheinbeim JI. Piezoelectricity in gamma-form nylon-11. J Appl Phys 1981;52:5939–42.

[52] Gao Q, Scheinbeim JI. Dipolar intermolecular interactions, structural development, and electromechanical properties in ferroelectric polymer blends of Nylon-11 and Poly(vinylidene fluoride). Macromolecules 2000;33:7564–72.

[53] Martins P, Lopes AC, Lanceros-Mendez S. Electroactive phases of poly(vinylidene fluoride): determination, processing and applications. Prog Polym Sci 2014;39:683–706.

[54] Kang G, Cao Y. Application and modification of poly(vinylidene fluoride) (PVDF) membranes – A review. J Memb Sci 2014;463:145–65.

[55] Murayama N, Nakamura K, Obara H, Segawa M. The strong piezoelectricity in polyvinylidene fluroide (PVDF). Ultrasonics 1976;14:15–24.

[56] Murata Y, Tsunashima K, Umemura J, Koizumi N. Ferroelectric properties of polyamides consisting of hepta- and nonamethylenediamines. IEEE Trans Dielectr Electr Insul 1998;5:96–102.

[57] Ueberschlag P. PVDF piezoelectric polymer. Sens Rev 2001;21:118–26.

[58] Farrokhzad H, Kikhavani T, Monnaie F, Ashrafizadeh SN, Koeckelberghs G, Van Gerven T, et al. Novel composite cation exchange films based on sulfonated PVDF for electromembrane separations. J Memb Sci 2015;474:167–74.

[59] Du Pasquier A. Plastic PVDF-HFP electrolyte laminates prepared by a phase-inversion process. Solid State Ionics 2000;135:249–57.

[60] Xu H, Cheng Z-Y, Olson D, Mai T, Zhang QM, Kavarnos G. Ferroelectric and electromechanical properties of poly(vinylidene-fluoride–trifluoroethylene–chlorotrifluoroethylene) terpolymer. Appl Phys Lett 2001;78:2360.

[61] Zhao X-Z, Bharti V, Zhang QM, Romotowski T, Tito F, Ting R. Electromechanical properties of electrostrictive poly(vinylidene fluoride–trifluoroethylene) copolymer. Appl Phys Lett 1998;73:2054.

[62] Nunes-Pereira J, Sencadas V, Correia V, Rocha JGG, Lanceros-Méndez S. Energy harvesting performance of piezoelectric electrospun polymer fibers and polymer/ceramic composites. Sensors Actuators A Phys 2013;196:55–62.

[63] Kakimoto K, Fukata K, Ogawa H. Fabrication of fibrous BaTiO3-reinforced PVDF composite sheet for transducer application. Sensors Actuators A Phys 2013;200:21–5.

[64] Costa CM, Silva MM, Lanceros-Méndez S. Battery separators based on vinylidene fluoride (VDF) polymers and copolymers for lithium ion battery applications. RSC Adv 2013;3:11404.

[65] Nunes-Pereira J, Lopes ACC, Costa CMM, Rodrigues LCC, Silva MMM, Lanceros-Méndez S. Microporous membranes of NaY zeolite/poly(vinylidene fluoride–trifluoroethylene) for Li-ion battery separators. J Electroanal Chem 2013;689:223–32.

[66] Martins P, Lanceros-Méndez S. Polymer-based magnetoelectric materials. Adv Funct Mater 2013;23:3371–85.

[67] Martins P, Gonçalves R, Lanceros-Mendez S, Lasheras A, Gutiérrez J, Barandiarán JMM. Effect of filler dispersion and dispersion method on the piezoelectric and magnetoelectric response of CoFe2O4/P(VDF-TrFE) nanocomposites. Appl Surf Sci 2014;313:215–9.

[68] Ribeiro C, Moreira S, Correia V, Sencadas V, Rocha JG, Gama FM, et al. Enhanced proliferation of pre-osteoblastic cells by dynamic piezoelectric stimulation. RSC Adv 2012;2:11504–9.

[69] Ribeiro C, Sencadas V, Ribelles JLG, Lanceros-Méndez S. Influence of processing conditions on polymorphism and nanofiber morphology of electroactive poly(vinylidene fluoride) electrospun membranes. Soft Mater 2010;8:274–87.

[70] Nalwa HS, editor. Ferroelectric polymers: chemistry, physics, and applications. Marcell Dekker, Incorporated; 1995.

[71] Harrison JS, Ounaies Z. Piezoelectric polymers; NASA Cr2001-21142. Hampton, Virgina: 2001.

[72] Z. Ounaies, J. A. Young JSH, Z. Ounaies J. S. Harrison JAY, Z. Ounaies JAYJSH, Z. Ounaies J. S. Harrison JAY. Design requirements for amorphous piezoelectric polymers; NASA/TM-1999-209359. 1999.

[73] Park C, Ounaies Z, Su J, Smith Jr. JG, Harrison JS. Polarization stability of amorphous piezoelectric polyimides; Piezoelectric polymers; NASA/Cr 2001-21142. ICASE Report No. 99-53. 1999.

[74] Simpson J, Ounaies Z, Fay C, O. SJ, Z. O, C. FC. Polarization and piezoelectric properties of a nitrile substituted polyimide. vol. 459. NASA Langley Technical Report Server; 1996.

[75] Mopsik FI, Broadhurst MG. Molecular dipole electrets. J Appl Phys 1975;46:4204.

[76] Ueda H, Carr SH. Piezoelectricity in polyacrylonitrile. Polym J 1984;16:661–7.

[77] Miyata S, Yoshikawa M, Tasaka S, Ko M. Piezoelectricity revealed in the copolymer of vinylidene cyanide and vinyl acetate. Polym J 1980;12:857–60.

[78] Tasaka S, Inagaki N, Okutani T, Miyata S. Structure and properties of amorphous piezoelectric vinylidene cyanide copolymers. Polymer (Guildf) 1989;30:1639–42.

[79] Sakurai M, Ohta Y, Inouje Y, Chujo R. An important factor generating piezoelectric activity of vinylidene cyanide copolymers. Polym Commun 1991;32:397–9.

[80] Bharti V, Kaura T, Nath R. Improved piezoelectricity in solvent-cast PVC films. IEEE Trans Dielectr Electr Insul 1995;2:1106–10.

[81] Park C, Ounaies Z, Wise KE, Harrison JS. In situ poling and imidization of amorphous piezoelectric polyimides. Polymer (Guildf) 2004;45:5417–25.

[82] Maceiras A, Martins P, San Sebastián M, Lasheras A, Silva M, Laza JM, et al. Synthesis and characterization of novel piezoelectric nitrile copolyimide films for high temperature sensor applications. Smart Mater Struct 2014;23:105015.

[83] San Sebastian M, Gonzalo B, Breczewski T, Vilas JL, Perez-Jubindo MA, De La Fuente MR, et al. Frozen polarization of piezoelectric polyimides. Ferroelectrics 2009;389:114–21.

[84] Gonzalo B, Vilas JL, San Sebastian M, Breczewski T, Perez-Jubindo MA, de la Fuente MR, et al. Electric modulus and polarization studies on piezoelectric polyimides. J Appl Polym Sci 2012;125:67–76.

[85] Gonzalo B, Vilas JL, Breczewski T, Pérez-Jubindo MA, De La Fuente MR, Rodriguez M, et al. Synthesis, characterization, and thermal properties of piezoelectric polyimides. J Polym Sci Part A Polym Chem 2009;47:722–30.

[86] Ghosh M. Polyimides: fundamentals and applications. New York: CRC Press; 1996.

[87] Kurosawa T, Higashihara T, Ueda M. Polyimide memory: a pithy guideline for future applications. Polym Chem 2013;4:16.

[88] Mehdipour-Ataei S, Bahri-Laleh N. Synthesis and properties of polyimides and copolyimides containing pyridine units: A review. Iran Polym J 2008;17:95–124.

[89] Yoon J-Y, Kim YH, Ka J-W, Hong S-K, Yi MH, Jang K-S. A high-temperature resistant polyimide gate insulator surface-modified with a YOx interlayer for high-performance, solution-processed Li-doped ZnO thin-film transistors. J Mater Chem C 2014;2:2191.

[90] Yoo S, Kim YH, Ka J-W, Kim YS, Yi MH, Jang K-S. Polyimide/polyvinyl alcohol bilayer gate insulator for low-voltage organic thin-film transistors. Org Electron 2015;23:213–8.

[91] Su F, Zhang S. Tribological properties of polyimide coatings filled with PTFE and surface-modified nano-Si 3 N 4. J Appl Polym Sci 2014;131:n/a – n/a.

[92] Lin Y, Gong Y, Wu Y, Wu H. Polyimide-coated fiber Bragg grating for relative humidity sensing. Photonic Sensors 2014;5:60–6.

[93] Kim S, Kim T-S. Adhesion improvement of silicon/underfill/polyimide interfaces by UV/ozone treatment and sol–gel derived hybrid layers. Microelectron Reliab 2014;54:833–9.

[94] Japip S, Wang H, Xiao Y, Shung Chung T. Highly permeable zeolitic imidazolate framework (ZIF)-71 nano-particles enhanced polyimide membranes for gas separation. J Memb Sci 2014;467:162–74.

[95] Alghunaimi F, Ghanem B, Alaslai N, Swaidan R, Litwiller E, Pinnau I. Gas permeation and physical aging properties of iptycene diamine-based microporous polyimides. J Memb Sci 2015;490:321–7.

[96] Gao H, Yorifuji D, Jiang Z, Ando S. Thermal and optical properties of hyperbranched fluorinated polyimide/mesoporous SiO2 nanocomposites exhibiting high transparency and reduced thermo-optical coefficients. Polymer (Guildf) 2014;55:2848–55.

[97] Hsiao S-H, Yeh S-J, Wang H-M, Guo W, Kung Y-R. Synthesis and optoelectronic properties of polyimides with naphthyldiphenylamine chromophores. J Polym Res 2014;21:407.

[98] Ji D, Jiang L, Cai X, Dong H, Meng Q, Tian G, et al. Large scale, flexible organic transistor arrays and circuits based on polyimide materials. Org Electron 2013;14:2528–33.

[99] Hsiao S-H, Chen Y-J. Structure–property study of polyimides derived from PMDA and BPDA dianhydrides with structurally different diamines. Eur Polym J 2002;38:815–28.

[100] Sroog CE. Polyimides. Prog Polym Sci 1991;16:561–694.

[101] Chen J-C, Wu J-A, Chang H-W, Lee C-Y, Li S-W, Chou S-C. Organosoluble polyimides derived from asymmetric 2-substituted-and 2,2′,6-trisubstituted-4,4′-oxydianilines. Polym Int 2014;63:352–62.

[102] Jiang G-MM, Jiang X, Zhu Y-FF, Huang D, Jing X-HH, Gao W-DD. Synthesis and characterization of organo-soluble polyimides derived from a new spirobifluorene diamine. Polym Int 2010;59:896–900.

[103] San Sebastian M, Martinez-Martinez V, Maceiras A, Vilas JL, Lopez-Arbeloa I, Leon LM. Enhanced charge-transfer emission in polyimides by cyano-groups doping. J Phys Chem B 2015;119:5685–92.

[104] Hasegawa M, Horii S. Low-CTE polyimides derived from 2,3,6,7-naphthalenetetracarboxylic dianhydride. Polym J 2007;39:610–21.

[105] Nishihara M, Christiani L, Staykov A, Sasaki K. Experimental and theoretical study of charge-transfer complex hybrid polyimide membranes. J Polym Sci Part B Polym Phys 2014;52:293–8.

[106] Ghaemy M, Movagharnezhad N, Khajeh S. Synthesis, characterization, and properties of poly(amide-imide)s from a new diimide-diacid by direct polycondensation with various diamines. J Appl Polym Sci 2011;121:3679–88.

[107] Nosova GI, Abramov IG, Solovskaya NA, Smirnov NN, Zhukova E V., Lyskov VB, et al. Synthesis and photophysical properties of soluble polyimides and polyquinazolones containing side-chain chalcones or azo chromophores. Polym Sci Ser B 2011;53:73–88.

[108] Liaw D-JJ, Wang K-LL, Huang Y-CC, Lee K-RR, Lai J-YY, Ha C-SS. Advanced polyimide materials: Syntheses, physical properties and applications. Prog Polym Sci 2012;37:907–74.

[109] Unsal E, Cakmak M. Real-time characterization of physical changes in polyimide film formation: from casting to imidization. Macromolecules 2013;46:8616–27.

[110] Zhuang Y, Gu Y. Probing structural evolution of the poly(amic acid) containing benzoxazole moieties in backbone during thermal imidization. J Polym Res 2012;19:14.

[111] Becker KH, Schmidt HW. Para-linked aromatic poly(amic ethyl esters): precursors to rodlike aromatic polyimides. 1. Synthesis and imidization study. Macromolecules 1992;25:6784–90.

[112] Yang W, Liu F, Li G, Zhang E, Xue Y, Dong Z, et al. Comparison of different methods for determining the imidization degree of polyimide fibers. Chinese J Polym Sci 2016;34:209–20.

[113] Muñoz DM, de la Campa JG, de Abajo J, Lozano AE. Experimental and theoretical study of an improved activated polycondensation method for aromatic polyimides. Macromolecules 2007;40:8225–32.

[114] Muñoz DM, Calle M, de la Campa JG, de Abajo J, Lozano AE. An improved method for preparing very high molecular weight polyimides. Macromolecules 2009;42:5892–4.

[115] Ayala D, Lozano AE, De Abajo J, De La Campa JG. Synthesis and characterization of novel polyimides with bulky pendant groups. J Polym Sci Part A Polym Chem 1999;37:805–14.

[116] Sadavarte N V., Halhalli MR, Avadhani CV V, Wadgaonkar PP. Synthesis and characterization of new polyimides containing pendent pentadecyl chains. Eur Polym J 2009;45:582–9.

[117] Chern YT, Tsai JY, Wang JJ. High Tg and high organosolubility of novel unsymmetric polyimides. J Polym Sci Part A Polym Chem 2009;47:2443–52.

[118] Oishi Y, Kakimoto M, Imai Y. Synthesis of aromatic polyimides from N,N'-bis(trimethylsilyl)-substituted aromatic diamines and aromatic tetracarboxylic dianhydrides. Macromolecules 1991;24:3475–80.

[119] Oishi Y, Kakimoto M-A, Imai Y. Synthesis of aromatic polyamide-imides from N,N′-bis(trimethylsilyl)-substituted aromatic diamines and 4-chloroformylphthalic anhydride. J Polym Sci Part A Polym Chem 1991;29:1925–31.

[120] Li D, Xia Y. Electrospinning of nanofibers: reinventing the wheel? Adv Mater 2004;16:1151–70.

[121] Li YX, Lu XF, Liu XC, Zhang CC, Li XA, Zhang WJ, et al. Ultra-low dielectric performance of polymer electrospun nanofiber mats. Appl Phys A Mater Sci Process 2010;100:207–12.

Chapter 2.

Materials, experimental techniques and apparatus

In this chapter we will give the description of the reagents, materials and apparatus used for the the synthesis of polyimides, fabrication of nanocomposite films and electrospinning fibers. Moreover, we will explain the experimental parameters and procedures used for obtaining the data discussed in this thesis.

2.1. MATERIALS

In Table 2.1 appear the characteristics of the commercial reagents and chemical products used in the thesis.

Table 2.1. Characteristics of the reagents and chemical products.

Product	**Company**	**Molecular weight ($g \cdot mol^{-1}$)**	**Purity**
4,4'-oxydiphtalic anhydride (ODPA)	Sigma-Aldrich	310.2	97%
1,3-Bis(3-aminophenoxy)benzene (diamine 0CN)	Tokyo Chemical Industry (TCI)	292.34	>96%
N,*N*-Dimethylacetamide (DMAc)	Sigma-Aldrich	87.1	>99.9%
N,N-dimethylformamide (DMF)	Sigma-Aldrich	73.09	99.8%
m-cresol	Sigma-Aldrich	108.14	99%
Toluene	Fluka	92.14	99.7%
Isoquinoline	Sigma-Aldrich	129.16	92%
Lithium hexafluorophosphate solution – in ethylene carbonate and dimethyl carbonate, 1.0 M $LiPF_6$ in EC:DMC= 50/50 (v/v) (battery grade)	Sigma-Aldrich	—	<15 ppm H_2O <50 ppm HF
Cobalt ferrite nanoparticles, 35-55 nm ($CoFe_2O_4$)	Nanoamor	—	98%

2.2. EXPERIMENTAL TECHNIQUES AND APPARATUS

2.2.1. BROADBAND DIELECTRIC SPECTROSCOPY

Dielectric spectroscopy measurements were carried out using an impedance analyzer Alpha-S trough the measurement of the capacitance (C) and the loss factor (tan δ). The temperature control was performed by a Quatro Cryosystem from Novocontrol GmbH (Figure 2.1). Circular gold electrodes (10 mm diameter) were deposited onto both sides of each sample, to form a parallel plate capacitor, by magnetron sputtering with a Polaron Coater SC502 under an Argon atmosphere.

The sample cell with active head dielectric converter was mounted on a cryostat (BDS 1100) and exposed to a heated gas stream evaporated from a liquid nitrogen Dewar. The isothermal experiments were performed from 25°C to 260°C (thermal stability: 0.5 °C) in 5°C steps. The complex dielectric permittivity $\varepsilon^* = \varepsilon' - i\varepsilon''$was determined as a function of frequency (10^{-1}–10^7 Hz) through the following equations:

$$\varepsilon' = \frac{Cd}{\varepsilon_0 A} \tag{2.1}$$

and

$$\varepsilon'' = tan\delta * \varepsilon' \tag{2.2}$$

where C is the capacitance, ε' is real part of the dielectric constant, ε'' is the imaginary part of the dielectric constant, ε_0 is the permittivity of the free space ($8.85 \cdot 10^{-12}$ F·m^{-1}), and *d* and *A* are the sample thickness and electrode area, respectively.

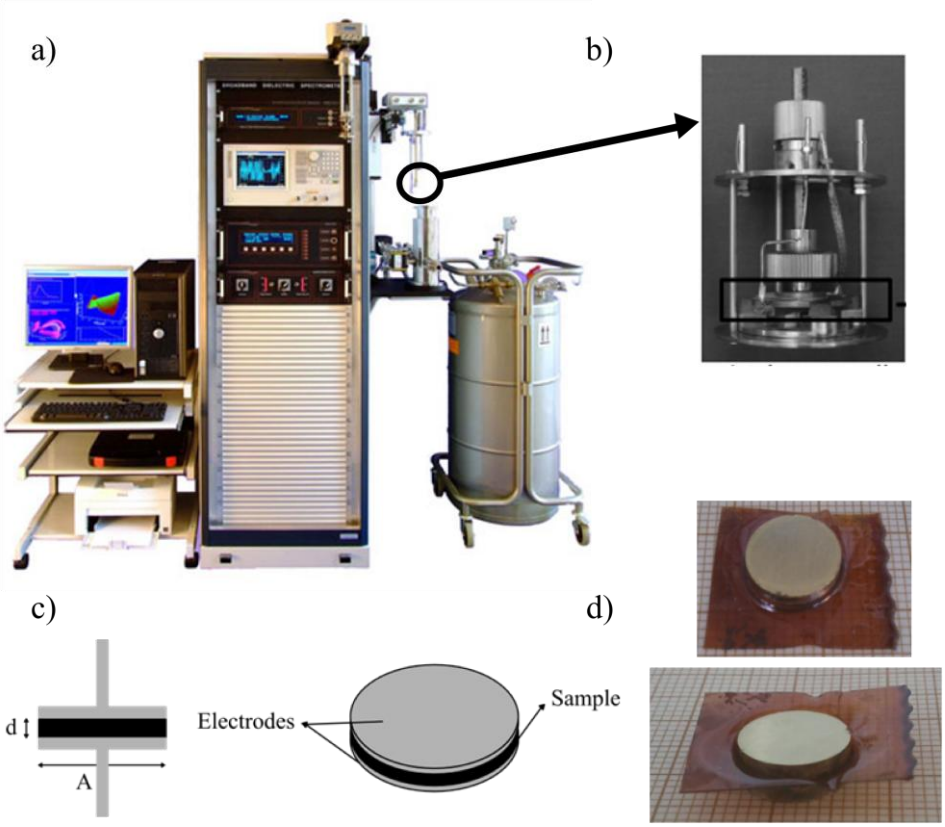

Figure 2.1. a) Picture of a Quatro Cryosystem from Novocontrol, b) sample cell, c) schematic of the capacitor formed by the polymer and the external electrodes, and d) real pictures of a polyimide sample after measurement.

Broadband dielectric spectroscopy (BDS), also called impedance spectroscopy and electrochemical impedance spectroscopy, measures the dielectric properties of a medium as a function of frequency. It is based on the interaction of an external field with the electric dipole moment of the sample, often expressed by permittivity. This technique measures the impedance of a system over a range of frequencies and temperatures, and therefore it is revealed the frequency response of the system, including the energy storage and dissipation properties. In the frequency regime the domain of broadband dielectric spectroscopy (BDS) is between 10^{-6} and 10^{12} Hz. In this range, molecular and collective dipolar fluctuations (relaxations), electrical conduction, charge transport and polarization effect, at inner and outer boundaries, take place, determining the dielectric properties of the material.

2.2.2. DIFFERENTIAL SCANNING CALORIMETRY (DSC)

DSC measurements were performed using a METTLER DSC 822 equipment (Figure 2.2) and the glass transition temperatures were determined by the onset method. The samples (5-15 mg) were heated from 30 to 250ºC at a heating rate of 20ºC·min^{-1}, under nitrogen atmosphere with a flow rate of 50 mL·min^{-1}, in aluminium pans. The Mettler Toledo Differential Scanning Calorimeter (DSC) measures the difference between the heat flows from the sample and reference sides of a sensor as a function of temperature or time. Differences in heat flow arise when a sample absorbs or releases heat due to thermal effects such as melting, crystallization, chemical reactions, polymorphic transitions…

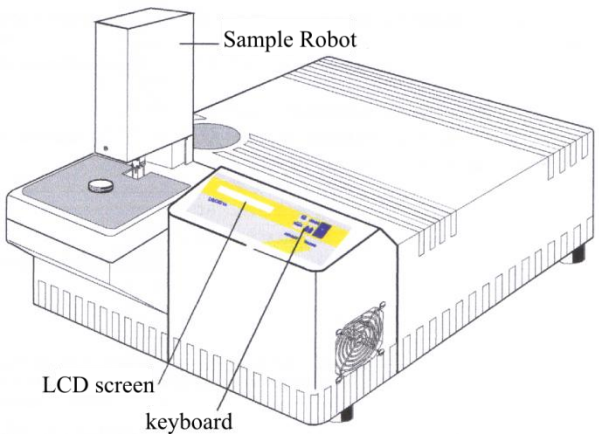

Figure 2.2. View of a DSC822^{e} Module equipped with a TS801RO sample robot.

Differential Scanning Calorimetry (DSC) is one of the most effective analytical techniques to characterize the physical properties of polymers. DSC allows determining heat capacities in both solid and liquid states and phase transition temperatures and the corresponding enthalpy and entropy changes as well as heat capacity changes. DSC is a thermoanalytical technique in which the difference in the amount of heat required to increase the temperature of a sample and reference is measured as a function of temperature. Both the sample and reference are maintained at nearly the same temperature throughout the experiment. The temperature program for a DSC analysis is

designed such that the sample holder temperature increases linearly as a function of time. The reference sample should have a well-defined heat capacity over the range of temperatures to be scanned.

The glass transition temperature can be defined in different ways. In literature, both the onset temperature and the inflection point temperature are used to report T_g. This represents point A and B as shown in Figure 2.3.

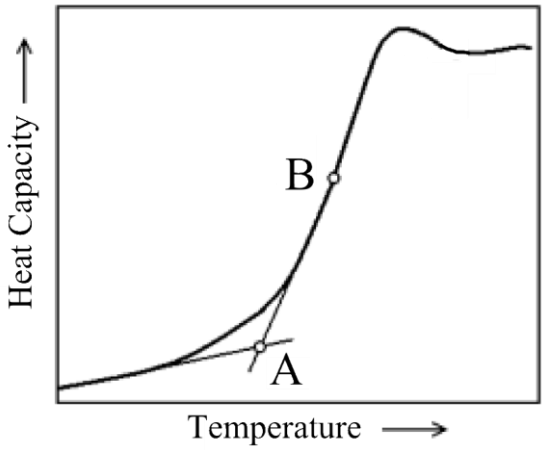

Figure 2.3. The onset temperature (A) and the inflection point (B) of a glass transition in a DSC curve.

2.2.3. DIGITAL TEMPERATURE CONTROLLER

Controlling the heating and the temperature during the poling process is a key factor. In his thesis a Shimaden digital temperature controller (model Lite FP93) and two PT100 resistances were employed (Figure 2.4).

The model Lite FP93 has programmable ramp controller, autotuning controller, expert PID processing with remote setting, analogue or digital. The device allows different inputs, such as thermocouple, current, voltage; and as outputs: current, voltage or relay.

Resistance thermometers or resistance temperature detectors (RTDs), such as the PT100, are sensors used to measure temperature by correlating the resistance of the RTD element with temperature. Most RTD elements consist of a length of fine coiled wire wrapped around a ceramic or glass core, because is usually quite fragile. The RTD

element is made from a pure material, typically platinum, nickel or copper. The material has a predictable change in resistance as the temperature changes and it is this predictable change that is used to determine temperature. Platinum resistance thermometers (PRTs) offer excellent accuracy over a wide temperature range. The operation principle is to measure the resistance of a platinum element. The most common type (PT100) has a resistance of 100 ohms at 0 °C and 138.4 ohms at 100 °C.

Figure 2.4. Image of a Shimaden digital temperature controller model Lite FP93 (Left) and a PT100 resistance (Left).

2.2.4. ELECTROCHEMICAL IMPEDANCE SPECTROSCOPY

Electrochemical impedance spectroscopy of electrospun polyimide fibers was evaluated on Biologic VMP3 instrument in a frequency range from 1 MHz to 10 mHz with an amplitude of 10 mV at room temperature (Figure 2.5).

Electrochemical techniques are very helpful for evaluation of batteries and cells during charge and discharge, and in service, as the nature of chemical and electrochemical processes occurring in these devices may be determined. Electrochemical impedance spectroscopy (EIS) has great advantages, because not only provide detailed kinetic information, but can also be used to monitor changes in battery properties under different usage or storage conditions. EIS is a very sensitive technique, and offers a wealth of information about battery systems such as: analysis of state of charge, study of reaction mechanisms, change of active surface area during operation, separator

evaluation, passivating film behavior, separation and comparison of electrode kinetics on each electrode, identification of possible electrode corrosion processes, and investigation of the kinetics at each electrode.

Since the perturbating ac signal is very small, the resultant polarization of the electrode is in a linear potential region. Therefore, there is no destructive damage to the electrode, and EIS can be used to evaluate the time relation of interface parameters. Due to the great advantages of electrochemical impedance spectroscopy and, although the interpretation and modeling of EIS data still remain a complex problem, this technique is now widely applied to the study of batteries and fuel cells.

Figure 2.5. Image of a multi-channel potentiostat VMP3.

2.2.5. FOURIER TRANSFORM INFRARED SPECTROSCOPY (FTIR)

Infrared measurements (FTIR) were performed at room temperature with Jasco FTIR 4100 apparatus (Figure 2.6) in Attenuated Total Reflectance (ATR) mode from 4000 to 600 cm^{-1} after 32 scans and a resolution of 4 cm^{-1}.

The use of ATR eliminates in many cases the need for sample preparation or at least simplifies the procedures. The ATR accessory fits in the sample compartment of the 6700. ATR is especially useful for strongly absorbing samples which cannot be measured by infrared transmission.

The IR beam, in this device, hits the interface with the sample at an angle greater than the critical angle, so that total internal reflection occurs. The internally reflected beam generates "evanescent waves" into the sample. ATR works well for these samples because the intensity of the evanescent waves decays exponentially with distance from the surface of the ATR crystal, making the technique largely insensitive to sample thickness.

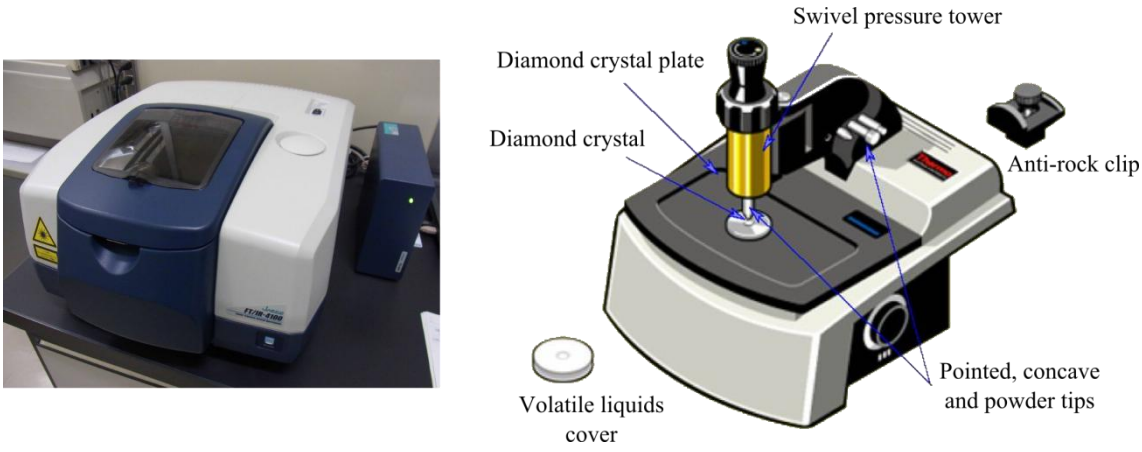

Figure 2.6. Photography of a Jasco FTIR 4100 apparatus (Left) and a scheme of an ATR accessory (Right).

2.2.6. GALVANOSTATIC CYCLING

Galvanostatic cycling was carried out at room temperature at different C rates (C/20, C/10 and C/5) between a minimum and a maximum limit of 2.5 and 4.0 V, respectively, using Landt CT2001A Instrument (Figure 2.7).

Characterization of Li-ion cells and batteries usually involves the galvanostatic charge and discharge during various cycles. During galvanostatic cycling of batteries, the charge and discharge current are often expressed as a C-rate, calculated from the battery capacity. The C-rate is a measure of the rate at which a battery is charged or discharged relatively to its maximum capacity.

The CT2001 series Battery Testing Systems are designed for energy storage materials research and single battery (coin cell, bag cell) test. It comes with eight channels which are independently programmed and fully controlled by the computer. The equipment

provides standard charge/discharge tests, cyclelife test with wide current and voltage choices and it can show different kinds of plots for specific cycles (Voltage vs. Capacity, Capacity vs. Cycle Number, Efficiency, etc.),. Each battery testing equipment is custom-built and is known for the high precision, high reliability and powerful software for data acquisition and process.

Figure 2.7. Image of a Landt CT2001A instrument.

2.2.7. HIGH VOLTAGE SOURCE

Two different high voltage sources (Figure 2.8) were employed. In chapter 2, during the poling process a Spellman high voltage source (model SMS 300W) with intensity and voltage control, connected to a Teflon (polytetrafluoroethylene, PTFE) chamber to assure a correct union with the corona tip, was used. In chapter 6, electrospinning was conducted at 1.5 kV cm^{-1} with a high voltage power supply from Glassman (model PS/FC30P04).

A voltage source is a two terminal device which can maintain a fixed voltage. An ideal voltage source maintains the fixed voltage independent of the load resistance or the output current. However, a real-world voltage source cannot supply unlimited current. A voltage source is the dual of a current source, where in electronics a dual of a relationship is formed by interchanging voltage and current in an expression. Since no ideal sources of either variety exist (all real-world examples have finite and non-zero source impedance), any current source can be considered as a voltage source with the same source impedance and vice versa.

Figure 2.8. Image of the high voltage sources: Spellman model SMS 300W (Left) and Glassman model PS/FC30P04 (Right).

2.2.8. MAGNETRON SPUTTERING

Several types of samples were coated with a thin gold-layer using a sputter coating Polaron, model SC502 sputter coater (Figure 2.9). Electrospinning fibers and nanocomposite films were coated with gold by magnetron sputtering prior to SEM measurement and circular gold electrodes (10 mm diameter) were deposited onto both sides of polyimide film samples, to form a parallel plate capacitor.

Magnetron Sputtering is a Plasma Vapor Deposition (PVD) process in which a plasma is created and positively charged ions from the plasma are accelerated by an electrical field superimposed on the negatively charged electrode or "target". The positive ions are accelerated by potentials ranging from a few hundred to a few thousand electron volts and strike the negative electrode with sufficient force to dislodge and eject atoms from the target.

The sputter coater uses an electric field and argon gas. The sample is placed in a small chamber at vacuum. The electric field causes an electron to be removed from the argon, making the atoms positively charged. The argon ions then become attracted to a negatively charged gold foil. The argon ions knock gold atoms from the surface of the gold foil and they fall and settle onto the surface of the sample producing a thin gold coating.

Figure 2.9. Image of a SC502 Polaron sputter coater.

2.2.9. SCANNING ELECTRON MICROSCOPY (SEM)

Two different SEM devices (Figure 2.10) were used. In chapter 5, the morphology of the CFO/P0CN2CN composites was studied by scanning electron microscopy (SEM) using a Quanta 650 FEI electron microscope with acceleration voltage of 10 kV. Prior to SEM, the samples were coated with gold by magnetron sputtering. However, in chapter 6, fiber size and morphology of electrospinning fibers were analyzed using a scanning electron microscopy (NanoSEM – FEI Nova 200) with an accelerating voltage of 10 kV. The size of fibers was measured on 10,000x magnified SEM images using the Image-J software.

A scanning electron microscope (SEM) is a type of electron microscope that produces images of a sample by scanning it with a focused beam of electrons instead of light to form an image. A beam of electrons is produced at the top of the microscope by an electron gun. The electron beam follows a vertical path through the microscope, which is held within a vacuum. The beam travels through electromagnetic fields and lenses, which focus the beam down toward the sample (Figure 2.11, Right). The electrons in the beam interact with the sample, producing various signals that can be used to obtain information.

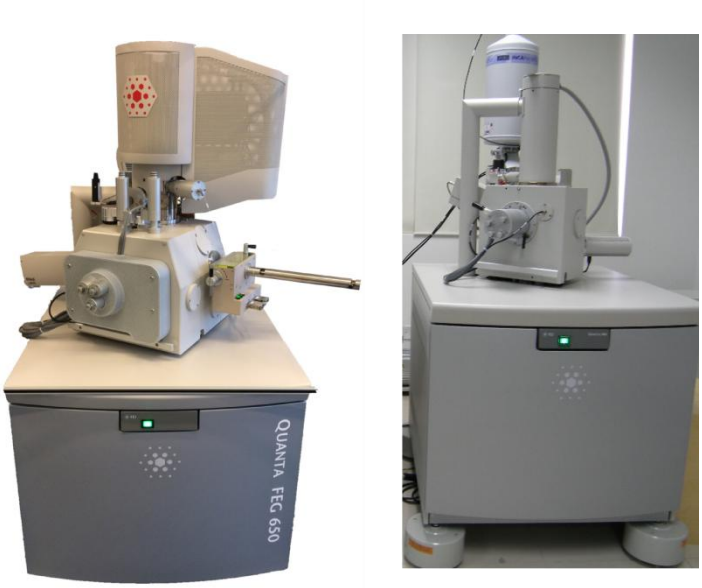

Figure 2.10. View of a Quanta 650 FEI (Left) and FEI Nova 200 (Right) scanning electron microscopy (SEM).

When the beam hits the sample electrons and X-rays are ejected from the sample. Detectors collect these X-rays, backscattered electrons, and secondary electrons and convert them into a signal that is sent to a screen similar to a television screen (Figure 2.11, Left). The signals that derive from electron-sample interactions reveal information about the sample including external morphology (texture), chemical composition, and crystalline structure and orientation of materials making up the sample. In most applications, data are collected over a selected area of the surface of the sample, and a 2-dimensional image is generated that displays spatial variations in these properties.

SEM employs vacuum conditions and uses electrons to form an image, because of that all non-metals need to be made conductive by covering the sample with a thin layer of conductive material, by using a sputter coater.

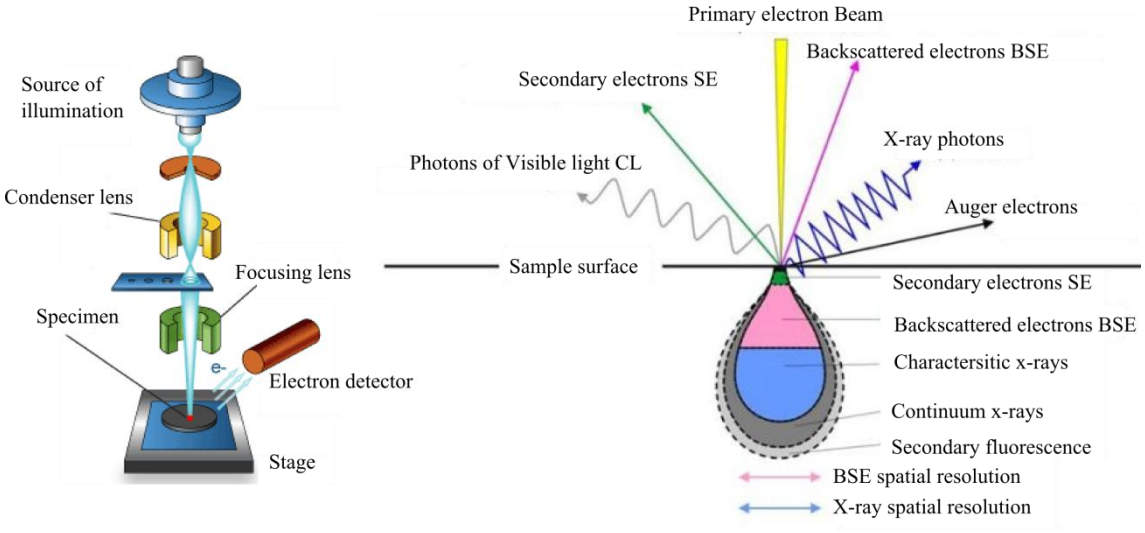

Figure 2.11. Scheme of the functioning of a SEM (Left) and electron beam interaction diagram with a sample (Right).

2.2.10. SYRINGE PUMP

In the electrospinning setup a NE-1000 Programmable Single Syringe Pump (from Syringepump) was used to feed the polymer solutions into the needle tip at 0.2 mL h^{-1} (Figure 2.12).

Figure 2.12. Photography of a NE-1000 Programmable Single Syringe Pump

The aim of the syringe pump is to administer a constant solution flow rate avoiding the presence of a person near the high voltage source. This model can hold one syringe from micro-liter sizes up to 60 mL (140 mL partially filled) and let different infusion rates from 0.73 $\mu L \cdot h^{-1}$ (1 mL syringe) to 2100 $mL \cdot h^{-1}$ (60 mL syringe). It is fully programmable and can operates stand-alone or from a computer.

2.2.11. LOCK-IN AMPLIFIER

The induced ME voltage of the CFO/P0CN2CN composite was measured with a Standford Research Lock-in amplifier (SR530). The SR530 is an analog lock-in amplifier which can measure AC signals as small as nanovolts in the presence of much larger noise levels. The dual phase SR530 has low-noise voltage and current inputs, high dynamic reserve, two stages of time constants, and an internal oscillator (Figure 2.13).

Figure 2.13. Image of a Standford Research Lock-in amplifier (SR530).

A lock-in amplifier is a type of amplifier that can extract a signal with a known carrier wave (a sinusoidal waveform that is modified with an input signal for the purpose of conveying information) from an extremely noisy environment. Signals up to 1 million times smaller than noise components and close in frequency can still be detected.

Lock-in amplifiers are used to detect and measure very small AC signals all the way down to a few nanovolts. Accurate measurements may be made even when the small signal is obscured by noise sources many thousands of times larger. Lock-in amplifiers use a technique known as phase-sensitive detection to single out the component of the signal at a specific reference frequency and phase. Noise signals, at frequencies other than the reference frequency, are rejected and do not affect the measurement.

Lock-in measurements require a frequency reference (Figure 2.14). Typically, during an experiment when the sample is excited at a fixed frequency (from an oscillator or function generator), and the lock-in detects the response from the experiment at the

reference frequency. In the diagram of Figure 2.14, the reference signal is a square wave at frequency ω_r. This might be the sync output from a function generator. If the sine output from the function generator is used to excite the experiment, the response might be the signal waveform show below. The signal is $V_{sig}\sin(\omega_r t + \theta_{sig})$ where V_{sig} is the signal amplitude, ω_r is the signal frequency, and θ_{sig} is the signal's phase.

Lock-in amplifiers generate their own internal reference signal usually by a phase-locked-loop locked to the external reference. In the diagram, the external reference, the lock-in's reference, and the signal are all shown. The internal reference is $V_L\sin(\omega_L t + \theta_{ref})$

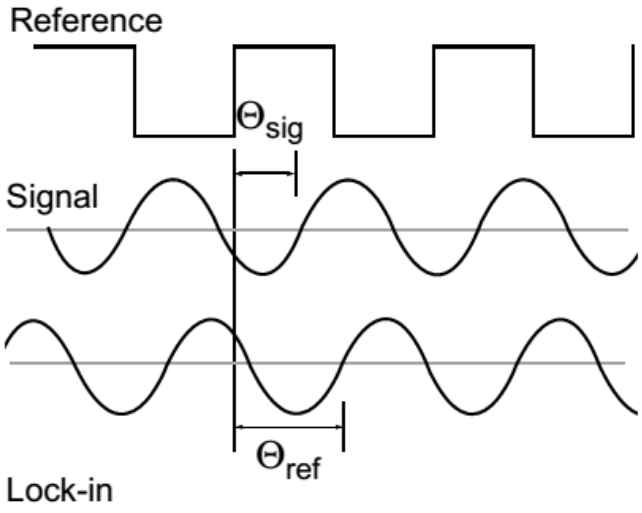

Figure 2.14. Diagram of the waves working in a lock-in amplifier.

The lock-in amplifies the signal and then multiplies it by the lock-in reference using a phase-sensitive detector or multiplier. The physical nature of this multiplication and filtering process is important in the different types of lock-ins. In traditional analog lock-ins, the signal and reference are analogue voltage signals. The signal and reference are multiplied in an analog multiplier, and the result is filtered with one or more stages of resistor–capacitor **(**RC) filters. In a digital lock-in, the signal and reference are represented by sequences of numbers. Multiplication and filtering are performed mathematically by a digital signal processing chip.

2.2.12. THERMOGRAVIMETRIC ANALYSIS (TGA)

Thermogravimetric (TG) measurements were performed in a METTLER TGA/SDTA 851 thermobalance (Figure 2.15). Samples (about 10 mg) were heated from room temperature up to 900ºC at 10ºC·min^{-1} under nitrogen atmosphere. A N_2(g) atmosphere was used to drag the gases produced in the measuring cell with a carrier flow rate of 50 mL·min^{-1}, and also another purge gas to protect the balance, with a flow rate of 100 mL·min^{-1}. The initial degradation temperature (T_d) was determined from the intersection between the tangent to the baseline and the inflection point in the thermogram.

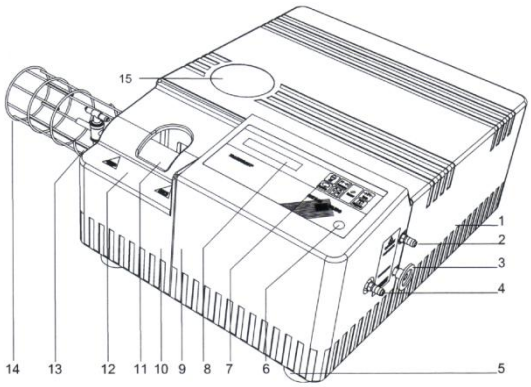

1 module housing
2 reactive gas inlet
3 vacuum connection and purge gas inlet
4 the protective gas inlet
5 screw feet
6 level indicator
7 keyboard
8 liquid crystal display
9 right front housing
10 left front housing
11 sample insert opening
12 insert surface
13 opening
14 protection
15 surface for hot crucibles

Figure 2.15. View of a TGA/SDTA851e Module (Left) and legend (Right).

In a typical thermogram several characteristics of the degradation process can be observed (Figure 2.16):

-Initial temperature of the degradation process (T_i): temperature when the mass change reaches a value that can be detected by the thermobalance.

-Degradation process temperature (T_{max} or T_d): reflects the temperature when the maximum rate of degradation takes place. It is determined from the intersection point between the line tangent to the curve at point maximum rate of degradation and the baseline, or with the maximum of the first derivative of the thermogravimetric curve. This temperature is the one that we used to establish the thermal stability of our materials.

-Final temperature (T_f): temperature when the mass change reach a maximum value corresponding to complete reaction.

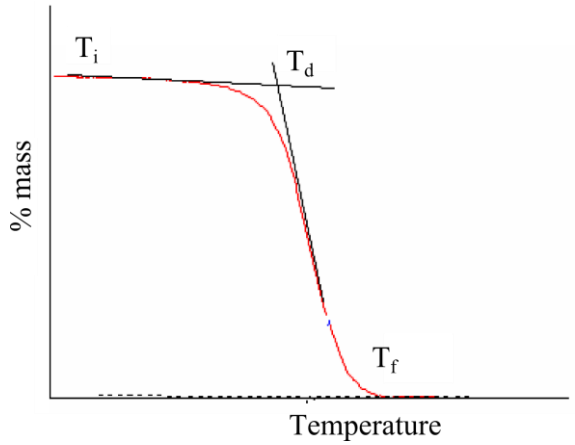

Figure 2.16. Thermogravimetric curve where the different characteristic temperatures can be observed.

2.2.13 VIBRATING SAMPLE MAGNETOMETER (VSM)

Magnetic hysteresis loops at room temperature of the obtained polyimide based magnetoelectric were measured using an ADE Technologies vibrating sample magnetometer (VSM).

A vibrating sample magnetometer is an instrument that measures magnetic properties, it is an easy and sensitive way for measuring magnetic moment and coercivity of thin films or studying the magnetic properties of liquids, powders, or bulk samples, for example.

In a VSM first it is necessary introducing the sample to be studied in a constant magnetic field (Figure 2.17). If the sample is magnetic, this constant magnetic field will magnetize the sample by aligning the magnetic domains, or the individual magnetic spins, with the field. The stronger the constant field, the larger the magnetization will be. The magnetic dipole moment of the sample will create a magnetic field around the sample. The sample is then physically vibrated sinusoidally, normally through the use

of a piezoelectric material. As the sample is moved up and down, this magnetic stray field is changing as a function of time and can be sensed by a set of pick-up coils.

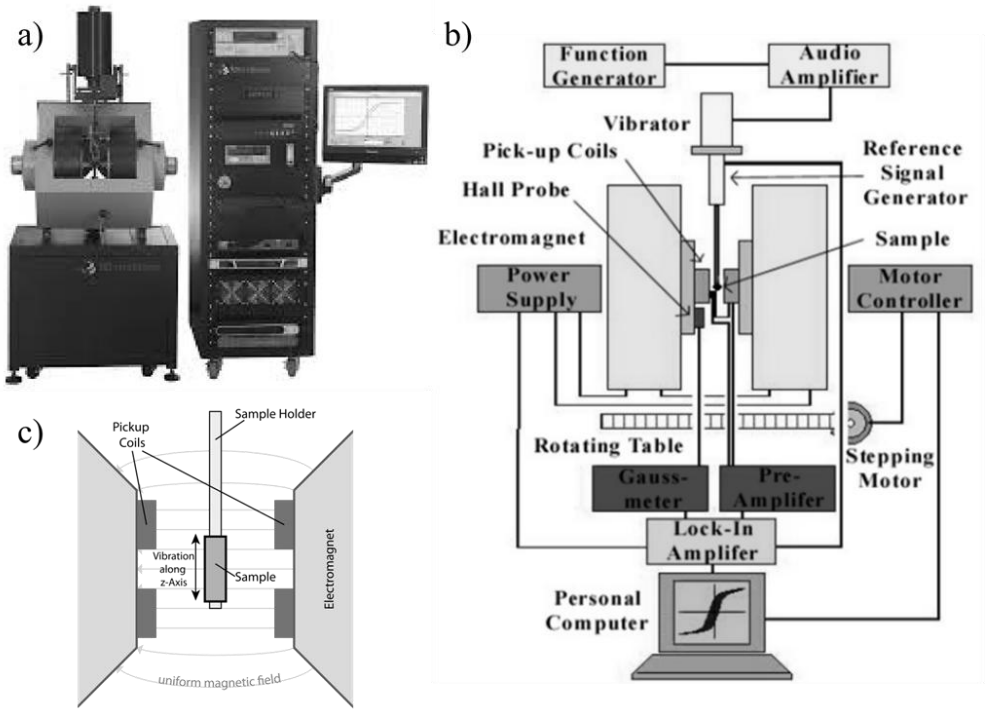

Figure 2.17. a) Image of an ADE Technologies vibrating sample magnetometer, b) schematic diagram of a VSM, and c) an amplified section of a VSM showing the sample holder and detection mechanism.

The alternating magnetic field will cause an electric field (induced voltage) in the pick-up coils according to Faraday's Law of Induction, but does not depend on the strength of the applied magnetic field. This current will be proportional to the magnetization of the sample. The greater the magnetization, the greater the induced current.

In a typical setup, the induced voltage is measured through the use of a lock-in amplifier using the piezoelectric signal as its reference signal. By measuring in the field of an external electromagnet, it is possible to obtain the hysteresis curve of a material, i.e., a plot of the magnetization (M) versus magnetic field strength (H). The vibrating sample magnetometer measures the magnetization of a small sample of magnetic material placed in an external magnetizing field by converting the dipole field of the sample into an ac electrical signal.

2.2.14. WIDE RANGE D_{33}-METER

The piezoelectric response of polyimide films after corona poling treatment was analysed with a wide range d_{33}-meter (model 8000, APC Int. Ltd) (Figure 2.18).

The d_{33} tester is a special instrument for directly measuring the piezoelectric constant d_{33} values of piezoelectric materials. It is capable of measuring the d_{33} value over a very large range (x1.0 range: from 10 to 2000 $pC \cdot N^{-1}$ and x0.1 range: 1 to 200 $pC \cdot N^{-1}$), at high resolution (x 0.1 range: 0.1 $pC \cdot N^{-1}$ and x 1 range: 1 $pC \cdot N^{-1}$) and high accuracy. The d_{33} tester uses a force with a frequency of 110 Hz and amplitude of 0.25 N.

This d_{33} tester will enable the user to measure d_{33} values over a very wide range, at high resolution, and with a high degree of reliability. The measurement is quick and easily made with minimal training required. A variety of sizes and shapes can be easily accommodated and measured that includes discs, blocks, rings, tubes and semispherical shell. No additional equipment is needed to operate the wide-range unit, either for obtaining d_{33} values or determining polarity. Polarity is indicated as part of the readout: a (–) sign indicates the upper face of the element in the tester is negative, no sign indicates the upper face is positive.

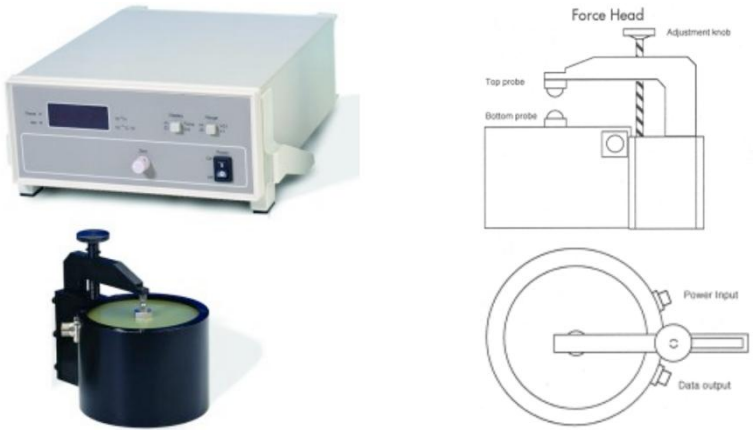

Figure 2.18. Photograph (Left) and scheme (Right) of a wide-range d_{33} tester (model 8000, APC Int. Ltd).

The system works by clamping the sample, and subjecting it to a low frequency force (Figure 2.18). Processing of the electrical signals from the sample, and comparison with

a built-in reference, enables the system to give a direct reading of the d_{33}, one of the most useful parameters in evaluating the material. This is a material coefficient representing charge per unit force in the direction of polarization. The method of operation is sometimes called the quasi-static or Berlincourt method. A key principle is that the test frequency is low compared with any likely system or sample resonances, yet high enough that a conclusive measurement can be made in a few seconds. The result is a quick, simple test.

Chapter 3.

Synthesis, corona poling and characterization

In this chapter the most important concepts and terms related with poling are explained, such as formation of electrets or the different poling methods. Moreover, the design and optimization of the corona poling method for a series of polyimide and copolyimide films are presented, followed by the measurement of their piezoelectric response with a wide range d_{33}-meter. Finally, the thermal stability of the polymer films is tested by means of DSC and TGA in order to check their aptitude for high temperature applications.

3.1. INTRODUCTION

Electret (formed of *elektr-* from "electricity" and *-et* from "magnet") is a dielectric material that has a quasi-permanent electric charge or dipole polarization. An electret is a solid dielectric piece polarized by the simultaneous application of heat and an electric field [1,2]. Thus, they are prepared by cooling a heated dielectric in a strong electric field, following the technique devised by the discoverer of the electrets, Mototaro Eguchi [3].

Electrets are considered as counterparts of magnets. They are electrified samples that exhibit electrical charges of opposite signs on its two sides. They are metastable, and their polarization decays slowly with time after the ending of the poling. However, the persistence of polarization depends on a number of factors, such as the material used for preparation, internal order of the material (semicrystalline or amorphous), the magnitude of the polarizing field, the polarizing temperature, polarization time, polarization technique (contact poling or corona poling), thickness of the sample, electrode material, etc.

The first electret was prepared by Eguchi. He melted equal parts of carnauba wax and rosin with the addition of some beeswax, and allowed the mixture to solidify in a strong DC field between two parallel electrodes. This innovative technique opened up a new way for studying the mechanism of polarization and absorption of charges in amorphous and crystalline dielectrics, a research continued by Gutmann, Pillai et al., Sessler, and several other workers in the field [2,4–9].

Electrets exhibit a quasi-permanent electrical charge after the polarization treatment is finished. As they are a source of electric field, they are particularly useful in instruments and devices where one requires a stable electrostatic field. Depending on the method of inducing polarization and the materials used for the preparation, they can be classified as: a) thermoelectrets, b) ceramic electrets, c) photoelectrets, d) thermophotoelectrets, e) magnetoelectrets, f) radioelectrets, etc.

In this thesis only thermoelectrets were used. Normally, they are prepared by the method called poling adopted by Eguchi with modifications to improve their characteristics [10]. That is, the simultaneous application of temperature and electric field. In general, the material from which an electret is to be made is melted or softened, and then a high voltage-is applied [11]. As the external field acts on this molten substance for considerable time, the necessary charge redistribution is attained. Then it is allowed to cool and slowly solidify under the same electric field. The charge distribution in the material is thus "frozen in" under these conditions. After solidification, the electric field is switched off and the solidified dielectric shows an electric field on either surface, usually positive on one side and negative on the other side. To retain the charge, the electrets should be short-circuited and kept under controlled conditions of humidity and temperature. Electrets can also be prepared at low temperatures. However, the magnitude of the resultant charge and the permanency of the electrets will be comparatively poorer than for electrets prepared with material in the molten state [12].

In the beginning, most investigators of electrets used waxes and wax mixtures and other organic compounds for preparation and study of electrets. But later it was emphasized the importance of preparing electrets using polymer substances, because their stability and magnitude of charge obtained. So, polymers are preferred for electrets preparation due to the following reasons:

Very good charge storage and retention capacity, because of high concentration of deep traps and very good insulating materials.	Superior thermomechanical properties.	Good processability into films or any other shape.

Polymers are of two types: a) polar polymers such as poly(vinylidene fluoride) (PVDF) and b) nonpolar polymers such as poly(ethylene) (PE) and poly (tetrafluoroethylene) (Teflon). When a polymeric material is subjected to an electric field, especially at high temperatures, the dipoles are reoriented. In nonpolar polymers, the dipole moment is

due to the induced dipoles; whereas in a polar material, it is due to the orientation of the dipoles in the field direction. But there are other contributions, because the total polarization is due to the contributions from atomic, dipolar, and space charge polarizations. These three types of polarizations are due to the charge carriers, which are particles free to move, carrying an electric charge, such as electrons or ions. They are locally bound in atoms or molecules or structures of the dielectric and can be mobile and migrate through the dielectric. In fact, these charge carriers give rise to space charge polarization or interfacial polarization (Maxwell-Wagner-Sillars polarization) when trapped in the material at the interfaces, near the electrodes or around chain folding, chain ends, etc [13]. This charge generation and retention properties of polymers depend very much on their chemical structure, can be modified by doping, co-polymerization, substitution, or blending; and can be studied via dielectric spectroscopy (further information in chapter 4).

3.1.1. POLING

Poling is the orientation of the microscopic molecular dipoles (orientational polarization). The polymer is heated close to its glass transition temperature (T_g), so as to increase the molecular mobility, while application of a DC electric field results in a polar orientation of the molecular dipoles along the field direction. Then the polar orientation is frozen in by cooling down to room temperature, while keeping the orientating field on [14]. But this orientation process and the chosen poling temperature depend on the internal order of the polymer electrets, i.e. if it is semicrystalline or amorphous.

In a ferroelectric semicrystalline polymer, the process of poling is the process of reorientation of the crystallites (or, generally speaking, the ferroelectric domains) within the polymer bulk medium. Theoretically, at an electric field high enough, almost all the domains are in the same direction resulting in a single large domain. The final quality of the alignment of crystallites (and consequently the piezoelectric coefficient *d*) depends on the following factors: the strength and time of the applied electrical field, the value

and degree of uniformity of the temperature applied on the polymer and the degree of contamination or voids in the sample. The material in this state possesses maximum polarization. If the material is maintained at a high temperature (close to the transition temperature but lower) while the electric field is applied, the orientation of the domains is improved. For some materials like PVDF, mechanical stretching of the polymer film during the poling process enhances the quality of the crystallite alignment. Stretching the polymer essentially aligns the amorphous chains in the film plane and facilitates uniform rotation of the crystallites by an electrical field. Depending on whether stretching is uniaxial or biaxial, the electrical and mechanical properties (and therefore the transduction response), are either highly anisotropic or isotropic in the plane of the polymer sheet. For semicrystalline polymers the amorphous phase supports the crystal orientation and the polarization is stable up to the Curie temperature (T_C).

But in amorphous systems, such as polyimides, the situation is different. While in a semicrystalline material, the locking-in of the polarization is supported by the crystalline structure, and is therefore stable above the glass transition temperature of the polymer, in an amorphous polymer, during poling, the temperature is lowered to room temperature while the field is still on, in order to freeze in the dipole alignment. Thus, the poling temperature in amorphous polymers must be higher than the glass transition temperature (T_g) because the remnant polarization is lost in the vicinity of T_g, and logically their use is limited to temperatures well below T_g. This means that the polymers are used in their glassy state, when they are quite stiff thus limiting the ability of the polymer to strain with an applied stress. The piezoelectric amorphous polymer may be used at temperatures near its T_g to optimize the mechanical properties, but not too close so as to maintain the remnant polarization. Although there is little data about the ability of piezoelectric activity in amorphous polymers, it is clear that time, humidity, pressure, and temperature can all contribute to dipole relaxation (depoling).

In conclusion, the process of poling amorphous polyimides involves the following steps summarized in Figure 3.1:

1. The material is heated to a temperature higher than the T_g and held at that temperature.

2. A sufficiently high electric field is applied to the material for about 1-2 h. The dipoles tend to get oriented in the direction of the electric field, and the material attains saturation polarization.
3. The material is cooled to room temperature with the electric field kept on. The dipoles remain frozen in the oriented state.
4. The electric field is now put off. The material remains in the maximum polarization state with most of the dipoles oriented in the same direction.

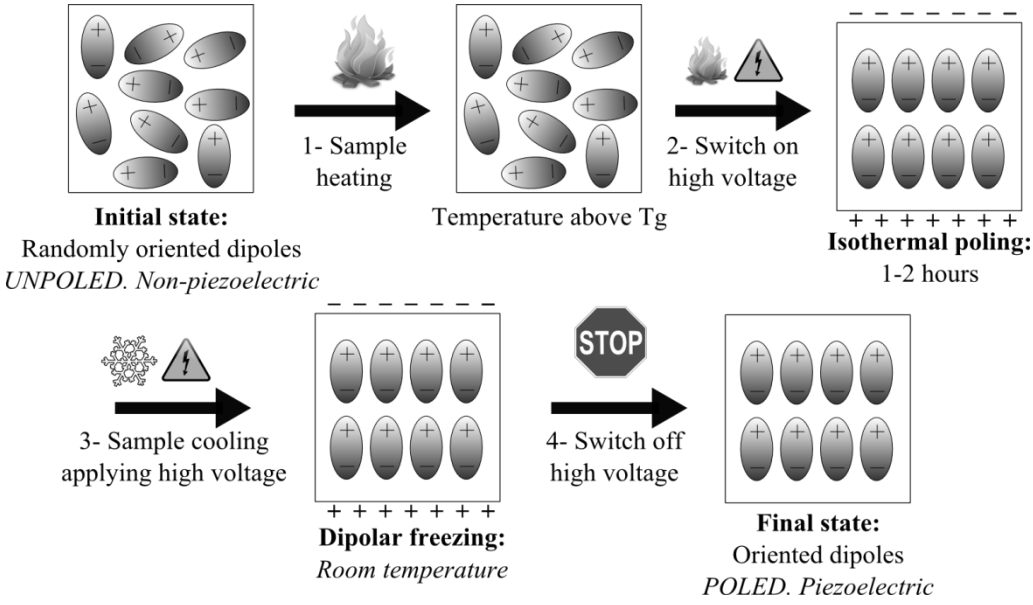

Figure 3.1. Poling process of an amorphous polymer.

There are several poling methods reported in bibliography. For instance, thermoelectrets can be prepared by the charge injection method, plasma poling, electron beam charging, liquid contact method and also by mechanical compression [15–18]. But the most common techniques are the contact and corona poling methods, schematized in Figure 3.2.

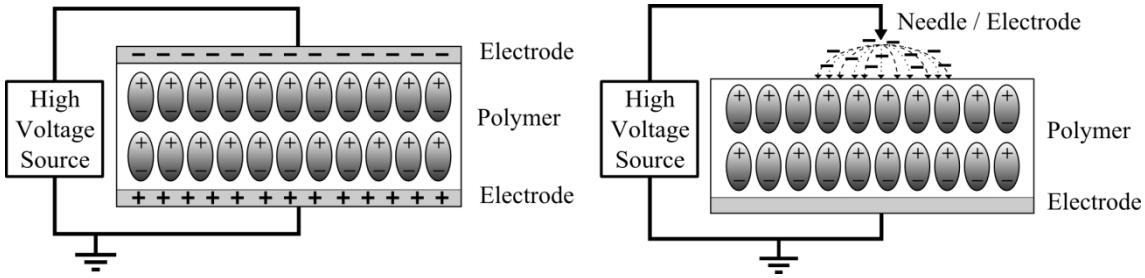

Figure 3.2. Schematic setup of a contact poling (Left) and negative corona poling (Right) experiment for polymer thermoelectrets.

A. CONTACT POLING

Contact poling is when the electric poling field is created between two conductive electrodes. The advantage of this poling configuration relies on the homogeneity and the direct control on the poling field. A sandwich (electrode-film-electrode) configuration (parallel plate electrodes) is used to achieve perpendicular poling. The electrode poling, is simpler than the corona poling. Conductive electrodes should be deposited or pressed on both sides of the polymer film to apply the high voltage across the polymer. Contact poling has different experimental setups, there are contact poling at room temperature, contact poling with a cycle of temperature (thermal poling) or the Bauer cyclic poling method [19–25]. Depending on your needs you can choose one or another.

The strong electric field could cause the polymer to dielectric breakdown; that's why the poling process can also be done in a vacuum chamber or immersed inside an electrically insulating fluid [26]. Moreover, it can be limited by charge injection processes near sharp electrode edges or internal voids, so a careful design of electrodes shape is necessary.

B. CORONA POLING

Corona is a self-sustainable, non-disruptive electrical discharge which occurs when a sufficiently high electric potential difference (voltage) exists between asymmetric electrodes. Intense electric fields are obtained with corona poling by depositing on the

film surface the charges created by ionization of the surrounding atmosphere [27–31]. Because of the high electric field (kilovolts) near the emitting electrode (tip, wire or a grid), the air that is normally insulating becomes ionized and the resulting ions are driven towards the low-field electrode. The threshold for the corona discharge depends upon the availability of a free electron that can trigger an avalanche responsible for ionizing the gas. Electrons are efficient ionizing agents because upon impact they transfer all their energy acquired from the electric field to gas molecules. That is, the gas molecules around the tip get ionized and accelerated towards the surface of the piezoelectric polymer (Figure 3.3).

Different regimes exist for the corona discharge. Just above the threshold both positive and negative coronas are pulsating, in the so-called autostabilization regime [32]. On increasing the corona voltage, the positive corona becomes a continuous glow discharge while the negative corona reaches the regular Trichel pulses regime. At very high corona voltages the negative corona also becomes a continuous glow discharge. At yet higher voltages streamers are formed until breakdown occurs.

The corona discharge may be classified as a glow discharge in which the ionization is confined to regions close to the high-field electrode, being much smaller than the conduction region for the point-to-plane geometry. That is, luminescence is observed in a small portion of the gap (Figure 3.3). The conduction region is characterized by the presence of charge carriers of only one polarity, and since the mobility of these carriers is low, the corona current always increases with increasing corona voltage. By convention, the discharge is said to have the same polarity as the high-field electrode.

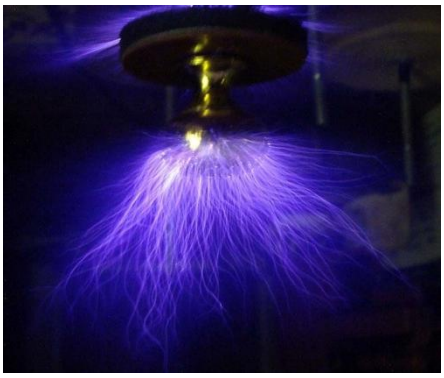

Figure 3.3. Photography of a corona discharge.

The glow near the point can also produce neutral activated species which in the charging process of polymer are carried to the sample surface by the corona wind [33]. Depending on the polarity of electrode, so called *negative* or *positive* poling can be achieved [34]. In positive corona poling, High Voltage (HV) electrodes are directly responsible for the ionization of molecules or atoms of the gas. In negative corona poling, the HV electrode is involved in sustaining the discharge avalanche, providing a source of electrons by secondary emission, ion impact or photoelectric effect [35].

Exactly, the types of ion generated in positive and negative coronas have been determined, and were found to depend strongly on the gas [36–39]. In air, the dominant species for positive corona are hydrated ions with the general formula $(H_2O)_nH^+$, where *n* is an integer that increases with increasing relative humidity. At low relative humidity other ion species, such as $(H_2O)_nNO^+$and $(H_2O)_n(NO_2)^+$, become dominant. For negative coronas, the most important ions are CO_3^- ions; at 50% of relative humidity about 10% of the ions are in the hydrated form $(H_2O)_nCO_3^-$.

The efficiency of corona poling depends upon several factors [35,40] that must be optimized: voltage, distance of electrode from film surface (typically 1-2 cm), temperature and type of atmosphere. Like the contact poling, the DC electric field is applied to the material at a temperature close to the polymer T_g and later frozen in by cooling the polymer to room temperature. But unlike the electrode poling process, corona poling requires only one side of the polymer film to be covered with an electrode. Due to the small dimension (curvature) of the electrode surface (normally a needle or a wire) an extremely high local voltage is deposited on the film. A constant voltage grid can be interposed between electrode and film to control more accurately the poling field (triode electrode system) [41,42]. The grid position and applied voltage controls the amount of deposited charges on the polymer surface, which is the way to control the applied electrical field across the polymer.

3.1.2. CONSERVATION OF ELECTRETS

Previously it was said that an electret is a dielectric material with a quasi-permanent electric charge or dipole polarization [43–45]. However, in order to obtain best results and permanency, the electrets must be kept with its charged forces short-circuited, exactly as a magnet must be kept with a soft iron keeper. If it is kept open-circuited, the electret shows a decay of its charge, but it regains its full charge after having been short-circuited for some time. Electrets are exceedingly sensitive to humidity. It has been reported by Pillai and others [46] that the surface charge decreases considerably with time of exposure to humid atmosphere. Therefore, instruments and devices using electrets elements should be kept under controlled conditions of humidity, pressure [47,48] and temperature for better stability and performance, as these parameters have definite bearing on the permanency and decay of electrets. Wieder and Kaufman [49] reported that when electrets are immersed in water or exposed to humid air or highly ionized air, their charges are irreversibly neutralized. Also, the negative effect of different types of vapors, both polar and nonpolar, on the behavior of electrets was studied by Beeler et al. [50].

3.1.3. CHARGE FORMATION IN ELECTRETS

When Eguchi prepared electrets from wax mixtures discovered that just after removal from the high-voltage electrode assembly, they presented charges which opposite sign to the initial electrodes. The surface in contact with the anode showed negative charge and the cathode positive charge, but these initial charges decayed within a few hours or days after the preparation of the electrets. Subsequently they passed through zero and assumed a sign equal to that of the corresponding initial electrode, reaching a maximum and later gradually decaying with time. This charge was found to be somewhat permanent, lasting for several years when used for practical applications [51]. Andrew Gemant [52] named the first type of charge “heterocharge” and the second type of charge “homocharge”. Afterwards, Gross [53–56] gave the “two-charge theory” to

explain the behavior of electrets; this theory was further amended by Perlman [57], Baumann and Wiseman, Feaster Wieder and Kaufman, Wild and Stranathan, Palm, and others [58,59], which showed the heterocharges and homocharges as interacting entities.

In the two-charge theory the electrets are treated as an absorptive dielectric (Figure 3.4). The electrification is due to the increase in the charging and discharging rate of the dielectric with rise of temperature, and the decay of electrification is caused partly by external and partly by internal conduction within the dielectric itself. The movement of ions or the orientations of dipoles in the interior of the dielectric gives rise to heterocharge, while the conduction in the dielectric-electrode interface produces the homocharge [1,60].

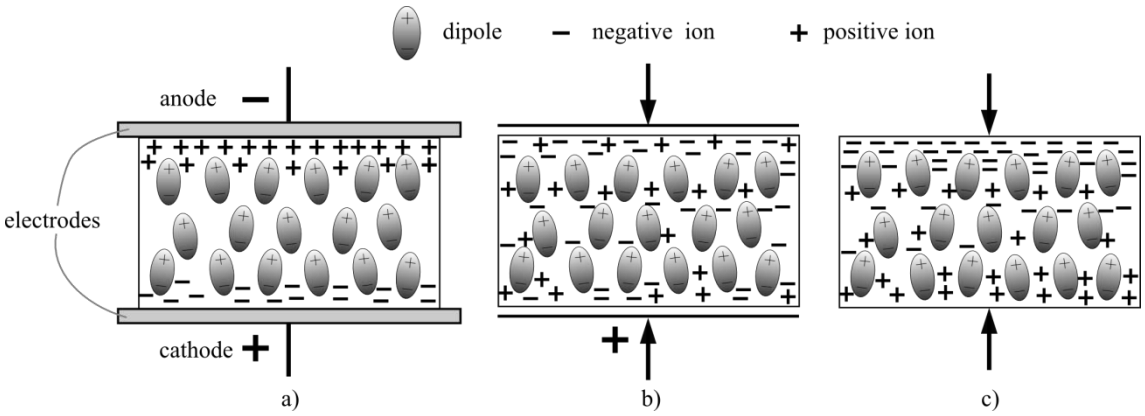

Figure 3.4. a) Displacement of ions and orientation of dipoles in the liquid state of dielectric during the formation of electrets. b) Ions of the same sign of the high-voltage electrodes sprayed on the dielectric surface at the solidification. c) Possible nature of the solidified electrets when it gives homocharge after the decay of initial heterocharge.

In polar materials, the formation of heterocharge is due mainly to the orientation of the dipoles. With sufficiently high field strengths, conduction currents emerge into the interface and consequently electrons are fed into the dielectric or extend from its surface and are transferred to the electrodes. This facilitates the formation of homocharges, which appear in the form of surface charges, later spraying over a certain depth within the dielectric. With short-circuit, a part of the dielectric polarization disappears immediately, and the rest follows more or less slowly. Due to this decay of the heterocharge, the homocharge component begins to prevail in the resulting field. There

exist two types of charges of opposite signs in a short-circuited dielectric. The heterocharge is associated with dielectric absorption which is due to a homogeneous volume polarization of the dielectric. Homocharge is due to the surface breakdown, which is purely an ionic surface charge. Therefore, heterocharges and homocharges coexist in a polarized sample (two-charge theory).

Other theory was developed by Andrew Gemant [52,61,62]. Three independent phenomena take place during the formation of electrets, and the observed effect is a superposition of them. During the poling, a displacement of ions and orientation of dipoles take place in the liquid state. The accumulation of cations near the cathode and anions near the anode remains froze-in while the liquid is being solidified with the external field on. Heterocharge is produced by the ionic displacement within the dielectric. While the dielectric solidifies, ions of the same sign as that of the high-voltage electrodes are sprayed over the respective dielectric surface, particularly during the time of solidification. Since the spray charges have the same sign as that of the forming electrodes, they explain the existence of homocharge. When the solidified dielectric is removed from the electrode assembly, it shows a heterocharge. Then the electric forces originating from the dielectric are repelled and a migration of the charge carriers is started, until they finally recombine to form neutral molecules. The ions sprayed over the molten surface are in turn attracted by the dipoles oriented in the bulk of the sample owing to their sign and stay there. At this state the electret has a homocharge which gradually decays as the dipolar orientation slowly disintegrates by taking up random orientation. However, the dipolar orientation in the electrets material accounts for the remarkably long lifetime of the homocharge.

3.2. EXPERIMENTAL AND RESULTS

The first step in obtaining a piezoelectric polyimide is the synthesis of the polymer, however, because the synthesis results and characterization were reported exhaustively in previous work [63], few details will be included in this Memory. After the synthesis and the film fabrication, the corona poling is a compulsory step in order to render them piezoelectric materials. Since the optimal conditions for corona poling are unique for every kind of sample, a previous optimization of the process is necessary [64]. Finally, the last step is the study of the thermal stability of both the polyimide and the d_{33} piezoelectric coefficient, determined by Differential Scanning Calorimetry (DSC), thermogravimetry (TGA) and wide range d_{33}-meter, respectively. The glass transition temperature is important, because this temperature is considered like the Curie temperature in amorphous piezoelectric polymers.

3.2.1. SYNTHESIS

The synthesis of the polyimides and copolyimides, APB–ODPA, was carried out by reaction between the 4,4′-oxydiphthalic anhydride (dianhydride ODPA) and one or both bis-aminophenoxybenzene (APB) aromatic diamines, 1,3-bis-2-cyano-3-(3-aminophenoxy)phenoxybenzene and 1,3-Bis(3-aminophenoxy)benzene, diamine 2CN and diamine 0CN, respectively [65]. Polyimides (poly 0CN and poly 2CN) were synthesized by using one of the diamines (diamine 0CN or diamine 2CN), whereas the copolyimides were synthesized by using both diamines in different proportions (molar percentage) [63]. Seven different compositions were synthesized in total:

	Poly 0CN	Copo 90/10	Copo 60/40	Copo 50/50	Copo 40/60	Copo 10/90	Poly 2CN
X% *0CN*	100%	90%	60%	50%	40%	10%	0%
Y% *2CN*	0%	10%	40%	50%	60%	90%	100%

In this synthesis a two-step procedure was used. In the first step, a nucleophilic attack of amine groups toward carbonyl groups in the dianhydride gives the copoly(amic acid); in the second step, the cyclodehydration reaction caused by thermal treatment gives rise to the copolyimide. The general scheme of the synthesis of a copolyimide is shown in Figure 3.5.

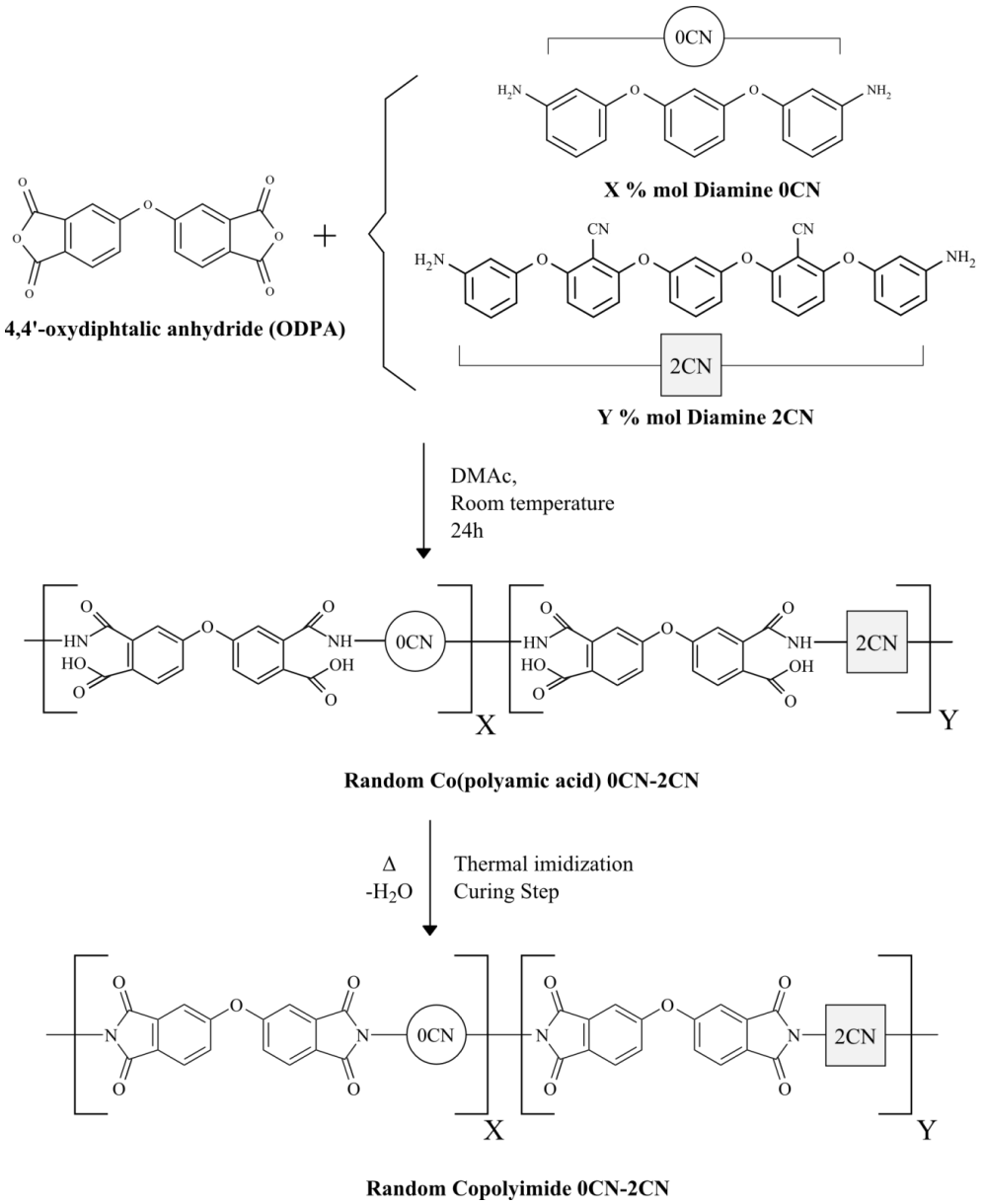

Figure 3.5. Scheme of the two-step reaction.

For instance, to obtain the poly(amic acid) with two cyano groups (poly 2CN), the stoichiometric amount of diamine 2CN and dianhydride ODPA were charged into a 100 mL round-bottom flask adjusting the content of solids to 20%. Both monomers were dissolved separately and the dianhydride was added to the reactor containing the dissolved diamine. The solution was kept at room temperature for 24 h under nitrogen atmosphere and with constant stirring, after which the polymer was precipitated from cold methanol, decanted, and dried at reduced pressure. Then, the brownish poly(amic acid) with two cyanos was obtained.

3.2.2. FILMS PREPARATION AND THERMAL IMIDIZATION

After synthesis, the corresponding polyimides and copolyimides were obtained by thermal imidization of the poly(amic acid) and copoly(amic acids), respectively. However, polyimides are not inherently piezoelectric materials, so they must be poled before their use as a sensor material. To proceed with the poling process and for measuring the electrical properties it is necessary to obtain polyimide films.

These polyimide films were prepared by using a silicon designed mould with a centred cavity with 45x45 mm dimensions, where poly(amic acids) imidization and films fabrication was carried out simultaneously. First, 0.6 g of poly(amic acid) or copoly(amic acid) was solved in N,N-dimethylacetamide (6 mL). Later, the poly(amic acid) was cast to form, approximately, 150 μm thick films, and subsequently thermally imidizated according the following thermal treatment:

a) Heated from 25ºC to 150ºC during 48 hours

b) Isotherm at 150ºC during 24 hours

c) Heated from 150ºC to 200ºC during 48 hours

d) Isotherm at 200ºC during 24 hours

The obtained polymer films showed good physical appearance and some of the compositions the capacity of being stretchable (Figure 3.6). It was observed that the presence of the comonomer with two cyano groups limited the mechanical properties, being the poly 2CN the most fragile of them, because poly 2CN presents the highest content of all the samples. In addition, it can be seen clearly that the presence of cyano groups obscures the polymer film, ranging from yellow to dark brown.

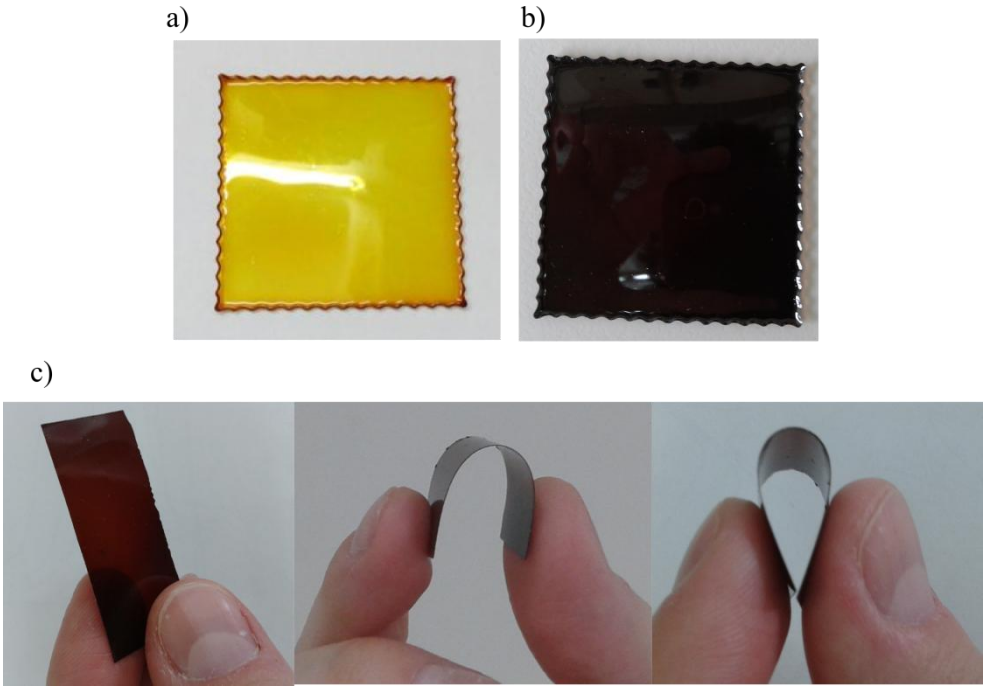

Figure 3.6. Images of a) Poly 0CN film, b) Copo 0CN-2CN film and c) stretched Copo 0CN-2CN film.

3.2.3. OPTIMIZATION OF CORONA POLING CONDITIONS

In the present Chapter, the corona poling process was optimized in order to obtain the best conditions for the poling of polyimides and copolyimides. The optimized poling conditions and the study of the influence of each comonomer in the piezoelectric response was analysed with a wide range d_{33}-meter (model 8000, APC Int. Ltd).

As it was explained above, to obtain a piezoelectric response from an amorphous polar polymer, the material should be poled by applying a strong electric field, E_p, at temperatures higher than its glass transition temperature, T_g [66,67]. It was used a standard corona poling procedure in which a high DC voltage is applied to generate a negative corona at a conductive metal tip. As a result of the corona poling discharge, dipoles are oriented parallel to the direction of the applied electric field at a poling temperature (T_p) above T_g, with subsequent cooling below T_g in the presence of the applied field in order to fix the orientation of the polar groups.

The corona poling setup of the Electroactive Smart Materials Group was designed for different types of samples and conditions. Therefore, the objective was to manufacture a system with its parameters modifiable as much as it was possible [68]. The device can be used as corona simple or as triode electrode system, but in our case it was only used as corona simple. In addition, other parameters can be changed in order to find the best possible conditions. For example, voltage, distance of electrode from film surface, temperature or isothermal poling time.

In the corona system (Figures 3.7 and 3.8) can be distinguished the following parts with the configuration we used:

1. Corona poling chamber (Faraday cage) made of 3 mm thickness brass.
2. Circular sample holder with 35 mm radio and 45 mm height, with holes for the PT100 resistances as heating system, and aluminum foil in the top.
3. Corona discharge tip. There were used 3 types: a 145 mm single tip, a 85 mm single tip, and a holder for several small tips in order to poling different areas.
4. Spellman high voltage source (model SMS 300W) with intensity and voltage control, connected to a Teflon (polytetrafluoroethylene, PTFE) chamber to assure a correct union with the corona tip.
5. Shimaden digital temperature controller (model Lite FP93) and two PT100 resistances for heating the samples.

Once the parts of the corona poling system have been explained is important to remember that the ideal poling conditions for a sample are specific of the sample type and also of the poling device (material and shape of the tip and sample holder, etc). Therefore, the first objective is optimizing the procedure, specifically for our type of polyimides and for the used corona poling device. Thanks to previous experience on the field, the number of variables during the poling was simplified, and in the case of the sample it was always worked with the same copolymer, i.e. with the copolyimide 0CN-2CN with a molar composition of 50% of each comonomer, because it has intermediate properties (mechanical, chemical and physical) among all the investigated polymers.

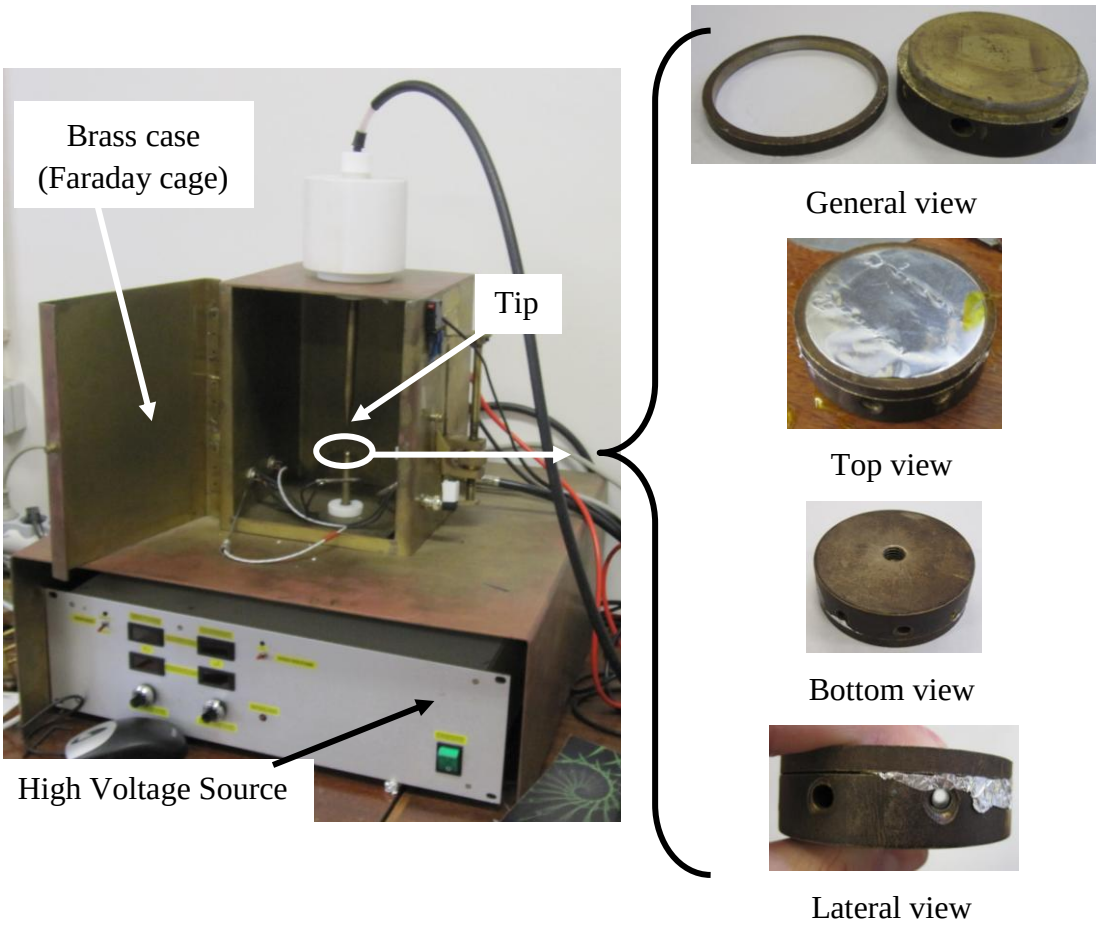

Figure 3.7. Photography of the corona poling setup (Left) and different views of the poling sample holder (Right).

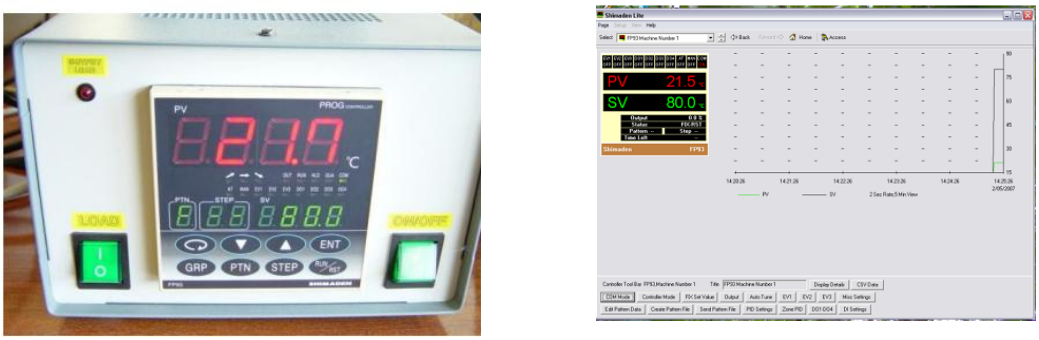

Figure 3.8. Shimaden Lite FP93 digital temperature controller (Left) and its software (Right)

An approximately current of 10 kV voltage and 30 µA was applied in all the experiments, because higher voltage provoked electrical breakdown. The other parameters that must be optimized are: polarization temperature, polarization time, tip-sample distance and type of point. There were chosen three different possibilities for each parameter, for polarization temperature 180, 200 and 220ºC, for polarization time 30, 60 and 90 minutes and for the tip-sample distance 0.5, 1 and 1.5 cm. In the case of the type of tip, they were used two single tips with different lengths (145 and 85 mm) and a holder for multiple small tips which allows using several of them with the aim of poling larger areas (Figure 3.9).

After trying out the explained possibilities showed in Table 3.1, it was concluded that the best conditions were: 200ºC, 60 minutes, 1 cm and the tip of 145 mm, because they showed the maximum value (8 pC·N^{-1}) of the piezoelectric coefficient d_{33}, measured with a wide range d_{33}-meter.

Therefore, after optimization of the poling time (1 h), voltage (10 kV) and current (10 µA) all samples (polyimides and copolyimides) were poled in such conditions (Figure 3.10), and their d_{33} coefficient determined.

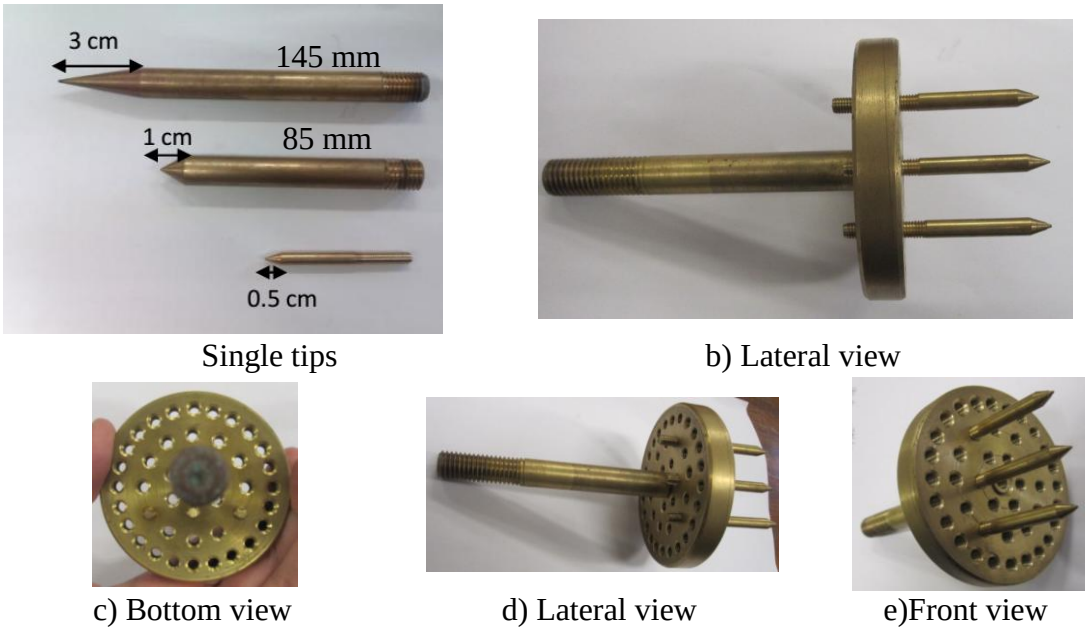

Single tips b) Lateral view

c) Bottom view d) Lateral view e)Front view

Figure 3.9. Images of the different tips.

Table 3.1. d_{33} obtained values during optimization for the Copo 50/50.

Temperature (ºC)	180 ºC	200 ºC	220 ºC
$\boldsymbol{d_{33}}$ **(pC·N^{-1})**	3	8	6
Polarization time (minutes)	30 min	60 min	90 min
$\boldsymbol{d_{33}}$ **(pC·N^{-1})**	5	8	8
Tip-sample distance	0.5 cm	1 cm	1.5 cm
$\boldsymbol{d_{33}}$ **(pC·N^{-1})**	3.5	8	2
Type of tip	85 mm	145 mm	Multiple needle system
$\boldsymbol{d_{33}}$ **(pC·N^{-1}))**	4	8	0

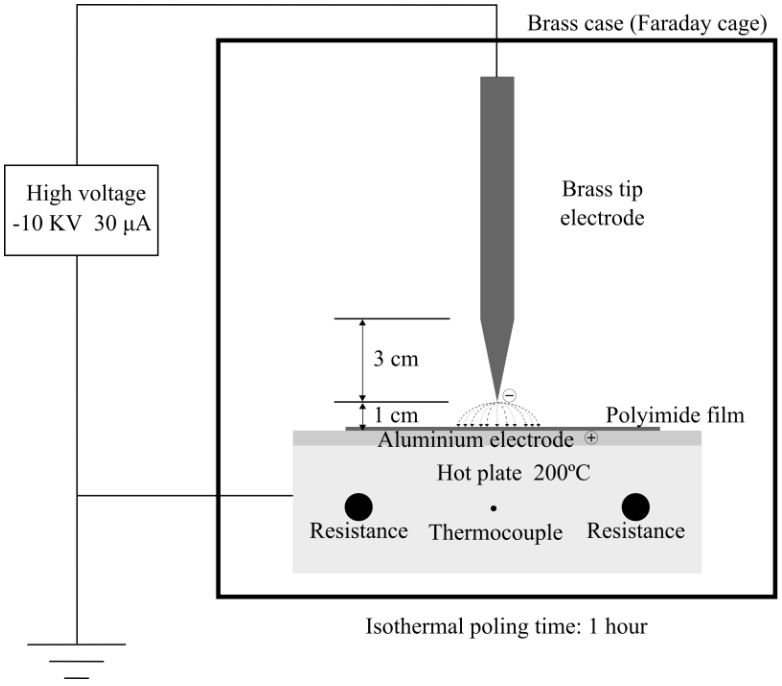

Figure 3.10. Scheme of the corona poling setup in the optimized conditions: temperature, polarization time, tip-sample distance and type needle.

3.2.4. INFLUENCE OF THE COMONOMER WITH TWO CYANO GROUPS

Once the poling method was optimized, this procedure was repeated for all the compositions. The obtained polarization is partly due to the orientation of the polar groups in the molecule, namely the pendant polar groups (cyano groups, also called nitriles) and the polar groups incorporated in the backbone (phthalimide groups), as can be seen in Figure 3.11.

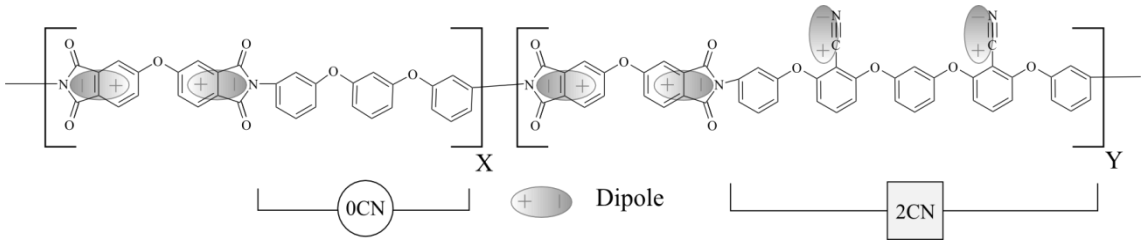

Figure 3.11. Scheme of the two repetitive units of the copolyimides with the polar groups.

Figure 3.12 reveals a linear dependence between the d_{33} values and the content of diamine 2CN, being the maxium d_{33} obtained value of 16 pC·N^{-1}. The piezoelectric values remain stable after two weeks at room temperature, maintaining the original value. To analyze the influence of temperature in the piezoelectric response, the piezoelectric response of the copolyimide 50/50 sample was measured after specific heat treatments. This copolymer was chosen because it has intermediate physical-chemical properties, i.e. thermal properties and d_{33} modulus. The same sample was heated up to the desired temperature during 15 minutes and later it was cooled down to room temperature. In that moment the d_{33} modulus was measured and the procedure was repeated for six temperatures. As it was expected, the sample maintained its piezoelectric properties until approaching T_g (around 170ºC). After T_g was reached, no piezoelectric response was detected due to the increased molecular mobility that leads to a random orientation of the dipolar moments (Table 3.2).

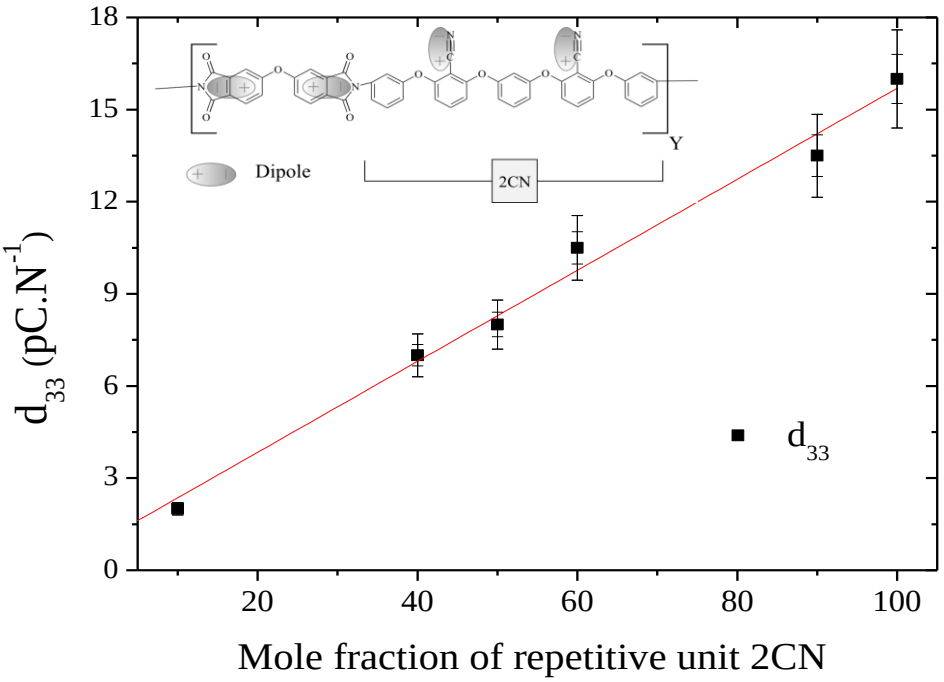

Figure 3.12. Linear representation of piezoelectric modulus (d_{33}) versus mole percentage of repetitive unit 2CN.

Table 3.2. Resume of the d_{33} results for all the poled polyimides at the optimized conditions and d_{33} modulus temperature dependence for the 0CN/2CN 50/50% sample.

d_{33}							
Name	Poly 0CN	Copo 90/10	Copo 60/40	Copo 50/50	Copo 40/60	Copo 10/90	Poly 2CN
d_{33} (pC N^{-1})	1	2	7	8	10.5	13.5	16
d_{33} modulus values of the Copo 0CN/2CN 50/50% after heat treatment							
Temperature (ºC)	80	100	120	140	160	180	
d_{33} (pC N^{-1})	8	8	8	8	8	0	

3.2.5. THERMAL CHARACTERIZATION

In semicrystalline polymers the amorphous phase supports the crystal orientation and the polarization is stable up to the Curie temperature (T_C), which is the melting temperature (T_M) of the polymer. But in amorphous systems, such as polyimides, the situation is different; the key temperature for amorphous polymer electrets is the glass transition temperature (T_g), because that temperature rules its maximum operating temperature and defines the poling conditions. The piezoelectric effect in amorphous polymers does not take place in a state of thermal equilibrium but in a quasi-stable state due to the freezing-in of molecular dipoles [69–73]. Apart from oriented dipoles, poling a piezoelectric amorphous polymer may result in space or real charge injection. The real charges are usually concentrated near the surface of the polymer, and they are introduced by the presence of the electrodes.

To sum up, knowing the thermal behavior of the polyimides is fundamental to predict, understand and determine the optimal poling conditions and the maximum operating service as piezoelectric material, because the remnant polarization is lost in the vicinity of T_g, and logically their use is limited to temperatures well below T_g. Therefore, two techniques were employed: Differential Scanning Calorimetry (DSC) to measure the glass transition temperature, and thermogravimetric analysis (TGA), because TGA is one of the most widely used techniques to evaluate the thermal decomposition of materials.

Since glass transition temperature is an important parameter in these amorphous piezoelectric materials, near that point piezoelectricity cannot longer be observed, is in our best interest to increase that value as much as possible. Nonetheless, we must not forget another point, in polyimides, glass transition temperature is closely related with the polymer structure, and the structure affects enormously the solubility and processability [74]. Thus, to create easily processed piezoelectric polyimides, a balance between these properties must be sustained without sacrificing their characteristic and inherent high temperature resistance. It is necessary to have high glass transition temperature and good solubility at the same time.

Aromatic polyimides often have rigid chains and strong interchain interactions, due to the highly symmetrical, highly polar groups and intra- and interchain charge transfer complex (CTC) formation and electronic polarization [75,76]. These interactions make them suffer from low solubility in common solvents and high softening temperatures, which makes their processing difficult or too expensive.

The general objective in the field of polyiimides is modifying their molecular interactions to allow processing by conventional techniques, such as melt processing or solvent casting, while maintaining their thermo-oxidative stability. There are three major structural modifications: incorporation of thermally stable but flexible or unsymmetrical linkages in the backbone, introduction of large pendant substituents to the polymer chain, and interruption of symmetry and regularity through copolymerization. However, these strategies generally suffer from a trade-off between

the thermal properties and the solubility of a polyimide because the same structural features that enhance one characteristic will decrease the other.

For instance, the incorporation of flexible linkages, such as –O–, $–CH_2–$, $–SO_2–$ and hexafluoroisopropylidene (6F) groups into the backbone, introduces "kinks" (crank and twisted noncoplanar structure) in the backbone that decrease the polymer rigidity and inhibit close packing of the chains, which reduces the interchain interactions and lead to enhanced solubility.

The inclusion of bulky substituents can provoke an increase of T_g and thermo-oxidative stability as well as increase the solubility of the polyimide, especially for polyimides with flexible or unsymmetrical and/or groups in the chain; but the extent of these effects depends on the number, size, and polarity of the substituent. Moreover, decrease the crystallinity and packing efficiency by distorting the backbone symmetry and restricting its segmental mobility.

Ding [77] established general rules for the relation between glass transition temperatures and structure of isomeric polyimides based on the experimental results. The T_g difference between the isomeric polyimides generally depends on the rigidity of the polymer chains. If we consider polyimides of comparable molecular weight (or inherent viscosity) based on isomeric dianhydride with a given diamine, T_g would increase following the order 4,4'- < 3,4'- < 3,3'-dianhydride. Ding attributed that behavior to the suppressed rotation around the bond between the phthalimide and the bridge atom in the 3-substituted phthalimide unit. On the other hand, the polyimides derived from *p,p'*-diamines (and a given dianhydride) usually have higher T_gs than those from *m,m'*-diamines. The probable cause is the substitution, which impedes the chain mobility but, at the same time, the bent chains, decrease the packing of the macromolecular chain, hence tend to decrease interactions between the macromolecular chains.

In our samples we determined that varying the number of lateral polar groups in the polyimide backbone has a clear effect in the piezoelectric coefficient: the higher the presence of the comonomer with two cyano groups, the higher the d_{33}-coefficient.

Respect to the thermal properties the interpretation is not so easy. In the DSC curves was observed that for all copolyimides an unique T_g is obtained indicating that they are random copolymers [78]. Regarding the glass transition temperatures, no clear trend is observed between composition and T_g values, but all the compositions showed high T_g values, around 160-180ºC. These small variation in T_gs values could be attributed to different molecular weights of the polyimide and copolyimide samples, after the thermal imidization of the poly(amic acid)s. Figure 3.13 and Table 3.3 show DSC curves and T_g values, respectively, for all the polyimides and copolyimides synthesized.

As indicated above, thermogravimetric analysis (TGA) is one of the most widely used procedures to evaluate the thermal decomposition of materials. Thermogravimetric data are presented in two ways. The TGA curve as a plot of the mass against time or temperature, being the mass loss on the ordinate plotted downward relative to a baseline (Figure 3.14). Alternatively, in Figure 3.15 data has been presented as a derivative thermogravimetric (DTG) curve, which is a plot of the rate of change of mass (m) with respect to time (t) or temperature (T) against time or temperature.

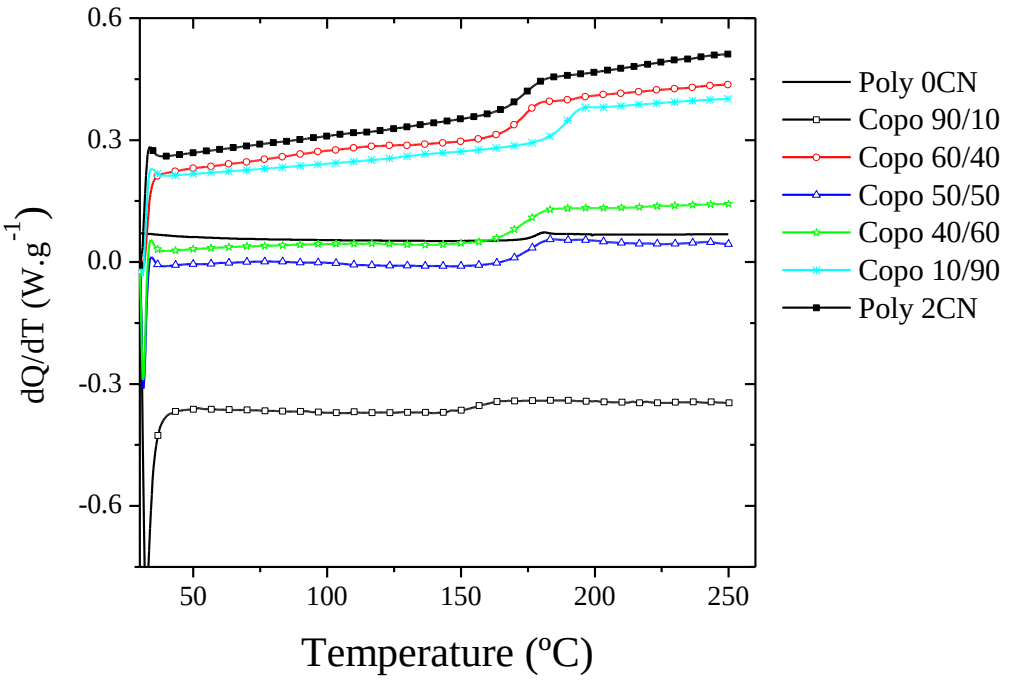

Figure 3.13. DSC curves of the polyimides and copolyimides.

As it can be observed in Figures 3.14 and 3.15, and Table 3.3, in our samples the polyimide without -CN dipolar groups (poly 0CN) has the highest initial degradation temperature (450ºC), whereas the polyimide containing two -CN dipolar groups (poly 2CN) has the lowest one (315ºC). In this case, although does not exist a linear relationship among the initial degradation temperature (T_d) and the comonomer proportion, it can be observed that as increases the proportion of 2CN repetitive units in the copolyimide the initial degradation temperature decreases. In any case, the degradation temperatures are high enough to ensure a good thermal stability of these materials which can be important for certain applications.

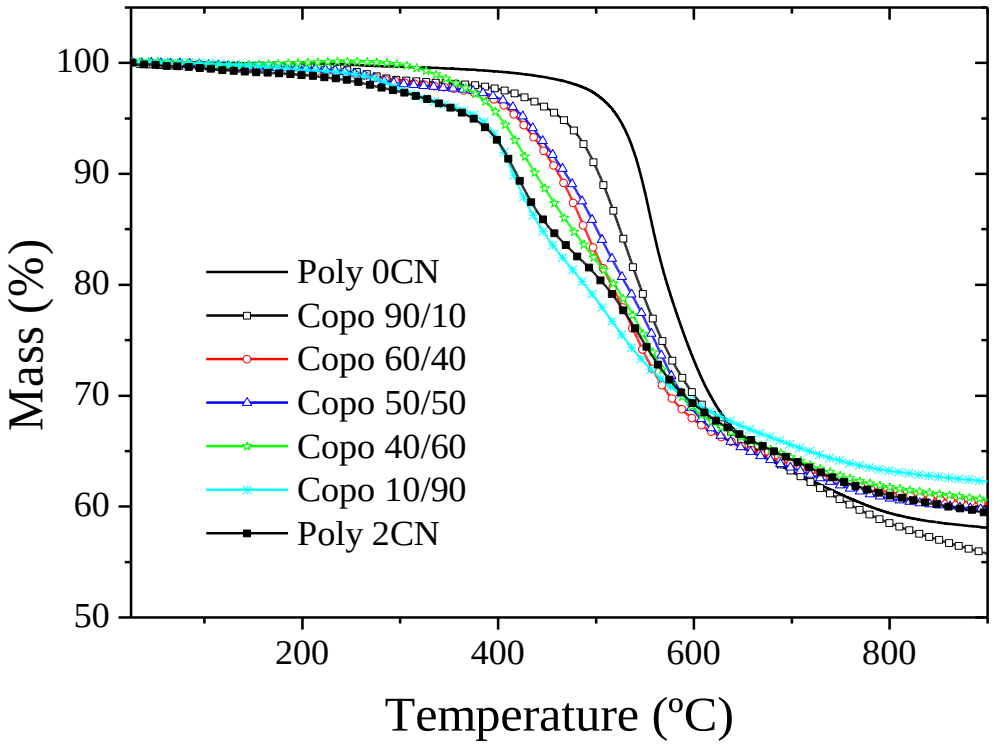

Figure 3.14. TGA curves of the polyimides and copolyimides.

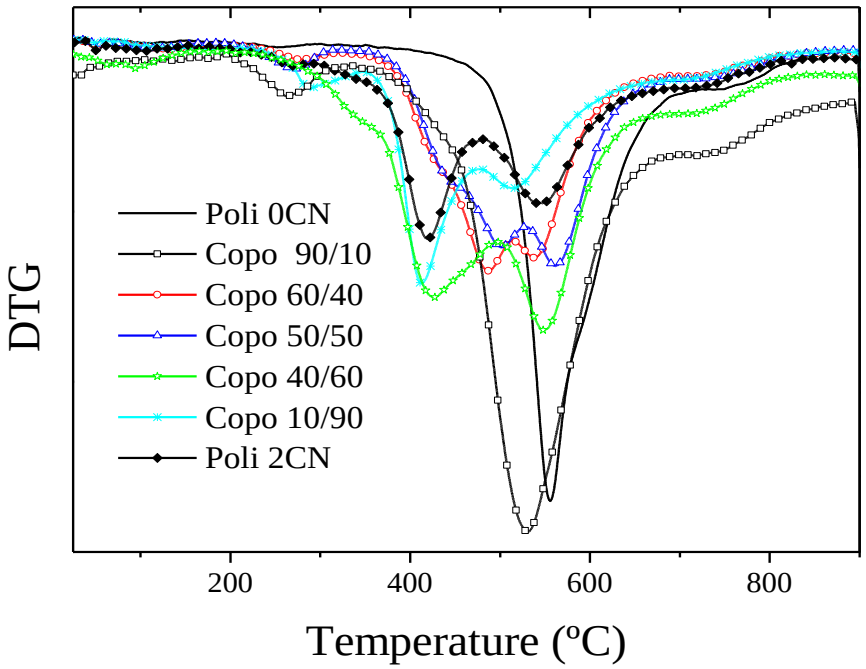

Figure 3.15. DTG curves of the polyimides and copolyimides.

Table 3.3. Glass transition temperature (T_g) and initial degradation temperature (T_d) for the polyimides and copolyimides

Sample name	**Mole Percentage (%)**		T_g (ºC)	T_d (ºC)
	0CN	**2CN**		
Poly 0CN	100	0	177.8	450
Copo 90/10	90	10	158.2	435
Copo 60/40	60	40	165.7	410
Copo 50/50	50	50	173.9	405
Copo 40/60	40	60	161.1	345
Copo 10/90	10	90	181.6	320
Poly 2CN	0	100	176.3	315

3.3. CONCLUSIONS

A series of nitrile (or cyano group) containing polyimide polymers and copolymers were obtained by a two-step method, based on a polycondensation reaction between the dianhydride ODPA and two different diamines (diamine 0CN and diamine 2CN), followed by thermal curing into their corresponding polyimide films.

All samples were poled by the corona poling method and their d_{33} coefficient values were determined. The influence of the repeating unit with two cyano groups in the piezoelectric properties was studied. It was observed that a progressive increase in the content of 2CN in the film improves the piezoelectric response, being obtained a maximum response of 16 $pC \cdot N^{-1}$ for the polyimide with two cyano groups (poly 2CN). Samples showed a good stability over time and high temperatures, up to 160ºC. Therefore, in combination with thermal stability proven by DSC and TGA, these new copolyimides have a promising future as sensors, especially for temperatures over 100ºC, where PVDF cannot be used.

Even though polyimides have d_{33} values below the usual ones for the PVDF, around 20–30 $pC \cdot N^{-1}$, they have the possibility of changing their structure in an easy way, by modifying the diamine structure or changing the dianhydride, opening large potential variability for designing novel piezoelectric polymers for sensors and transducers with large thermal stability.

3.4. REFERENCES

[1] Nalwa HS, editor. Ferroelectric polymers: chemistry, physics, and applications. Marcell Dekker, Incorporated; 1995.

[2] Gutmann F. The electret. Rev Mod Phys 1948;20:457–72.

[3] Eguchi M. On the permanent electret. Philosphical Mag 1925;49.

[4] Pillai PKC, Jain K, Jain VK. Thermally stimulated discharge current studies in shellac wax electrets. Phys Status Solidi 1973;17:221–7.

[5] Pillai PKC, Jain K, Jain VK. Thermal current measurements in PVC(SR11) electrets. Phys Lett A 1972;39:216–8.

[6] Jain VK, Pillai PKC. Characteristics of plastic electrets. Phys Status Solidi 1968;28:415–9.

[7] Gross B. Charge dynamics for electron-irradiated polymer-foil electrets. J Appl Phys 1974;45:2841.

[8] Sessler GM. Electrets, topics in applied physics. J Electrochem Soc 1980;127:530C.

[9] Sessler GM, West JE. Foil-electret microphones. J Acoust Soc Am 1966;40:1433.

[10] Sessler GM, West JE. Charging of polymer foils with monoenergetic low-energy electron beams. Appl Phys Lett 1970;17:507.

[11] Russo MV, editor. Advances in macromolecules: Perspectives and applications. Heidelberg: Springer Science & Business Media; 2010.

[12] Pillai PKC, Jain VK, Kamdar M. Investigations of the variations of dielectric constant and surface charge of polyvinyl chloride electrets with time. J Electrochem Soc 1971;118:465.

[13] Kremer F, Schönhals A. Broadband dielectric spectroscopy. Berlin, Heidelberg: 2002.

[14] Faccini M, Balakrishnan M, Diemeer MBJ, Hu Z, Clays K, Asselberghs I, et al. Enhanced poling efficiency in highly thermal and photostable nonlinear optical chromophores. J Mater Chem 2008;18:2141.

[15] Yang GM. Thermally stimulated discharge of electron-beam-and corona-charged polypropylene films. J Phys D Appl Phys 1993;26:690–3.

[16] Gross B, Gerhard-Multhaupt R, Berraissoul A, Sessler GM. Electron-beam poling of piezoelectric polymer electrets. J Appl Phys 1987;62:1429.

[17] Bharti V, Xu HS, Shanthi G, Zhang QM, Liang K. Polarization and structural properties of high-energy electron irradiated poly(vinylidene fluoride-trifluoroethylene) copolymer films. J Appl Phys 2000;87:452.

[18] McKinney JE, Davis GT, Broadhurst MG. Plasma poling of poly(vinylidene fluoride): Piezo- and pyroelectric response. J Appl Phys 1980;51:1676.

[19] Sessler GM. Poling and properties of polarization of ferroelectric polymers and composites. Ferroelectr Polym Ceram Compos 1994;92-9:249–74.

[20] Kenney JM, Roth SC. Room temperature poling of poly(vinylidene fluoride) with deposited metal electrodes. J Res Natl Bur Stand (1934) 1979;84:447.

[21] Jiang Y, Ye Y, Yu J, Wu Z, Li W, Xu J, et al. Study of thermally poled and corona charged poly(vinylidene fluoride) films. Polym Eng Sci 2007;47:1344–50.

[22] Wang TT. Polarization of poly(vinylidene fluoride) by application of breakdown fields. J Appl Phys 1982;53:6552.

[23] Wang TT, von Seggern H. High electric field poling of electroded poly(vinylidene fluoride) at room temperature. J Appl Phys 1983;54:4602.

[24] Heywang W, Lubitz K, Wersing W. Piezoelectricity: Evolution and future of a technology. vol. 14. Springer Science & Business Media; 2008.

[25] Bauer F. Ferroelectric PVDF polymer for high pressure and shock compression sensors. Proceedings. 11th Int. Symp. Electrets, IEEE; 2002, p. 219–22.

[26] Zakrevskiĭ VA, Sudar NT. Electrical breakdown of thin polymer films. Phys Solid State 2005;47:961.

[27] Southgate PD. Room-temperature poling and morphology changes in pyroelectric polyvinylidene fluoride. Appl Phys Lett 1976;28:250.

[28] Giacometti JA, DeReggi AS. Thermal pulse study of the polarization distributions produced in polyvinylidene fluoride by corona poling at constant current. J Appl Phys 1993;74:3357.

[29] Migahed MDD, Abdel-Hamid MII, Abo El Wafa AMM. Corona charging and pyroelectric behaviour in acrylonitrile-co-methylacrylate films. Polym Test 2001;20:805–10.

[30] Giacometti JA, Oliveira ON. Corona charging of polymers. IEEE Trans Electr Insul 1992;27:924–43.

[31] Das-Gupta DKK. Molecular processes in polymer electrets. J Electrostat 2001;51-52:159–66.

[32] Trichel G. The mechanism of the negative point to plane corona near onset. Phys Rev 1938;54:1078–84.

[33] Robinson M. Movement of air in the electric wind of the corona discharge. Trans Am Inst Electr Eng Part I Commun Electron 1961;80:143–50.

[34] Hampsch HL, Torkelson JM, Bethke SJ, Grubb SG. Second harmonic generation in corona poled, doped polymer films as a function of corona processing. J Appl Phys 1990;67:1037.

[35] Hampsch HL, Yang J, Wong GK, Torkelson JM. Dopant orientation dynamics in

doped second-order nonlinear optical amorphous polymers. 1. Effects of temperature above and below Tg in corona-poled films. Macromolecules 1990;23:3640–7.

[36] Shahin MM. Nature of charge carriers in negative coronas. Appl Opt 1969;8 Suppl 1:106–10.

[37] Shahin MM. Mass-spectrometric studies of corona discharges in air at atmospheric pressures. J Chem Phys 1966;45:2600.

[38] Brandvold DK, Martinez P, Dogruel D. Polarity dependence of N2O formation from corona discharge. Atmos Environ 1989;23:1881–3.

[39] Gravendeel B, Hoog FJ de. Clustered negative ions in atmospheric negative corona discharges in the Trichel regime. J Phys B At Mol Phys 1987;20:6337–61.

[40] Moreno RA, Gross B. Measurement of potential buildup and decay, surface charge density, and charging currents of corona-charged polymer foil electrets. J Appl Phys 1976;47:3397.

[41] Dao PT, Williams DJ, McKenna WP, Goppert-Berarducci K. Constant current corona charging as a technique for poling organic nonlinear optical thin films and the effect of ambient gas. J Appl Phys 1993;73:2043.

[42] Giacometti JA, Ribeiro PA, Raposo M, Marat-Mendes JN, Carvalho Campos JS, DeReggi AS. Study of poling behavior of biaxially stretched poly(vinylidene fluoride) films using the constant-current corona triode. J Appl Phys 1995;78:5597.

[43] Sessler GM. Charge storage in dielectrics. IEEE Trans Electr Insul 1989;24:395–402.

[44] Paralı L. The electret effects of crystallized polymer–ferropiezoelectric composite under electric discharge plasma. J Electrostat 2015;76:89–94.

[45] Hillenbrand J, Pondrom P, Sessler GM. Electret transducer for vibration-based energy harvesting. Appl Phys Lett 2015;106:183902.

[46] Pillai PKC, Jain K, Jain VK. Effect of water vapour on thermoelectret behaviour. Nuovo Cim B 1972;11:339–48.

[47] Miller ML. Persistent polarization in polymers. I. Relationship between the structure of polymers and their ability to become electrically polarized. J Polym Sci Part A-2 Polym Phys 1966;4:685–95.

[48] Miller ML, Murray JR. Persistent polarization in polymers. II. Depolarization currents. J Polym Sci Part A-2 Polym Phys 1966;4:697–704.

[49] Wieder HH, Kaufman S. Plastic electrets. J Appl Phys 1953;24:156.

[50] Beeler JR, Stranathan JD, Wiseman GG. Some effects of vapors on electret behavior. J Chem Phys 1960;32:442.

[51] Sessler GM, Gerhard-Multhaupt R, von Seggorn H, West JE. Charge and

polarization profiles in polymer electrets. IEEE Trans Electr Insul 1986;EI-21:411–5.

[52] Gemant A. Recent investigations on electrets. Philos Mag 1935;20:929–52.

[53] Gross B. Experiments on electrets. Phys Rev 1944;66:26–8.

[54] Gross B. Charge storage in charged dielectrics ESL, 1964. 1966.

[55] Gross B. Electret research - Stages in its development. IEEE Trans Electr Insul 1986;EI-21:249–69.

[56] Sessler GM. Bernhard Gross and the evolution of modern electret research. Brazilian J Phys 1999;29:220–5.

[57] Perlman MM. Decay of wax electrets. J Appl Phys 1960;31:356.

[58] Roos J. Electrets, semipermanently charged capacitors. J Appl Phys 1969;40:3135.

[59] Wiseman GG, Feaster GR. Experiments on the polarization and decay of electrets. J Chem Phys 1957;26:521.

[60] Camacho González F. Charge-storage mechanisms in polymer electrets. 2006.

[61] Gemant A. The field of electrets in the presence of gaseous ions. Phys Rev 1942;61:79–83.

[62] Gemant A. The use of electrets in electrical instruments. Rev Sci Instrum 1940;11:65.

[63] San Sebastian M. Síntesis y propiedades de poliimidas piezoeléctricas. University of the Basque Country (UPV/EHU), 2012.

[64] Maceiras A, Martins P, San Sebastián M, Lasheras A, Silva M, Laza JM, et al. Synthesis and characterization of novel piezoelectric nitrile copolyimide films for high temperature sensor applications. Smart Mater Struct 2014;23:105015.

[65] Gonzalo B, Vilas JL, Breczewski T, Pérez-Jubindo MA, De La Fuente MR, Rodriguez M, et al. Synthesis, characterization, and thermal properties of piezoelectric polyimides. J Polym Sci Part A Polym Chem 2009;47:722–30.

[66] Giacometti JA, Fedosov S, Costa MM. Corona charging of polymers: Recent advances on constant current charging. Brazilian J Phys 1999;29:269–79.

[67] Martins P, Lasheras A, Gutierrez J, Barandiaran JM, Orue I, Lanceros-Mendez S. Optimizing piezoelectric and magnetoelectric responses on CoFe2O4/P(VDF-TrFE) nanocomposites. J Phys D Appl Phys 2011;44:495303.

[68] de Carvalho Gomes JM. Construção, desenvolvimento e optimização de sistema de polarização por Corona para materiais ferroelétricos. Universidade do Minho, 2009.

[69] Harrison JS, Ounaies Z. Piezoelectric polymers; NASA Cr2001-21142. Hampton, Virgina: 2001.

[70] Ounaies Z, Young JA, Harrison JS. Design requirements for amorphous

piezoelectric polymers; NASA/TM-1999-209359. 1999.

[71] Park C, Ounaies Z, Su J, Smith Jr. JG, Harrison JS. Polarization stability of amorphous piezoelectric polyimides; Piezoelectric polymers; NASA/Cr 2001-21142. ICASE Report No. 99-53. 1999.

[72] Simpson J, Ounaies Z, Fay C, O. SJ, Z. O, C. FC. Polarization and piezoelectric properties of a nitrile substituted polyimide. vol. 459. NASA Langley Technical Report Server; 1996.

[73] Ounaies Z, Young JA, Harrison JS. An overview of the piezoelectric phenomenon in amorphous polymers. In: Khan IM, Harrison JS, editors. F. responsive Polym., vol. 726, American Chemical Society; 1999, p. 88–103.

[74] Liaw D-JJ, Wang K-LL, Huang Y-CC, Lee K-RR, Lai J-YY, Ha C-SS. Advanced polyimide materials: Syntheses, physical properties and applications. Prog Polym Sci 2012;37:907–74.

[75] Hasegawa M, Horie K. Photophysics, photochemistry, and optical properties of polyimides. Prog Polym Sci 2001;26:259–335.

[76] San Sebastian M, Martinez-Martinez V, Maceiras A, Vilas JL, Lopez-Arbeloa I, Leon LM. Enhanced charge-transfer emission in polyimides by cyano-groups doping. J Phys Chem B 2015;119:5685–92.

[77] Ding M. Isomeric polyimides. Prog Polym Sci 2007;32:623–68.

[78] Runt J, Huang J. Chapter 8 Polymer blends and copolymers. In: Cheng SZD, editor. Handb. Therm. Anal. Calorim., vol. 3. First Edit, Amsterdam: Elsevier; 2002, p. 273–94.

Chapter 4.

Dielectric spectroscopy study

The objective in this chapter is to understand the dielectric behavior of our polyimide and copolyimide films by using dielectric spectroscopy. The most important terms and concepts, such as types of polarizations, macro- and microscopic interaction with the electric field, dielectric loss and different relaxation processes are explained. Experimentally, dielectric complex function, ac conductivity and electric modulus of the polymers has been studied as a function of CN group content in the frequency range from 0.1 Hz to 10^7 Hz at temperatures from 25 to 260°C.

4.1. INTRODUCTION

Dielectric materials (dielectrics for short) are the materials that do not normally conduct electricity (electrical insulators), have the ability to storage electrical charge and can be polarized by an applied electric field. They can be classified into two major categories: nonferroelectric (or normal dielectric or paraelectric) materials and ferroelectric materials.

Electric charges under the influence of an electric field do not flow through the dielectric material as they do in a conductor; they only shift a little from their average equilibrium positions causing dielectric polarization. In dielectric polarization, positive charges are displaced toward the field and negative charges shift in the opposite direction, creating an internal electric field that reduces the overall field within the dielectric itself. When the dielectric is composed of weakly bonded molecules, those molecules become polarized and reoriented so that their symmetry axes align to the field. The behavior of dielectric in electric field is an area of study very useful for scientists [1–4]. It concerns storage and dissipation of electric and magnetic energy in materials, because it is important for explaining various phenomena in electronics, optics, and solid-state physics. Scientists are interested in understanding the role of long chain molecules, because the interaction between electric fields and molecules has resulted in many new applications.

Dielectric phenomena, like other natural phenomena, were first discovered long before the time of Christ. As early as 600 BC, the Greek philosopher Thales discovered that amber, when rubbed with cloth, attracted light objects such as bits of chaff. It is noteworthy that the first particle known to carry electric charge, the electron, is named for the Greek word for amber, ἤλεκτρον (*ēlektron*).

Many substances possess this property to some extent. A glass or metal rod, after being rubbed with a polyester sheet, will attract a light piece of paper due to the charge on the rod tip is polarizing the paper nearby. The electric polarization produces an opposite charge on the paper surface close to the charged rod tip, resulting in an attraction.

An electromagnetic wave induces polarization in dielectric materials and magnetization in magnetic materials [5]. The polarization and magnetization produce their own fields, which interact with the external fields, resulting in dielectric and magnetic phenomena.

Nevertheless, dielectric phenomena did not receive much attention until the middle of the 18th century. In 1837 Faraday was the first to report that the capacitance of a condenser was dependent on the material inside the condenser [6]. Then, he called the ratio of the capacitance of the condenser filled with a dielectric material to that of the same condenser, empty inside (free space), the specific inductive capacity, which is now called the permittivity. Faraday discovered the dependence of the capacitance of condenser on the material filled between the two metallic plates and the induction law. In that time, Henry discovered the self-induction of the electric current, which led to the development of electromagnets. About 10 years before this discovery, in 1820, Oersted observed the magnetic effect of an electric current. After that, Ampère discovered in 1824 the circuital law and finally Maxwell unified these discoveries together. He developed four equations, known as Maxwell's equations, to govern all the macroscopic electromagnetic phenomena, being the dielectric phenomena a part of it. Therefore, it is very important to understand the meaning of these four equations.

Maxwell's four equations are:

$$\nabla \times H = J + \frac{\partial D}{\partial t} \tag{4.1}$$

$$\nabla \times \mathrm{E} = -\frac{\partial B}{\partial t} \tag{4.2}$$

$$\nabla \cdot \mathrm{B} = 0 \tag{4.3}$$

$$\nabla \cdot \mathrm{B} = \rho \tag{4.4}$$

where *E*, *D*, *H*, and *B* are four vectors denoting, respectively, the electric field, the electric flux density (or electric displacement), the magnetic field, and the magnetic flux density (or magnetic induction); *J* is also a vector denoting the electric current density;

and ρ is a scalar quantity that denotes the net charge density. These Maxwell's equations describe the coupling between the electric field and the magnetic field and their interaction with the material, resulting in all electromagnetic phenomena.

The parameter *B* may be tied to parameter *H*, and so *D* to *E*, by the following relations:

$$B = \mu H \tag{4.5}$$

$$D = \varepsilon E \tag{4.6}$$

$$J = \sigma E \tag{4.7}$$

where μ, ε, and σ are the permeability, the permittivity, and the conductivity of the material (medium), respectively. Microscopic theory may deduce the physical properties of a material from its atomic structure which may be represented by the previous parameters. The nature of these parameters is directly associated with the deformation of the atomic structure and the movement of electric charges caused by the electromagnetic field, which is mainly due to magnetization, polarization, and electrical conduction.

In this world, there is no lossless material. All materials are lossy. Only in a perfect vacuum can there be no loss and, hence, no dispersion in the presence of an electromagnetic field. But in the real world, a perfect vacuum on earth is impossible to achieve. However, at the normal range of temperatures and pressures, the gas media can be considered to be very close to the so-called free space. In free space,

$$\mu_0 = 4\pi \times 10^{-7} henry \cdot \ m^{-1} = 1.257 \times 10^{-6} henry \cdot m^{-1}$$

The velocity of light in free space is:

$$c = (\mu_0 \varepsilon_0)^{-1/2} = 2.998 \times 10^8 m \cdot s^{-1} = 3 \times 10^8 m \cdot s^{-1}$$

In free space σ = 0 and J = 0. In isotropic media, we would expect that at any point *D* and *J* are parallel to *F*, and *B* is parallel to *H*. Thanks to the Maxwell's equations a vast variety of electromagnetic phenomena can be described with only a few variables. Normally, they are used the relative values of μ and ε, expressed as:

$$\mu_r = {}^{\mu}/_{\mu_0} \tag{4.8}$$

$$\varepsilon_r = {}^{\varepsilon}/_{\varepsilon_0} \tag{4.9}$$

μ_r and ε_r are called the relative permeability and the relative permittivity (or simple dielectric constant), respectively.

4.1.1. DEFINITIONS AND TERMS

An important point in dielectric materials is the presence or not of dipoles. Remembering what a dipole is: a pair of equal and opposite charges situated close enough compared with the distance to an observer; in other words, an entity made up by a positive charge *q* separated a relatively short distance *l* from an equal negative charge. μ is a vector quantity the direction of which is taken the negative to the positive charge and has the unit of coulomb × m (C·m). A unit of dipole moment is 1 Debye = 3.33 x10 $^{-30}$ C·m. Find the dipole moment of a molecule containing a few atoms is quite easy, but in more complicated polyatomic molecules it is necessary to take into account not only the geometric structure of the molecule but also the interactions with other surrounding molecules.

In real systems we work with a continuous medium having an enormous number of elementary dipoles [7]. Dipolar substances contain permanent dipoles from the asymmetrical location of electric charges. Under an electric field, these dipoles tend to orient because of the action of torques. As a result it is achieved the orientation polarization of the material. In addition, the effect of the applied electric field also induces a new type of polarization by distortion of the electronic clouds (electronic polarization) and the nucleus (atomic polarization) of the atomic structure of the matter. This type of polarization is practically instantaneous. The orientation polarization scarcely contributes to the total polarization. However, this contribution increases when the frequency diminishes (time increases), and this is an essential feature of the dielectric dispersion.

In a static case, i.e. for zero-frequency polarizability, the field *E* acting on a dipole is different from the applied field E_0. The average moment for an isotropic material is expressed as:

$$m = \alpha E \tag{4.10}$$

where α is the total polarizability which includes the electronic, α_e, the atomic, α_a, and the orientational, α_0, contributions. When *E* is small there are no saturation effects and the relationship between the induced moment and the electric field is linear. The total polarization of N_1 dipolar molecules per unit volume, each of them having an average moment *m*, is:

$$P = N_1 m = \frac{N}{V} m \tag{4.11}$$

where *N* is the total number of molecules. In addition, the average field caused by the induced dipoles of the dielectric placed between two parallel plates is given by:

$$\langle E_z \rangle = \frac{1}{V} \int_{\perp} E_z(r) d^3 r = -\frac{4\pi N m}{V} = -4\pi P \tag{4.12}$$

The mean electric field $\langle E_z \rangle$ is added to the field formed by the charge densities in the plates. This field is given by:

$$E_0 + 4\pi P = D \tag{4.13}$$

where D is the electric displacement.

The dielectric susceptibility is defined as:

$$\chi = \frac{\varepsilon - 1}{4\pi} = \frac{P}{E_0} \tag{4.14}$$

Thus, the permittivity is given by:

$$\varepsilon = 1 + 4\pi\chi = \frac{D}{E_0} \tag{4.15}$$

This equation is also be written as:

$$D = \varepsilon E_0 = \varepsilon_0 \varepsilon_r E_0 \tag{4.16}$$

where:

$$\varepsilon_r = \frac{\varepsilon}{\varepsilon_0} = \frac{C}{C_0} = \frac{E_0}{E} \tag{4.17}$$

ε_r is the relative permittivity and ε_0 (=8.854×10^{-12}C·kg^{-1}·m^{-3}·s^2) is the permittivity of the free space. In cgs units, $\varepsilon_0 = 1$ and $\varepsilon_r = \varepsilon$. Note that, in the present context, D and E_0 are aligned, and thus ε is a scalar.

In this way, there are important terms that must be known [8], such as the **dielectric constant**. It is a measure of how easily charges are polarized in a material under the influence of an applied electric field. The dielectric constant (4.17) provides a measure of its effect on a capacitor [9], since it is the ratio of the **capacitance** ($\boldsymbol{C}$) of a capacitor containing the dielectric to that of an identical but **empty capacitor** ($\boldsymbol{C_0}$) [10].

$$C = \frac{Q}{\Delta V} = \frac{\varepsilon\, A}{d} = \varepsilon_0\, \varepsilon\, \frac{A}{d} \tag{4.18}$$

where C is Capacitance (F, farad), Q is Charge (C, coulomb), ΔV is Voltage (V, volts), A is the Electrode Area and d the Plate Spacing (thickness of dielectric), ε is Dielectric constant.

The **dielectric constant** or **relative permittivity** can be referred with different symbols, because there is no standardized terminology, it can be seen as $\boldsymbol{\varepsilon_r}$, $\boldsymbol{\kappa}$, $\boldsymbol{\varepsilon}$ or $\boldsymbol{\varepsilon'}$. In addition, the absolute permittivity may also be given by the symbol ε and the symbol κ is often used for Coulomb's constant.

The **dielectric constant** is the relative permittivity of a dielectric material. It is an important parameter in characterizing capacitors, because provides a measure of its effect on a capacitor. Then, it is the ratio of the field without the dielectric (E_0) to the net field (E) with the dielectric (4.17). E is always less than or equal to E_0, so the dielectric constant is greater than or equal to 1. In conclusion, the larger the dielectric constant, the more charge can be stored. Completely filling the space between capacitor plates with a dielectric increases the capacitance by a factor of the dielectric constant:

The capacitance is maximized if the dielectric constant is maximized, and the capacitor plates have large area and are placed as close together as possible. If a metal was used for the dielectric instead of an insulator the field inside the metal would be zero, corresponding to an infinite dielectric constant. The dielectric usually fills the entire space between the capacitor plates.

In order to understand this phenomena is necessary to apply the Gauss's law. This law states that the electric flux outward from a volume is equal to the total net charge enclosed inside it. We use a simple system consisting of two metal plates parallel to each other with an area A each and a separation d. Suppose we introduce a positive charge $+Q$ on the upper plate and negative charge $-Q$ of the same magnitude on the lower plate. This can be easily done by conecting a steady DC voltage supply across the plates and charging the system as a capacitor, and then disconnecting the supply from the system as soon as the charge has been accumulated to the desired value Q. These charges on the plates will create a potential difference between the plates V that is proportional to Q, as it can be observed in Figure 4.1.

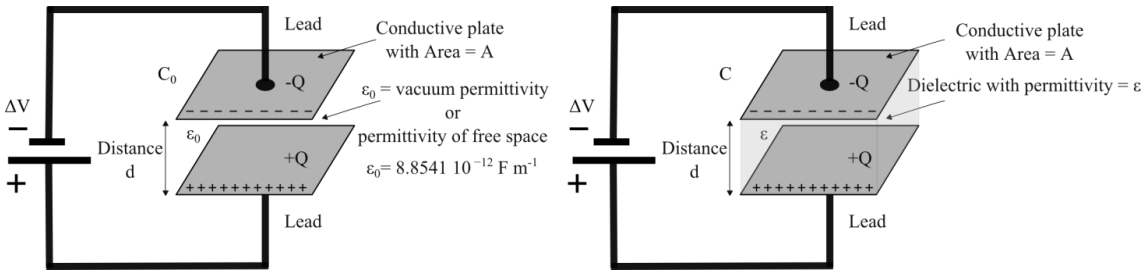

Figure 4.1. Schematic representation of an empty capacitor (Left) and a capacitor with a dielectric (Right).

An alternative definition of the dielectric constant is related to the permittivity of the material. **Absolute permittivity** $(\boldsymbol{\varepsilon})$ is a quantity that describes the effect of a material on an electric field: the higher the permittivity, the more the material tends to reduce any field set up in it. Since the dielectric material reduces the field by becoming polarized, an entirely equivalent definition is that the permittivity expresses the ability of a material to polarize in response to an applied field. The dielectric constant (relative permittivity) is the ratio of the permittivity of the dielectric to the permittivity of a

vacuum, so the greater the polarization developed by a material in an applied field of given strength, the greater the dielectric constant will be:

$$\varepsilon = \varepsilon_r \, \varepsilon_0 = (1 + \chi) \, \varepsilon_0 \tag{4.19}$$

where ε is the absolute permittivity, $\boldsymbol{\varepsilon_0}$ is the **vacuum permittivity**, permittivity of free space, and χ (also written as $\boldsymbol{\chi_e}$) is the **electric susceptibility** of the material. χ_e is a dimensionless proportionality constant that indicates the degree of polarization of a dielectric material in response to an applied electric field. For most materials, the dielectric constant is independent of the electric field strength for fields below a certain critical field, at or above which carrier injection into the material becomes important. The dielectric constant depends strongly on the frequency of the alternating electric field or the rate of the change of the time-varying field. It also depends on the chemical structure and the imperfections (defects) of the material, as well as on other physical parameters including temperature and pressure, etc.

Electric susceptibility can also be defined as the constant of proportionality (which may be a tensor) relating an electric field (E) to the induced dielectric polarization density (P).

$$P = \varepsilon_0 \, \chi_e \, E \tag{4.20}$$

The greater the electric susceptibility, the greater is the ability of the material to be polarized in response to the field, and thus reduce the total electric field inside the material and store energy. In addition, the electric susceptibility influences other phenomena in the medium, such as the electric permittivity or the capacitance. The susceptibility of a medium is related to its relative permittivity ε_r by: $\chi = \varepsilon_r - 1$. Therefore, in vacuum χ is equal to 0 ($\chi = 0$).

The **electric displacement** $(\boldsymbol{D})$ is also related to the **polarization density** $(\boldsymbol{P})$ by:

$$D = \varepsilon_0 E + P = \varepsilon_0 (1 + \chi) E = \varepsilon_r \, \varepsilon_0 \, E \tag{4.21}$$

The physical constant $\boldsymbol{\varepsilon_0}$, also called the **vacuum permittivity**, **permittivity of free space** or **electric constant**, is an ideal (baseline) physical constant, which is the value of the absolute dielectric permittivity of classical vacuum. By true vacuum space, or free

space, we mean that in the space there are no detectable particles. However, a true vacuum is not available on the earth. The best vacuum system that can be produced by today's technology can achieve only a vacuum of about 10^{-14} torr, in which there are still about 300 particles per cm^3. Its value is:

$$\varepsilon_0 = \frac{1}{c^2 \mu_0} = 8.8542\ x\ 10^{-12}\ F\ m^{-1} = 8.854\ x\ 10^{-12}\ C^2\ N^{-1}\ m^{-2}$$

$\boldsymbol{\mu_0}$ is the **vacuum permeability**, permeability of free space, or magnetic constant is an ideal (baseline) physical constant, which is the value of magnetic permeability in a classical vacuum, being $\mu_0 = 4\pi \times 10^{-7}$ V·s/(A·m) ≈ 1.2566370614...×10^{-6} H·m^{-}1. The unit H is a henry.

4.1.2. ELECTRIC POLARIZATION

All dielectric phenomena arise from an electric force which is primarily due to the attraction and the repulsion of electric charges. The action of the force tends to reduce the potential energy of the whole electrically stressed system to a minimum. This is a universal law of nature.

The most important electric charges are electrons and protons, they are the main elementary particles of any material. The electron and the proton are the elementary charges; they are equal in magnitude, but opposite in charge polarity. An electron has a negative charge $-q$, and a proton has a positive charge $+q$, where q = 1.602 x 10^{-19} C.

An electric field can be considered a region in which a particle with a charge q would experience an electric force acting on it. The electric field strength F is determined by the magnitudes and the locations of all other charges, as well as the surrounding medium. For a single-point charge with total net charge $+Q$ in free space, F can be written as:

$$F = \frac{Q}{4\pi\varepsilon_0 r^2} \tag{4.22}$$

where *r* is the distance between the location of +*Q* and point *P*, and ε_0 is the permittivity of the medium.

A dielectric material is made up of atoms or molecules that possess one or more of five types of electric polarization [11] (Figure 4.2):

Each type of polarization requires time to be performed, that is why the degree of the overall polarization depends on the time variation of the electric field. From now, only the polarization under static fields will be considered. In the first place, it is considered a perfect dielectric material. The so-called "perfect" material implies that inside the material no mobile charge carriers (electrons or ions) are present. The system will tend to attract this piece of material into the vacuum space between the two plates in order to reduce the potential energy of the system.

But in the case that the piece of the material is inside the space between the metal plates with the original surface of density σ_S unaltered, causes the potential between the plates produced by the original charge Q on the plates to decrease to a smaller value. In fact, with Q on the plates remaining constant, the ratio of the electric field in free space, E_0, to that filled with the dielectric material, E, is the so-called dielectric constant. Thanks the dielectric material, part of σ_S is used to compensate the polarization charges on the surfaces of the material in contact with the metal plates. This portion of σ_b is bound at the locations with its charge opposite in polarity and equal in magnitude to the polarization charges of the material.

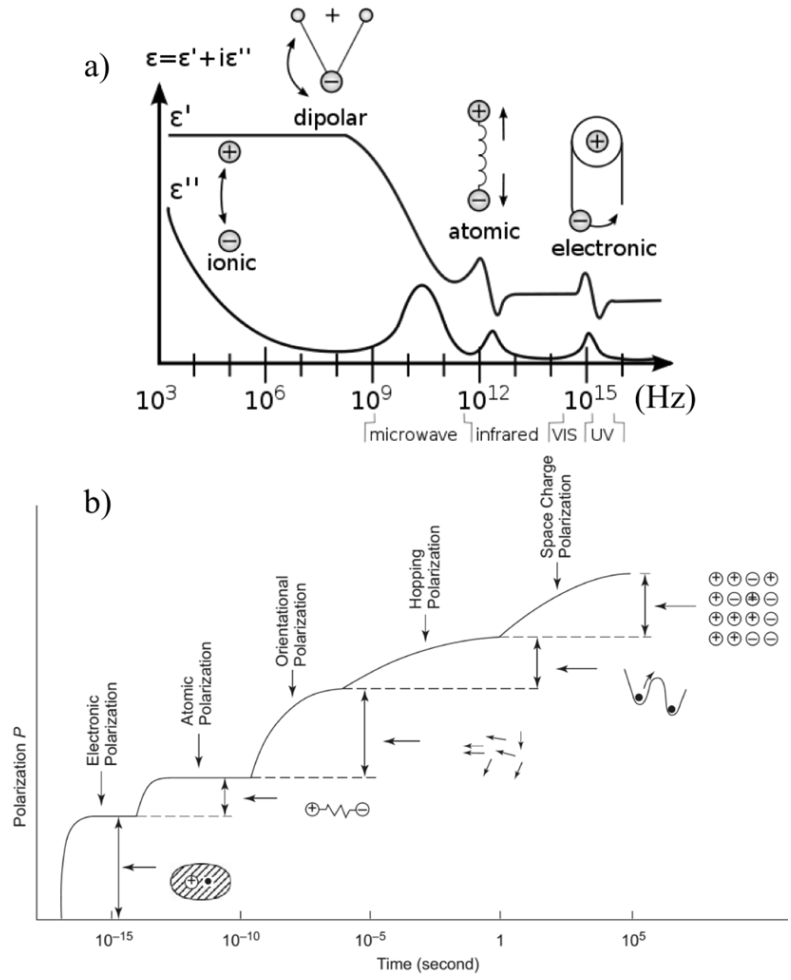

Figure 4.2. Schematic of a) a dielectric permittivity spectrum over a wide range of frequencies and b) the variation of different types of polarization with time under an electric field.

This portion of charge is termed the bound charge density σ_b. By denoting the number of atoms (or molecules) per unit volume of the material as *N*, and the average separation between charges $+q_d$ and $-q_d$ of each dipole (each atom or molecule produces one dipole) as δ, we can write:

$$\sigma_b = N\langle q_d \delta \rangle \tag{4.23}$$

The other portion $\sigma_S - \sigma_b$ is the free surface charge density, which acts in the same manner as that in a vacuum, creating an electric flux density $D_0 = \varepsilon_0$. Thus, it can be written:

$$\sigma_S = (\sigma_s - \sigma_b) + \sigma_b$$

$$= D = D_0 + P \tag{4.24}$$

$$= \varepsilon_S E = \varepsilon_0 E + (\varepsilon_s - \varepsilon_0)$$

Therefore, polarization *P* can be defined as:

$$P = (\varepsilon_s - \varepsilon_0)E = \sigma_b = polarization$$

$$= \frac{Bound\ charge}{Surface\ area} = N\langle q_d \delta \rangle \tag{4.25}$$

$$= \frac{Number\ of\ Induced\ Dipole\ Moments}{Volume} = N\langle \vec{u} \rangle$$

where $\langle \vec{u} \rangle$ is the average value of the dipole moment, which is given by

$$\langle \vec{u} \rangle = \langle q_d \delta \rangle = \alpha \vec{E}_{loc} \tag{4.26}$$

where α is called the polarizability and is a scalar quantity if the constituent particles (atoms or molecules) in a material are spherically symmetrical in shape and $\langle \vec{u} \rangle$ is in the direction of *E*. However, if the particles (atoms or molecules) are not spherically symmetrical in shape, particularly those with permanent dipoles, then $\langle \vec{u} \rangle$ is not exactly in the direction of *E*. Taking into account that $\langle \vec{u} \rangle$ depends on the local field at which the individual particle is polarized, this field E_{loc} is different from the applied external field *E*. Therefore, by making $\langle \vec{u} \rangle$ proportional to *E*, the polarizability α is related to the local field. It can also be written:

$$\alpha = \frac{\varepsilon_s - \varepsilon_0}{N} \tag{4.27}$$

The polarizability α of a particle in a dielectric material is induced by local field. It is sometimes convenient to use the relative permittivity ε_r (i.e., the dielectric constant) to describe the dielectric properties

$$\varepsilon_r = \frac{\varepsilon_s}{\varepsilon_0} = \left(1 + \frac{N\alpha}{\varepsilon_0}\right) = 1 + \chi \tag{4.28}$$

where $= \frac{N\alpha}{\varepsilon_0}$, the electric susceptibility can also be expressed as:

$$\chi = \varepsilon_r - 1 = \frac{P}{D_0} = \frac{Bound\ surface\ charge\ density\ of\ the\ plates}{Free\ surface\ charge\ density\ of\ the\ plates} \tag{4.29}$$

Remember that the discussion is limited to the phenomena under a static field. It is assumed that at time $\mathrm{t} = 0$ the material is inside the vacuum space and starts to be polarized by the field created by the charges on the metal plates. The polarization produced by the elastic displacement of electron clouds of the particles (atoms and molecules) requires a very little time, while the polarization involving the movement of the particles, such as the orientation of permanent dipoles or the migration of charge carriers (electrons or ions), requires a much longer time to perform. All types of polarization encounter some inertia counteracting the change and, therefore, involve some dielectric loss.

In the system being considered, σ_s on the plates is constant, but the permittivity starts to rise from $\varepsilon = \varepsilon_0$ and the corresponding field to decrease from $E = E_0$ at time zero. It takes a very little time for ε to increase to ε_∞ and for E to decrease to E_∞ due to the polarization contributed by the elastic displacement of electron clouds of atoms or molecules (electron and atomic polarization). The time involved in this polarization is about of 10^{-14} to 10^{-13} second.

However, for the permittivity to increase from ε_∞ to its steady state value ε_s and for the corresponding field to decrease from E_∞ to its final value E_s, a larger amount of time is required, because this change is caused by the polarization associated with the inelastic movement of particles such as the collective orientation of dipoles or the migration of charge carriers to form space charges near the electrodes or grain boundaries. Ignoring the small loss due to elastic displacement of electron clouds, the transition from $\mathrm{P}_\infty = (\varepsilon_{\infty\mathrm{r}} - 1)\varepsilon_0 \mathrm{E}_\infty$ to $\mathrm{P_s} = (\varepsilon_\mathrm{r} - 1)\varepsilon_0 \mathrm{E_s}$ involves some energy loss, which must be consumed to overcome the inertia resistance. This energy loss is called the **dielectric loss ($\boldsymbol{\varepsilon''}$)**, which always accompanies time-varying electric fields. At static fields, it appears only during the transient period in which the electric field across the dielectric materials is time-varying, although the charges on the metal plates are constant. This

loss per unit time will become zero when the polarization has reached its final steady value $\varepsilon = \varepsilon_s$.

After the overall polarization process is completed, we short-circuit the two metal plates. Under this short-circuiting condition, the charges on plate A and plate B will be immediately neutralized, leaving only the polarized particles in the dielectric material to be gradually depolarized. It would take time, depending on the environmental temperature, for all polarized particles to become completely depolarized, particularly for those whose polarization involves the orientation of permanent dipoles or the migration of charge carriers. After the short-circuit current, due to the neutralization of the charges on the metal plates, reverse depolarization current will follow, due to the depolarization of the polarized particles.

A. MECHANISMS OF ELECTRIC POLARIZATION

The polarizability (α) previously defined implies that if $\langle \vec{u} \rangle$ is proportional to the local field E_{local} at which the particles are polarized, then $\langle u \rangle$ is expressed as $\langle \vec{u} \rangle = \alpha E_{local}$ and the polarizability (α) depends only on the mechanism of polarization and can be defined simply as the average dipole moment per unit field strength of the local field E_{local}, which is different from the externally applied field E. But if $\langle \vec{u} \rangle$ is expressed as $\langle \vec{u} \rangle = \alpha_{eff} E$, i.e., $\langle \vec{u} \rangle$ is proportional to E, in this case, α_{eff} should also be defined similarly to the effective dipole moment per unit field strength of the applied field E. However, α_{eff} depends not only on the mechanism of polarization, but also on the factor of E_{loc}/E. We shall consider first the mechanisms responsible for the polarizability (α).

There are three major mechanism of electric polarization at moderate electric fields (i.e., at fields much lower than the inner atomic or molecular fields), and for materials with a very low conductivity (σ) (i.e., the concentration of charge carriers inside the materials is so low that its effect can be neglected), these mechanisms prevail.

At higher fields, carrier injection becomes important. For materials consisting of a high concentration of charge carriers (i.e., with a high conductivity), polarization due to the migration of charge carriers to form space charges at interfaces or grain boundaries becomes important. This type of polarization is called space charge polarization.

Then, the polarizability of material α comprises four components

$$\alpha = \alpha_e + \alpha_i + \alpha_0 + \alpha_d \tag{4.30}$$

where α_e, α_i, α_0, and α_d are the polarizabilities due to electronic, atomic, orientational, and space charge polarization, respectively [4].

A.1. ELECTRONIC POLARIZATION

In the classical view of the structure of the atom the center of the atom consists of positively charged protons and electrically neutral neutrons. The electrons move about the nucleus in closed orbits. The electron and the nucleus can form a dipole with a moment directed from the negative charge to the positive charge. However the axis of the dipole changes with the motion of the electron and the time average of the dipole moment is zero. Further, the motion of the electron must give rise to electromagnetic radiation and electrical noise. The absence of such effects leads to the concept that the total electronic charge is distributed as a spherical cloud the center of which coincides with the nucleus, the charge density decreases with increasing radius from the center.

When the atom is situated in an electric field the charged particles experience an electric force as a result of which the center of the negative charge cloud is displaced with respect to the nucleus. A dipole moment is induced in the atom and the atom is said to be electronically polarized (Figure 4.3).

The electronic polarizability (α_e) may be calculated by making an approximation that the charge is spread uniformly in a spherical volume of radius *R*. The dipole moment induced in the atom is:

$$\mu_e = (4\pi\varepsilon_0 R^3)E \tag{4.31}$$

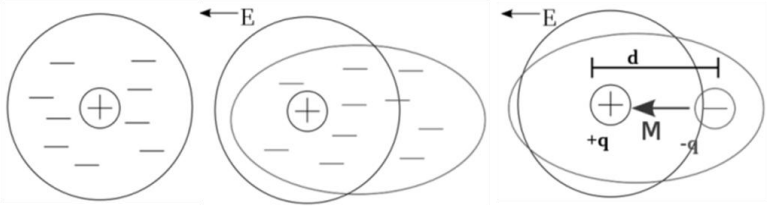

Figure 4.3. Scheme of the electronic polarization where it can be observed the shift of the electron cloud in the presence of an external electric field.

For a given atom the quantity inside the brackets is a constant and therefore the dipole moment is proportional to the applied electric field. The dipole moment is zero again when the field is removed, because the charge centers are restored to the undisturbed position.

The electronic polarizability (α_e) of an atom is defined as the dipole moment induced per unit electric field strength and is a measure of the ease with the charge centers may be dislocated. α_e has the dimension of F·m^2. α_e can be calculated to a first approximation from atomic constants. It is also possibly to derive a relationship between the dielectric constant and the electronic polarizability.

A.2. ATOMIC POLARIZATION

Atomic polarizability (α_i) arises due to the displacement of the nuclei of atoms forming the molecule, relative to each other, in contrast with the electronic polarizability that arises as consequence of electronic displacement, in an electric field (Figure 4.4). There are two groups, one group does not possess permanent dipoles so that the lattice symmetry and the overall charge neutrality ensure that electric dipoles formed by each ion pair everywhere cancel each other. The other group possesses permanent dipoles, but they are foreseen in the solid state and cannot be aligned by an electric field. This is

why in most ionic solids belonging to this group, the permanent dipole moments do not contribute to the polarizability in the solid state although the materials possess them.

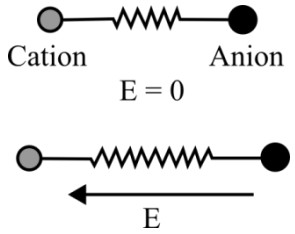

Figure 4.4. Scheme of the atomic or ionic polarization.

Whether a molecule possesses a permanent dipole or not, if it has polar bonds the applied field induces a displacement; this displacements is superimposed on the electronic displacement. Though atomic polarization exists in all molecules, it is more pronounced in molecules that have relatively weak bonds.

The distinction between electron and ionic polarizations is not sharp, due to the fact that the displacement of ions is always accomplished by the displacement of electrons. It is much easier to measure the electronic polarizability than the ionic polarizability. The time required for electronic polarization is about 10^{-15} seconds, and for the ionic polarization is about 10^{-13} seconds, simply because ions are heavier than electrons by more than 10^3 times. This is why the resonances for these two polarizations occur in different frequency regions.

A.3. ORIENTATIONAL POLARIZATION

First of all, it is important to understand why some molecules possess permanent dipole moments and some do not. An ionic bond molecule possesses a permanent dipole moment, which is the product of the charge of the portion of the valence electrons transferred from atom *A* to atom *B* and the interatomic distance.

In paraelectric materials α_e and α_i are considered independent of temperature for the normal temperature range in most applications, because the electronic structure does not change in the normal temperature range. However, the orientational polarizability (α_0) depends strongly of temperature. Those molecules with asymmetrical structure are dipolar, resulting in the formation of a permanent dipole moment, such as the CO_2 molecule showed in Figure 4.5. Orientational polarization occurs only in the materials composed of molecules with an asymmetrical structure in which the centroid of the negative charge (mainly electrons) and that of the positive charge (mainly nuclei) are not coincident, so they possess permanent dipole moments in the absence of external fields. The directions of these dipoles are randomly distributed in the material. An electric field will cause them to reorient toward the direction of the field, resulting in orientational polarization. The net polarization will return to zero after the removal of the external field. For that reason the total polarization in which the orientational polarization is dominant decreases with increasing temperature. In general, orientational polarizability is much larger than electronic and atomic polarizabilities at normal conditions, since α_e and α_i are practically independent of temperature (dependence at normal conditions is not significant) but α_0 is strongly temperature dependent. Thus, α_0 can be easily differenced from α_e and α_i by the temperature dependence measurement of ε_r.

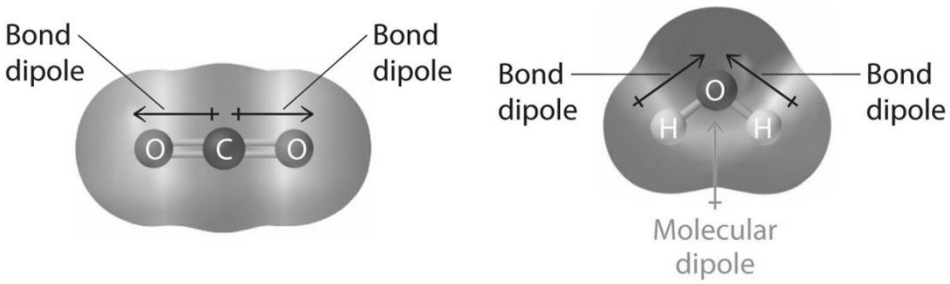

Figure 4.5. CO_2 molecule without net dipole moment (Left). H_2O molecule with net dipole moment (Right).

A.4. SPONTANEOUS POLARIZATION

Other type of polarization is the so-called spontaneous polarization. In analogy with magnetization may be grouped into two major polarizations: paraelectric polarization and ferroelectric polarization.

Spontaneous polarization occurs in materials whose crystalline structure exhibits electrical order. This implies that it occurs only in single crystals or crystallites in polycrystalline materials with a non-centrosymmetric structure, because the centroid of the negative charges does not coincide with that of the positive ones. In ferroelectric materials, electric polarization occurs spontaneously due to a phase transition up to a critical temperature called Curie temperature (T_C).

Those dipole moments will gradually form a domain and gradually increase the free energy of the system until this process cannot continue, when it has reached a certain size, and another domain with dipole moments pinting in the opposite direction will be formed in order to reduce the free energy of the system. In a single crystal or a crystallite, there are many domains with moments pointing in various directions, but the vector sum of the dipole moments of all domains vanishes. Each domain can be considered as a large dipole. Under an external electric field, all of these randomly arranged domains tend to move toward the direction of the field, resulting in a net total spontaneous polarization. Upon the removal of the field, spontaneous polarization does not vanish but remains inside the material. The field polarization relation forms a hysteresis loop for ferromagnetic materials.

A.5. SPACE CHARGE POLARIZATION

The electronic, atomic, orientational and spontaneous polarizations are due to the bound positive and negative charges within the atom or the molecule itself, which are linked intimately to each other and which normally cannot be separated. However, electric polarization may also be associated with mobile and trapped charges. A type of polarization generally named space charge polarization (P_d) occurs mainly in

amorphous or polycrystalline solids or in materials consisting of traps. Charge carriers (electrons, holes, or ions), which may be injected from electrical contacts, may be trapped in the bulk or at the interfaces (interface polarization or Maxwell-Wagner-Sillars polarization), or may be impeded to be discharged or replaced at the electrical contacts (electrode polarization) (Figure 4.6). For example, charges pile up in the volume or on the surface of the dielectric, predominantly due to change in conductivity that occurs at boundaries, imperfections such as cracks and defects, and boundary regions between the crystalline and amorphous regions within the same material. Regions of occluded moisture also cause an increase in conductivity locally, leading to accumulation of charges. As indicated, the most important ways in which space charge polarization may occur are:

Interfacial polarization: the space charge, or interfacial polarization, is produced by the separation of mobile positively and negatively charged particles under an applied field, which form positive and negative space charges in the bulk of the material or at the interfaces between different materials. These space charges, in turn, modify the field distribution.

Hopping Polarization: in a dielectric material, localized charges (ions and vacancies, or electrons and holes) can hop from one site to the neighboring site, creating so-called hopping polarization [12]. These charges are capable of moving freely from one site to another site for a short time, then becoming trapped in localized states and spending most of their time there. Occasionally, these charges make a jump surmounting a potential barrier to other sites. In fact, the movement of ions or vacancies in ionic crystals and the movement of electrons and holes in glasses and amorphous semiconductors are essentially due to the hopping process.

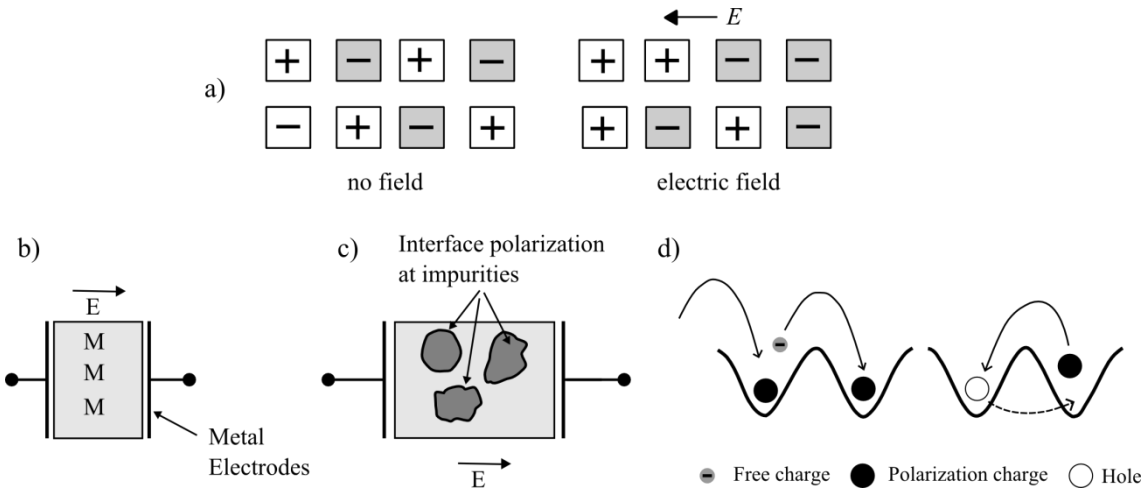

Figure 4.6. Scheme of a) space charge polarization, b) electrode polarization, c) interface polarization at impurities and d) hopping polarization processes.

4.1.3. MACROSCOPIC AND MICROSCOPIC INTERACTION WITH THE ELECTRIC FIELD

In this section it will be connected the macroscopic property, permittivity (ε) with the microscopic properties: molecular polarizability (α) and molecular dipole moment (μ).

—Non-polar molecules in the gas phase

The simplest case is non-polar molecules in the gas phase, where intermolecular interactions can be ignored [13]. The polarization can be expressed in terms of electric permittivity (macroscopic) or the molecular polarizability (microscopic):

$$\varepsilon_0(\varepsilon_r - 1)\vec{E} = \vec{P} = \frac{N}{Vol}\vec{\mu}_{ind} = \frac{N}{Vol}\alpha\vec{E} \tag{4.32}$$

Thus, here the relation between macroscopic and microscopic quantities is:

$$\varepsilon - \varepsilon_0 = \frac{N\alpha}{Vol} \tag{4.33}$$

Interactions between non-polar molecules cannot be neglected. It can be used the solution for the problem of a dielectric sphere in a uniform electric field. The sphere contains a large number N of molecules but is viewed as a (induced) single point dipole moment:

$$\vec{\mu} = 4\pi\varepsilon_0 \frac{\varepsilon_r - 1}{\varepsilon_r + 2} R^3 \vec{E}_0 \tag{4.34}$$

Therefore, the induced (electronic and atomic) polarizability would be obtained as:

$$4\pi\varepsilon_0 \frac{\varepsilon_r - 1}{\varepsilon_r + 2} R^3 = N\alpha \implies \frac{\varepsilon_r - 1}{\varepsilon_r + 2} = \frac{1}{3\varepsilon_0} \frac{N}{Vol} \alpha \tag{4.35}$$

This is named as the **Clausius-Mossotti** (or Lorentz-Lorentz if $\varepsilon_r = n^2$) equation [14]. It is derived assuming that the relative displacement of electrons and nucleus is elastic, i.e., the dipole moment is zero after the applied voltage is removed. However a large number of substances possess a dipole moment even without the presence of an electric field. In this case, the temperature variation was not considered, implying that polarization is independent of temperature. However the dielectric constant of many dielectrics depends on temperature. The theory for calculating the dielectric constant of materials possessing a permanent dipole moment is given by Debye [15,16].

—Polar molecules in condensed phase

If molecules possess a permanent dipole moment, these molecules will tend to reorient in the applied field. The full alignment of the dipoles will be disrupted by thermal motion that tends to randomize the orientation of the dipoles. As a consequence a net polarization that depends on the applied electric field is obtained. The orientational polarization will be an equilibrium (or ensemble) average of dipoles aligned in the field. As the energy of a dipole in the electric field is given by: $W = -\mu_0 \langle \cos\theta \rangle$, what is relevant is the average dipole moment in the field direction.

The total polarization will be given by the sum of the two contributions the orientational and the induced one, the later as that above-calculated for non-polar molecules.

$$\vec{P} = \vec{P}_{ind} + \vec{P}_{or} = \frac{N}{Vol}\,\alpha\vec{E} + \frac{N}{Vol}\,\frac{\mu_0^2\vec{E}}{3kT} = \frac{N}{Vol}\left(\alpha + \frac{\mu_0^2}{3kT}\right)\vec{E} \tag{4.36}$$

By including this contribution in the Clausius-Mossotti equation one obtains **the Debye relation**:

$$\frac{\varepsilon_r - 1}{\varepsilon_r + 2} = \frac{1}{3\varepsilon_0}\frac{N}{Vol}\left[\alpha + \frac{\mu_0^2}{3kT}\right] \tag{4.37}$$

The Debye relation works well only for very dilute dipoles, i.e. either in diluted gas phases or solutions of polar molecules in non-polar solvents. In the gas case the following approximation holds ($\varepsilon_r + 2 \approx 3$):

$$\varepsilon_r - 1 = \frac{1}{\varepsilon_0}\frac{N}{Vol}\left[\alpha + \frac{\mu_0^2}{3kT}\right] \tag{4.38}$$

A main reason for the failure of the Debye approach in dense dipolar systems is because neglects the effect of the dipole in the surrounding when evaluating the local electric field.

—The Onsager treatment of the orientational polarization

Onsager treated the orientational polarization by taking the reaction field into account [17]. Thus, the directing field E_d (responsible of the dipole reorientation) is introduced. The direction field would be given by the cavity field plus the reaction field due to the induced dipole.

It can be established the final relationship between macroscopic and microscopic. If the effective dipole moment is expressed in terms of the molecular quantity, one obtains the Onsager equation.

$$\mu_0^2 = \varepsilon_0 kT\frac{Vol}{N}\,\frac{9(2\varepsilon_r + \varepsilon_\infty)}{\varepsilon_r(\varepsilon_\infty + 2)^2}(\varepsilon_r - \varepsilon_\infty) \tag{4.39}$$

—The Kirkwood-Fröhlich equation

The Onsager treatment neglects the correlation between neighboring dipoles and subsequently if fails in accounting properly for the connection between macroscopic and microscopic quantities when there are significant orientational correlations. In this way the Onsager equation can be modified resulting in:

$$g\,\mu_0^2 = \varepsilon_0 kT\frac{Vol}{N}\frac{9(2\varepsilon_r+\varepsilon_\infty)}{\varepsilon_r(\varepsilon_\infty+2)^2}(\varepsilon_r-\varepsilon_\infty) \tag{4.40}$$

where, g is the Kirkwood correlation factor. When the molecule is surrounded by *z* equivalent molecules, g can be expressed as: $= 1 + z\cos\gamma$, where γ is the angle between the test dipole and the neighbor. Thus, $g = 1$ means no correlation, $g > 1$ indicates a tendency to parallel alignment and $g < 1$ a tendency to anti-parallel alignment.

The Kirkwood-Fröhlich equation is required to account for the molecular dipole moment in associated liquids [18–20]. However, the evaluation of the g factor, which is required for the calculation, demands a detailed modeling of the molecular organization.

—Temperature dependence of the permittivity

In non-polar compounds the dominant factor determining the temperature dependence of ε_r is the sample density. Thus, one only expect a weak decreasing with temperature of ε_r accomplishing thermal expansion. This is the general case (including polar molecules) for ε_∞ and n.

However, for polar systems the orientational part presents additional temperature dependence, since temperature appears explicitly in the obtained equations of the permittivity. It is expected an apparent decreasing of what is going to be called 'dielectric relaxation strength', $\Delta\varepsilon = \varepsilon_r - \varepsilon_\infty$, according to a Curie-like law, i.e.:

$$\Delta\varepsilon \equiv \varepsilon_r - \varepsilon_\infty \propto \frac{1}{T} \tag{4.41}$$

By increasing the temperature the relaxation processes move to higher frequencies (or shorter times). However, not all the relaxation processes move at the same rate upon increasing temperature. It is empirically found for a vast number of processes that the rate constant *k* is related to the absolute temperature by the Arrhenius equation. Arrhenius considered that the majority of the trials to overcome the potential barrier are ineffective because the energy is insufficient. According to the Boltzmann principle the fraction of trials in which the energy is in excess of a particular value *E* is $e^{-E/RT}$. This fraction is larger the higher the temperature *T* and the lower the energy *E*. The rate constant should therefore be proportional to this fraction. In many cases the temperature dependence of the relaxation times can be approximated by the empirical Vogel-Fulcher-Tammann (VTFH) equation.

—Time scale of the dipole reorientation

The connection between the macroscopic electric permittivity and the molecular dipole moment has also implications in the relationship between the characteristic time of the dielectric response and the time scale of the dipole reorientation. This can be illustrated in the simple Debye model for which the dipole moment and the complex frequency dependent permittivity are related as:

$$\frac{\varepsilon_r^*(\omega)-1}{\varepsilon_r^*(\omega)+2}=\frac{1}{3\varepsilon_0}\frac{N}{Vol}\left[\alpha+\frac{\mu_0^2}{3kT}\frac{1}{1+i\omega\tau_\mu}\right] \qquad \text{with} \qquad \tau_\mu=\frac{3\eta V_m}{kT} \qquad (4.42)$$

by using the Clausius-Mossotti equation for the polarizability one find:

$$\varepsilon_r^*\varepsilon_r^*(\omega)=\varepsilon_\infty+\frac{\varepsilon_S-\varepsilon_\infty}{1+i\omega\tau} \qquad \text{with} \qquad \tau=\tau_\mu\frac{\varepsilon_S+2}{\varepsilon_\infty+2} \qquad (4.43)$$

being $\varepsilon_S=\varepsilon_r(\omega\approx 0)$. Thus, the macroscopic determined time is usually larger than the molecular timescale. Only if the dispersion is weak (small changes with frequency of ε_r) the timescales of the macroscopic and microscopic responses are nearly the same, so the observed relaxation time would represent the time characteristic for the reorientation of the molecular dipole.

The connection between the macroscopic dielectric magnitudes and the corresponding molecular characteristics is difficult and can only be properly established in special cases, especially when detailed molecular information is required. Nevertheless, there is a direct correlation between the dielectric properties and the molecular characteristics that permits an approach. The dipolar entities can be used as 'molecular probes' of the molecular motions in the system. When a give molecular motion involves fluctuations of dipole moments it would be detectable by dielectric relaxation experiments.

4.1.4. DIELECTRIC LOSS AND RELAXATION

According to Maxwell's equations ε^* is time (or frequency) dependent if time dependent processes takes place within the sample [12]. That is, the complex dielectric function $\varepsilon^*(\omega)$ in its dependence on angular frequency $\omega = 2\pi\nu$ (ν, frequency of the external electrical field) and temperature originates from different processes: a) microscopic fluctuations of molecular dipoles, b) the propagation of mobile charge carriers (translational diffusion of electrons, holes or ions), and c) the separation of charges at interfaces which gives rise to an additional polarization. The last of them can happen at inner dielectric boundary layers (Maxwell-Wagner-Sillars polarization) on a mesoscopic scale and/or at the external electrodes contacting the sample (electrode polarization) on a macroscopic scale. Its contribution to the dielectric loss can be orders of magnitude larger than the dielectric response due to molecular fluctuations. Each of the mentioned processes has specific features in the frequency and temperature dependence of the real and imaginary part of the complex dielectric function. It is the objective of this chapter to analyze, separate, and quantify their contributions to the dielectric spectra of our polyimides.

In general, time dependent processes within a material lead to a difference of the time dependencies of the outer electrical field $E(t)$ and the resulting dielectric displacement $D(t)$. For a periodic electric field $E(t) = E_0 \exp(-i\omega t)$ (ω is the radial frequency, $i = \sqrt{-1}$) the complex dielectric function ε^* is defined by

$$\varepsilon^*(\omega) = \varepsilon'(\omega) - i\varepsilon''(\omega) \tag{4.44}$$

where $\varepsilon'(\omega)$ is the real part and $\varepsilon''(\omega)$ the imaginary part of the complex dielectric function. In the stationary case, the difference of the time dependencies of $E(t)$ and $D(t)$ is a phase shift.

Relaxation processes are characterized by a peak in the imaginary part ε'' and a step-like decrease of the real part ε' of the complex dielectric function $\varepsilon^*(\omega)$ with increasing frequency. In contrast, conduction phenomena show an increase of the imaginary part of the dielectric function with decreasing frequency.

For pure ohmic conduction the real part of $\varepsilon^*(\omega)$ is independent of frequency while for non-ohmic conduction or polarization effects (at inner boundaries or external electrodes) the real part $\varepsilon^*(\omega)$ increases with decreasing frequency. A schematic representation of the frequency dependence of ε^* is given in Figure 4.7.

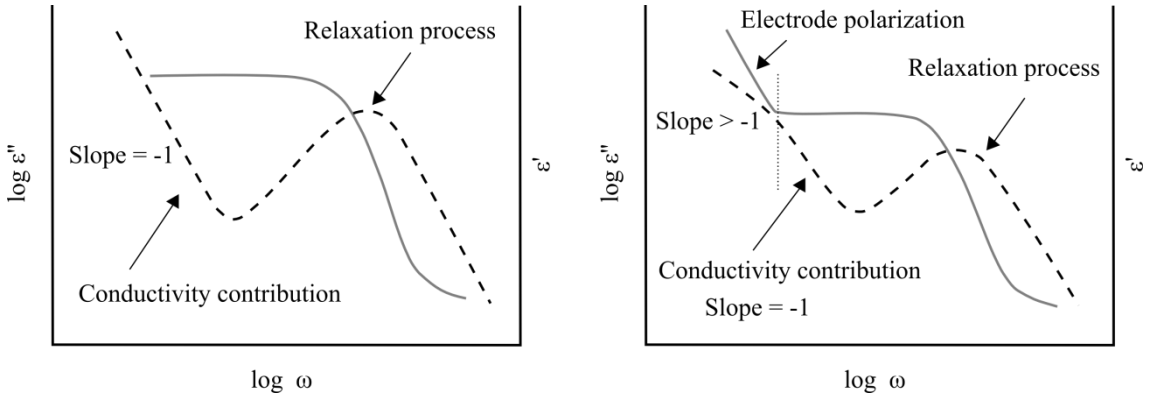

Figure 4.7. Scheme of the real ε' (*solid line)* and the imaginary ε'' *(dashed line*) part of the complex dielectric function for a relaxation process and an ohmic (Left) or non-ohmic conductivity in combination with electrode polarization (Right) [3].

The complex dielectric function (4.44) can be measured in the broad frequency regime from 10^{-6} Hz to 10^{12} Hz. Dielectric data are also often presented in terms of the complex conductivity $\sigma^* = i\omega\varepsilon_0\varepsilon^*$ or the complex electrical modulus $M^* = 1/\varepsilon^*$. For dipolar relaxation processes ε^* is usually used while for systems with mainly conductive

processes σ^* or M^* prevails. An analysis of the polarization processes leads to the important Debye equation [15], which is compared with other relaxation functions due to Cole-Cole, Davidson-Cole and Havriliak-Negami relaxation theories [21–25].

One of the most important applications of dielectric spectroscopy is the investigation of relaxation processes which are due to rotational fluctuations of molecular dipoles. As they are related to characteristic parts of a molecule (functional groups etc.) or to the molecule as a whole, information about the dynamics of a molecular ensemble can be obtained by analyzing the dielectric function. If the frequency $\nu = \omega/2\pi$ of the applied external electric field corresponds to reorientation times τ of molecular dipoles, the complex dielectric function shows a characteristic pattern. With increasing ω the real part $\varepsilon''(\omega)$ exhibits a maximum. The essential quantities which characterize a dielectric relaxation process can be extracted from that behavior. The frequency of maximal loss ν_p is related to a characteristic relaxation rate $\omega_p = 2\pi\nu_p$ or relaxation time $\tau_p = 1/\omega_p$ of the fluctuating dipoles. From the shape of the loss peak the distribution of relaxation times can be deduced. The dielectric strength $(\Delta\varepsilon)$ of a relaxation process can be determined either from the area under the loss peak $\varepsilon''(\omega)$ or from the step in $\varepsilon'(\omega)$. Since $\varepsilon'(\omega)$ and $\varepsilon''(\omega)$ are interrelated by the Kramers-Kronig relations, dielectric relaxation processes are usually analyzed using model functions. Starting from the theoretically well founded Debye function (Figure 4.8) several formulas for both the frequency and the time domain have been suggested to describe the experimentally observed spectra.

In the Debye equation showed in Table.4.1, $(\varepsilon_S - \varepsilon_\infty) = \Delta\varepsilon$ is the dielectric relaxation strength, τ_D is the Debye relaxation time, which is related to the position of maximal loss by $\omega_p = 2\pi\nu_D = 1/\tau_D$. The loss peak is symmetric with a half with ω_D of 1.14 decades. In most cases the half width of measured loss peaks is much broader than predicted by Debye (up to six decades) and in addition their shapes are asymmetric with a high frequency tail. This is called non-Debye (or non ideal) relaxation behavior. Several empirical model functions (Cole-Cole, Davidson-Cole and Havriliak-Negami) have been developed and probed to describe broadened and/or asymmetric loss peaks. They are compilated in Table 4.1.

$$D(t) = \varepsilon_0 E_0 \varepsilon_\infty + \varepsilon_0 E_0 (\varepsilon_S - \varepsilon_\infty)\gamma(t)$$

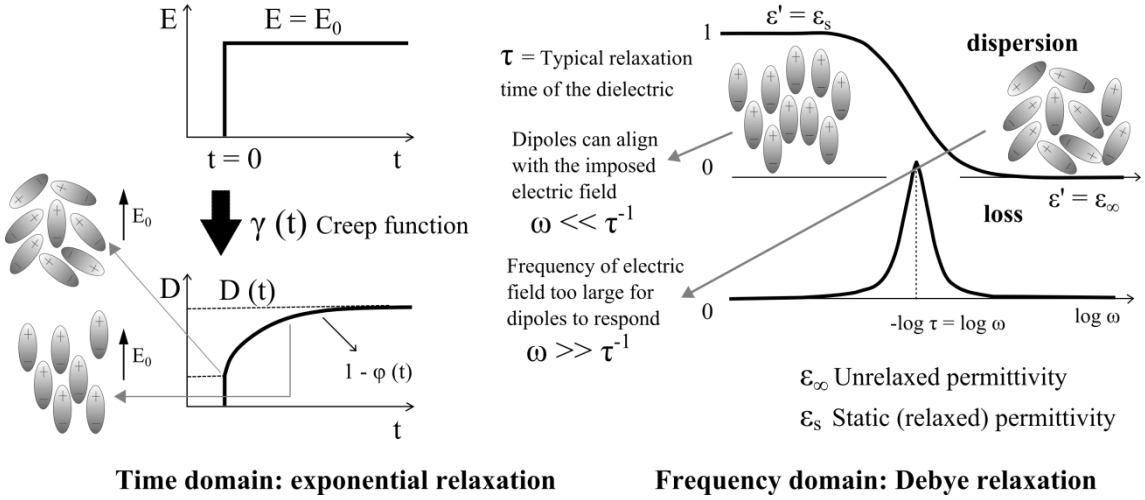

Time domain: exponential relaxation **Frequency domain: Debye relaxation**

Figure 4.8. Schematic of the dielectric response for the Debye model: step dielectric field (Left) and orientational dynamics (Right).

In many cases the non-Debye relaxation behavior in the time domain is empirically described by the Kohlrausch-Williams-Watts (KWW) function. The stretching parameter $\beta_{KWW}(0 < \beta_{KWW} \leq 1)$ leads to an asymmetric broadening of $\varphi(\tau)$ at short times (high frequencies) compared with the exponential decay($\beta_{KWW} = 1$), being τ_{KWW} the related relaxation time.

In the frequency domain, a broadening of the dielectric function can be described by the Cole-Cole function where $0 < \alpha \leq 1$ leads to a symmetrical broadening for the relaxation function. For $\alpha = 1$ the Debye function is obtained. In the Cole-Davidson function the parameter $\beta(0 < \beta \leq 1)$ describes an asymmetric broadening of the relaxation function, and for $\beta = 1$ the Debye function is recovered.

A more general model function was introduced by Havriliak and Negami [24,25] which is in fact a combination of the Cole-Cole [26,27] and the Cole-Davidson [21–23] models. For the fractional shape parameters α and β which describe the symmetric and asymmetric broadening of the complex dielectric function $0 < \alpha,\ \alpha\beta \leq 1$ holds. Figure 4.9 gives some examples of the Havriliak-Negami function for selected shape parameters.

Table 4.1. Compilation of different relaxation functions and parameters for the time and frequency domain.

Domain	Model function	Equation	Parameter
Time	KWW function	$\varphi(t) = exp\left[-(t/\tau_{KWW})^{\beta}\right]$	$0 < \beta \leq 1$
Frequency	Debye	$\varepsilon^*(\omega) = \varepsilon_\infty + \frac{(\varepsilon_S - \varepsilon_\infty)}{1 + i\omega\tau_D}$	—
	Cole-Cole	$\varepsilon^*(\omega) = \varepsilon_\infty + \frac{(\varepsilon_S - \varepsilon_\infty)}{1 + (i\omega\tau_{CC})^{\alpha}}$	$0 < \alpha \leq 1$
	Cole-Davidson	$\varepsilon^*(\omega) = \varepsilon_\infty + \frac{(\varepsilon_S - \varepsilon_\infty)}{1 + (i\omega\tau_{CD})^{\beta}}$	$0 < \beta \leq 1$
	Havriliak-Negami	$\varepsilon^*(\omega) = \varepsilon_\infty + \frac{(\varepsilon_S - \varepsilon_\infty)}{[1 + (i\omega\tau_{HN})^{\alpha}]^{\beta}}$	$0 < \alpha, \quad \alpha\beta \leq 1$

Note: The parameter α quantifies the symmetrical and β the asymmetrical broadening of the relaxation function.

Alternative representations of the dielectric properties of a material are the complex conductivity $\sigma^*(\omega)$ or the complex electric modulus M^*. They emphasize different aspects of polarization and charge transport in a material as discussed below.

In similarity to the Ohm's law:

$$j = \sigma^* E \tag{4.45}$$

gives the relationship between the electric field and the current density (j) where $\sigma^*(\omega) = \sigma'(\omega) + i\sigma''(\omega)$ is the complex **electric conductivity**. $\sigma'$and σ'' are the corresponding real and imaginary parts. Because the current density and the time derivative of the dielectric displacement are equivalent quantities it holds $\sigma^* = i\omega\varepsilon_0\varepsilon^*$.

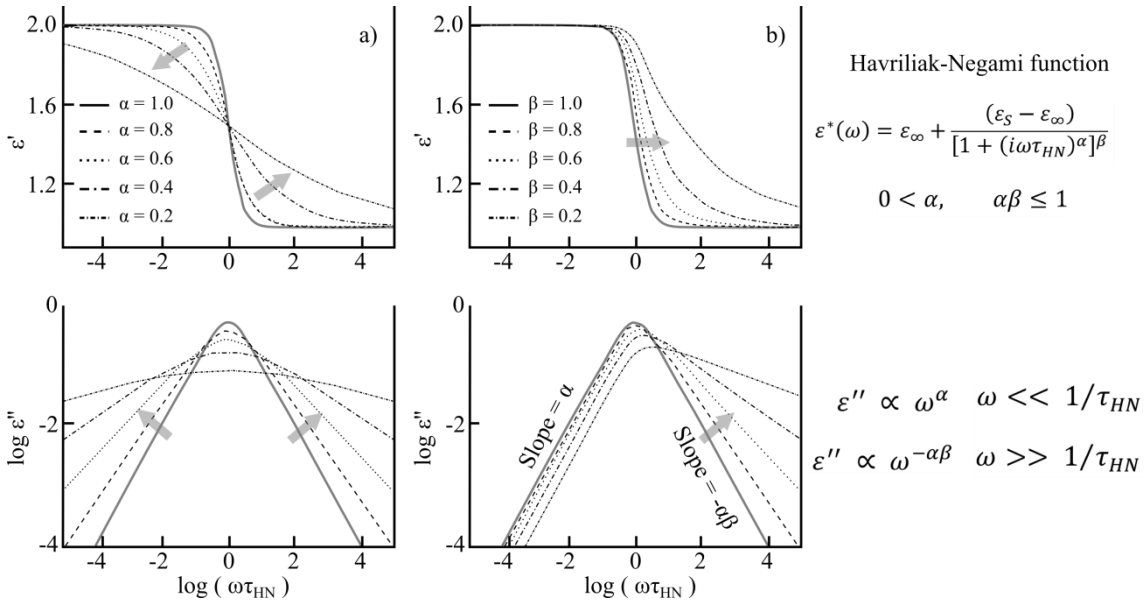

Figure 4.9. Complex dielectric permittivity for the Havriliak-Negami function with fixed: a) $\beta = 1$; b) α ($\tau_{HN} = 1s,\ \Delta\varepsilon = 1,\ \varepsilon_\infty = 1$) [3].

Many dielectrics possess conductivity due to motion of charges and such conductivity is normally expressed by a volume conductivity. The motion of charges in the dielectric gives rise to the conduction current and additionally polarizes the dielectric. The conductivity may therefore be visualized as contributing to the dielectric loss. The loss factor is expressed as:

$$\varepsilon'' = \varepsilon''(\omega) + \frac{\sigma}{\omega\varepsilon_0} \tag{4.46}$$

On the basis of experimentally observed similarity of the $\omega - \varepsilon''$ curves for a large number of polymers, Jonscher proposed an empirical "Universal Law" which is supposed to apply to all dielectrics in the condensed phase being denoted the exponents at low frequency and high frequency as *m* and *n* respectively:

$$\sigma(\omega) = \sigma_{dc} + A\omega^n \tag{4.47}$$

where the exponent is observed to be within $0.6 \leq n \leq 1$ for most materials. The exponent either remains constant or decreases slightly with increasing temperature and the range mentioned is believed to suggest hopping of charge carriers between traps. The real part of the dielectric constant also increases due to conductivity. A relatively

small increase in ε' at low frequencies or high temperatures is possibly due to the hopping charge carriers and a much larger increase is attributed to the interfacial polarization due to space charge. For pure electronic conduction no contribution arises to ε' while ε'' increases linearly with decreasing frequency. σ_0 is the (electronic) d.c. conductivity. Thus, in the conductivity representation for electronic conduction the real part $\sigma'(\omega)$ is constant (σ_0) and the imaginary part σ'' increases linearly with frequency.

The dielectric properties for a electronic conduction can also be expressed in the modulus representation. It is similar to the imaginary part of $M^*(\omega)$ for a Debye-like relaxation process and peaks at $\omega_M \tau_{Cond} = 1$ with $\tau_{Cond} = \varepsilon_0 \varepsilon_\infty / \sigma_0$. Therefore from the position of maximum loss ω_M the d.c. conductivity can be estimated. The corresponding real part of the modulus increases from zero to $M_\infty = 1/\varepsilon_\infty$. The related modulus is called **electric modulus** $M(t)$ in the time domain and complex electric modulus $M^*(\omega) = M'(\omega) + iM''(\omega)$ in the frequency domain where M' and M'' denote corresponding real and imaginary parts (Figure 4.10a). In case of a dominating conductivity contribution the data may be represented in $\varepsilon^*(\omega)$, $\sigma^*(\omega)$, or $M^*(\omega)$. From fits based on a random free-energy barrier model as developed by Dyre the direct current (dc) conductivity and the electrical relaxation time can be deduced. The random free energy barrier model, developed by Dyre [28], assumes that conduction takes place by hopping of charge, where the hopping charge carriers are subject to spatially randomly varying energy barriers.

One of the most characteristic properties of electrical conduction in disordered solids is a strong dispersion of the conductivity with respect to frequency and temperature, $\sigma(\omega, T)$. At low frequencies one observes a constant conductivity while at higher frequencies the conductivity becomes strongly frequency dependent. Disordered solids show similar behavior with respect to their ac properties, not only for the frequency dependence of the conductivity but also for the temperature dependence. For the real part $\sigma'(\omega)$ on the low frequency side a plateau vale is obtained which can be extrapoled to the d.c. conductivity σ_0 for $\omega \rightarrow 0$. At a critical frequency $\omega_c = 2\pi\nu_c$ the dispersion of σ' sets in (Figure 4.10b). The imaginary part of the complex conductivity $\sigma''(\omega)$ increases with increasing frequency (Figure 4.10c). The increase at low frequencies

indicates electrode polarization. Moreover, it can be observed a strongly temperature-dependent (usually Arrhenius) dc conductivity, while the ac conductivity depends much less on temperature and becomes almost temperature independent as $T \rightarrow 0$.

In disordered systems the charge transport takes place due to hopping conduction. Moreover the motion of a charge in these systems is accompanied by an electrical relaxation: an ionic or electronic charge is surrounded by negative or positive counter charges.

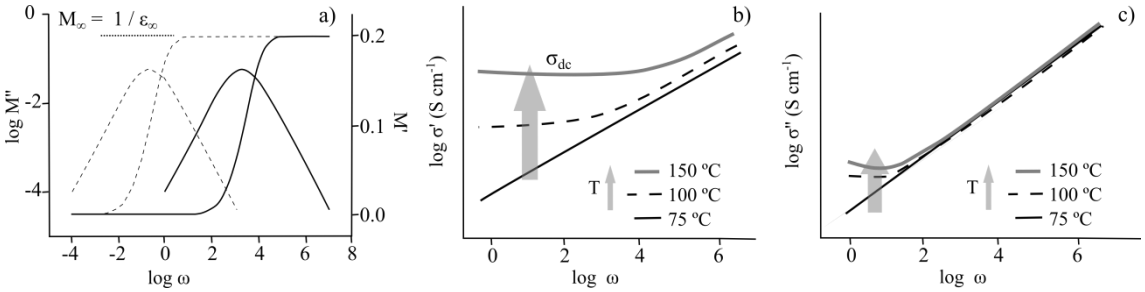

Figure 4.10. Theoretical examples for a) the real part M' and imaginary part (M'') of the complex electric modulus with a pure ohmic contribution $\sigma_0/\varepsilon_0 = 1$ *(dashed line),* $\sigma_0/\varepsilon_0 = 10^4$ *(solid line),* b) real part of the conductivity (σ'), and c) Imaginary part of the conductivity (σ''), and

In this way, charge carriers can be blocked at inner dielectric boundary layers (Maxwell-Wagner-Sillars polarization) on a mesoscopic scale or at the external electrodes contacting the sample (electrode polarization) on a macroscopic scale. In both cases this leads to a separation of charges which gives rise to an additional contribution to the polarization. The charges may be separated over considerable distance. Therefore the contribution to the dielectric loss can be by orders of magnitude larger than the dielectric response due to molecular fluctuations. At the internal phase boundaries charges can be blocked which gives rise to a Maxwell-Wagner polarization.

Electrode polarization is an unwanted parasitic effect during a dielectric experiment because it can mask the dielectric response of the sample and influences the dielectric properties at low frequencies. Both the magnitude and the frequency position of electrode polarization depend on the conductivity of the sample and can result in extremely high values of the real and imaginary part of the complex dielectric function.

The molecular origin of that effect is the (partial) blocking of charge carriers at the sample/electrode interface. This leads to a separation of positive and negative charges which gives rise to an additional polarization.

In conclusion, experimental data by dielectric spectroscopy are regarded as a complex electrical impedance $Z^*(\omega)$, expressed in terms of the resistance, $R(\omega)$ and capacitance $C(\omega)$, which are frequency-dependent extensive properties (here $\omega = 2\pi f/Hz$ where f is the measuring frequency). The intensive complex dielectric quantities of dielectric permittivity $\varepsilon^*(\omega)$, electrical modulus $M^*(\omega)$, electrical conductivity $\sigma^*(\omega)$ and resistivity $\rho^*(\omega)$ are immediately derivable from $Z^*(\omega)$. Using one or another terminology has relevance depending on the information you want to share. Generally, represented in terms of ε^* and electric conduction behavior in term of σ^*, M^*, ρ^*or Z^*, and other terms. Specifically, in this chapter will be used the terms summarized in the scheme of Figure 4.11.

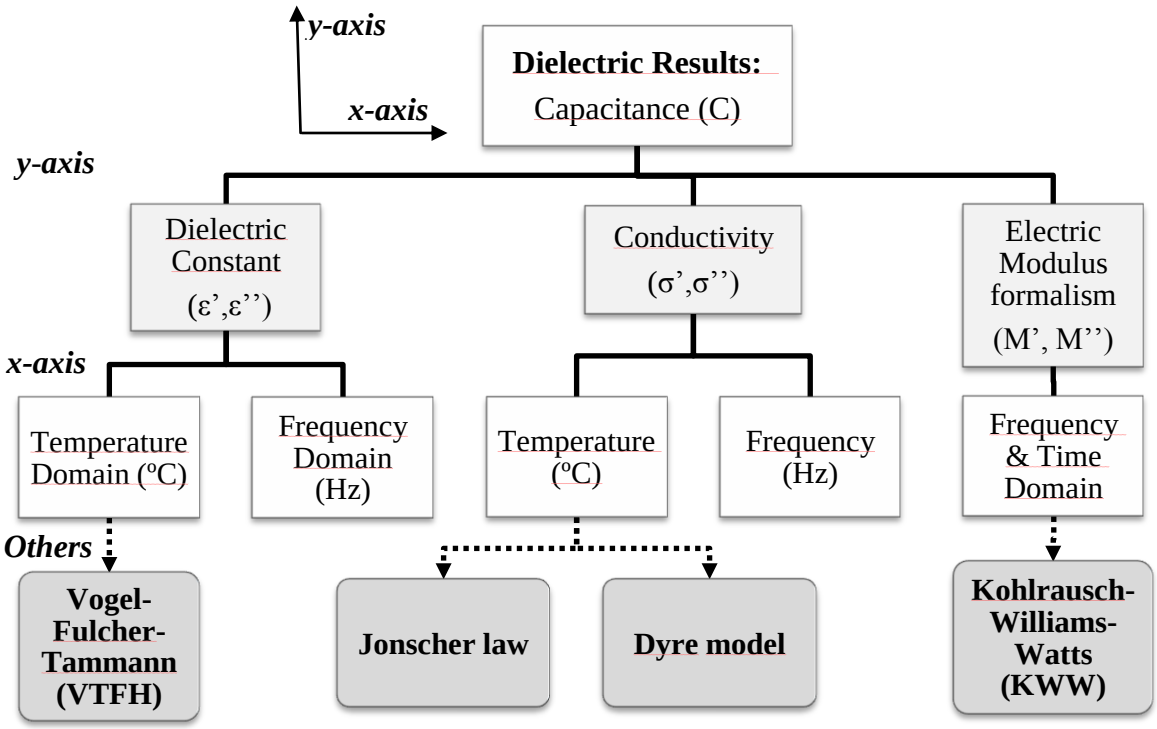

Figure 4.11. Scheme of the expressions used in the dielectric study.

4.2. EXPERIMENTAL

This section reports on the dielectric relaxation spectrum, electrical conductivity and electric modulus as a function of frequency and temperature of some of the different polyimide and copolyimides obtained in chapter 3 [29,30]. The synthesis of the polyimides was carried out by starting the reaction between the 4,4'- oxydiphthalic anhydride (ODPA) and two diamines, the 1,3-bis(3-aminophenoxy)bencene (diamine 0CN) and/or the 1,3-bis-2-cyano-3-(3-aminophenoxy) phenoxybenzene (diamine 2CN) [31,32]. Polyimides were synthesized using both single diamines (0CN diamine and diamine 2CN) and copolyimides by using the diamines in different proportions (Figure 4.12). As indicated in Chapter 3 the two-step procedure was used: a nucleophilic attack of amine groups toward carbonyl groups in the dianhydride produces the copoly(amic acid) (first step), and the subsequent cyclodehydration reaction caused by thermal treatment gives rise to the copolyimide (second step).

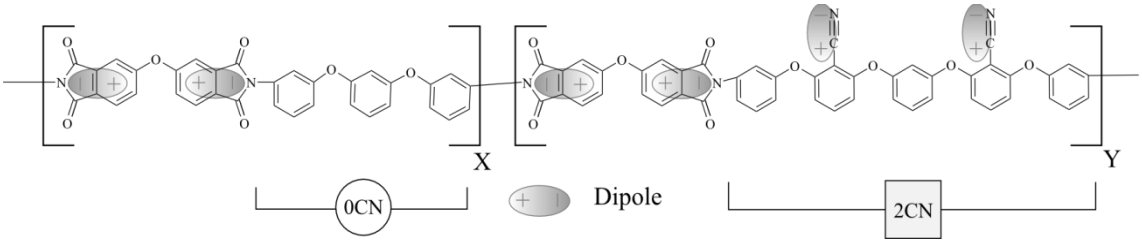

Figure 4.12. Scheme of the two repetitive units of the copolyimides with the polar groups.

Polymer 0CN, copolymer 0CN/2CN (60/40) and 0CN/2CN (50/50) and polymer 2CN were prepared and will be called hereafter 0CN, 0CN/2CN (60/40), 0CN/2CN (50/50) and 2CN, respectively. The results of the both copolymers are very similar and for this reason only will be shown the figures for copolymer 0CN/2CN (50/50).

4.3. RESULTS AND DISCUSSION

Dielectric spectroscopy measurements were carried out through the measurement of the capacitance (*C*) and the loss factor (*tan δ*). Circular gold electrodes (10 mm diameter) were deposited onto both sides of each sample, to form a parallel plate capacitor.

The isothermal experiments were performed from 25°C to 260°C (thermal stability: 0.5 °C) in 5°C steps. The complex dielectric permittivity $\varepsilon^* = \varepsilon' - i\varepsilon''$ was determined as a function of frequency (10^{-1}–10^7 Hz) through the following equations:

$$\varepsilon' = \frac{Cd}{\varepsilon_0 A} \qquad \text{and} \qquad \varepsilon'' = tan\delta * \varepsilon' \qquad (4.48)$$

where C is the capacitance, ε' is real part of the dielectric constant, ε'' is imaginary part of the dielectric constant, ε_0 is the permittivity of the free space ($8.85 \cdot 10^{-12}$ F·m^{-1}), and d and A are the sample thickness and electrode area, respectively.

4.3.1. OVERALL DIELECTRIC RESPONSE

The dielectric response will be discussed highlighting first the temperature dependent features and then the frequency dependent ones.

A. TEMPERATURE DEPENDENCE

Figures 4.13, 4.14 and 4.15 shows the evolution of real (ε') and imaginary parts (ε'') of the dielectric function as a function of temperature at different frequencies for the different samples. For all samples, the real part of the dielectric constant increases as frequency decreases in all temperature range due to the increasing inability of the dipoles to orient with the rapidly varying applied electric field as frequency increases [33]. The same tendency is found in the d.c. conductivity contribution to the imaginary

part of dielectric permittivity while the peak due to dipolar relaxation appearing in ε'' shifts to higher temperatures at increasing frequencies.

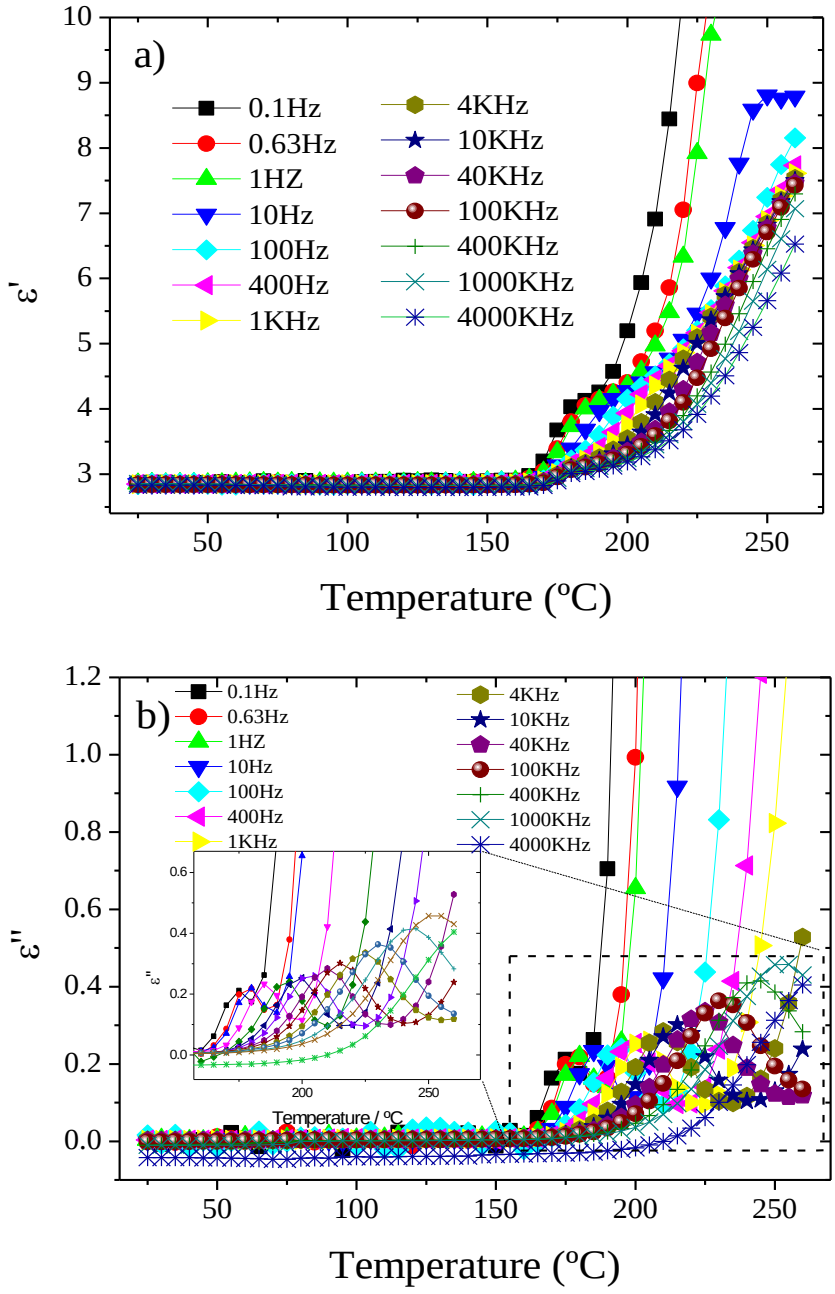

Figure 4.13. a) Real and b) imaginary part of the dielectric function as a function of temperature at different frequencies for 0CN.

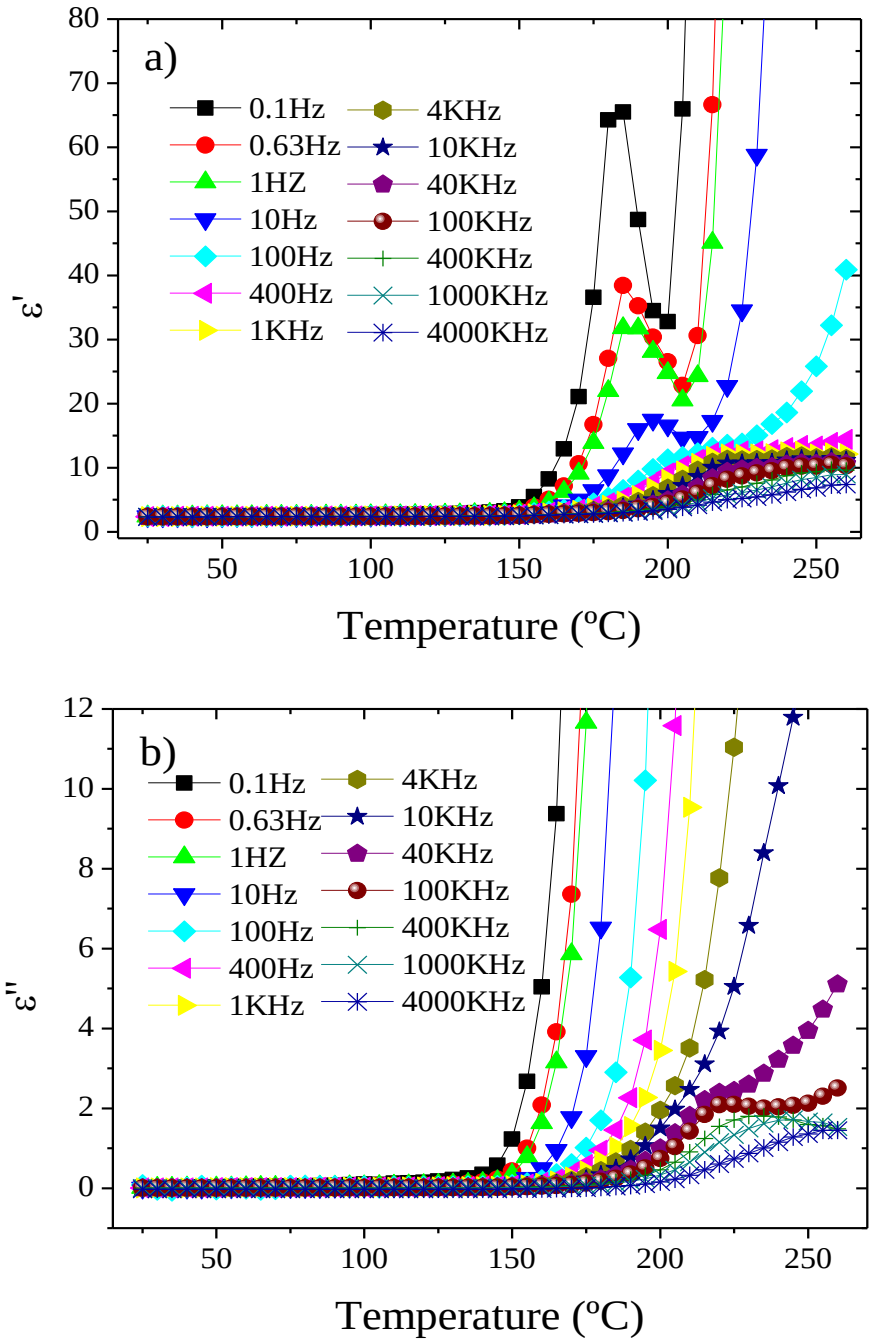

Figure 4.14. a) Real and b) imaginary part of the dielectric function as a function of temperature at different frequencies for 0CN/2CN (50/50).

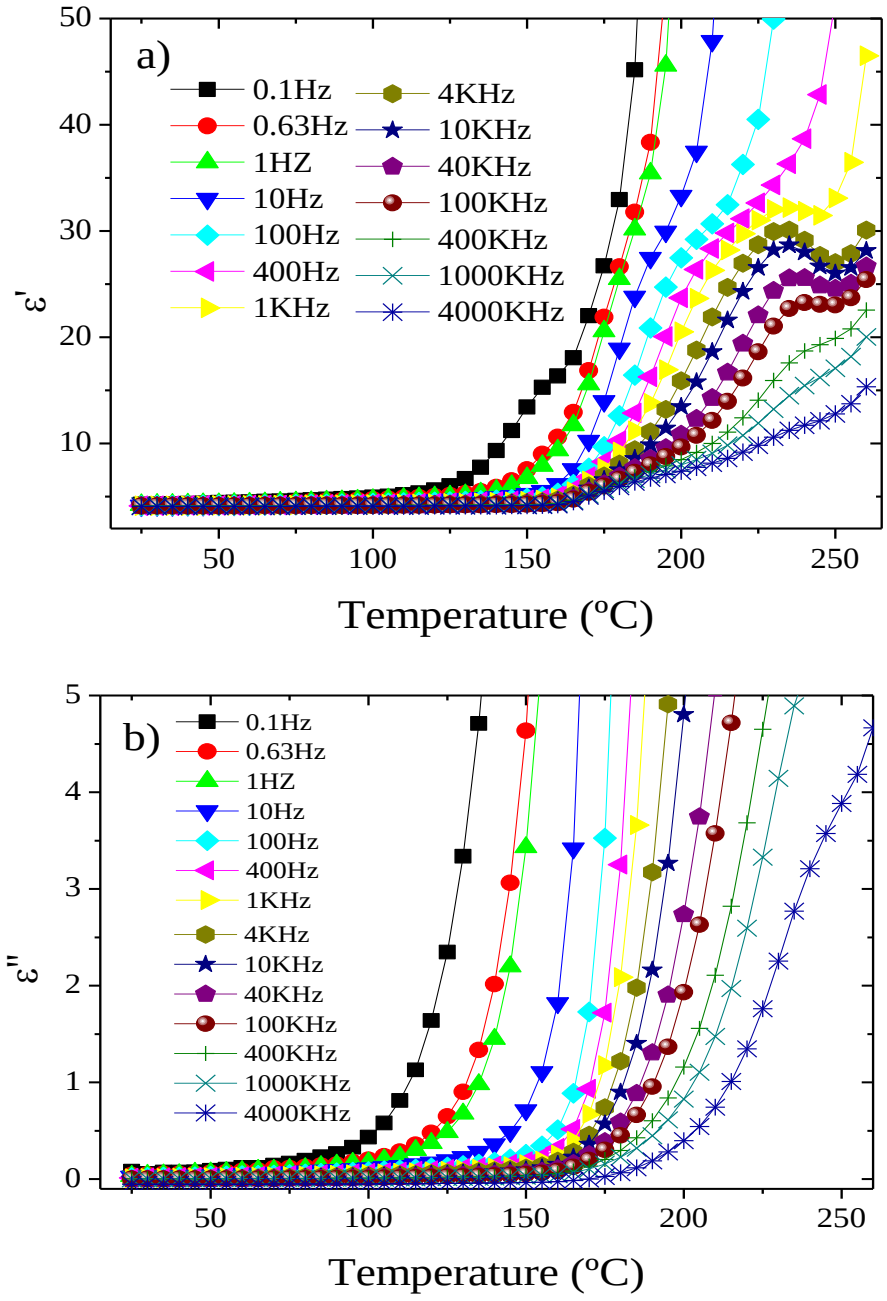

Figure 4.15. a) Real and b) imaginary part of the dielectric function as a function of temperature at different frequencies for 2CN.

The dielectric response is practically constant up to 150ºC for all samples, independently of the frequency. No significant differences are observed between the dielectric response of the 0CN/2CN (60/40) and 0CN/2CN (50/50) copolymer so just the data for the 50/50 copolymer are shown.

Figure 4.14a shows a low frequency peak (up to ~100 Hz) in the dielectric constant (around 175ºC) in the 0CN/2CN (50/50) copolymer. The presence of this peak in both copolymers is due to a decrease of the ionic mobility related to imidization of dianhydride groups [34]. This decrease cannot be attributed to a relaxation process, as it is characterized by a peak in the real part of the dielectric constant.

The room temperature values of the dielectric response are summarized in Table 4.2 for a frequency of 1 kHz, together with the values at 200ºC. The room temperature values are in agreement with the values found in the literature for other polyimides [35]. The differences observed in the dielectric constant for the 0CN and 2CN polymers at room temperature are fully attributed to the presence of nitrile groups in the 2CN polymer.

Table 4.2. Dielectric constant for the samples at 1kHz.

Sample	**T= 25ºC**		**T= 200ºC**	
	$\boldsymbol{\varepsilon'}$	$\boldsymbol{\varepsilon''}$	$\boldsymbol{\varepsilon'}$	$\boldsymbol{\varepsilon''}$
0CN	2.8	0.003	3.8	0.30
0CN/2CN (60/40)	3.0	0.009	8.0	3.5
0CN/2CN (50/50)	2.4	0.006	8.0	3.5
2CN	4.1	0.007	21	17

For temperatures above 150ºC and for all samples, the dielectric constant increases with increasing temperature due to enhancement of the dipolar mobility and increased conductivity, i.e. dielectric losses (Figures 4.13b, 4.14b and 4.15b), as reflected in the comparison of the values of the dielectric response at room temperature and 200ºC presented in Table 4.2.

The insert of Figure 4.13b) for the 0CN polymer shows the α-relaxation above 150ºC related to the glass transition and attributed to the cooperative segmental motions of the amorphous sample [3].

The dynamics of the α-relaxation observed in the 0CN polymer (Figure 4.13b) was analyzed in the scope of the Vogel-Fulcher-Tammann (VTFH) formalism [36–38]:

$$\tau(T) = \tau_0 e^{\frac{E_{VFTH}}{k_B(T-T_0)}} \tag{4.49}$$

where τ is the relaxation time, E_{VFTH} is the VFTH energy (1 eV = 1.602176565·10^{-19} J), k_B the Boltzmann constant (1.38064852·10^{-23} J·K^{-1} = 8.6173324·10^{-5} eV·K^{-1}) and T_0 is the critical temperature at which molecular motions become infinitely slow [39].

From the obtained VTFH fitting parameters (E_{VFTH}, τ_0 and T_0 are obtained by fitting Eq. 4.49 to experimental data), the fragility parameter (m) [30,40,41] can be calculated:

$$m = \frac{E_{VTFH}/kT_g}{(\ln 10)\left(1 - T_0/T_g\right)^2} \tag{4.50}$$

where m is an indication of the steepness of the variation of the material properties (viscosity, relaxation time, …) as T_g is reached. A high m value defines a fragile material whereas a strong material is characterized by small m values [42].

The $m(T_g)$ value calculated with the VTF parameters was determined at the glass transition temperature (T_g) where the relaxation time is equal to 100 s.

The α-relaxation observed for the 0CN polymer was thus obtained from the fitting with equation (4.49) and is shown in Figure 4.16. The obtained fitting parameters are shown in Table 4.3.

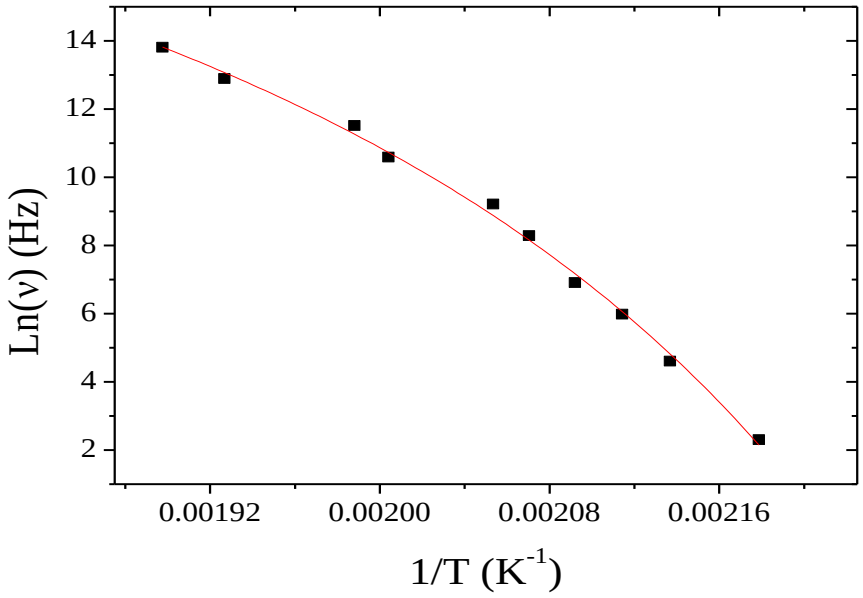

Figure 4.16. VFTH fitting for the α-relaxation of 0CN polymer

Table 4.3. VFTH fitting parameters of the α-relaxation of the 0CN polymer

Sample	τ_0 (s)	E_{VFT} (eV)	T_0 (K)	T_g (K)	m
0CN	5.1×10^{-12}	0.15	387	443	105

The results shown in Table 4.3 indicate that the cooperative motions of the amorphous chains ($\tau_0$value) are very slow and with high VFTH energy. The glass transition temperature determined through this formulation is very similar to the value determined by DSC technique (T_0= 449K = 176ºC) [43]. The fragility parameter for the 0CN polymer is equal to the one observed for the semi crystalline polymer α-PVDF [30]. T_0 is typically defined as the real glass transition temperature, which is found to be (30-70ºC) below the measured T_g. For 0CN polymer, T_0 is below T_g and the difference between both temperatures is 329K (56ºC) [3]. For 2CN polymer and the respective copolymers, the α-relaxation is not detected due to the overlapping of the electric conductivity contributions, particularly high at high temperatures and low frequencies.

B. FREQUENCY DEPENDENCE

In the frequency domain representation (Figure 4.17), ε'' versus frequency at isothermal conditions is used for the identification of the dipolar relaxations. Amorphous polymers show different motional processes as it can be seen as peaks in the ε'' versus ν graphical representations (Figure 4.15).

Figures 4.17 and 4.18 show the imaginary part of the dielectric function for the different samples. For the 0CN polymer (Figure 4.17a) the α-relaxation is clearly identified. A detailed representation of this relaxation is represented in Figure 4.17b (above 195ºC), where it is observed that as the temperature increases, the α-relaxation is shifted to higher frequencies. This relaxation is related to a long timescale and corresponds to an overall structure rearrangement of the system [44].

For the 0CN polymer (Figure 4.17a) and for low frequencies and temperatures below 195ºC, the conductivity contribution in the frequency domain is prominent, being this contribution the main one for the rest of the samples (Figures 4.18a-b). The α-relaxation is not resolved in the copolymers and the 2CN polymer due to the overlapping of dielectric relaxation and conductivity contributions. The conductivity contribution decreases with decreasing temperature, being larger for low frequencies. Further, it can be stated an increase of the conductivity associated to the addition of the nitrile (-CN) dipolar group.

As it will also be shown later, the conductivity effect contributes to the increase of the dielectric loss in all samples (Figures 4.17 and 4.18), which is also influenced by the Maxwell-Wagner-Sillars process. The charges can be blocked at internal phase boundaries, related to the different constitutents of the copolymers, submicropores or at the interface between the sample and the electrodes (electrode or space charge polarization) [45].

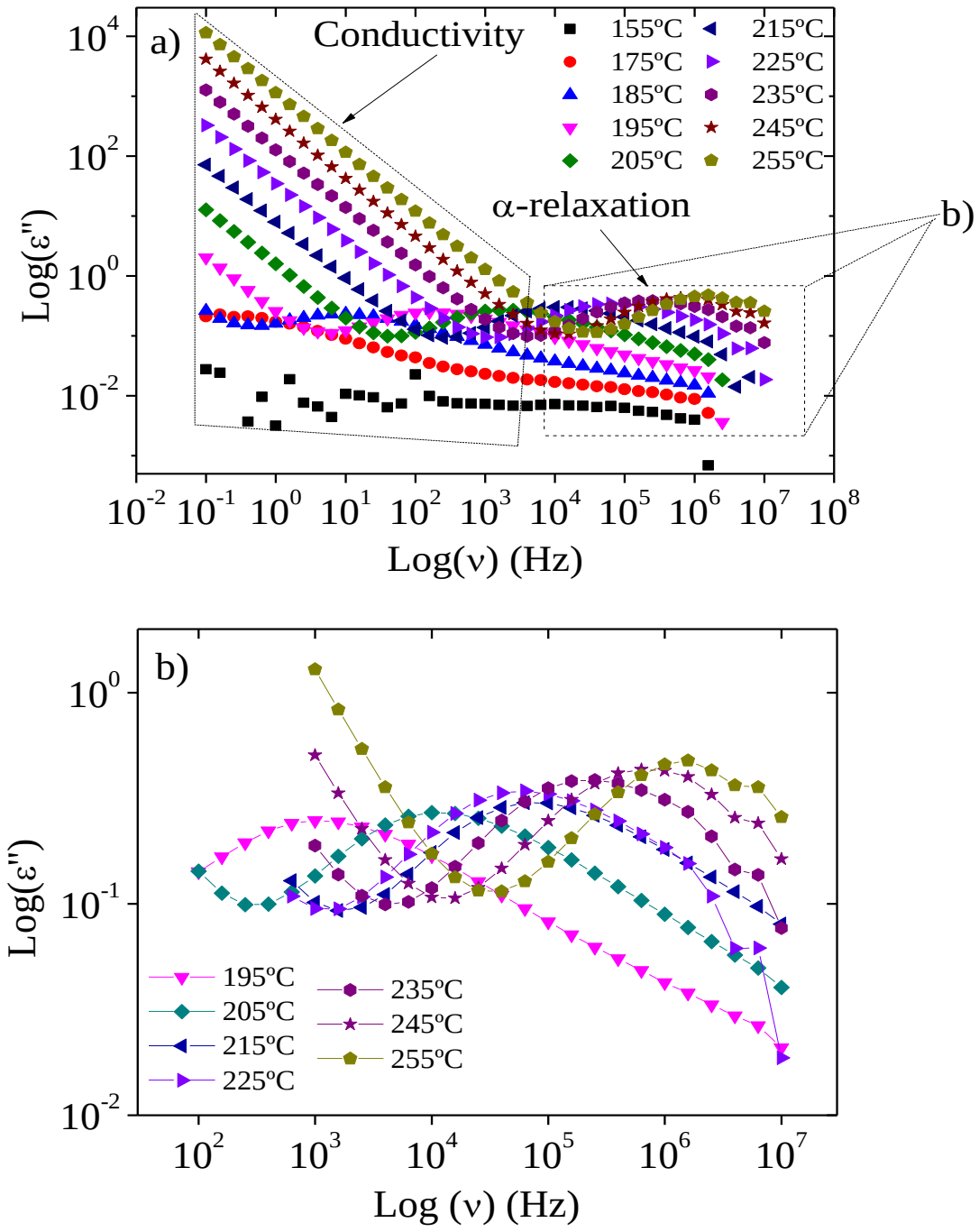

Figure 4.17. Frequency dependence of the imaginary part of the dielectric function of a) 0CN at various temperatures and b) details of the α-relaxation in 0CN.

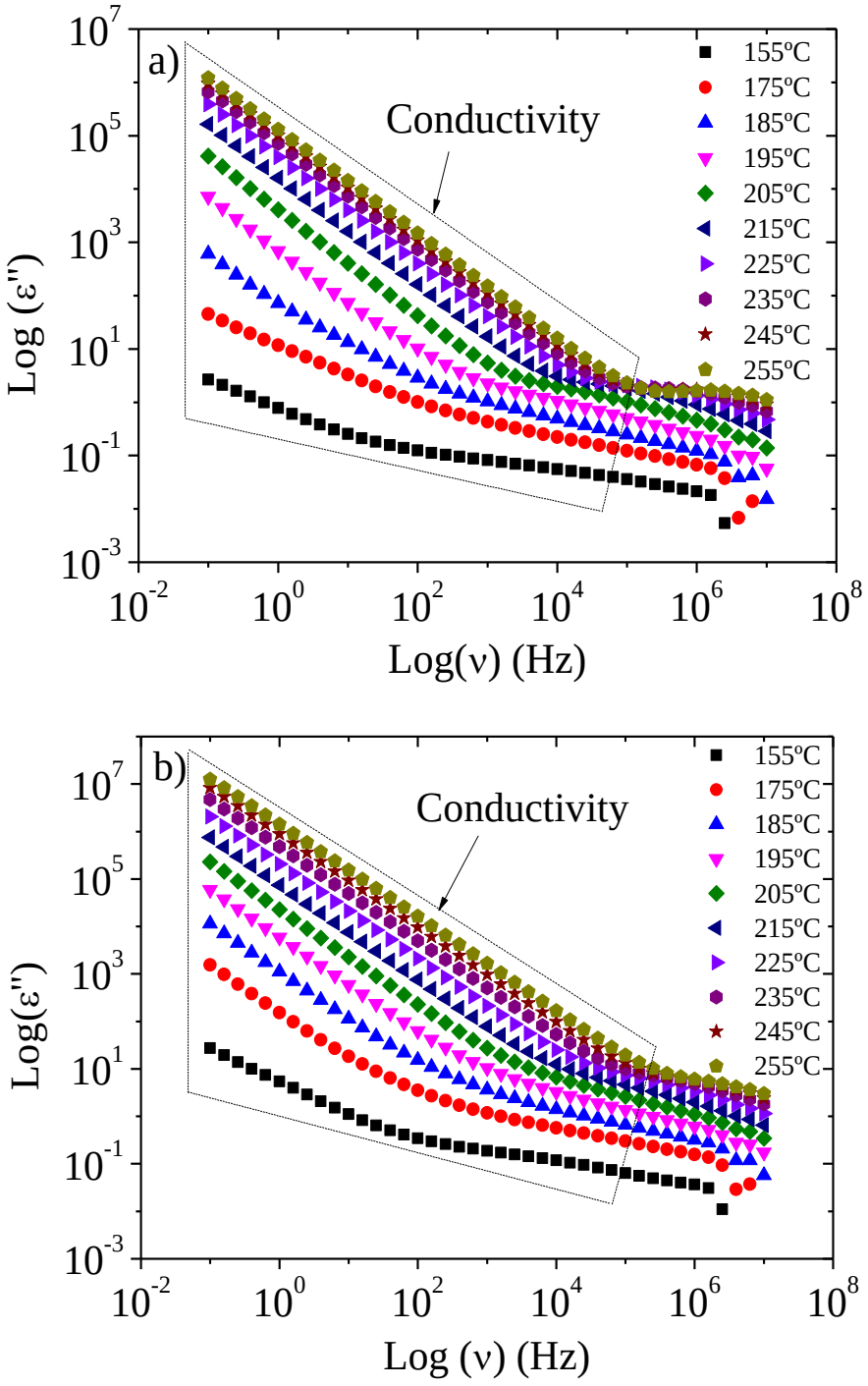

Figure 4.18. Frequency dependence of the imaginary part of the dielectric function of a) 0CN/2CN (50/50) and b) 2CN at various temperatures.

4.3.2. OVERALL CONDUCTIVITY

In order to further explain relaxation dynamics of charge carriers and the characteristics of the ionic conduction with certain influence of a MWS process, it is more appropriate the representation of frequency and temperature dependence of complex conductivity, σ^*, which can be calculated from the dielectric function through the following equation:

$$\sigma^* = i\varepsilon_0\omega\varepsilon^*(\omega) = i\varepsilon_0\omega\big(\varepsilon'(\omega) - \varepsilon''(\omega)\big) = \varepsilon_0\omega\varepsilon''(\omega) + i\varepsilon_0\omega\varepsilon'(\omega) \quad (4.51)$$

Thus, the real part of the conductivity is given by:

$$\sigma'(\omega) = \varepsilon_0\omega\varepsilon''(\omega) \quad (4.52)$$

and the imaginary part of the conductivity is given by:

$$\sigma''(\omega) = \varepsilon_0\omega\varepsilon'(\omega) \quad (4.53)$$

where ε_0 ($8.85\text{x}10^{-12}$ $\text{F}\cdot\text{m}^{-1}$) is the permittivity of free space and $\omega = 2\pi f$ is the angular frequency.

The real and imaginary parts on the complex electrical conductivity, $\sigma^*(\omega)$, are plotted in Figures 4.19 , 4.20 and 4.21 as a function of frequency for several temperatures.

For all samples it is observed two well identified regimes which are dependant of the temperature and frequency. For low temperatures up to T=135ºC, the conductivity increases rapidly with increasing frequency. For temperatures above T=185ºC, it is observed a plateau, in which the conductivity (Figures 4.19a, 4.20a and 4.21a) is nearly independent of frequency in the low frequency region, being this regime thus dominated by the dc conductivity.

At higher frequencies and temperatures a power law dependence of the ac electrical conductivity is observed, which is related to hopping transport of localized charge carriers [46]. The electrical conductivity is larger for the samples with larger CN content. There are also found deviations from a pure plateau region in the low frequency conductivity spectrum that can be attributed to electrode polarization effects and to the charge blocking at the interphase regions as well as the imperfections (i.e.

submicropores due to the solvent evaporation process) that occur as consequence of the polymer processing method.

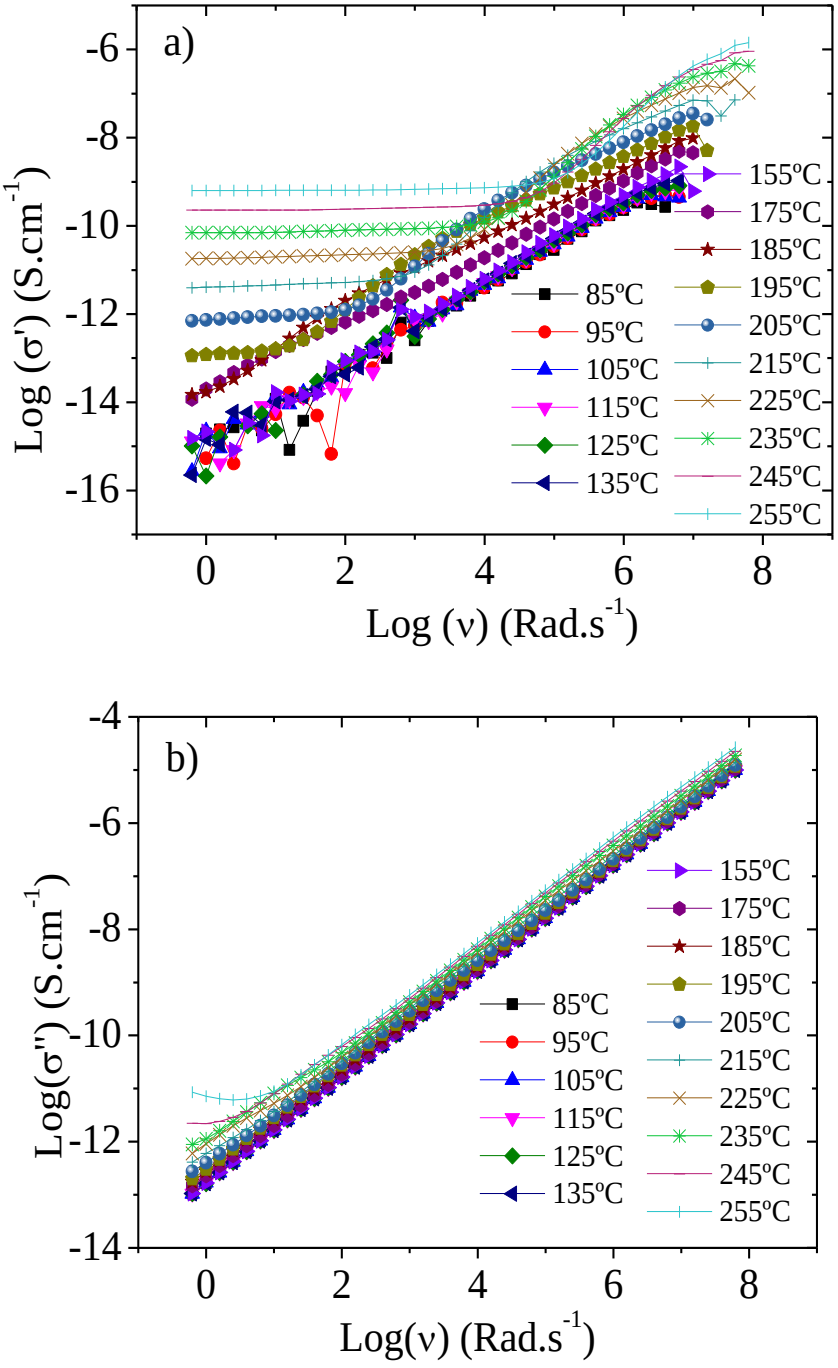

Figure 4.19. a) Real and b) imaginary parts of the electrical conductivity of 0CN/2CN (50/50) as a function of frequency at different temperatures.

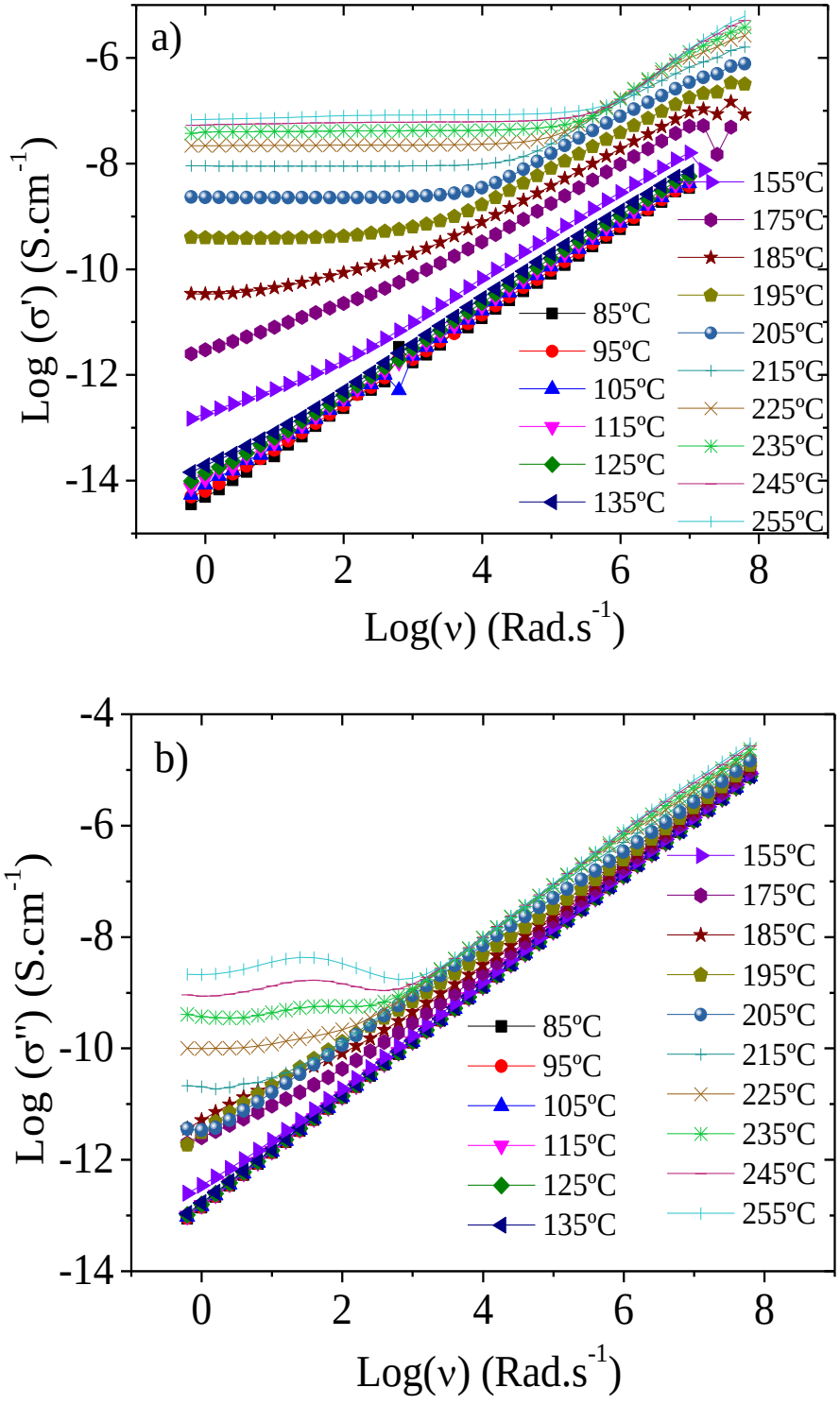

Figure 4.20. a) Real and b) imaginary parts of the electrical conductivity of 0CN as a function of frequency at different temperatures.

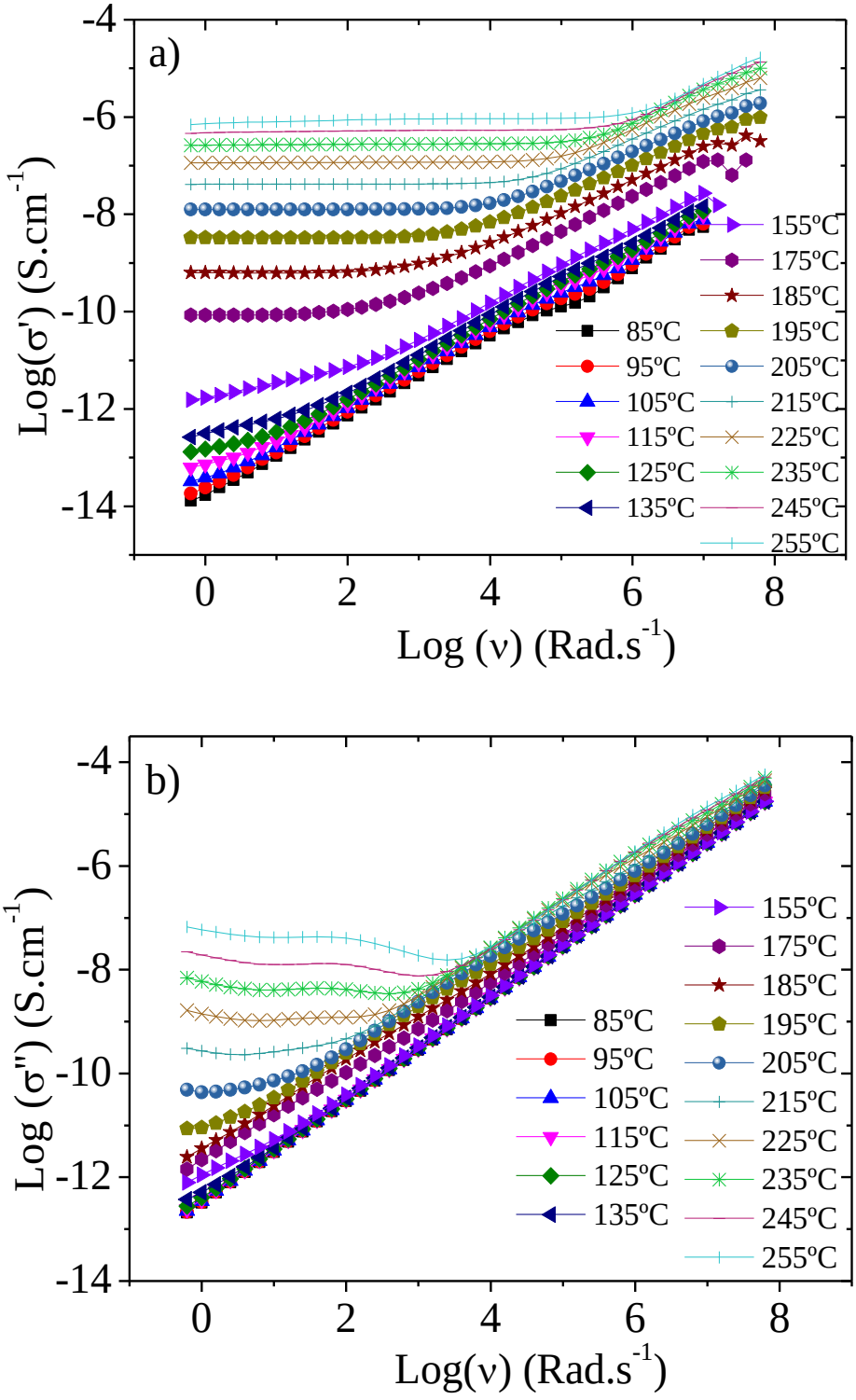

Figure 4.21. a) Real and b) imaginary parts of the electrical conductivity of 2CN as a function of frequency at different temperatures.

This behaviour can be thus ascribed to contribution of MWS and then at still higher frequencies dipolar relaxation modes. It is evident that 2CN polymer (Figure 4.21a) and the copolymers (Figure 4.20a) show higher conductivity due of the presence of the nitrile groups in the polymer chain in comparison to the 0CN polymer (Figure 4.19a).

The presence of the nitrile group affects also the MWS relaxation that is related to the existence and blocking of free charge carriers inside the system. The MWS relaxation becomes increasingly important at high temperatures, reflecting the enhancement of the mobility of charge carriers.

The ac conductivity at constant temperature as a function of frequency can be expressed as [47]:

$$\sigma'(\omega) = \sigma_{dc} + A\omega^n \tag{4.54}$$

where σ_{dc} is the DC conductivity, *A* is the pre-exponential factor and *n* is the fractional exponent $(0 < n < 1)$ that depends on temperature. The value of *n* is used to a better understanding of the conduction or relaxation mechanism in insulating materials [48].

Figure 4.22 left shows that σ_{dc} increases with increasing temperature in a similar way for all samples. This behavior reflects the mechanism of charge transport of carriers. There are not significant differences in values or behavior for the two copolymers, the values of the conductivity being intermediate between the ones obtained for the pure polymers. With respect to the two homopolymers, 2CN polymer shows higher σ_{dc} than 0CN polymer in all temperature range, attributed to the presence of the nitrile group.

In relation to the *n* parameter, it decreases with increasing temperature until 227ºC for all polyimide films. Independently of the sample type, the *n* parameter extends between 0.6 and 0.9, as corresponds to a hopping conductivity process (Figure 4.22 right) [49].

In this way, the transport mechanism of the samples is thermally activated hopping across an energy barrier. For the evaluation of the dependence of the ac conductivity with temperature at different frequencies, the Dyre model [50] (random free energy barrier model or symmetric model) was applied [28]:

$$\sigma(T) = Be^{\frac{E_a}{K_B T}} \tag{4.55}$$

where B is a pre-exponential factor identified as the attempt frequency, E_a is the activation energy of the process, T is temperature and k_B is the Boltzmann constant.

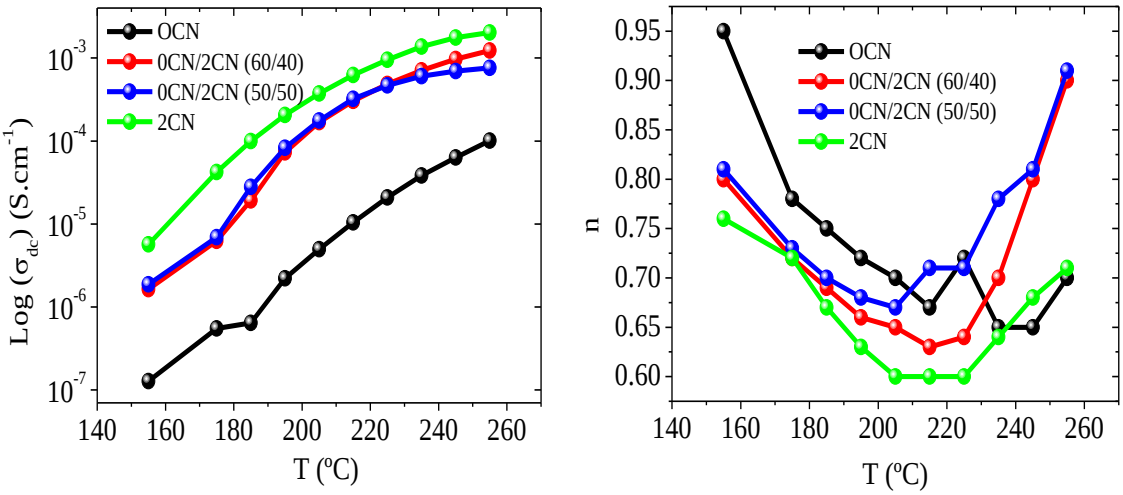

Figure 4.22. σ_{dc} (left) and n (right) as a function of temperature for the different samples.

The application of the Dyre model in order to obtain the dependence of the electrical conductivity on the reciprocal temperature at different frequencies is shown in Figure 4.23 and the activation energy, E_a, calculated are plotted in Figure 4.23 also.

Figure 4.23 shows the ac conductivity for the 0CN polymer (Figure 4.23a), with noteworthy differences from the rest of polymers in both temperature dependence behaviour (Figures 4.23b and 4.23c) and activation energy (Figure 4.24)

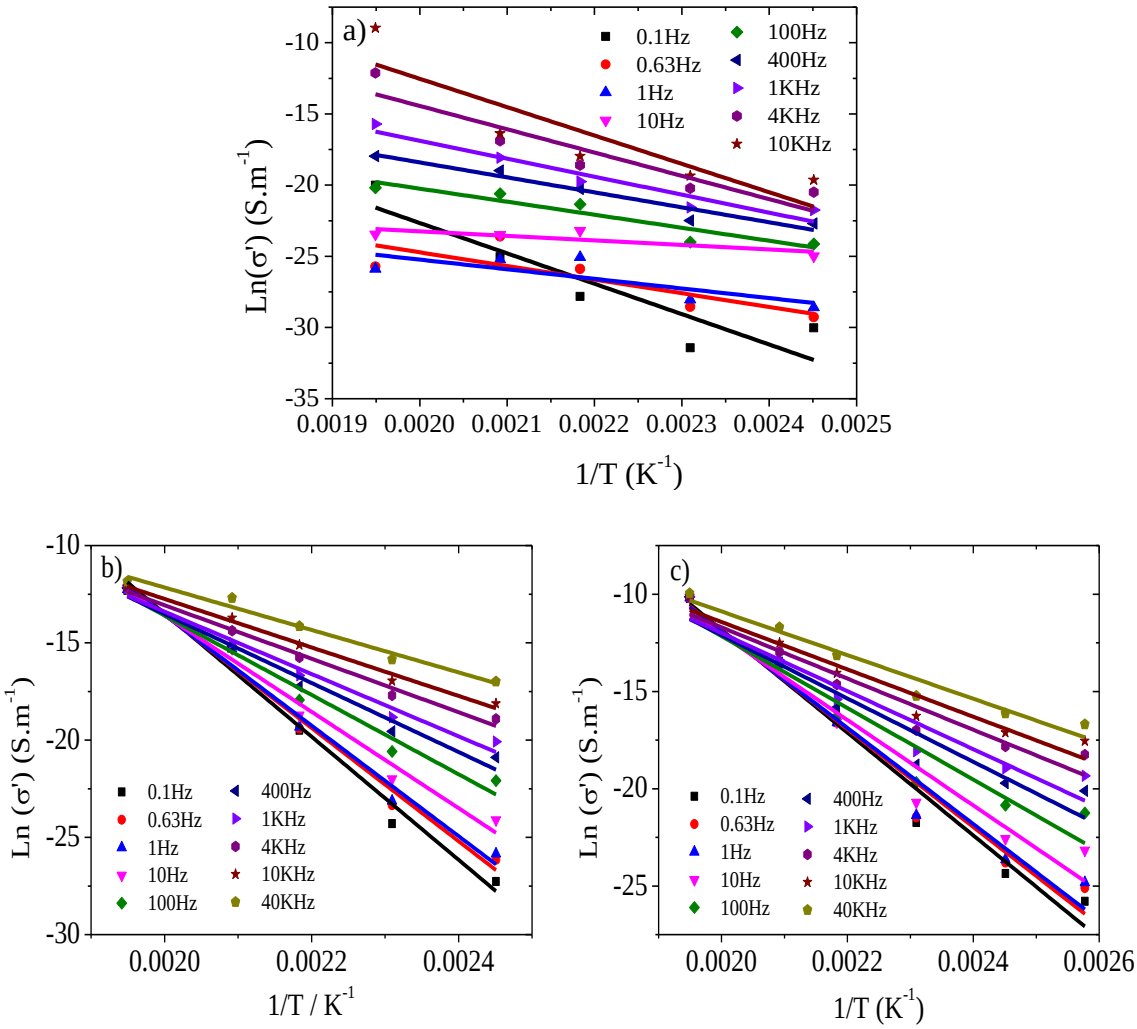

Figure 4.23. Fitting of the electrical conductivity as a function of inverse temperature with the Dyre model: a) 0CN, b) 0CN/2CN (50/50) and c) 2CN.

It can be observed that for the copolymers and the 2CN polymer, the activation energy is larger (with the exception of the higher frequencies) and decrease with increasing of the frequencies. This fact is linked to the mobility of nitrile groups, determining the electrical response of these samples. The activation energy for 0CN polymer shows a strong decrease at low frequencies with respect to the other samples, increasing for frequencies above 10 Hz. This variation can be ascribed to the presence of free charges contributing to the MWS relaxation processes, as will be shown in the next section.

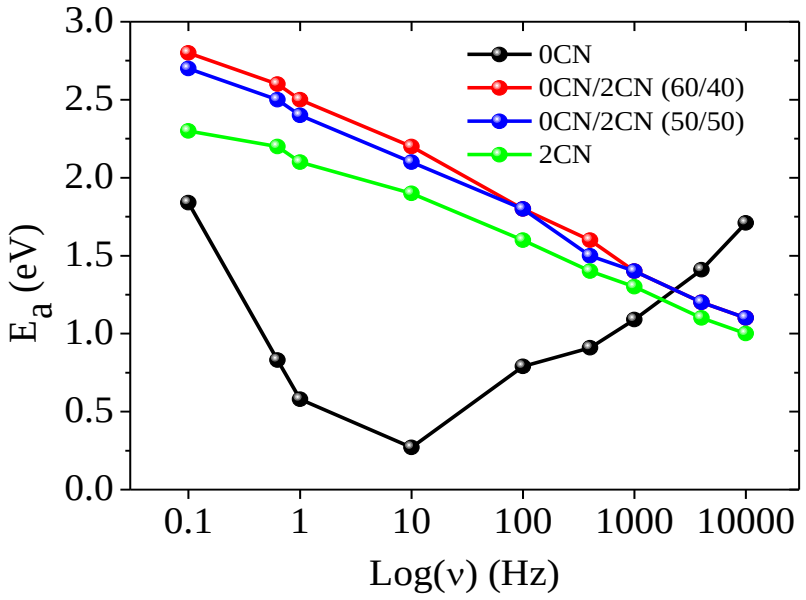

Figure 4.24. Evolution of the activation energy as a function of frequency for the different samples.

4.3.3. ELECTRIC MODULUS FORMALISM

In order to further explore the conduction behaviour (ionic conductivity and interfacial polarization, the so-called Maxwell-Wagner-Sillars (MWS) effect), the electric modulus formalism, M^* [51], is the most appropriate representation and can be used for differentiate dielectric relaxation processes from long-range conductivity [52]. Typically, for samples with higher conductivity, a high peak related to the conductivity is detected in the frequency spectra of the imaginary electric modulus formalism, M'', in the same temperature interval where the conductivity process is shown in the imaginary part of the dielectric function (ε').

The electrical modulus, M^*, is defined as the reciprocal of the complex relative permittivity, $\varepsilon^*(\omega)$:

$$M^*(\omega) = \frac{1}{\varepsilon^*(\omega)} = M'(\omega) + iM''(\omega) = \frac{\varepsilon'(\omega)}{\varepsilon'^2(\omega) + \varepsilon''^2(\omega)} + i\frac{\varepsilon''(\omega)}{\varepsilon'^2(\omega) + \varepsilon''^2(\omega)} \quad (4.56)$$

where M', M'' are the real and imaginary components of the complex electric modulus, respectively.

For a dipolar relaxation process, equation (4.56) yields a relaxation peak in M'' and a drop of M' with decreasing frequency. On the other hand for a pure d.c. conduction process in which ε' is independent of frequency and ε'' is inversely proportional to frequency, equation (4.56) yields the same frequency dependence than in a Debye single relaxation time process. The imaginary component of dielectric modulus can be used to define a relaxation time for conductivity.

$$M'' = M_\infty \frac{\omega\tau_{Cond}}{1 + (\omega\tau_{Cond})^2} \tag{4.57}$$

MWS processes also yield narrow relaxation processes in electric modulus formalism while exhibit a clear increase of ε' with decreasing frequency.

Deviations with respect to the Debye single relaxation time model in the electric field relaxation due to motions of charge carriers are generally described by the empirical Kohlrausch-Williams-Watts (KWW) function in the time domain [53,54]:

$$M^*_{\beta KWW}(\omega) = M_\infty\left[1 - \int_0^\infty exp(i\omega t)\,(-d\varphi/dt)dt\right] \tag{4.58}$$

with

$$\varphi(t) = exp\left[-(t/\tau_{KWW})^\beta\right], \quad 0 < \beta \leq 1 \tag{4.59}$$

where τ_{KWW} and β are the conductivity relaxation time and the Kohlrauch exponent, respectively. The smaller the value of β, the larger the deviation of the relaxation with respect to a Debye-type relaxation ($\beta = 1$).

Values of the Kohlrauch exponential parameter β in the KWW function were approximately estimated by means of [55]:

$$\beta = {}^{1.14}/_{w} \tag{4.60}$$

where w is the peak's full width at half maximum.

The temperature dependence of the real M' and imaginary M'' electric modulus for various frequencies is shown in Figures 4.25, 4.26 and 4.27 for all samples.

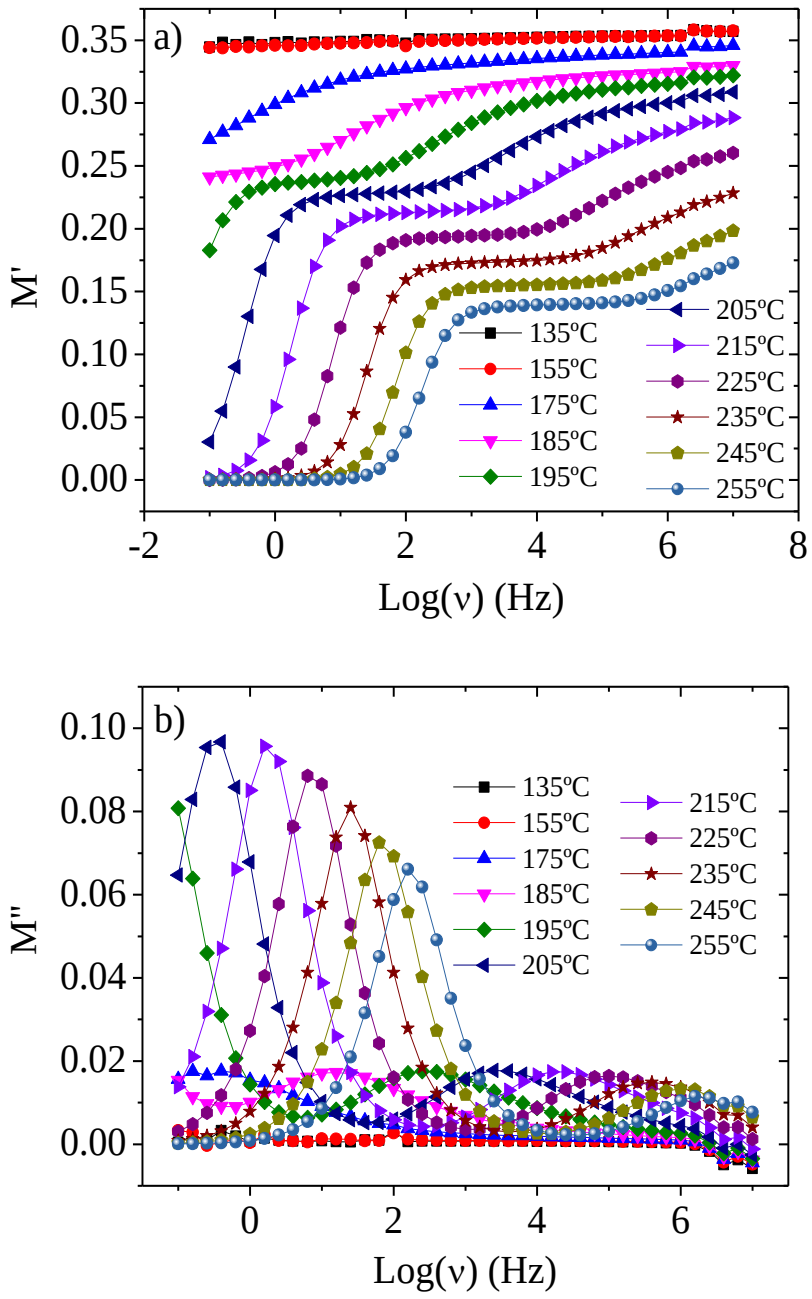

Figure 4.25. a) Real and b) imaginary parts of the electric modulus of 0CN as function of frequency at different temperatures.

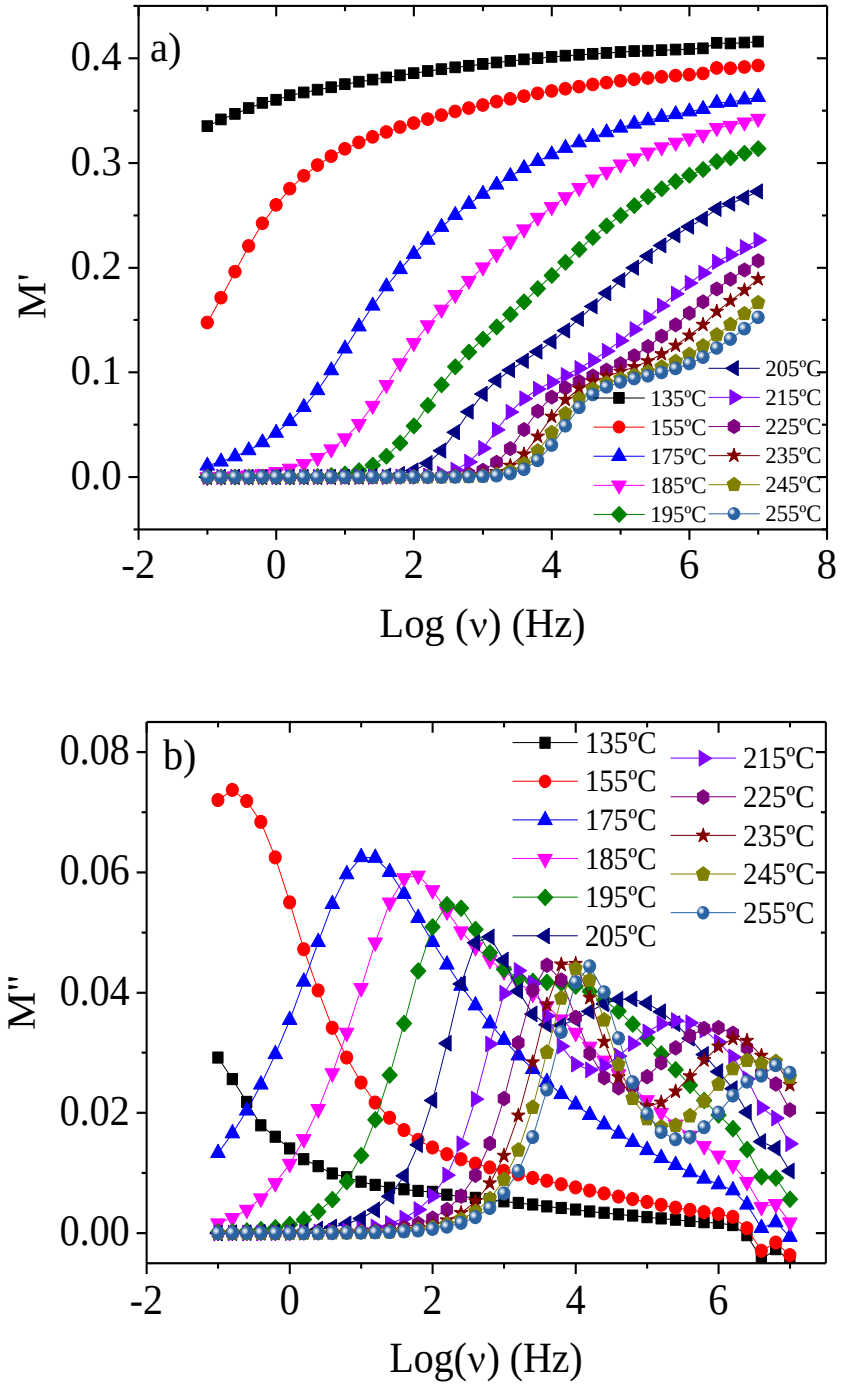

Figure 4.26. a) Real and b) imaginary parts of the electric modulus of 0CN/2CN (50/50) as function of frequency at different temperatures.

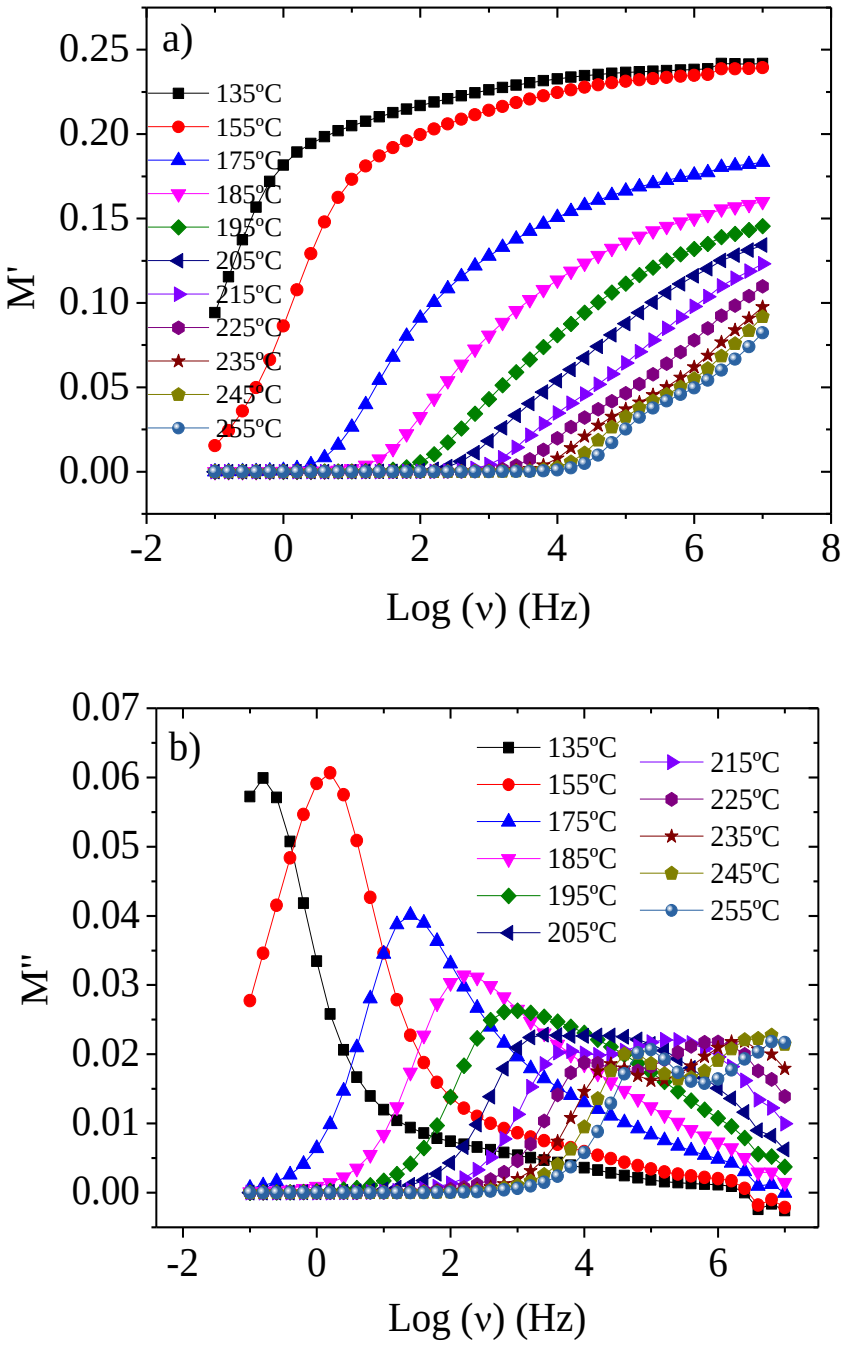

Figure 4.27. a) Real and b) imaginary parts of the electric modulus of 2CN as function of frequency at different temperatures.

The M^* spectra of the 0CN sample clearly shows the space charge mechanism at low frequencies appearing as a step in M' and a narrow peak in M'' (the value of the

Kohlrausch parameter calculated for this peak using equation (4.60) is $\beta = 0.9$) followed by the dipolar relaxation process appearing as a second step in M' and a broad peak in M'' (Figures 4.25a and 4.25b). The relaxation time for conductivity τ_{Cond} is related to the frequency at which the peak in M'' appears, f_{max}, (equation 4.58) through $\tau_{Cond} = 1/2\pi f_{max}$.

In the 2CN samples, space charge and dipolar relaxation are closer to each other and partially overlaps. In addition, the low frequency M'' peak, due to free charge motions is broader than in the 0CN samples (Kohlrausch parameter calculated for this peak using equation (4.60) is β=0.60 at 155ºC). The peak of this process appears at lower temperatures than in the 0CN sample and shows a smaller temperature variation, meaning that lower energy barriers obstruct the motions of space charge carriers in the 2CN sample. The presence of the high frequency relaxation can be noticed above 175ºC by the loss of the symmetry of the conductivity peak by the lifting of its high frequency side. At higher temperatures the shape of the M'' plot clearly shows the overlapping of two processes. Some indications of the presence of this high frequency peak could be observed in the permittivity plot in Figure 4.18b. Interestingly, the drop of the real part of permittivity that takes place in the 2CN sample in the temperature interval between 225 and 250ºC, which was ascribed to the imidization of dianhydride groups [34], is not reflected in the dielectric modulus formalism.

The behaviour of the copolymer is between that of the two components. The space charge M'' peak is even broader than in 2CN sample and Kohlrausch parameter is only β=0.5. The presence of the high frequency dipolar relaxation is now clear above 200ºC and the sharp decrease of ε'due to the imidization of dianhydride groups has not a counterpart in M''. Instead, for the copolymers and 2CN polymer (Figures 4.26 and 4.27) two peaks appear above 205°C, which shift to higher frequency with increasing temperature, both samples showing similar relaxation process behaviour. The peak observed for all temperatures at low frequencies represents the movement of charge carriers over a long distance, i.e., charge carriers can perform successful hopping from one site to a neighboring site [56]. For higher frequencies, the observed peak indicate the presence of charges confined to local motions [52].

4.4. CONCLUSIONS

The dielectric properties of the samples are determined by the presence of the CN groups. The dielectric constant, ε', increases with increasing temperature for all samples. The α-relaxation is only detected for 0CN polymer being overlapped by the large conductivity contributions in the remaining samples.

The conductivity behavior reflects the mechanism of charge transport behavior. For copolymers and 2CN polymer at high temperature, the spectrum is dominated by ionic conductivity and interfacial polarization.

The differences observed for the activation energy between the samples in the conductivity process are attributed to the presence of the MWS relaxation process. The presence of the CN group in the copolymers and 2CN polymer increases the MWS contribution as detected in the electric modulus formalism plots.

4.5. REFERENCES

[1] Raju GG. Dielectrics in electric fields. New York: CRC Press; 2003.

[2] Riande E, Diaz-Calleja R. Electrical properties of polymers. Berlin Heidelberg: CRC Press; 2004.

[3] Kremer F, Schönhals A. Broadband dielectric spectroscopy. Berlin, Heidelberg: 2002.

[4] Kao K-C. Dielectric phenomena in solids: with emphasis on physical concepts of electronic processes. San Diego: Elsevier Academic Press; 2004.

[5] Lerner LS. Physics for scientists and engineers, Volume 2. Jones & Bartlett Learning; 1997.

[6] Ho J, Jow TR, Boggs S. Historical introduction to capacitor technology. IEEE Electr Insul Mag 2010;26:20–5.

[7] Capri AZ, Panat P V. Introduction to electrodynamics. Alpha Science; 2002.

[8] IEEE Standard definitions of terms for radio wave propagation. 1998.

[9] Brusso B, Chaparala S. The evolution of capacitors [History]. IEEE Ind Appl Mag 2014;20:8–12.

[10] Schulz AL. Capacitors: theory, types, and applications. Nova Science Publishers, Incorporated; 2010.

[11] Meurant G. Theory of electric polarization: dielectrics in static fields. Elsevier; 2012.

[12] Jonscher AK. Dielectric relaxation in solids. J Phys D Appl Phys 1999;32:R57–70.

[13] Buckingham AD, Pople JA. The dielectric constant of an imperfect non-polar gas. Trans Faraday Soc 1955;51:1029.

[14] Urano K, Inoue M. Clausius-Mossotti formula for anisotropic dielectrics. J Chem Phys 1976;71:791–4.

[15] Debye P. Polar molecules. J Soc Chem Ind 1929;48:1036–7.

[16] Debye P. Part I. Dielectric constant. Energy absorption in dielectrics with polar molecules. Trans Faraday Soc 1934;30:679.

[17] Onsager L. Electric moments of molecules in liquids. J Am Chem Soc 1936;58:1486–93.

[18] Bordewijk P. On the derivation of the Kirkwood-Fröhlich equation. Physica 1973;69:422–32.

[19] Bordewijk P. Extension of the Kirkwood-Fröhlich theory of the static dielectric permittivity to anisotropic liquids. Physica 1974;75:146–56.

[20] Gold PI, Perrine RL. Kirkwood-Frohlich correlation parameter and the structure of alcohol and carbon tetrachloride mixtures. J Phys Chem 1967;71:4218–22.

[21] Davidson DW, Cole RH. Dielectric relaxation in glycerine. J Chem Phys 1950;18:1417.

[22] Davidson DW, Cole RH. Dielectric relaxation in glycerol, propylene glycol, and n-propanol. J Chem Phys 1951;19:1484.

[23] Cole RH, Davidson DW. High frequency dispersion in n-propanol. J Chem Phys 1952;20:1389.

[24] Havriliak S, Negami S. A complex plane analysis of α-dispersions in some polymer systems. J Polym Sci Part C Polym Symp 1966;14:99–117.

[25] Havriliak S, Negami S. A complex plane representation of dielectric and mechanical relaxation processes in some polymers. Polymer (Guildf) 1967;8:161–210.

[26] Cole KS, Cole RH. Dispersion and absorption in dielectrics I. Alternating current characteristics. J Chem Phys 1941;9:341.

[27] Cole KS. Dispersion and absorption in dielectrics II. Direct current characteristics. J Chem Phys 1942;10:98.

[28] Dyre JC. The random free-energy barrier model for ac conduction in disordered solids. J Appl Phys 1988;64:2456.

[29] Maceiras A, Costa CM, Lopes AC, San Sebastián M, Laza JM, Vilas JL, et al. Dielectric relaxation dynamics of high-temperature piezoelectric polyimide copolymers. Appl Phys A 2015;120:731–43.

[30] Lopes AC, Costa CM, Serra RS i, Neves IC, Ribelles JLG, Lanceros-Méndez S. Dielectric relaxation, ac conductivity and electric modulus in poly(vinylidene fluoride)/NaY zeolite composites. Solid State Ionics 2013;235:42–50.

[31] Gonzalo B, Vilas JL, Breczewski T, Pérez-Jubindo MA, De La Fuente MR, Rodriguez M, et al. Synthesis, characterization, and thermal properties of piezoelectric polyimides. J Polym Sci Part A Polym Chem 2009;47:722–30.

[32] Maceiras A, Martins P, San Sebastián M, Lasheras A, Silva M, Laza JM, et al. Synthesis and characterization of novel piezoelectric nitrile copolyimide films for high temperature sensor applications. Smart Mater Struct 2014;23:105015.

[33] Sakthivel S, Shekar BC, Mangalaraj D, Narayandass SK, Venkatachalam S, Prabhakaran PV. Structure, dielectric, AC and DC conduction properties of acid doped polyaniline films. Eur Polym J 1997;33:1747–52.

[34] Gonzalo B, Breczewski T, Vilas JL, Perez-Jubindo MA, De La Fuente MR, Dios JR, et al. Dielectric properties of piezoelectric polyimides. Ferroelectrics 2008;370:3–10.

[35] Muruganand S, Narayandass SK, Mangalaraj D, Vijayan T. Dielectric and conduction properties of pure polyimide films. Polym Int 2001;50:1089–94.

[36] Scherer GW. Relaxation in glass and composites. vol. 1. Krieger Publishing Company; 1991.

[37] Mauro JC, Yue Y, Ellison AJ, Gupta PK, Allan DC. Viscosity of glass-forming liquids. Proc Natl Acad Sci U S A 2009;106:19780–4.

[38] Ikeda M, Aniya M. Bond strength—coordination number fluctuation model of viscosity: an alternative model for the Vogel-Fulcher-Tammann equation and an application to bulk metallic glass forming liquids. Materials (Basel) 2010;3:5246–62.

[39] Boyd RH. Relaxation processes in crystalline polymers: experimental behaviour - a review. Polymer (Guildf) 1985;26:323–47.

[40] Lanceros-Mendez S, Moreira M V., Mano JF, Schmidt VH, Bohannan G. Dielectric behavior in an oriented β-PVDF film and chain reorientation upon transverse mechanical deformation. Ferroelectrics 273:15–20.

[41] Sencadas V, Costa CM, Moreira V, Monteiro J, Mendiratta SK, Mano JF, et al. Poling of β-poly(vinylidene fluoride): dielectric and IR spectroscopy studies. E-Polymers 2005;5:10–21.

[42] Firmino Mendes S, Costa CM, Sencadas V, Serrado Nunes J, Costa P, Gregorio R, et al. Effect of the ceramic grain size and concentration on the dynamical mechanical and dielectric behavior of poly(vinilidene fluoride)/Pb(Zr0.53Ti0.47)O3 composites. Appl Phys A 2009;96:899–908.

[43] San Sebastian M, Gonzalo B, Breczewski T, Vilas JL, Perez-Jubindo MA, De La Fuente MR, et al. Frozen polarization of piezoelectric polyimides. Ferroelectrics 2009;389:114–21.

[44] Chan RK, Pathmanathan K, Johari GP. Dielectric relaxations in the liquid and glassy states of glucose and its water mixtures. J Phys Chem 1986;90:6358–62.

[45] Lu H, Zhang X. Investigation of MWS relaxation in Nylon 1010 using dielectric relaxation spectroscopy. J Macromol Sci Part B Phys 2006;45:933–44.

[46] Lunkenheimer P, Götzfried T, Fichtl R, Weber S, Rudolf T, Loidl A, et al. Apparent giant dielectric constants, dielectric relaxation, and ac-conductivity of hexagonal perovskites La1.2Sr2.7BO7.33 (B=Ru, Ir). J Solid State Chem 2006;179:3965–73.

[47] Jonscher AK. The "universal" dielectric response. Nature 1977;267:673–9.

[48] Deligöz H, Yalcinyuva T, Özgümüs S, Yildirim S. Electrical properties of conventional polyimide films: Effects of chemical structure and water uptake. J Appl Polym Sci 2006;100:810–8.

[49] Nada A. Dielectric properties and ac-conductivity of cellulose polyethylene glycol blends. Mater Chem Phys 2004;84:205–15.

[50] Dyre J, Schrøder T. Universality of ac conduction in disordered solids. Rev Mod Phys 2000;72:873–92.

[51] Tsangaris G, Psarras GC, Kouloumbi N. Electric modulus and interfacial

polarization in composite polymeric systems. J Mater Sci 1998;33:2027–37.

[52] Molak A, Paluch M, Pawlus S, Klimontko J, Ujma Z, Gruszka I. Electric modulus approach to the analysis of electric relaxation in highly conducting (Na0.75Bi0.25)(Mn0.25Nb0.75)O3 ceramics. J Phys D Appl Phys 2005;38:1450–60.

[53] Ngai K, Martin S. Correlation between the activation enthalpy and Kohlrausch exponent for ionic conductivity in oxide glasses. Phys Rev B 1989;40:10550–6.

[54] Lu H, Zhang X, Zhang H. Influence of the relaxation of Maxwell-Wagner-Sillars polarization and dc conductivity on the dielectric behaviors of nylon 1010. J Appl Phys 2006;100:054104.

[55] Dixon P. Specific-heat spectroscopy and dielectric susceptibility measurements of salol at the glass transition. Phys Rev B 1990;42:8179–86.

[56] Prakash T, Prasad KP, Kavitha R, Ramasamy S, Murty BS. Dielectric relaxation studies of nanocrystalline CuAlO2 using modulus formalism. J Appl Phys 2007;102:104104.

Chapter 5.

Polyimide based magnetoelectric nanocomposites

In this chapter was developed a novel type of magnetoelectric nanocomposite, based on a piezoelectric polyimide matrix and cobalt ferrite nanoparticles, as magnetostrictive constituent. Several compositions were initially obtained and their thermal properties were studied by differential scanning calorimetry and thermogravimetry, and morphology by SEM. After the optimal composition was chosen, this sample was poled by corona poling and its magnetic and piezoelectric characterization was carried out. *Finally, its ME voltage coefficient (α_{33}) was measured.*

5.1. INTRODUCTION

A **composite** material (also called a composition material or composite) can be defined as the material made from two or more constituent materials with significantly different physical or chemical properties, that when combined, produce a material with characteristics different from the individual components. The individual components remain separate and distinct within the finished structure.

Specifically, a **nanocomposite** [1–3] is a multiphase solid material where one of the phases has one, two or three dimensions of less than 100 nanometers (nm), or solid structures having nano-scale repeat distances between the different phases that make up the material. These materials typically consist of an inorganic (host) solid containing an organic component or vice versa, or they can be made of two or more inorganic/organic phases in some combinatorial form with the constraint that at least one of the phases or features must be in the nanosize scale. Normally their mechanical, electrical, thermal, optical, electrochemical and catalytic properties differ markedly than those of each individual component. The multifunctional behavior for any specific property of the material is often more than the sum of the individual components.

In general terms, apart from the properties of individual components in a nanocomposite, interfaces play an important role in enhancing or limiting the overall properties of the system. Nanocomposites differ from conventional composite materials due to the high surface to volume ratio of the reinforcing phase and/or its high aspect ratio. In addition, the large areas of nano inclusions lead to enormous interfacial surfaces which may improve interactions in the composite. Special properties of nanocomposite materials often arise from interaction of its phases at interfaces. An illustrative example of this phenomenon could be the mechanical behavior of nanotube filled polymer composites. Despite adding nanotubes could probably improve the strength of polymers (thanks to the superior mechanical properties of the nanotubes), a non-interacting interface serves only to create weak regions in the composite, resulting in no enhancement of its mechanical properties. In most occasions, the reinforcing material can be made up of particles (e.g. minerals), sheets (e.g. exfoliated clay stacks)

or fibers (e.g. carbon nanotubes or electrospun fibers). The area of the interface between the matrix and reinforcement phases is typically an order of magnitude greater than for conventional composite materials.

Self-organization and directed assembly of biological macromolecules and inorganic materials plays an important role in the creation of the nanocomposite materials so commonly found in biology, for instance in the structure of the abalone shell and bone. In the industry, from the 50s nanoscale organo-clays have been used to control flow of polymer solutions or the constitution of gels and by the 70s polymer/clay composites were the topic of textbooks, although the term "nanocomposites" was not yet very used.

Depending on the composition there are different types of nanocomposite materials. Apart from that they can be entirely inorganic, entirely organic, or a mixture of inorganic and organic materials; they are divided in ceramic-matrix, metal-matrix, polymer-matrix nanocomposites, but concretely in this thesis only the polymeric ones were used.

5.1.1. POLYMER NANOCOMPOSITES

Polymer nanocomposites are defined as the combination of a polymer matrix and additives that have at least one dimension in the nanometer range. Over the last decade, polymer nanocomposites have attracted considerable interests in both academia and industry, owing to their outstanding mechanical and other superior properties, such as barrier resistance, flame retardancy, scratch/wear resistance, optical, magnetic or electrical properties. They can be classified depending on the production method and the filler shape.

On the basis of the shape (Figure 5.1), nanoparticles can be distinguished in: a) (quasi)-spherical particles (1-D), b) whiskers and rod particles (2-D) and c) platelet (lamellar) particles (3-D). Shape is one of the most important characteristics of nanofillers, as it may influence significantly the interaction between nanoparticles and the polymer matrix.

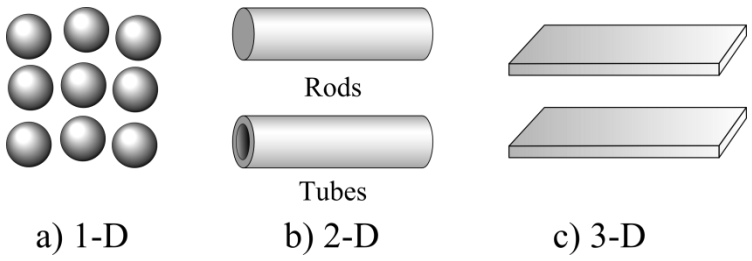

Figure 5.1. Types of particles used in nanocomposites a) (quasi)-spherical (1-D), b) rods and tubes (2-D) and c) platelets (lamellar) (3-D).

By creating nanometer-scale structures, it is possible to control the fundamental properties of materials, such as their melting temperature, magnetic properties, charge capacity, and even their colour, without changing the materials' chemical compositions. Making use of this potential will lead to new, high-performance products and technologies that were not possible before. Nanoscale structures such as nanoparticles and nanolayers have very high surface-to-volume and aspect ratios, making them ideal for use in polymer materials [2].

As a result, molecular interaction between the polymer and the nanoparticles will give to polymer nanocomposites unusual material properties that conventional polymers do not possess. Nanoscale science and technology gives opportunities to develop revolutionary materials. It is attracting a great attention because of its potential applications in areas such as electronics, optics, catalysis, ceramics, magnetic data storage, and polymer nanocomposites. The unique properties and improved performance of nanomaterials are determined by their sizes, surface structures, and interparticle interactions. The role played by particle size is comparable to the role of the particle's chemical composition, adding another parameter for designing and controlling particle behaviour.

There are different types of commercially available nanoparticles that can be incorporated into the polymer matrix to form polymer nanocomposites. The most used in the literature are: montmorillonite organoclays (MMT), carbon nanofibers (CNFs),

polyhedral oligomeric silsesquioxane (POSS), carbon nanotubes [multiwall (MWNTs), small-diameter (SDNTs), and single-wall (SWNTs)], nanosilica (N-silica), nanoaluminum oxide (Al_2O_3), nanotitanium oxide (TiO_2) and others.

There are two main challenges to developing polymer nanostructured materials after the type of nanoparticle has been selected for the polymer. First, the choice of nanoparticles requires an interfacial interaction and/or compatibility with the polymer matrix. Second, the proper processing technique should be selected to uniformly disperse and distribute the nanoparticles or nanoparticle aggregates within the polymer matrix.

Normally, polymer nanostructured materials exhibit multifunctionality. For instance, several of these functions are: thermal *(increased thermal resistance, higher glass transition temperature, reduced coefficient of thermal expansion...),* mechanical (*increased modulus, strength, toughness, elongation...),* chemical *(improved solvent resistance, improved moisture resistance...),* electrical *(improved thermal conductivity, lower resistivity),* barrier *(reduced oxygen, moisture transmission...),* optical *(clear, transparency)* and others *(abrasion resistance, reduced shrinkage...).*

Habitually, polymer matrix can be classified into the three families of resins namely thermoplastics, thermosets, and elastomers. After the selection of a particular polymer matrix and the appropriate nanoparticles for a specific application, the next challenge is to determine the proper synthesis method to create the desired polymer nanocomposite.

In general, for solid thermosetting reactive prepolymers or thermoplastic polymers with solid nanoparticles, the following processing methods are recommended: solution intercalation, melt intercalation and roll milling [4,5]. For liquid thermosetting reactive prepolymers or thermoplastic polymers with solid nanoparticles, the following methods are: In situ polymerization, emulsion polymerization and high-shear mixing [4,5].

There are different techniques for production of polymer nanocomposites, some are more useful than others depending on the specific characteristics of the polymer and nanoparticles. For example, in the case of laminated sheets six synthesis approaches [4,5] can be identified:

a) **Solution intercalation.** The layered silicate is exfolitated into single layers using a solvent in which the polymer or prepolymer is soluble. The polymer then absorbs onto the delaminated sheets, and when evaporated (or the mixture precipitated), the sheets reassembles, sandwiching the polymer to form an ordered, multilayered structure.

b) **Melt intercalation.** The layered silicate is mixed with the solid polymer matrix in the molten state. Under these conditions and if the layer surfaces are suficiently compatible with the selected polymer, the polymer can be inserted into the interlayer space and form either an intercalated or an exfoliated nanocomposite. No solvent is required.

c) **High-shear mixing.** The solid or liquid nanoparticles are mixed with the liquid polymer matrix using high-shear equipment. Under these conditions and if the nanoparticles are compatible with the selected polymer, the high-shear mixing will disrupt the nanoparticle aggregates and disperse the polymer matrix into the nanoparticle layers. An intercalated or an exfoliated nanocomposite will result. This technique may or may not, (especially in the case of water-based polymers) require solvent.

d) **Roll milling.** Three-roll milling is considered as low-shear mixing for incorporating solid nanoparticles into a liquid polymer, as compared to high-shear mixing.

e) **Emulsion polymerization.** In a manner analogous to the solution intercalation technique, the layered silicate is dispersed in the aqueous phase, and the polymer nanocomposites are formed.

f) **In-situ polymerization.** The layered silicate is swollen within the liquid monomer (or a monomer solution) so that the polymer formation can occur between the intercalated sheets. Polymerization can be initiated by different polymerization methods such as heat or radiation, diffusion of a suitable initiator, or an organic initiator or catalyst fixed through cationic exchange inside the inter layer before the swelling step of the monomer.

A. POLYIMIDE NANOCOMPOSITES

Aromatic polyimides (PI) have being used in the industry for their great dielectric, thermal stability, chemical and radiation resistance [6]. They are widely used as high-temperature insulators [7], circuit boards [8], packaging materials [9], dielectric interlayers [10] and in microelectronics [11]. In addition, they have other applications in fuel cells [12] or separation membranes [13,14]. Another interesting field is related with their photophysical properties, with many applications [15–25] in photovoltaic, electrochromic, photochromic, thermo-optical, and/or electroluminescent devices.

However, for other applications more improvements in their inherent properties are still desirable [26], being the fabrication of composites or nanocomposites a possible solution. Moreover, nanoparticles have been proved to be effective additives for introducing new properties or characteristics in polymer materials [27].

The variety of polyimide nanocomposites is very wide, because the number of possible uses and applications is huge. There are examples with carbon nanotubes (CNTs) [28], clays [29,30], graphene [31,32] and with nanoparticles, such as copper (Cu) [33], silver (Ag) [34], barium titanate ($BaTiO_3$) [35], silicon dioxide (SiO_2) [36,37], titanium oxide (TiO_2) [38], or calcium carbonate ($CaCO_3$) [39]. But in comparison, the examples using ferrites in polyimides for magnetic applications are relatively few in number [40].

In general, polymer matrix magnetic composites, commonly referred to as magnetic polymers, are receiving an increasing interest due to their wide range of potential applications. A particular type of composite is the one consisting of polymeric matrices hosting ferrite particles as dispersed phase [41], because ferrites are an important magnetic material with a wide range of applications in sensors, electronics, communication, magnetic recording, microwave absorption-based devices, electrical and automobile industries as well as an increasing applicability in the biomedical and biotechnology field [42,43]. In addition, ferrites can be used as magnetostrictive phase in **magnetoelectric (ME) composites**, because they show the largest magnetostrictive coefficients and high Curie temperatures among magnetic oxides [44–46]. In this chapter, composite films with 0–3 connectivity type were prepared via in-situ

polymerization method, using spherical cobalt ferrite nanoparticles ($CoFe_2O_4$) as fillers and an amorphous copolyimide, (β-CN)APB/ODPA, as matrix (Figure 5.2). A copolyimide formed by the 4,4′ oxydiphthalic anhydride (ODPA) dianhydride and two different bis-aminophenoxybenzene (APB) diamines, one of them nitrile substituted, (β-CN).

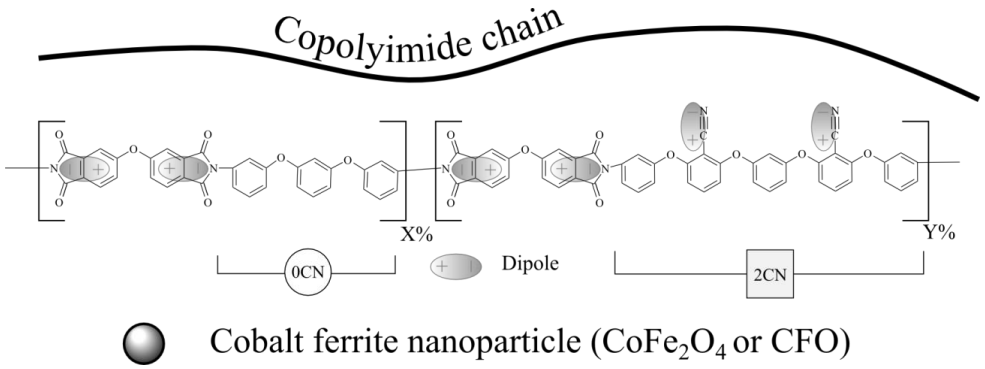

Figure 5.2. Scheme of the two repetitive units of the copolyimide with the polar groups (Up) and of a cobalt ferrite nanoparticle (Down).

In this way, the use of polymer based magnetoelectric materials for sensing and actuation applications has been the subject of increasing scientific and technological interest [47]. One of the drawbacks to be overcome in this field is to increase the temperature range of application above 100ºC.

The amorphous copolyimide, (β-CN)APB/ODPA can be used as an alternative to the semicrystalline polyvinylidene fluoride (PVDF) and family polymers [48–51]. PVDF is the best known and most used piezoelectric polymer, because it has the highest piezoelectric, pyroelectric and ferroelectric properties, added to its excellent chemical resistance and mechanical properties, allowing an important variety of technological applications [52]. Probably, the major limitation of PVDF is its relative low maximum operating temperature, limited to below 100ºC, which is the Curie temperature (T_C) of the material [53]. Thus, there was an important interest in using piezoelectric polymers with higher maximum operating temperature, above 100ºC, being some amorphous polymers a possible solution.

Piezoelectricity in amorphous polymers is due to the freezing-in of molecular dipoles [54]. Therefore, one of the most important parameter is the glass transition temperature (T_g), because that temperature dictates its maximum operating temperature and defines the poling process conditions. The number of examples is much more limited than that for semi-crystalline systems. Much of the work is in the area of nitrile (-CN) substituted polymers [51,55–57], where some aromatic polyimides [51,58,59] are the most promising polymers because their high T_g and thermal stability.

5.1.2. MAGNETOELECTRIC EFFECT

Multiferroics are defined as materials that exhibit more than one primary ferroic order parameter (ferroelectric, ferromagnetic or ferroelastic) simultaneously in a single phase (Figure 5.3). Multiferroic materials have drawn interest due to their potential for applications as multifunctional devices. Among them, the coexistence of ferroelectricity and ferromagnetism is highly desired. The coupling interaction between the different order parameters could produce new effects, such as **magnetoelectric (ME) effect** [60,61].

Research on the magnetoelectric (ME) effect, discovered more than a century ago, progressed through pioneering work in the 1950s and 1960s, and has now seen a resurgence driven by long-term technological aspirations. The concept of magnetoelectricity was first theorized in the 50s by Landau, Lifshitz, and Dzyalonshinkii, and finally realized in Cr_2O_3 during the late 50s by Astrov in Russia and Rado in USA. For its first 50 years as a discipline of study, the magnetoelectric (ME) effect remained a curiosity: simply due to the miniscule exchange between magnetic and polar subsystems. However, by the turn of the millennium, various groups were beginning to unlock giant magnetoelectricity in magnetostrictive and piezoelectric composites. Multiferroic materials are particularly appealing not only because they have the properties of their parent compounds, but also interactions between the magnetic and electric orders lead to additional functionalities [62].

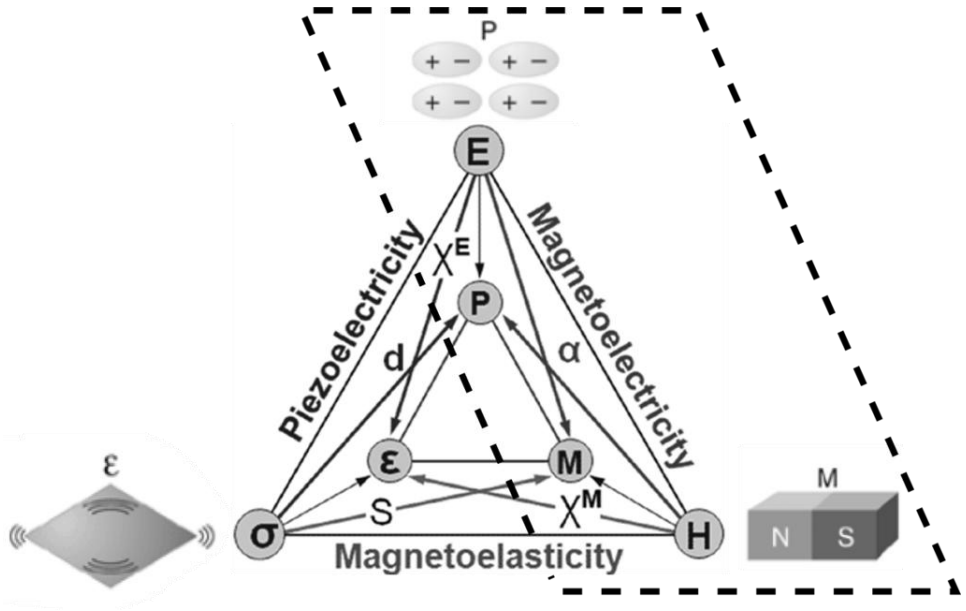

Figure 5.3. Schematic illustrating different types of coupling present in multiferroic materials. Materials where electric and magnetic order is coupled are highlighted with dotted lines.

The magnetoelectric (ME) effect is defined as the electric polarization (P) of a material in an applied magnetic field (H) or as an induced magnetization (M) in an external electric field (E). The so-called direct ME effect is the appearance of an electric polarization (P) upon applying a magnetic field (H):

$$\Delta P = \alpha \Delta H \qquad \text{or} \qquad \Delta E = \alpha_{ME} \Delta H \qquad (5.1)$$

where α_{ME} is the ME coefficient (ME voltage). It may arise directly between the two order parameters as in single-phase multiferroics, or indirectly via strain/stress as in ME composites. Thus, the electric polarization can be modified by a magnetic field or a voltage output can be produced by applying a magnetic field on the materials via the ME coupling.

In addition to this direct ME effect, there is simultaneously the converse ME effect, i.e., the appearance of magnetization (M) upon applying an electric field (H):

$$\Delta M = \alpha_{ME} \Delta E \tag{5.2}$$

which means the modulation of magnetism by an electric field. In a multiferroic material with ferroelectric and ferromagnetic orders co-existing as well as strong enough ME coupling, ideally, the electric or magnetic polarization would present a hysteresis response as a function of the applied magnetic or electric field.

Magnetoelectricity has been observed as intrinsic effect in some natural material systems at low temperature motivated by potential applications in spintronics, information storage and multiple-state memories [63,64]. Although different compounds have been extensively investigated as multiferroic ME materials, a high inherent coupling between multiferroic order parameters (especially above room temperature) has not yet been found in single-phase compounds [65]. Accordingly, these very few single-phase ME materials with very weak ME coupling at room temperature do not allow their use in most application areas. Composites emerged as a solution to this problem since in composites consisting on magnetostrictive and piezoelectric phases, the ME effect is the result of a product property, i.e., mechanical deformation due to magnetostriction results in a dielectric polarization variation because of the piezoelectric effect, allowing high ME effects at room temperature [66,67].

In this way, **magnetostriction** is the changing of a material's physical dimensions ($\lambda = \Delta l/l$) in response to changing its magnetization. A magnetostrictive material will change its shape when it is subjected to a magnetic field [68,69]. The parameter that measures magnetostriction is the saturation magnetostriction constant (λ_S) which reflects the maximum (saturation) relative deformation of a material with respect to the random demagnetized state. λ_S can be either positive (elongation) or negative (contraction) (Figure 5.4). Magnetostriction has the same the origin as the magnetocrystalline anisotropy (directional dependence of a material's magnetic properties) that fixes some preferential directions for magnetization, those that minimize the repulsion energy of the orbitals. It is an effect ranging from $\lambda_S = 10^{-7}$ for "zero" magnetostriction materials to $\lambda_S = 10^{-3}$ for "giant" magnetostrictive ones. Most ferromagnetic materials exhibit some measurable magnetostriction. The inverse effect is

called magnetoelasticity and refers to the changes in magnetization under the effect of applied stress or strain in a ferromagnet.

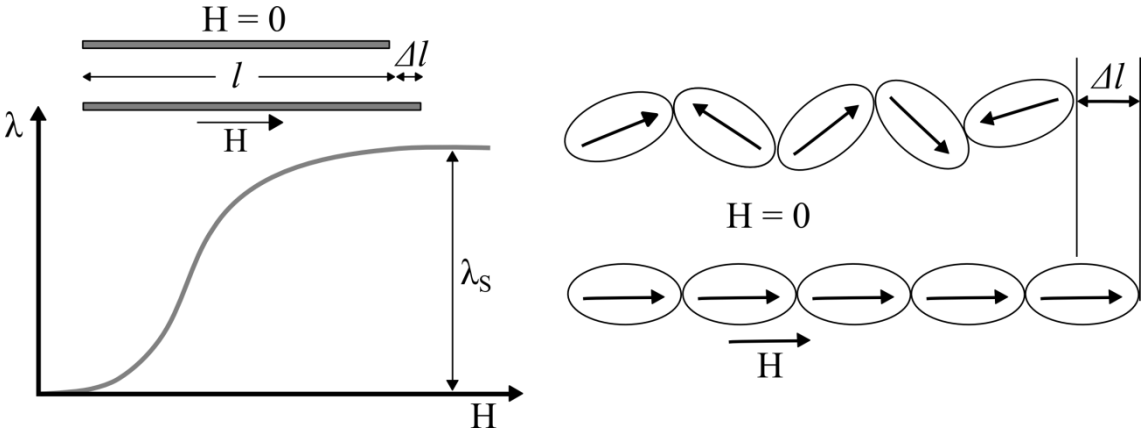

Figure 5.4. Saturation magnetostriction variation in function of the applied magnetic field (H) (Left) and orientation of magnetic domains caused by magnetization provokes the elongation (Δl) of the material (Right).

In the last few years the ME effect in magnetostrictive-piezoelectric composites has achieved its potential for a wide range of practical applications because of the discovery of strong magnetization-polarization interactions that are orders of magnitude larger than anything previously known. The ME effect in composites is due to the product property of the magnetostrictive phase on a piezoelectric one that is elastically bonded to it, or vice versa. Appropriate choice of phases with high magnetostriction and piezoelectricity has allowed the achievement of ME voltage coefficients necessary for applications in several areas such as computer memories, smart sensors, actuators and high frequency microelectronic devices [45,70–72].

$$Direct\ ME\ effect = \frac{magnetic}{mechanical} \times \frac{mechanical}{electric} \tag{5.3}$$

$$Converse\ ME\ effect = \frac{electric}{mechanical} \times \frac{mechanical}{magnetic} \tag{5.4}$$

This product tensor property results from the cross elastic interaction between different orderings of the two phases in the composite. Neither the piezoelectric nor magnetic

phase has the ME effect, but composites of these two phases have remarkable ME effect. It is a consequence of the product of the magnetostrictive effect (magnetic/mechanical effect) in the magnetic phase and the piezoelectric effect (mechanical/electrical effect) in the piezoelectric one (Figure 5.5).

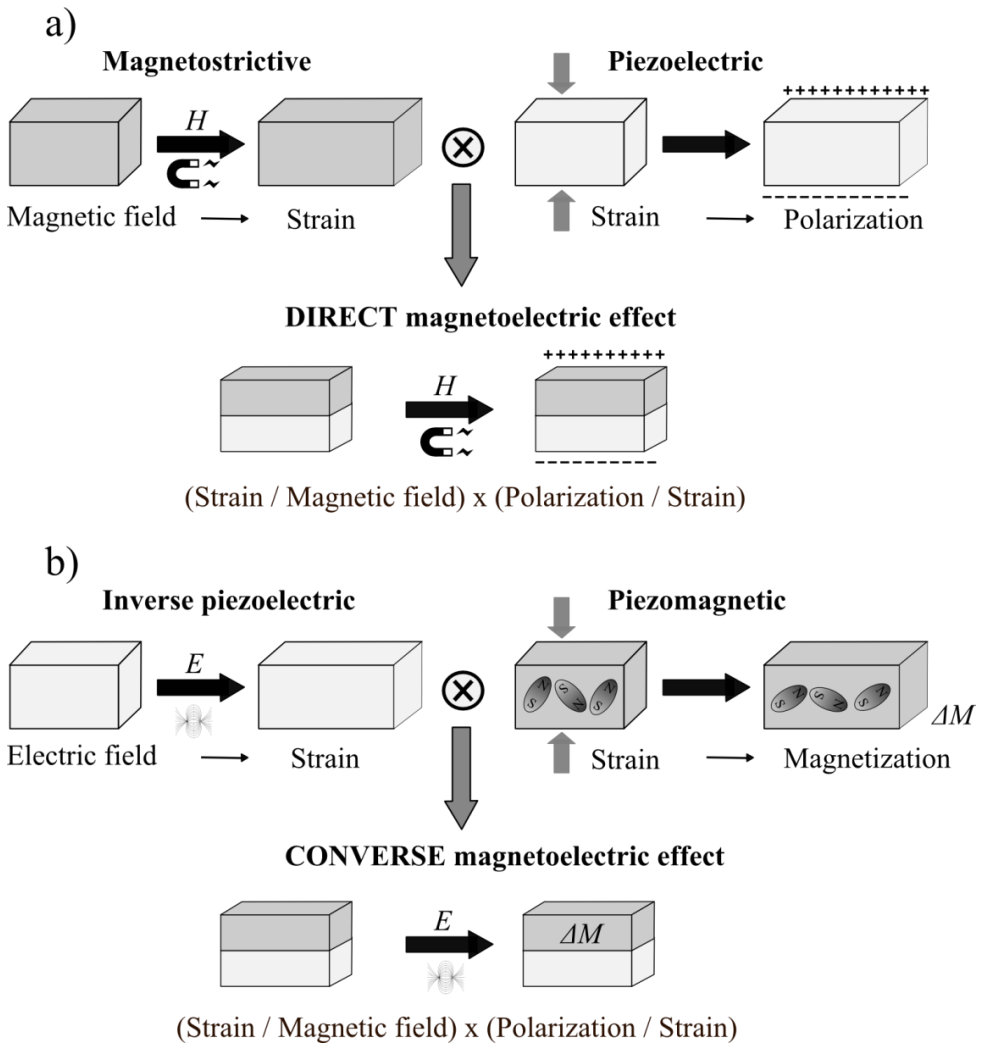

Figure 5.5. Schematic of the a) direct and b) inverse (or converse) strain mediated magnetoelectric effect.

For the direct ME effect, when a magnetic field is applied to a composite, the magnetic phase changes its shape due to magnetostriction. The strain is then passed along to the piezoelectric phase, resulting in an electric polarization. And, vice versa, under the inverse ME effect and the action of electric field, stresses arise in piezoelectric phase

due to piezoelectric effect and, due to magnetostriction, they are transferred to the magnetostrictive phase. So, depends on the composite microstructure and coupling interaction across magnetic-piezoelectric interfaces.

The magnetoelectric effect (ME) is described by the magnetoelectric coefficient (α_{ME}) that can be obtained from the experiment as [73]:

$$\alpha_{ME} = \frac{\partial E}{\partial H} = \frac{1}{t}\left(\frac{\partial V}{\partial H}\right) \tag{5.5}$$

where dH is the ac magnetic field amplitude applied to the biased composite, dV the measured induced voltage and t is the thickness of the piezoelectric element, being the ME strongly enhanced at the magnetoelastic resonance of the magnetostrictive element.

In 1972 Van Suchtelen proposed the concept of a product property in two-phase composite materials, arising from an elastic coupling between two phases (one magnetostrictive and one piezoelectric) of different properties. When an input magnetic field is applied to this composite material:

$$\frac{\partial S}{\partial H} = e^m \tag{5.6}$$

For the magnetic phase, and for the piezoelectric phase:

$$\frac{\partial P}{\partial S} = e \tag{5.7}$$

P is the electric polarization, H the electric field, S the strain, e^m the piezomagnetic and e the piezoelectric coefficients, respectively. Then, this two-phase composite material can be characterized by:

$$\frac{\partial P}{\partial H} = \alpha_{ME} = k_c e^m e \tag{5.8}$$

where k_c is a coupling factor ($0 \leq |k_c| \leq 1$) between the two phases, and α_{ME} is the ME coefficient of the composite. High piezomagnetic and piezoelectric coefficients and strong coupling (large k_c) favor a large ME coefficient.

The constitutive equation for describing the mechanical-electric-magnetic response in the composites [74] can be written by direct notation for tensors as:

$$\sigma = cS - e^T - q^T H$$

$$D = q^S + \varepsilon E + \alpha H \tag{5.9}$$

$$B = qS + \alpha^T E + \mu H$$

where σ is the stress, S the strain, D the electric displacement, E the electric field, B the magnetic induction and H the magnetic field. The stiffness is c, the dielectric constant is ε, permeability is μ, the piezoelectric coefficient is e, q the piezomagnetic coefficient and α the ME coefficient. The superscript T means transpose of the tensor. The tensors c, e, q, ε, μ, and α are (6×6), (3×6), (3×6), (3×3), (3×3), and (3×3) matrices, respectively, by means of the compressive representation. The effective ME coefficient depends on details of the composite microstructures: component phase properties, volume fraction, grain shape, phase connectivity, etc.

Green's function technique [75,76] was developed for solving the constitutive equation (5.9) above for the ME composites and derived the effective properties of the composites, defined in terms of averaged fields. All effective properties of the composites can be got by this approach. The effective ME coefficient tensor (α^*) of the composites was obtained as:

$$\alpha^* = \langle (e^* - e) T^{13} \rangle \langle T^{33} \rangle^{-1} = \langle (q^* - q) T^{12} \rangle \langle T^{22} \rangle^{-1} \tag{5.10}$$

where angular brackets denote the microstructural average; e^* and q^* are, respectively, the effective piezoelectric and piezomagnetic coefficients of the composites. T^{ij} are so-called *t*-matrix tensors [77].

Similarly, the constitutive equation (5.9) for the ME composites can also be solved by using micromechanics methods [78]. These models give almost the same approximations as the Green's functions technique.

The ME coefficient relates the polarization/voltage produced by an applied magnetic field and are called the α coefficients. It is a tensor, with components α_{ij}, where i

indicates the direction of polarization/voltage generated in the material when the electric field is zero (or the direction of applied electric field), and j is the direction of the applied magnetic field (or the induced magnetization) (Figure 5.6).

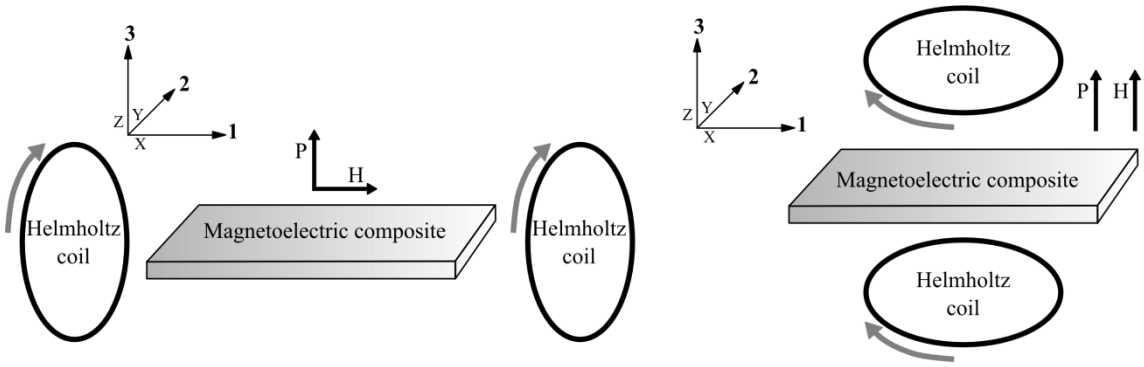

Figure 5.6. Schematic of the ME effect measurement for longitudinal orientation of fields (in-plane, α_{31}) (Left) and transverse orientation of fields (out-of-plane, α_{33}) (Right).

According to this, there are different ME voltage coefficients. The most used are the following ones:

—Longitudinal ME effect (out-of-plane ME effect, α_{33})

We assume as the film plane and the direction-3 perpendicular to the sample plane. The composition is poled with an electric field E along direction-3. The bias field H_0 and the ac field H are along the same direction as E and the resulting induced electric field E is estimated across the sample thickness. Then we find an expression for ME voltage coefficient:

$$\alpha_{E,L} = \alpha_{33} = E_3/H_3 \tag{5.11}$$

—Transverse ME effect (in-plane ME effect, α_{31})

This case corresponds to the poling direction along direction-3 and H_0 and H along direction-1 (in the same plane). Here we estimate the ME coefficient:

$$\alpha_{E,T} = \alpha_{31} = E_3/H_1 \tag{5.12}$$

A. TYPES OF ME COMPOSITES

Thanks to their greater design flexibility, multiferroic ME composites made by combining piezoelectric and magnetic substances together and using different shapes and connectivities have attracted interest because of their multifunctionality (Figure 5.7).

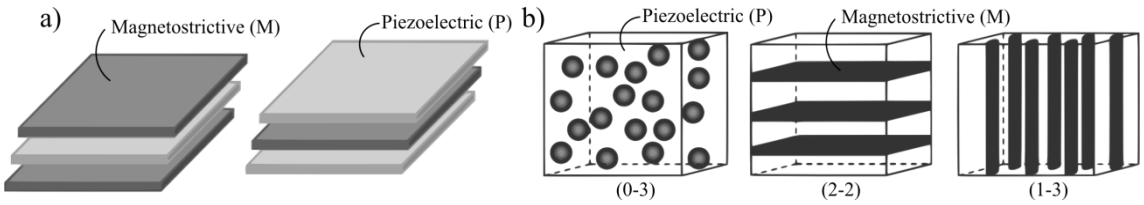

Figure 5.7. a) Magnetoelectric laminated composites (M-P-M and P-M-P trilayer) and b) Magnetoelectric nanocomposites with different connectivity schemes.

Over the last years various ME composites in different systems have been investigated, such us a) bulk ceramic ME composites of piezoelectric ceramics and ferrites, b) two-phase ME composites of magnetic alloys and piezoelectric materials, c) three-phase ME composites, and d) thin films (nanostructured composites) of ferroelectric and magnetic oxides [73,79].

For example, magnetostrictive metallic glasses materials have been employed as constituents of magnetoelectric composites. These hybrid systems are composed by piezoelectric and magnetostrictive elements in different geometries. The most sensitive is the L-T (longitudinal-transverse) laminated one, composed by sheets or ribbons of magnetostrictive material with longitudinal magnetization (M) sandwiching the piezoelectric one with transverse polarization (P). They produce large electrical signals when applying a magnetic field.

Using the concept of phase connectivity introduced by Newnham *et al.* [80] the structures of a two-phase composite can be described using the notations 0-3, 2-2, 1-3, etc., in which each number denotes the connectivity of the respective phase. For instance, a 0-3-type particulate composite means one-phase particles (denoted by 0) embedded in the matrix of another phase (denoted by 3) [66].

Initially ME composites did not attract attention, and the field went dormant for almost 20 years across the world. Then in the early 90s, Newnham's group and Russia scientists prepared particulate ceramic composites of ferrites and $BaTiO_3$ or $Pb(ZrTi)O_3$ (PZT) by a conventional sintering process [66]. These studies inspired significant theoretical work on ME ceramic composites and models to predict the resultant ME responses in composites.

An resurgence in the multiferroic ME composite research appeared in the early 2000s, especially a milestone was the development in 2001 of ME bulk composites using the giant magnetostrictive rare-earth-iron alloy $Tb_{1-x}Dy_xFe_2$ (Terfenol-D) in laminates or embedded in a piezoelectric polymer matrix, such as poly(vinylidene fluoride-trifluorethylene) copolymer [P(VDF-TrFE)] or a piezoelectric ceramic matrix such as PZT [73,81].

Since the ME coefficient is typically three orders of magnitude higher in ceramic or laminated composites, ME multilayer and ceramic composite materials have attracted particular attention. Laminated composites, however, are difficult to shape and miniaturize as a result of their inherent heterogeneous toughness and the performance of these composites is compromised by the brittleness of the epoxy bonding [66,82,83]. Ceramic composites also have their restrictions, being limited by deleterious reactions at the interface regions which lead to low electrical resistance and high dielectric losses, hindering sustainable device applications [82].

Magnetoelectric composites based on magnetostrictive nanoparticles embedded in a piezoelectric polymer matrix can overcome the above mentioned problems: strain coupling typically does not deteriorate with operation, as the magnetostrictive material is in direct contact with and completely surrounded by the piezoelectric material, have a

feasible and scalable production method compatible with industrial requirement and show a flexible structure without large leakage currents [45,66,67,70,71,82].

Additionally, polymer-based ME composite materials can be fabricated by conventional low-temperature polymer processing into a variety of forms, such as thin sheets or molded shapes, can exhibit improved tailored mechanical properties, flexibility, lightweight, versatility, low cost and in some cases biocompatibility, offering obvious advantages from the point of view of applications [82,84].

Nevertheless in specific areas such as automobile industry, biomedical and machinery used in material processing, most of the polymer-based ME composites do not meet the recent requirement of smart materials working under extreme conditions such as high temperatures [85–88]. Such poor performance at temperatures above 80ºC of polymer based ME materials is related with the fact that most of them are based on poly(vinylidene fluoride) or copolymers, the family of polymers with the largest piezoelectric response [52], undergoing shrinking above this temperature [52,89]. This limitation can be solved by using an amorphous copolyimide containing nitrile groups, with good piezoelectric performance at temperatures up to 130ºC, as the piezoelectric constituent of ME materials.

Gutierrez *et al.* presented [14,90] results concerning the magnetoelectric response of laminated composites when Metglas 2826 MB ($Fe_{40}Ni_{35}Mo_4B_{18}$) is used as the magnetostrictive amorphous element and polyimides with CN groups act as the piezoelectric constituent. They used the longitudinal magnetized and transversely poled or (L-T) mode (Figure 5.8).

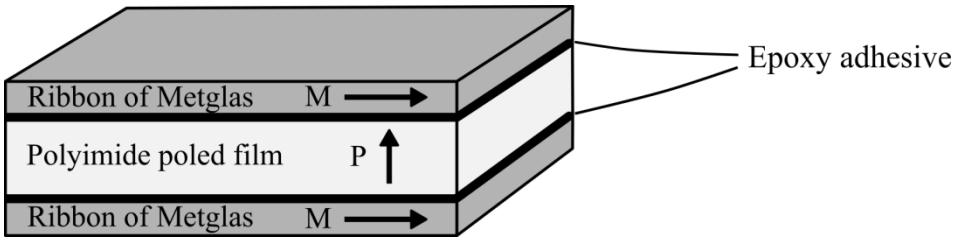

Figure 5.8. Schematic of: a three layer sandwich laminate formed by a poled polyimide among two ribbons of magnetostrictive Metglas.

In order to impart piezoelectricity, piezoelectrics must be subjected to a poling process for a certain duration to align the spontaneous polarization (in ferroelectric materials) or to orient the dipoles (amorphous piezoelectric materials) [91]. In addition, the duration should be sufficient for free charges to accumulate at the interface, to counteract the depolarization field, and to stabilize the polarization of the inclusion particles. The existence of interfacial charge in a poled composite sample is thus essential in this context. Thus, the effect on the piezoelectric properties of polyimide 0-3 composites must be examined.

B. ENHANCED ME EFFECTS AT RESONANCE

Bichurin *et al.* developed for the first time a theory for the ME effect at electromechanical, ferromagnetic, and magnetoacoustic resonances in the composites [92]. As the ME effect in the composites is due to mechanical coupling between the piezoelectric and magnetic phases, the ME effect would be greatly enhanced when the piezoelectric or magnetic phase undergoes resonance, i.e., electromechanical resonance (EMR) for the piezoelectric phase and ferromagnetic resonance (FMR) for the magnetic phase. Mechanical oscillation of a medium are induced either by alternating magnetic or electric fields [93,94].

The ME voltage coefficients are estimated from known material parameters (piezoelectric coupling, magnetostriction, elastic constants, etc.) of composite components using the procedure showed in Figure 5.9. Mechanical oscillation of a ME composite can be induced by alternating magnetic or by electric fields. Under a H_{ac} magnetic excitation applied along the length axis, the magnetostrictive element will elongate and shrink along that direction. This will make the film of piezoelectric component to undergo an ac longitudinal strain, inducing an electric polarization change and developing a voltage in its transverse direction. Usually a Bias dc magnetic field is used to drive the magnetostrictive element to the optimum operation point.

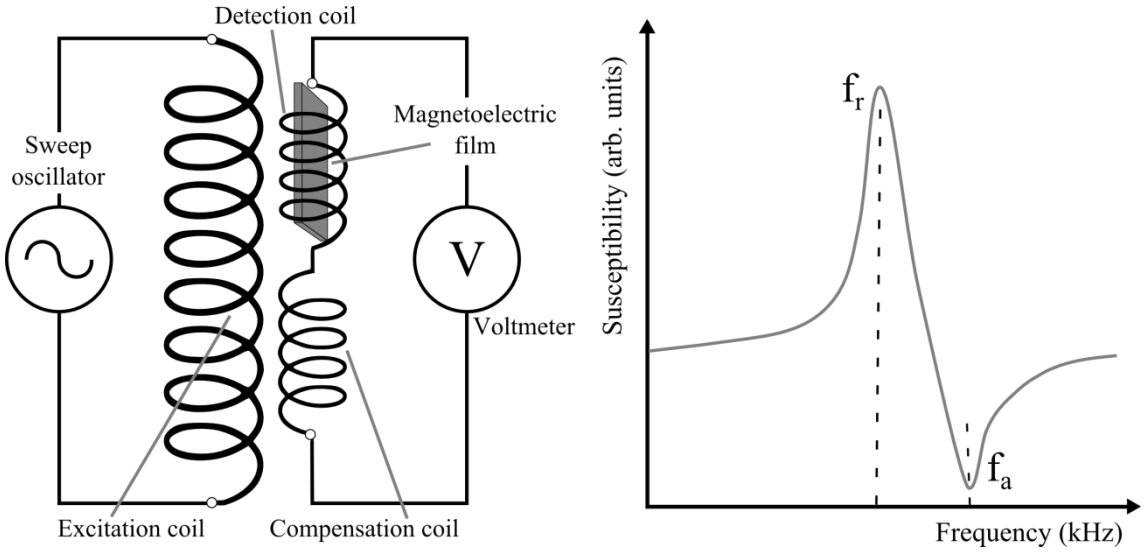

Figure 5.9. Detection of the magnetoelastic resonance for a magnetoelectric film in a coil (Left) and the induced voltage is proportional to the permeability and passes through a sharp maximum at resonance (f_r) and a minimum at anti-resonance (f_a) (Right).

A voltage applied to a magnetostrictive material causes the elastic wave propagation through the material [95]. Because of the magnetoelastic coupling in these materials, these waves can be generated either by mechanical or magnetic excitation. Under certain boundary conditions (e.g. leaving free the ends of the sample), propagated waves may become stationary, obtaining, at the frequency of natural mode of vibration, magnetoelastic resonances. A stationary wave, also known as standing wave, is a wave in a medium in which each point on the axis of the wave has an associated constant amplitude. The locations at which the amplitude is minimum are called nodes, and the locations where the amplitude is maximum are called antinodes (Figure 5.10).

For a sample of length *L*, an alternating magnetic field is applied to allow the magnetization oscillate with small amplitude. The magnetoelastic effect will induce a deformation which propagates as an elastic wave through the material. If the mechanical vibrations caused by the process of magnetization have a frequency close to the mechanical resonance, then the magnetoelastic resonance can occur. The frequency for which the received signal amplitude is maximum is called resonance frequency (f_r), while the frequency for which the amplitude is minimal is known as anti-resonant frequency (f_a).

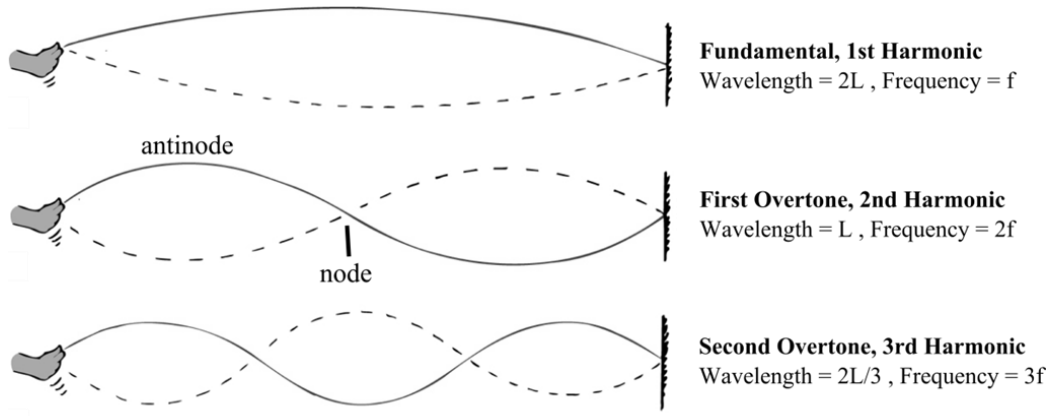

Figure 5.10. Schematic of standing waves.

Hence, the exchange between elastic and magnetic energy (Magnetoelastic resonance) can be described by the *magnetoelastic coupling factor* (k) which is defined as the ratio of the mutual magnetoelastic energy (F_{me}) to the geometric mean of the elastic (F_{el}) and magnetic (F_m) self-energies [96]. The *magnetoelastic coupling factor* (k) can be expressed in terms of the relative change of the Young's modulus, at constant field (E^H) or induction (E^B) or the magnetic permeability at constant stress (μ^σ) or constant strain, (μ^ε) as:

$$k^2 = \frac{F_{me}^2}{F_{el}\,F_m} = \frac{E^B - E^H}{E^B} = \frac{\mu^\sigma - \mu^\varepsilon}{\mu^\sigma} \tag{5.13}$$

In some metallic glasses extremely large magnetoelastic coupling coefficient close to unity can be achieved. $k^2 = 1$ indicates that all the elastic energy provide to it is transformed into magnetic energy (or vice versa), which is of great importance in transducers. The maximum value obtained so far is 0.97 for an amorphous ribbon annealed Metglas 2605SC near its Curie temperature.

In its most simplified form, a magnetoelastic resonator is formed by a ribbon or wire surrounded by a coil. The coil is excited by an ac current of varying frequency and when it coincides with the elastic resonance frequency of the sample (f_r), a large strain

and magnetization changes will appear in response to the magnetic excitation . The apparent permeability of the sample increases suddenly and the coil's self-inductance is largely increased. At the frequency (f_a) the out of phase coupling between the strain and the magnetization produces an anti-resonance and the permeability goes to zero. The resonant frequency (f_r) and Young's modulus (E_Y) for a sample of length L with free ends are mutually related by the same expression in two ways:

$$f_r = \frac{1}{2L}\sqrt{\frac{E_Y}{\rho}} \qquad \text{or} \qquad E_Y = (2L \cdot f_r)^2 \cdot \rho \qquad (5.14)$$

where ρ is the density of the material and E_Y the Young's modulus.

Young's modulus (elastic modulus or tensile modulus) is a mechanical property that defines the relationship between stress (σ) (force per unit area, F/A) and strain (ε) (proportional deformation, $\Delta L/L$) in a linear elastic solid material. It is a number that measures the material resistance to being elastically deformed (non-permanently). In a tensile stress-strain curve, Young's modulus (E_Y) is the initial region, where the material behaves linearly, and is defined by the slope of that initial region. (Figure 5.11).

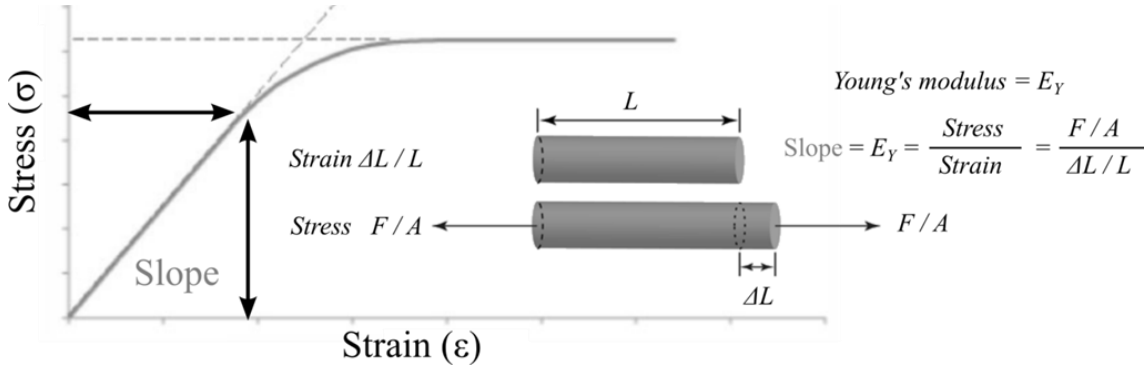

Figure 5.11. Scheme of a tensile strain–stress curve where Young's modulus is calculated.

Magnetoelastic coupling coefficient expresses the amount of magnetic energy converted into mechanical energy and vice versa. It is a parameter that gives an energy conversion

value, its value range between $0 < k \leq 1$. This magnetoelastic coupling coefficient can be deduced from the resonance (f_a) and anti-resonance (f_r) frequencies by:

$$k^2 = \frac{\pi^2}{8}\left[1 - \left(\frac{f_r}{f_a}\right)^2\right] \tag{5.15}$$

C. MAGNETOELECTRIC EFFECT IN POLYMER COMPOSITES

There exist some sophisticated theoretical models for particulate composites [81] and Wong *et al.* [97] proposed simplification of those models. The objective was to study theoretically the ME responses of dilute particulate composites comprising magnetostrictive inclusions dispersed in piezoelectric matrix. Following the assumption that the constituent materials are dielectrically and elastically isotropic, both longitudinal (α_{33}) and transverse (α_{31}) coefficients were studied.

The volumetric average electric displacement for the piezoelectric constituent materials in the composite is expressed as $D_j = \varepsilon_j + P_j$ where symbol D denotes electric displacement, ε is permittivity, E is electric field, and P is polarization. The subscript $j = i$ for inclusion and $j = m$ for matrix.

It is considered as a dielectric sphere surrounded by a piezoelectric matrix medium with an uniform electric field applied along the z direction far away from the inclusion [97]. In addition, it is assumed that the matrix material is homogeneously polarized and that is covered with surface charge of density q_0 at the pole along the polarizing direction.

For a composite comprising a dilute suspension of spherical particles uniformly distributed in the matrix material, the volumetric averages of the electric field and electric displacement are [91,98]:

$$E = \phi E_i + (1 - \phi)E_m \tag{5.16}$$

$$D = \phi D_i + (1-\phi) D_m$$

where ϕ is the volume fraction of the inclusion phase. After some algebraic manipulation we obtain:

$$D = \varepsilon E + (1-\phi)\bar{L}_E P_m + \phi(1-\phi)(L_E - \bar{L}_E) q_0$$

where $\varepsilon = \varepsilon_m\{(\varepsilon_i + 2\varepsilon_m) + 2\phi(\varepsilon_i - \varepsilon_m)\}/\{(\varepsilon_i + 2\varepsilon_m) - \phi(\varepsilon_i - \varepsilon_m)\}$ and

$$L_E = \frac{3\varepsilon_m}{(1-\phi)\varepsilon_i + (2+\phi)\varepsilon_m}$$
$$\bar{L}_E = \frac{1-\phi L_E}{1-\phi} = \frac{\varepsilon_i + 2\varepsilon_m}{(1-\phi)\varepsilon_i + (2+\phi)\varepsilon_m} \tag{5.17}$$

If stresses are also presented in the system, then assuming permittivities ε_i and ε_m, and the charge density q_0 do not vary with stress, the change of D can be evaluated by [91]:

$$\Delta D = \frac{\partial D}{\partial E}\Delta E_i + \frac{\partial D}{\partial P_m}\Delta P_m + \frac{\partial D}{\partial \phi}\Delta\phi \tag{5.18}$$

where

$$\Delta P_m = d_{31m} T_{xm} + d_{32m} T_{ym} + d_{33m} T_{zm} \tag{5.19}$$

$$\Delta\phi = \phi(\gamma_i - \gamma) \tag{5.20}$$

d_{31}, d_{32}, d_{33} are piezoelectric coefficients, γ is the volumetric strain which is the summation of tensile strain components, i.e., $\gamma = e_x + e_y + e_z$ for the composite and similarly γ_i for the inclusions. T_x and e_x represent the tensile stress and strain in the x direction, respectively. To facilitate the subsequent calculations, equation (5.20) may be transformed to $\Delta\phi = \phi(1-\phi)(\gamma_i - \gamma_m)$ using the relation $= \phi\,\gamma_i + (1-\phi)\gamma_m$.

The ME coefficient α_{3f} is defined as $t^{-1}\,dV/dH$, where V, H, and t denote output voltage, applied magnetic field, and the sample thickness, respectively. The first index "3" denotes the poling direction (assumed along z direction) of the composite and the second index "f" $(= 1, 2, or\ 3)$ addresses the direction of magnetic field. At short

circuit condition, $E = \Delta E = 0$, and the output voltage is calculated from the measurement of charge generated from the sample (denoted by Q) with $V = Q/C$, where C is the capacitance of the sample. Since $\Delta D = Q/A$ and $C = \varepsilon A/t$, we differentiate equation (5.18) once with H to get

$$\alpha_{3f} = (1-\phi)\frac{\overline{L}_E}{\varepsilon}\left(d_{31m}\frac{dT_{xm}}{dH_i} + d_{32m}\frac{dT_{ym}}{dH_i} + d_{33m}\frac{dT_{zm}}{dH_i}\right) \times \left(\frac{dH_i}{dH}\right) + \alpha_\phi \qquad (5.21)$$

where

$$\alpha_\phi = \varepsilon^{-1}\frac{d(\Delta\phi)}{dH_i}\left\{-\left[\overline{L}_E - (1-\phi)\frac{\partial \overline{L}_E}{\partial \phi}\right]P_{rm} + \left[(1-2\phi)\left(L_E - \overline{L}_E\right) + \phi(1-\phi)\frac{\partial\left(L_E - \overline{L}_E\right)}{\partial\phi}\right]q_0\right\} \times \left(\frac{dH_i}{dH}\right) \qquad (5.22)$$

and

$$\frac{\partial \overline{L}_E}{\partial \phi} = \frac{(\varepsilon_i + 2\varepsilon_m)(\varepsilon_i - \varepsilon_m)}{[(1-\phi)\varepsilon_i + (2+\phi)\varepsilon_m]^2} \qquad (5.23)$$

It is considered that all internal electric fields vanish at first and that $P_m = P_{rm}$ (i.e., remnant polarization of the matrix phase) in equation (5.22). We also have $q_0 = P_m - P_i + 3\varepsilon_m E_m - (\varepsilon_i - \varepsilon_m)E_i$ and $P_i = E_i = E_m = 0$. In other words, the polarization in the matrix phase is initially fully compensated by the free-surface charge. α_ϕ [equation (5.22)] is the contribution arising from the change in inclusion volume fraction with the embedded interfacial charge effect. Thus the consideration of change in ϕ due to stress also leads to an interfacial charge effect in the ME response.

The derivative of H_i with respect to H [in equations (5.21) and (5.22) can be obtained by first considering the constitutive magnetostatic equations

$$B_i = \xi_i H_i + M_i$$
$$B_m = \xi_m H_m \qquad (5.24)$$

where B is the magnetic flux density, ξ is the magnetic permeability, and M is the magnetization. Normally we can take $\xi_m = \xi_0$ for nonmagnetic piezoelectric matrix. Since the particulate composite is subjected to an applied magnetic field, we have:

$$H = \phi H_i + (1 - \phi) H_m \tag{5.25}$$

The boundary conditions of the magnetic field and magnetic flux density gives the following equation [99]:

$$B_i + 2\xi_m (H_i - H_m) = B_m \tag{5.26}$$

Combining equations (5.24) - (5.26):

$$\frac{dH_i}{dH} = \frac{2\xi_m}{(1 - \phi)(\xi_i + dM_i/dH_i) + (2 + \phi)\xi_m} \tag{5.27}$$

Thus for a given external field H acting on the composite, it can be obtained dH_i/dH when the $M_i - H_m$ relation is known. The model suggested by Duenas, Hsu, and Carman may be adopted in this calculation [100].

$$M_i = M_{sat,i} \tanh\left(3\chi_i H_i / M_{sat,i}\right) \tag{5.28}$$

where M_{sat} is the saturation magnetization and χ is a relaxation factor.

In conclusion, Wong et al. [97] proposed a relatively simple model for the theoretical comprehension of the longitudinal ME response (α_{33}) in 0–3 composites which allows fairly good agreement with experimental results.

5.2. EXPERIMENTAL

5.2.1. SYNTHESIS AND FABRICATION OF POLYIMIDE BASED ME NANOCOMPOSITES

The composites developed consist of an amorphous copolyimide containing nitrile groups and magnetostrictive nanoparticles embedded in the polymer matrix. With the aim of obtaining ME voltage at temperatures above 100ºC, different nanoparticle embedded systems were tested, using particulate composites of magnetostrictive ferrites (Figure 5.12).

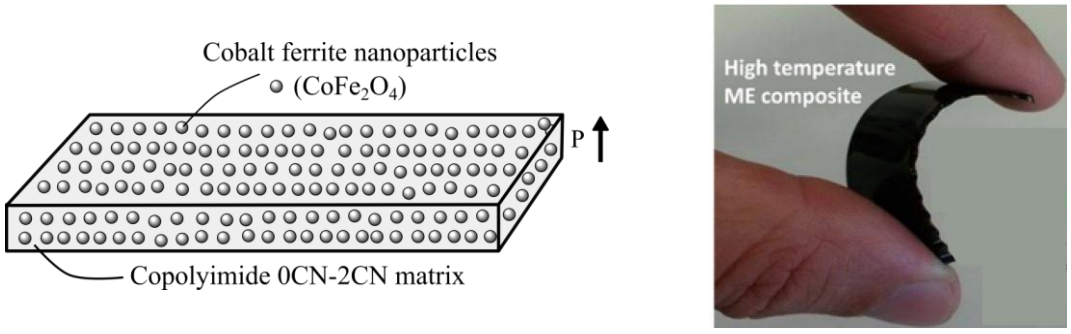

Figure 5.12. Schematic of a $CoFe_2O_4$ nanoparticles/copolyimide 0CN-2CN nanocomposite (Left) and photography of a 10wt% $CoFe_2O_4$ nanoparticles/copolyimide 0CN-2CN nanocomposite (Right).

Magnetoelectric CFO/0CN2CN films were synthesized by the 4,4'-oxydiphthalic anhydride (ODPA) and a mixture of two aromatic diamines, 1,3-bis-2-cyano-3-(3-aminophenoxy)phenoxybenzene (diamine 2CN) and 1,3-Bis(3-aminophenoxy)benzene (diamine 0CN) with cobalt ferrite magnetic nanoparticles ($CoFe_2O_4$, CFO) using the scheme of Figure 5.13. CFO nanoparticles were chosen as magnetic/magnetostrictive phase due to the large magnetostrictive coefficients, high Curie temperatures and chemical stability [101,102]. The experimental procedure employed was similar as for the samples of chapter 3 and 4, but not exactly the same, since in previous experiments that system didn't allow a good dispersion of the nanoparticles in the polymer matrix.

So, it was necessary to be changed and adapted, and we chose the following in-situ polymerization method.

Firstly (step 1), the nanoparticles were introduced into a vial containing dimethylacetamide (DMAc), and the vial was placed in an ultrasonic dispersion reactor for 60 min to ensure the uniform dispersion of the CFO on DMAc. Then (step 2), a mixture of the two aromatic diamines (50% mole percentage) was added and stirred until the complete dissolution of the diamines, being the content of solids of a 20%. The content of ferrite nanoparticles was variable. Several concentrations were studied: 0, 5, 7, 10, 20, 40 and 50 wt%. Thus, seven different compositions were synthesized in total:

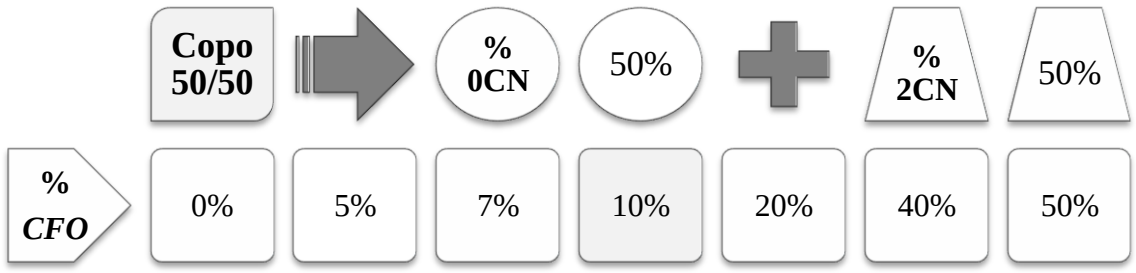

Later, 4,4'-oxydiphthalic anhydride (ODPA) was introduced to the mixture and (step 3) stirred at room temperature in a dry nitrogen atmosphere resulting in a viscous polyamic acid (PAA) solution containing CFO nanoparticles after 24h. Finally, (step 4), the mixture was cast in 150 µm thick films and (step 5) thermally imidizated according to the same thermal treatment applied to the pristine polyimides of chapter 3 and 4 (Figure 5.14).

Once the 0-3 composite film is fabricated is necessary to impart piezoelectricity to the polyimide in order to present magnetoelectric effect. The film must be subjected to a poling process during a period of time long enough to align the dipoles as well as to allow free charges to accumulate at the inclusion-matrix interfaces to counteract the depolarization field and to stabilize the polarization. It is important to remember that in order to conserve the capability to be poled, the nanocomposite must remain insulator (dielectric). So, the presence of metallic inclusions (cobalt ferrite nanoparticles) in a

high percentage, could be counter-productive, and make impossible the piezoelectricity in the material. In addition, the presence of nanoparticles can affect the mechanical and thermal performance of the composites.

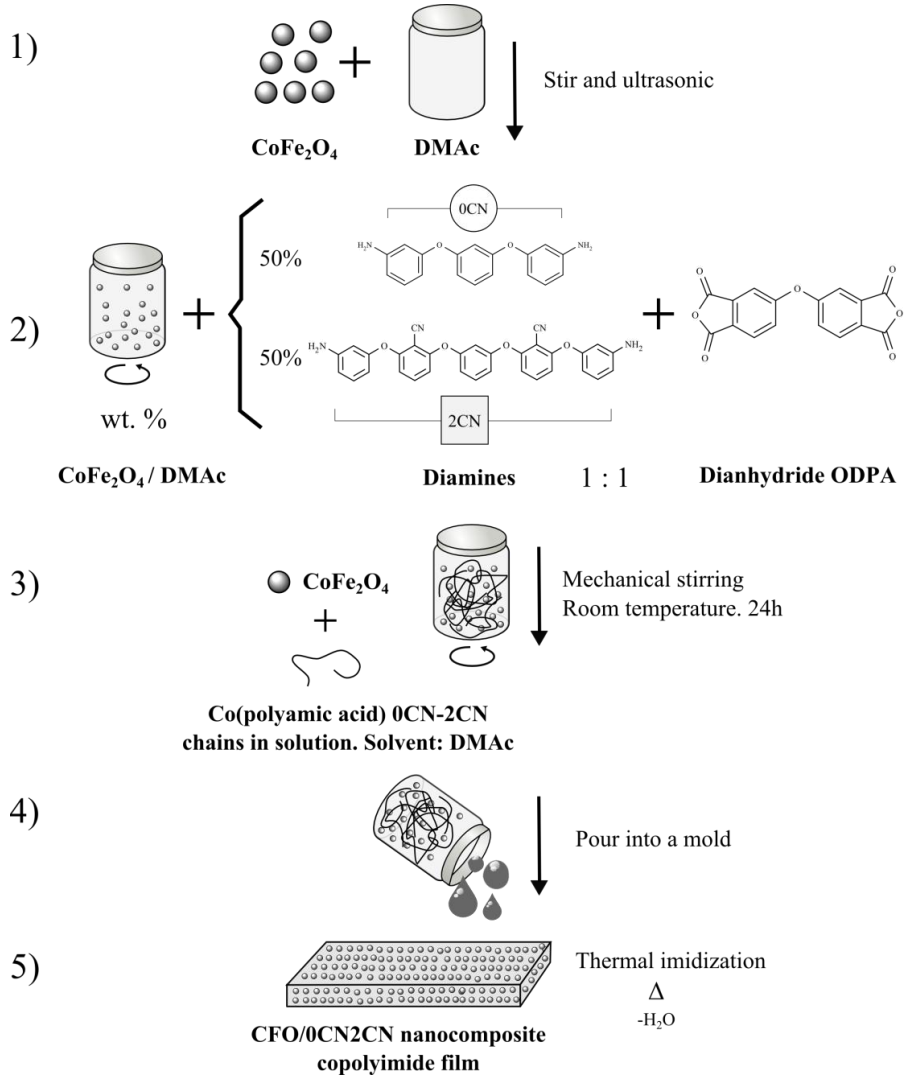

Figure 5.13. Schematic of the polyimide based ME nanocomposites fabrication procedure.

The poling procedure employed was the one optimized in chapter 3 corresponding to the corona poling of copolyimide 50/50 samples. Since the matrix type was the same in both chapters, it was assumed that the optimum conditions were exactly the same as for pristine copolyimide 50/50. The material was heated at 200ºC and an isothermal corona poling of 10 kV was applied during 60 minutes. Later, the material is cooled to room

temperature with the electric field kept on, to maintain the dipoles frozen in the oriented state and the free charges accumulated at the inclusion-matrix interfaces. Finally, the piezoelectric response (d_{33}) of the sample was analyzed with a wide range (d_{33})-meter (model 8000, APC Int Ltd).

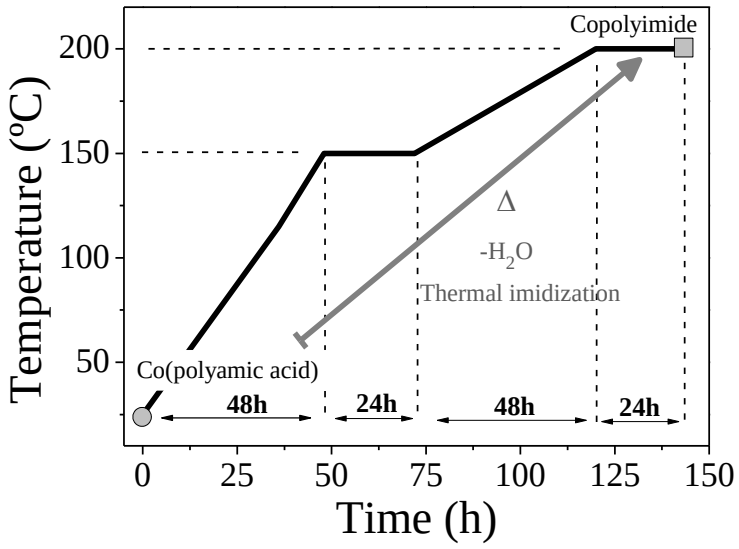

Figure 5.14. Thermal treatment used in the preparation of the CFO/P0CN2CN ME nanocomposites

5.2.2. CHARACTERIZATION OF NANOCOMPOSITES

In polymer nanocomposites there are important factors related with the chosen nanoparticle. For instance, nanoparticles require an interfacial interaction and/or compatibility with the polymer matrix. Second, the proper processing technique should be selected to uniformly disperse and distribute the nanoparticles or nanoparticle aggregates within the polymer matrix. Therefore, in order to verify if our materials fulfil these requirements, they were characterized using several techniques such as DSC, TGA or SEM.

A. THERMAL AND MORPHOLOGICAL CHARACTERIZATION

Since our polyimide based magnetoelectric composites are in principle aimed to temperatures higher than 100ºC, thermal characterization is fundamental to establish the glass transition temperature and degradation temperature, to analyze the suitability of the material. DSC and TG measurements were performed following the specifications defined in chapter 2.

The morphology of the CFO/0CN2CN composites previously coated with gold by magnetron sputtering was studied by scanning electron microscopy (SEM).

B. MAGNETIC AND PIEZOELECTRIC CHARACTERIZATION

Magnetic hysteresis loops at room temperature were measured using an ADE Technologies vibrating sample magnetometer.

Aiming to impart piezoelectric activity in a 0-3 magnetoelectric composite, the material was subjected to a poling process during 60 min of corona poling at 10 kV and at 200 °C in a home-made chamber. After that, the piezoelectric response (d_{33}) of the samples was analyzed with a wide range (d_{33})-meter (model 8000, APC Int Ltd).

C. MAGNETOELECTRIC EFFECT MEASUREMENT

In order to obtain the out-of-plane ME coefficient, DC and AC magnetic fields were applied along the same direction of the electric polarization of the copolyimide, i.e., perpendicular to the composite surface. An AC driving magnetic field varying from 0.5 to 1.5 Oe amplitude at 7 kHz (electromechanical resonance frequency of the composite) was provided by a pair of Helmholtz coils. The DC field with a maximum value of 0.5 T was applied by an electromagnet. The induced ME voltage was measured with a

Standford Research Lock-in amplifier (SR530). The electromechanical resonance was calculated by $f_n \approx (n/2\mathrm{L})\sqrt{E_Y/\rho}$, where L is the length along the resonant direction, n is the order of the harmonic mode, and ρ and E_Y are density and Young's modulus, respectively. Volume fraction and density of the nanocomposites were calculated from the density of the components. In-plane Young's modulus values (E_Y) of the composite films were obtained from the initial slope of strain–stress curves (not shown). The size of the measured samples is 2.5 cm x 1 cm x 150 μm.

Finally, piezoelectric and magnetoelectric responses were measured after thermal annealing for 10 minutes at different temperatures up to 200ºC in order to evaluate the thermal stability of the signals.

5.2. RESULTS AND DISCUSSION

5.2.1. THERMAL AND MORPHOLOGICAL CHARACTERIZATION

The understanding of the nanofiller-polymer interface, the interaction, as well as their effects on long chain dynamics and thermo-mechanical properties of the nanocomposites are topic of great interest. The glass transition temperature (T_g) and degradation temperature (T_d) are important probes for the particle-polymer interface and interaction. Therefore, in order to study the thermal properties of the prepared nanocomoposite films, the effect of the CFO nanoparticles on the thermal stability of the nanocomposite films was investigated by DSC and TGA in the total seven different compositions.

In polymer nanocomposites the effect of nanoparticle inclusion on the glass transition is profound and has been addressed in many occasions. For example, experimental data suggest that the glass transition temperatures of nanocomposites can either go up or go down relative to those of the neat polymer, depending on the nature of the nanoparticle-chain interaction. Sometimes T_g increases compared to that of the pure matrix, suggesting that the mobility of the entire volume of the polymer is restricted by the presence of the nanoparticles [103,104]. However, reduction of T_g has also been reported in the case of weak interactions between filler and polymer [105] and, in other cases, the addition of nanoparticles causes no significant change in the glass transition. There are also examples where an initial increase in T_g is followed by a decrease with increasing nanofiller loading, and vice versa [106].

In our CFO/0CN-2CN nanocomposites, the DSC curves showed an unique T_g for all the samples indicating that they are random copolymers (Figure 5.15 and Table 5.1). Regarding the glass transition temperatures, no clear trend is observed among nanoparticle content and T_g values, but all the compositions showed similar and high T_g

values, around 150–160ºC. This no clear trend is probably due to different polymer molecular weights in the nanocomposites. Moreover, the little value variation with respect to the pure matrix (0% CFO) means that nano-sized filler inclusion has little impact on T_g of the polymer matrix. In addition, it can be observed that the T_g value for the pristine film (0% CFO, T_g= 155 ºC) is quite lower than the Copo 50/50 studied in chapter 3 (T_g= 173.9ºC). This behavior is understandable since the synthetic methods are different and the result cannot be the same. In chapter 3, the poly(amic acid)s were precipitated from cold methanol, decanted, and dried at reduced pressure, before being converted into polyimide by thermal imidization. However, in chapter 5, the reaction mixture ($CoFe_2O_4$ nanoparticles and copoly(amic acid) chains in solution) were directly poured into a mould and subsequently thermally imidizated, avoiding the precipitation in cold methanol. Therefore, it is probable that in the example of chapter 5, the sample had impurities that worked as plasticizers reducing the T_g.

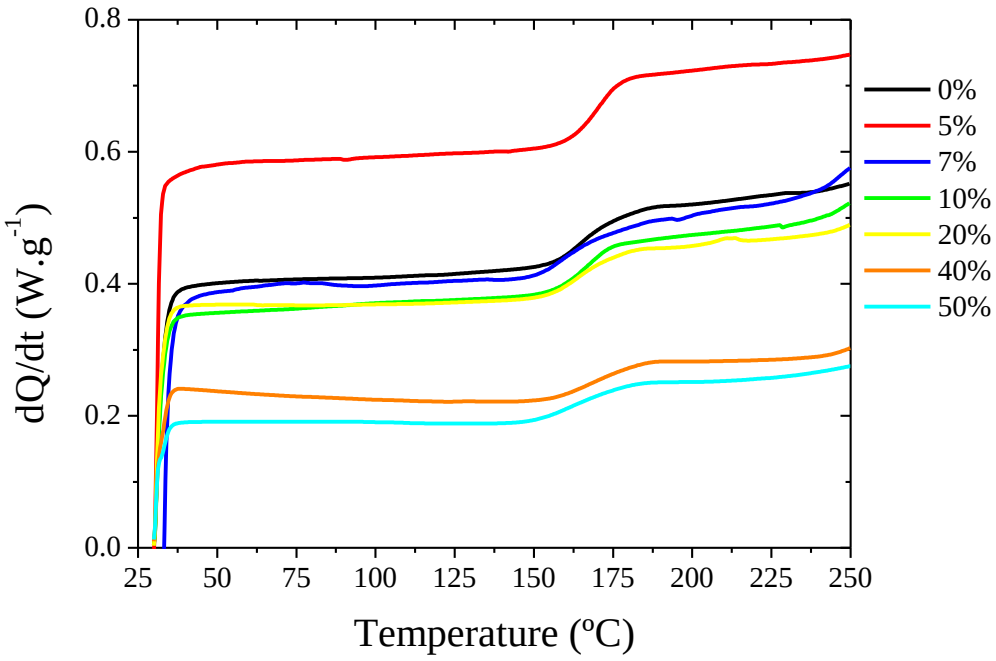

Figure 5.15. DSC curves of CFO/0CN2CN nanocomposites with different ferrite content: 0%, 5%, 7%, 10%, 20%, 40%, and 50 wt.%.

The influence of nanoparticles in the thermal properties of nanocomposites is an important topic of study, because there are cases where inorganic components, such as silica, with inherently good thermal stability, greatly improve the thermal stability of organic materials through forming a cross-linked form between the polyimide and the silica framework [27]. However, there are other examples where the effect is just the contrary. For instance, Wang *et al.* [34] reported the incorporation of AgNPs, functioning as the catalyst in the decomposition of polyimide and accelerating the decomposition of polyimide at a high temperature. Moreover, the introductions of AgNPs occupy a part of the volume of the hybrid system, making it difficult for the end-groups of a polyimide unit to reach another monomer to react, thus shortening the polymer chain. Therefore, the van der Waals forces in the polymer chain decreased, resulting in a decrease in the initial mass reduction temperature of the nanocomposites.

From the TGA curves showed in Figure 5.16, one can observe that the thermal degradation of the pure polyimide and its nanocomposite films ocurred through two degradation steps. The first step, with a 4% of weight loss, is probably caused by the liberation of rest of occluded solvent in the nanocomposites structure and perhaps because of the low molecular weight of the polymer chains. The second step, approximately 40–50% of weight loss, is the main degradation process and occurs around 385–400ºC.

As it can be seen in Table 5.1, the thermal stability of the composites is high and similar to that of the net copolyimide, no clear dependence being observed with the nanoparticle content. The only influence of CFO's is a decrease in the weight residue percentage at 900ºC, showing all the CFO/0CN2CN nanocomposites less percentage (46-54%) than the pristine 0CN2CN (0% CFO), with a 57%.

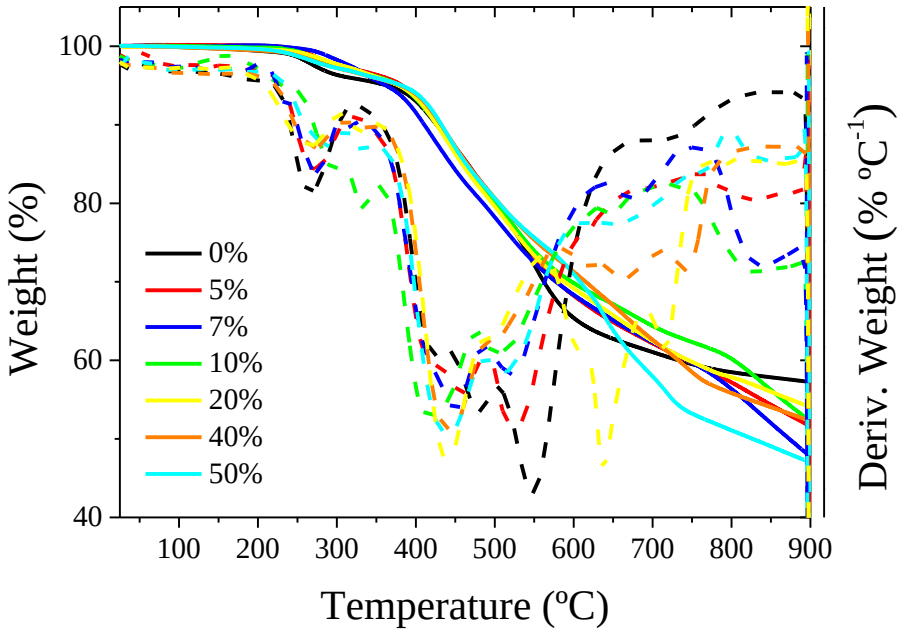

Figure 5.16. TGA (solid) and DTG (dash) curves of the nanocomposites.

Table 5.1. Glass transition temperature (T_g) and degradation temperature (T_d) results.

Sample	T_g	T_d1	T_d2
0%	155	243	392
5%	153	249	392
7%	160	274	383
10%	160	244	388
20%	155	254	400
40%	154	234	404
50%	150	229	405

A reliable magnetoelectric material must show a balance between its capacity as sensor-transductor and its mechanical properties. Therefore, in this chapter we analyzed several percentages of ferrite nanoparticles with the aim to choose the best option. Although several concentrations were analyzed (0, 5, 7, 10, 20, 40 and 50 wt%), we concluded that the optimum concentration was around 10 weight percentage (wt.%) since this concentration allows suitable nanoparticle dispersion to obtain ME response without affecting composites easy shaping, flexibility and lightweight.

According to that, we observed that the nanocomposites, as they increase their content in CFO, showed a decrease in their mechanical properties. This was especially evident for the 40 and 50% samples, where the loss of flexibility was visible to the naked eye. In addition, in the composite with 20% the poling was limited by the excessive presence of inclusions, because to conserve the capability to be poled, the nanocomposite must remain insulator (dielectric). On the other hand, it seems clear that the presence of higher content of magnetostrictive elements would be necessary for measuring a higher magnetoelectric effect. That is why, to find a compromise among the compulsory requirements, we decided that the best option for an initial analysis would be the nanocomposites with a 10% of cobalt ferrite nanoparticles. In conclusion, the optimum concentration was around 10 weight percentage (wt.%) since this concentration allows suitable nanoparticle dispersion to obtain ME response without affecting composites easy shaping, flexibility and lightweight [45,82,101]. From now on, the rest of characterization and measurements will be devoted only to this composition.

Figure 5.17 shows a SEM image of the sample with 10% CFO, wherein the CFO nanoparticles are well distributed within the polymer matrix 0CN2CN, not being significantly altered the structure of the polyimide by the addition of CFO nanoparticles [107]. The inset of Figure 5.17b reveals that the average size of the CFO agglomerates is ≈100 nm corresponding to the size of two CFO nanoparticles. Such agglomeration will not have any negative effect in the ME response of the resulting nanocomposite [101].

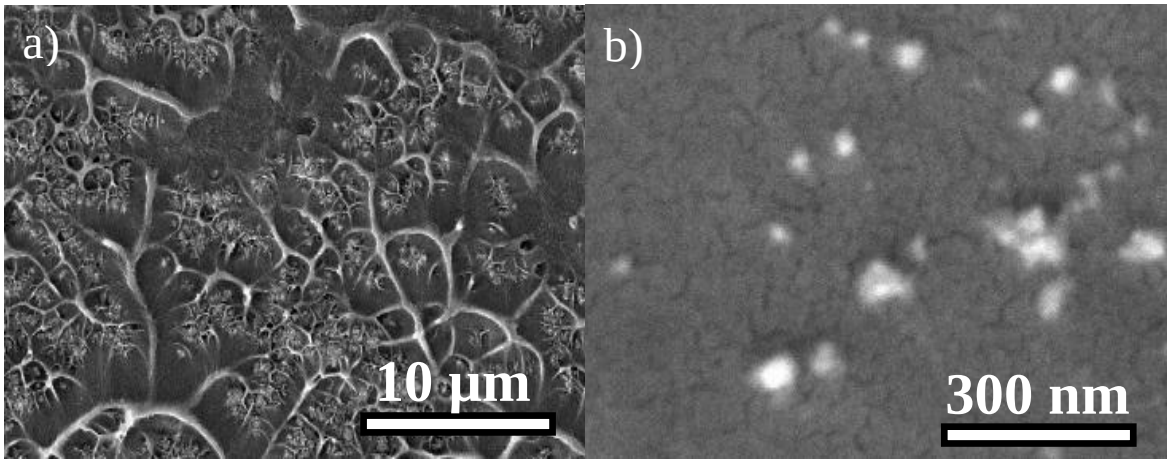

Figure 5.17. a) SEM image of CFO/0CN2CN nanocomposites with 10 wt.% ferrite content; b) Detail of the CFO nanoparticle distribution in the 0CN2CN matrix. The inset shows the size distribution of the CFO agglomerates/nanoparticles.

5.2.2. MAGNETIC AND PIEZOELECTRIC CHARACTERIZATION

The magnetic hysteresis loop of the 10%CFO/0CN2CN composite is presented in Figure 5.18.

The shape and magnetization maximum value (6 emu·g^{-1} that corresponds to ≈10% of the maximum magnetization of the pure CFO nanoparticles) of the measured hysteresis loop demonstrates that magnetic particles are randomly oriented and well distributed within the polymer matrix. A coercive field of ≈0.2 T was measured (Figure 5.18b). Additionally it can be noted that contrary to what was reported for other magnetic nanoparticles [108], the nanoparticle magnetic response is independent of the nanoparticle aggregation state, at least with respect to clusters up to ~5 nanoparticles [101].

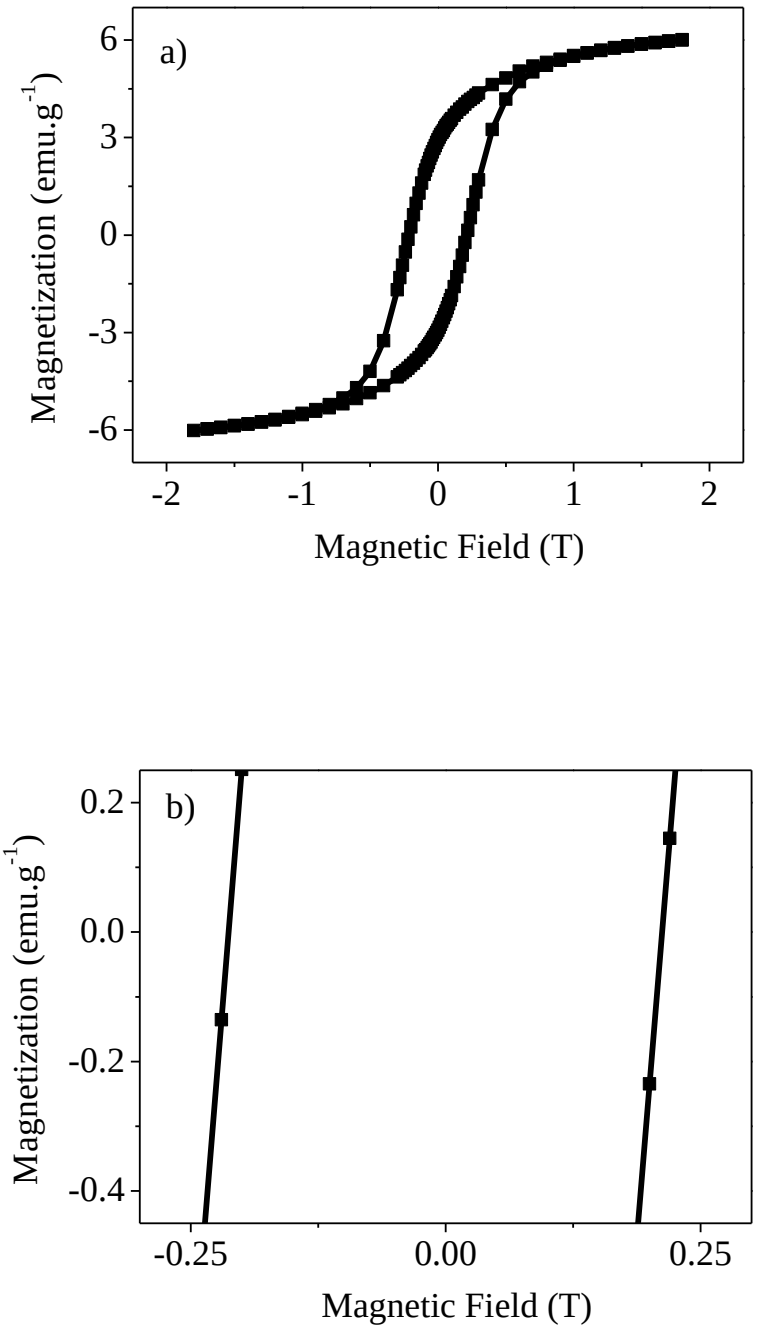

Figure 5.18. a) Room temperature hysteresis loop measured for the CFO/0CN2CN nanocomposite with 10 wt.% ferrite content; b) Magnification of Figure 3a.

After poling, the piezoelectric response over time as well as in function of temperature) of the CFO/0CN2CN composite was studied and shown in Figure 5.19.

Figure 5.19 reveals that the piezoelectric response of the 0CN2CN polymer matrix (≈11 $pC \cdot N^{-1}$) suitably compares with the piezoelectric response of the best piezoelectric polymers [52] and starts to decrease only when the composite is subjected to temperatures above 130ºC (Figure 5.19a). The piezoelectric response disappears completely when the sample is exposed to temperatures higher than 190ºC, which is related to the increase polymer chain mobility around the glass transition temperature of the polymer (≈155ºC) [14].

Additionally, such response is stable over time, as evaluated for a 2 months period (Figure 5.19b).

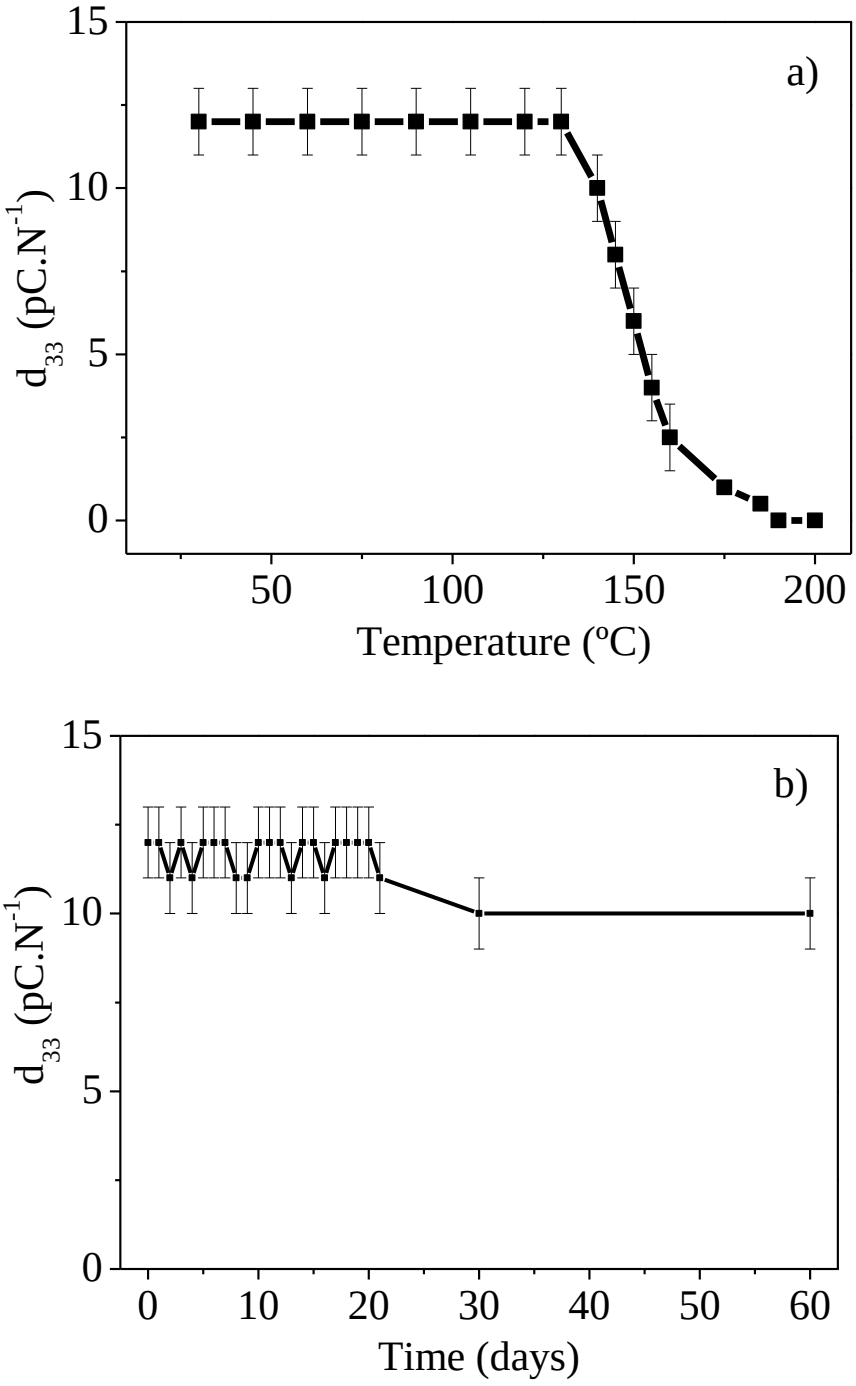

Figure 5.19 a) Piezoelectric response over time measured for the CFO/0CN2CN nanocomposites with 10 wt.% ferrite content; b) piezoelectric response after thermal annealing of the CFO/0CN2CN nanocomposites with 10 wt.% ferrite content.

5.2.3. MAGNETOELECTRIC EFFECT MEASUREMENT

Finally, the ME voltage coefficient (α_{33}) of the 10%CFO/OCN2CN was measured as a function of both the applied DC and AC magnetic fields (Figure 5.20).

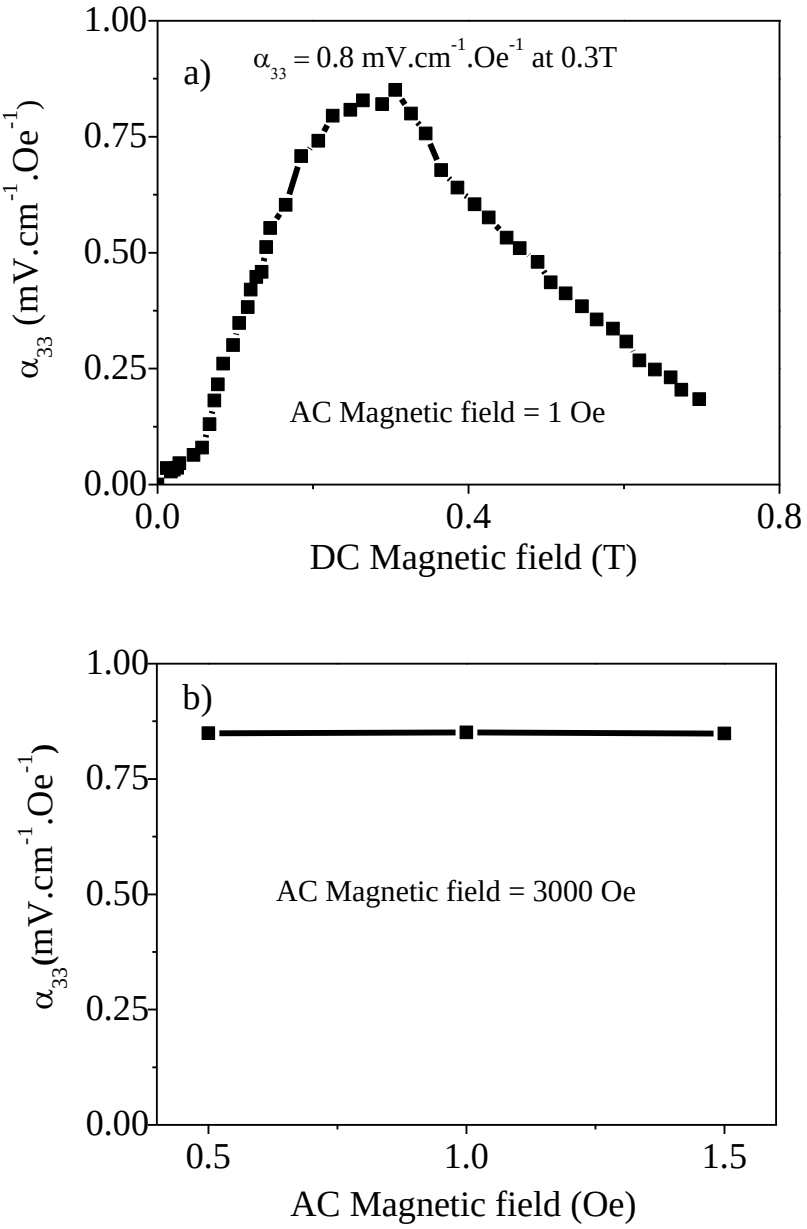

Figure 5.20. Room temperature ME coefficients as a function of a) DC magnetic field (measured at 1 Oe AC magnetic field) and b) AC magnetic field (measured at 3000 Oe DC magnetic field)

Figure 5.20a shows that the α_{33} value increases with the applied DC magnetic field until reaching its maximum value (0.8 mV cm^{-1} Oe^{-1}) at the ME peak (≈0.3 T); increasing the magnetic field further leads to a decrease in the α_{33}. Further, the α_{33} value is stable for AC fields up to 1.5 Oe. Despite this ME voltage coefficient value being two orders of magnitude lower than the highest α_{33} obtained in polymer based multiferroic nanocomposites [82], this value also remains stable when the samples are subjected to annealing temperatures up to 130ºC, which proves its suitability for applications in high temperatures devices.

5.3. CONCLUSIONS

All nanocomposite compositions showed quite high glass transition temperature and good thermal stability in our working range.

By the introduction of 10wt.% of CFO nanoparticles into a polymer matrix composed of 0CN/2CN amines, high temperature ME nanocomposites have been successfully developed by combining the magnetostrictive properties of the filler and the piezoelectric properties of the polymer matrix.

The resulting composite shows a maximum magnetization value of 6 $emu.g^{-1}$, a piezoelectric d_{33} coefficient of 11 pC N^{-1} (stable over time and temperatures up to 130ºC and a maximum magnetoelectric voltage coefficient of 0.8 $mV.cm^{-1}.Oe^{-1}$.

Such features evidence the applicability of this material to be used on high-temperature magnetoelectric technological devices in areas such as automobile industry, biomedical and machinery.

5.4. REFERENCES

[1] Ajayan PM, Schadler LS, Braun P V. Nanocomposite science and technology. Weinheim, FRG: Wiley-VCH Verlag GmbH & Co. KGaA; 2003.

[2] Koo J. Polymer nanocomposites: processing, characterization, and applications. McGraw Hill Professional; 2006.

[3] Paul DR, Robeson LM. Polymer nanotechnology: nanocomposites. Polymer (Guildf) 2008;49:3187–204.

[4] Mai Y-W, Yu Z-Z. Polymer nanocomposites. Elsevier Science; 2006.

[5] Nelson JK. Dielectric polymer nanocomposites. Springer Science & Business Media; 2009.

[6] Mittal KL, editor. Polyimides and other high temperature polymers: synthesis, characterization and applications, Volumen 3. 2005.

[7] Yoon J-Y, Kim YH, Ka J-W, Hong S-K, Yi MH, Jang K-S. A high-temperature resistant polyimide gate insulator surface-modified with a YOx interlayer for high-performance, solution-processed Li-doped ZnO thin-film transistors. J Mater Chem C 2014;2:2191.

[8] Furukawa N, Yuasa M, Omori F, Yamada Y. Adhesive properties of siloxane modified polyimides and application for multi-layer printed circuit boards. J Adhes 1996;59:281–94.

[9] Usui M, Ishibashi S, Hirata H, Ishizawa S, Koshoubu N, Hayashi T, et al. Opto-electronic chip-on-film packaging technology using low-CTE fluorinated polyimide optical waveguide films. IEEE Trans Components, Packag Manuf Technol 2014;4:1582–8.

[10] Kuntman A, Kuntman H. A study on dielectric properties of a new polyimide film suitable for interlayer dielectric material in microelectronics applications. Microelectronics J 2000;31:629–34.

[11] Kurmvanshi SK, Patel PR, Patel AK, Bajpai R, Keller JM. Polyimide/tetraethoxysilane-based hybrid polyfilms for microelectronics application. Microsyst Technol 2012;18:603–11.

[12] Pan H, Zhang Y, Pu H, Chang Z. Organic–inorganic hybrid proton exchange membrane based on polyhedral oligomeric silsesquioxanes and sulfonated polyimides containing benzimidazole. J Power Sources 2014;263:195–202.

[13] Wiegand JR, Smith ZP, Liu Q, Patterson CT, Freeman BD, Guo R. Synthesis and characterization of triptycene-based polyimides with tunable high fractional free volume for gas separation membranes. J Mater Chem A 2014;2:13309.

[14] Gutierrez J, Lasheras A, Barandiaran JM, Vilas JL, Maceiras A, Leon LM. Improving the performance of high temperature piezopolymers for magnetoelectric applications. Mater Appl Sensors Transducers II 2013;543:439–

42.

[15] Schab-Balcerzak E, Konieczkowska J, Siwy M, Sobolewska A, Wojtowicz M, Wiacek M. Comparative studies of polyimides with covalently bonded azo-dyes with their supramolecular analoges: thermo-optical and photoinduced properties. Opt Mater (Amst) 2014;36:892–902.

[16] Lee BKM, Koerner H, Wang DH, Tan L-S, White TJ, Vaia RA. Tailoring the photomechanical response of glassy, azobenzene-functionalized polyimides by physical aging. Macromolecules 2012;45:7527–34.

[17] Hsiao S-H, Chou Y-T. Synthesis and electrochromic properties of aromatic polyamides with pendent triphenylamine units. Macromol Chem Phys 2014;215:958–70.

[18] Ji D, Jiang L, Cai X, Dong H, Meng Q, Tian G, et al. Large scale, flexible organic transistor arrays and circuits based on polyimide materials. Org Electron 2013;14:2528–33.

[19] Yen H-J, Chen C-J, Liou G-S. Flexible multi-colored electrochromic and volatile polymer memory devices derived from starburst triarylamine-based electroactive polyimide. Adv Funct Mater 2013;23:5307–16.

[20] Lim J-W, Cho D-Y, Eun K, Choa S-H, Na S-I, Kim J, et al. Mechanical integrity of flexible Ag nanowire network electrodes coated on colorless PI substrates for flexible organic solar cells. Sol Energy Mater Sol Cells 2012;105:69–76.

[21] Zhang K, Niu H, Wang C, Bai X, Lian Y, Wang W. Novel aromatic polyimides with pendent triphenylamine units: Synthesis, photophysical, electrochromic properties. J Electroanal Chem 2012;682:101–9.

[22] Grucela-Zajac M, Filapek M, Skorka L, Bijak K, Smolarek K, Mackowski S, et al. Photophysical, electrochemical and thermal properties of new (co)polyimides incorporating oxadiazole moieties. Synth Met 2014;188:161–74.

[23] Yen H-J, Wu J-H, Wang W-C, Liou G-S. High-efficiency photoluminescence wholly aromatic triarylamine-based polyimide nanofiber with aggregation-induced emission enhancement. Adv Opt Mater 2013;1:668–76.

[24] Gorkovenko AI, Plekhanov AI, Simanchuk AE, Yakimanskii A V., Smirnov NN, Solovskaya NA, et al. Nonlinear optical properties of chromophore-containing polyimides with covalently attached dyes. Optoelectron Instrum Data Process 2014;50:96–101.

[25] San Sebastian M, Martinez-Martinez V, Maceiras A, Vilas JL, Lopez-Arbeloa I, Leon LM. Enhanced charge-transfer emission in polyimides by cyano-groups doping. J Phys Chem B 2015;119:5685–92.

[26] Wang J, Jiao Q, Li H, Zhao Y, Guo B. In situ preparation of polyimide/amino-functionalized carbon nanotube composites and their properties. Polym Compos 2014;35:1952–9.

[27] Ye X, Wang J, Xu Y, Niu L, Fan Z, Gong P, et al. Mechanical properties and thermostability of polyimide/mesoporous silica nanocomposite via effectively

using the pores. J Appl Polym Sci 2014;131:n/a – n/a.

[28] Jiang X, Bin Y, Matsuo M. Electrical and mechanical properties of polyimide–carbon nanotubes composites fabricated by in situ polymerization. Polymer (Guildf) 2005;46:7418–24.

[29] Wang J, Iroh JO, Hall S. Effect of polyaniline-modified clay on the processing and properties of clay polyimide nanocomposites. Appl Clay Sci 2014;99:215–9.

[30] Tabatabaei-Yazdi Z, Mehdipour-Ataei S. Poly(ether-imide) and related sepiolite nanocomposites: investigation of physical, thermal, and mechanical properties. Polym Adv Technol 2015;26:308–14.

[31] Qian Y, Lan Y, Xu J, Ye F, Dai S. Fabrication of polyimide-based nanocomposites containing functionalized graphene oxide nanosheets by in-situ polymerization and their properties. Appl Surf Sci 2014;314:991–9.

[32] Ye X, Gong P, Wang J, Wang H, Ren S, Yang S. Fluorinated graphene reinforced polyimide films with the improved thermal and mechanical properties. Compos Part A Appl Sci Manuf 2015;75:96–103.

[33] Choi DJ, Maeng JS, Ahn K-O, Jung MJ, Song SH, Kim Y-H. Synthesis of Cu or Cu2O-polyimide nanocomposites using Cu powders and their optical properties. Nanotechnology 2014;25:375604.

[34] Wang L, Li J, Wang D, Wang D, Li H. Preparation and properties of core–shell silver/polyimide nanocomposites. Polym Bull 2014;71:2661–70.

[35] Hamciuc E, Hamciuc C, Bacosca I, Cristea M, Okrasa L. Thermal and electrical properties of nitrile-containing polyimide/BaTiO3 composite films. Polym Compos 2011;32:846–55.

[36] Sakamoto M, Nohara S, Miyatake K, Uchida M, Watanabe M, Uchida H. Effects of incorporation of SiO2 nanoparticles into sulfonated polyimide electrolyte membranes on fuel cell performance under low humidity conditions. Electrochim Acta 2014;137:213–8.

[37] Ahmad MB, Gharayebi Y, Salit MS, Hussein MZ, Shameli K, Dehzangi A, et al. Effect of SiO2 particles on dispersion of montmorillonite (MMT) in polyimide nanocomposite during thermal imidization. Res Chem Intermed 2013;41:1657–71.

[38] Chang C-C, Hong S-Y, Cheng L-P, Yu Y-Y. TiO2 nanoparticles synthesized in an aprotic solvent and applied to prepare high-refractive-index TiO2-polyimide hybrid thin films. J Sol-Gel Sci Technol 2014;71:129–35.

[39] Nam K-H, Seo J, Seo K, Jang W, Han H. Residual stress behavior and physical properties of transparent polyimide/surface-modified CaCO3 nanocomposite films. Macromol Res 2014;22:669–77.

[40] Mazuera D, Perales O, Suarez M, Singh S. Synthesis, characterization and thermal analysis of polyimide–cobalt ferrite nanocomposites. Mater Sci Eng A 2010;527:6393–9.

[41] García-Cerda LA, Escareño-Castro MU, Salazar-Zertuche M. Preparation and characterization of polyvinyl alcohol–cobalt ferrite nanocomposites. J Non Cryst Solids 2007;353:808–10.

[42] Harris VG, Geiler A, Chen Y, Yoon SD, Wu M, Yang A, et al. Recent advances in processing and applications of microwave ferrites. J Magn Magn Mater 2009;321:2035–47.

[43] Paulsen JA, Ring AP, Lo CCH, Snyder JE, Jiles DC. Manganese-substituted cobalt ferrite magnetostrictive materials for magnetic stress sensor applications. J Appl Phys 2005;97:044502.

[44] Wang J, Li Z, Shen Y, Lin Y, Nan CW. Enhanced magnetoelectric coupling in Pb(Zr0.52Ti0.48)O3 film-on-CoFe2O4 bulk ceramic composite with LaNiO3 bottom electrode. J Mater Sci 2012;48:1021–6.

[45] Martins P, Lasheras A, Gutierrez J, Barandiaran JM, Orue I, Lanceros-Mendez S. Optimizing piezoelectric and magnetoelectric responses on CoFe2O4/P(VDF-TrFE) nanocomposites. J Phys D Appl Phys 2011;44:495303.

[46] Martins P, Costa CM, Benelmekki M, Botelho G, Lanceros-Méndez S. Interface characterization and thermal degradation of ferrite/poly(vinylidene fluoride) multiferroic nanocomposites. J Mater Sci 2012;48:2681–9.

[47] Spaldin NA. Magnetic materials: fundamentals and applications. Cambridge University Press; 2010.

[48] Ounaies Z, Young JA, Simpson JO, Farmer BL. Dielectric properties of piezoelectric polyimides. NASA Langley Technical Report Server; 1996.

[49] Harrison JS, Ounaies Z. Piezoelectric polymers; NASA Cr2001-21142. Hampton, Virgina: 2001.

[50] Harrison JS, Ounaies Z. Piezoelectric polymers; NASA/Cr 2001-21142. ICASE Report No. 2001-43. John Wiley & Sons, Inc.; 2002.

[51] Park C, Ounaies Z, Wise KE, Harrison JS. In situ poling and imidization of amorphous piezoelectric polyimides. Polymer (Guildf) 2004;45:5417–25.

[52] Martins P, Lopes AC, Lanceros-Mendez S. Electroactive phases of poly(vinylidene fluoride): determination, processing and applications. Prog Polym Sci 2014;39:683–706.

[53] Nalwa HS, editor. Ferroelectric polymers: chemistry, physics, and applications. Marcell Dekker, Incorporated; 1995.

[54] Park C, Ounaies Z, Su J, Smith Jr. JG, Harrison JS. Polarization stability of amorphous piezoelectric polyimides; Piezoelectric polymers; NASA/Cr 2001-21142. ICASE Report No. 99-53. 1999.

[55] Ueda H, Carr SH. Piezoelectricity in polyacrylonitrile. Polym J 1984;16:661–7.

[56] Miyata S, Yoshikawa M, Tasaka S, Ko M. Piezoelectricity revealed in the copolymer of vinylidene cyanide and vinyl acetate. Polym J 1980;12:857–60.

[57] Tasaka S, Inagaki N, Okutani T, Miyata S. Structure and properties of amorphous piezoelectric vinylidene cyanide copolymers. Polymer (Guildf) 1989;30:1639–42.

[58] Sakurai M, Ohta Y, Inouje Y, Chujo R. An important factor generating piezoelectric activity of vinylidene cyanide copolymers. Polym Commun 1991;32:397–9.

[59] San Sebastian M, Gonzalo B, Breczewski T, Vilas JL, Perez-Jubindo MA, De La Fuente MR, et al. Frozen polarization of piezoelectric polyimides. Ferroelectrics 2009;389:114–21.

[60] Ma J, Hu JM, Li Z, Nan CW. Recent progress in multiferroic magnetoelectric composites: from bulk to thin films. Adv Mater 2011;23:1062–87.

[61] Eerenstein W, Mathur ND, Scott JF. Multiferroic and magnetoelectric materials. Nature 2006;442:759–65.

[62] Wang Y, Hu J, Lin Y, Nan C-W. Multiferroic magnetoelectric composite nanostructures. NPG Asia Mater 2010;2:61–8.

[63] Hill NA. Why are there so few magnetic ferroelectrics? J Phys Chem B 2000;104:6694–709.

[64] Neaton JB, Ederer C, Waghmare U V, Spaldin NA, Rabe KM. First-principles study of spontaneous polarization in multiferroic BiFeO3. Phys Rev B 2005;71:14113.

[65] Cheong S-W, Mostovoy M. Multiferroics: a magnetic twist for ferroelectricity. Nat Mater 2007;6:13–20.

[66] Nan C-W, Bichurin MI, Dong S, Viehland D, Srinivasan G. Multiferroic magnetoelectric composites: historical perspective, status, and future directions. J Appl Phys 2008;103:031101.

[67] Liang WI, Liu Y, Liao SC, Wang WC, Liu HJ, Lin HJ, et al. Design of magnetoelectric coupling in a self-assembled epitaxial nanocomposite via chemical interaction. J Mater Chem C 2014;2:811–5.

[68] Lee EW. Magnetostriction and magnetomechanical effects. Reports Prog Phys 1955;18:184.

[69] Barandiarán JM, Gutiérrez J, García-Arribas A. Magneto-elasticity in amorphous ferromagnets: Basic principles and applications. Phys Status Solidi 2011;208:2258–64.

[70] Shah J, Kotnala RK. Induced magnetism and magnetoelectric coupling in ferroelectric BaTiO3 by Cr-doping synthesized by a facile chemical route. J Mater Chem A 2013;1:8601.

[71] Lefevre C, Roulland F, Thomasson A, Meny C, Porcher F, André G, et al. Magnetic and polar properties' optimization in the magnetoelectric Ga2– x Fex O3 compounds. J Phys Chem C 2013;117:14832–9.

[72] Bichurin M, Viehland D. Magnetoelectricity in composites. vol. 11. CRC Press;

2011.

[73] Ryu J, Priya S, Carazo AV, Uchino K, Kim H-E. Effect of the magnetostrictive layer on magnetoelectric properties in lead zirconate titanate/terfenol-D laminate composites. J Am Ceram Soc 2001;84:2905–8.

[74] Shi Z, Nan C-W, Liu J, Filippov D, Bichurin M. Influence of mechanical boundary conditions and microstructural features on magnetoelectric behavior in a three-phase multiferroic particulate composite. Phys Rev B 2004;70:134417.

[75] Nan C-W, Clarke DR. Effective properties of ferroelectric and/or ferromagnetic composites: a unified approach and its application. J Am Ceram Soc 2005;80:1333–40.

[76] Pan E, Chen W. Static green's functions in anisotropic media. Cambridge University Press; 2015.

[77] Srinivas S, Li JY, Zhou YC, Soh AK. The effective magnetoelectroelastic moduli of matrix-based multiferroic composites. J Appl Phys 2006;99:043905.

[78] Xiong S-M, Hou P-F. Magneto-electro-thermoelastic problems: fundamental solutions and green's function. Encycl Therm Stress 2014:2827–35.

[79] Bichurin MI, Kornev IA, Petrov VM, Lisnevskaya I V. Investigation of magnetoelectric interaction in composite. Ferroelectrics 1997;204:289–97.

[80] Newnham RE, Skinner DP, Cross LE. Connectivity and piezoelectric-pyroelectric composites. Mater Res Bull 1978;13:525–36.

[81] Nan CW, Li M, Huang JH. Calculations of giant magnetoelectric effects in ferroic composites of rare-earth–iron alloys and ferroelectric polymers. Phys Rev B 2001;63:144415.

[82] Martins P, Lanceros-Méndez S. Polymer-based magnetoelectric materials. Adv Funct Mater 2013;23:3371–85.

[83] Bharathi KK, Markandeyulu G, Ramana C V. Structural, magnetic, electrical, and magnetoelectric properties of Sm- and Ho-substituted nickel ferrites. J Phys Chem C 2011;115:554–60.

[84] Fukada E. Recent developments of polar piezoelectric polymers. IEEE Trans Dielectr Electr Insul 2006;13:1110–9.

[85] Abderrahmane A, Koide S, Sato S-I, Ohshima T, Sandhu A, Okada H. Robust hall effect magnetic field sensors for operation at high temperatures and in harsh radiation environments. IEEE Trans Magn 2012;48:4421–3.

[86] Ueno T, Higuchi T. Magnetic sensor for high temperature using a laminate composite of magnetostrictive material and piezoelectric material. In: Armstrong WD, editor. Smart Struct. Mater., International Society for Optics and Photonics; 2005, p. 156–63.

[87] Moglia RS, Robinson JL, Muschenborn AD, Touchet TJ, Maitland DJ, Cosgriff-Hernandez E. Injectable PolyMIPE scaffolds for soft tissue regeneration. Polymer (Guildf) 2014;56:426–34.

[88] Tang Z, Xiong Y, Tang M, Xiao Y, Zhang W, Yuan M, et al. Temperature dependence of magnetoelectric effect in Bi3.15Nd0.85Ti3O12–La0.7Ca0.3MnO3 multiferroic composite films buffered by a LaNiO3 layer. J Mater Chem C 2014;2:1427.

[89] Sencadas V, Lanceros-Méndez S, Sabater i Serra R, Andrio Balado A, Gómez Ribelles JL. Relaxation dynamics of poly(vinylidene fluoride) studied by dynamical mechanical measurements and dielectric spectroscopy. Eur Phys J E Soft Matter 2012;35:41.

[90] Gutierrez J, Lasheras A, Barandiaran JM, Vilas JL, San Sebastian M, Leon LM. Improving the magnetoelectric response of laminates containing high temperature piezopolymers. IEEE Trans Magn 2013;49:42–5.

[91] Wong CK, Shin FG. Role of interfacial charge in the piezoelectric properties of ferroelectric 0-3 composites. J Appl Phys 2005;97:034111.

[92] Bichurin MI, Petrov VM, Kiliba Y V., Srinivasan G. Magnetic and magnetoelectric susceptibilities of a ferroelectric/ferromagnetic composite at microwave frequencies. Phys Rev B 2002;66:134404.

[93] Bichurin MI, Petrov VM, Averkin S V., Liverts E. Present status of theoretical modeling the magnetoelectric effect in magnetostrictive-piezoelectric nanostructures. Part II: Magnetic and magnetoacoustic resonance ranges. J Appl Phys 2010;107:053905.

[94] Filippov DA, Bichurin MI, Petrov VM, Laletin VM, Poddubnaya NN, Srinivasan G. Giant magnetoelectric effect in composite materials in the region of electromechanical resonance. Tech Phys Lett 2004;30:6–8.

[95] Lasheras A. Magnetoelasticidad y efecto magnetoeléctrico en materiales hibridos. University of the Basque Country (UPV/EHU), 2010.

[96] Grimes CA, Roy SC, Rani S, Cai Q. Theory, instrumentation and applications of magnetoelastic resonance sensors: a review. Sensors (Basel) 2011;11:2809–44.

[97] Wong CK, Shin FG. Effect of inclusion deformation on the magnetoelectric effect of particulate magnetostrictive/piezoelectric composites. J Appl Phys 2007;102:063908.

[98] Wong CK, Poon YM, Shin FG. Explicit formulas for effective piezoelectric coefficients of ferroelectric 0-3 composites. J Appl Phys 2001;90:4690.

[99] Zhou Y, Shin FG. Modeling of magnetostriction in particulate composite materials. IEEE Trans Magn 2005;41:2071–6.

[100] Zheng XJ, Liu XE. A nonlinear constitutive model for Terfenol-D rods. J Appl Phys 2005;97:053901.

[101] Martins P, Gonçalves R, Lanceros-Mendez S, Lasheras A, Gutiérrez J, Barandiarán JMM. Effect of filler dispersion and dispersion method on the piezoelectric and magnetoelectric response of CoFe2O4/P(VDF-TrFE) nanocomposites. Appl Surf Sci 2014;313:215–9.

[102] Fan Y, Shi W, Zhang X, Huang Y. Mesoporous material-based manipulation of the enzyme-like activity of CoFe2O4 nanoparticles. J Mater Chem A 2014;2:2482.

[103] Rittigstein P, Torkelson JM. Polymer–nanoparticle interfacial interactions in polymer nanocomposites: Confinement effects on glass transition temperature and suppression of physical aging. J Polym Sci Part B Polym Phys 2006;44:2935–43.

[104] Shang X, Zhu Z, Yin J, Ma X. Compatibility of soluble polyimide/silica hybrids hnduced by a coupling agent. Chem Mater 2002;14:71–7.

[105] Ash B. J, Schadler L. S, Siegel R. W. Glass transition behavior of alumina/polymethylmethacrylate nanocomposites. Mater Lett 2002;55:83–7.

[106] Zou H, Wu S, Shen J. Polymer/silica nanocomposites: preparation, characterization, properties, and applications. Chem Rev 2008;108:3893–957.

[107] Ma X, Lee N-H, Oh H-J, Hwang J-S, Kim S-J. Preparation and characterization of silica/polyamide-imide nanocomposite thin films. Nanoscale Res Lett 2010;5:1846–51.

[108] Huang J, Zhong X, Wang L, Yang L, Mao H. Improving the magnetic resonance imaging contrast and detection methods with engineered magnetic nanoparticles. Theranostics 2012;2:86–102.

Chapter 6.

Electrospun polyimide for polymer membranes in Li-ion battery applications

In this chapter novel types of polyimides (with and without –CN dipolar groups) have been prepared by electrospinning technique. The different prepared membranes were characterized for determining their usability as separators in rechargeable lithium-ion battery applications. Their average fiber diameter and porosity was determined by SEM and the method of dry-wet weight, respectively. The thermal stability, uptake, tortuosity and ionic conductivity values were determined by thermogravimetric analysis and impedance spectroscopy. The batteries performance was tested by measuring their C-rate and cyclability performance.

6.1. INTRODUCTION

There are many different kinds of batteries, but they all function based on the same idea. "A **battery** is a device that is able to store electrical energy in the form of chemical energy, and convert that energy into electricity". A battery consists of two or more electrochemical cells. Each cell has a positive terminal, or cathode, and a negative terminal, or anode. The terminal marked positive $(+)$ is at a higher electrical potential energy than is the terminal marked negative $(-)$.

There are three compulsory components in a battery: two terminals made of different chemicals, the anode and the cathode, and the electrolyte, which separates these terminals. The electrolyte is a chemical medium that allows the flow of electrical charge between the cathode and anode. When a device (light bulb or an electric circuit) is connected to a battery chemical reactions occur on the electrodes that create a flow of electrical energy to the device. During a discharge of electricity, the chemical on the anode releases electrons to the negative terminal and ions in the electrolyte through what's called an oxidation reaction. Meanwhile, at the positive terminal, the cathode accepts electrons, completing the circuit for the flow of electrons. The electrolyte is there to put the different chemicals of the anode and cathode into contact with one another, in a way that the chemical potential can equilibrate from one terminal to the other, converting stored chemical energy into useful electrical energy. That is, the ions transport current through the electrolyte and, at the same time, the electrons flow in the external circuit.

If the battery is disposable, it will produce electricity until it runs out of reactants (same chemical potential on both electrodes). These batteries only work in one direction, transforming chemical energy to electrical energy. But in other types of batteries, the reaction can be reversed. Rechargeable batteries are designed so that electrical energy from an outside source can be applied to the chemical system, and reverse its operation, restoring the battery's charge [1–3].

While some ancient societies may have first developed this kind of devices (the so-called Baghdad Battery is probably dated 200 BC), its "invention" in modern times is

ascribed to Alessandro Volta in the beginning of the 19th century. Since then many different types of batteries have been developed. Batteries come in many shapes and sizes, from miniature cells used to power MP3 players or mobile phones, to battery banks the size of rooms that provide standby power for computer data centers.

Depending on the origin of the energy source, there are different types of batteries, which are summarized in the scheme of Figure 6.1: chemical batteries, (produce electric energy by chemical reaction), physical batteries (produce electric energy by physical change) and biological batteries (produce electric energy by biochemical reaction).

Chemical batteries can be divided into three categories: primary and secondary batteries and, fuel batteries. A primary battery is a disposable kind of battery. Once used, it cannot be recharged. Secondary batteries are rechargeable batteries. Once empty, it can be recharged again. This charging and discharging can happen many times depending on the battery type. Alkaline batteries, Mercury batteries, Silver-Oxide batteries, and Zinc carbon batteries are examples of primary batteries whereas Lead-Acid batteries and Lithium batteries fall into the secondary battery's category.

A fuel cell is a device that converts the chemical energy from a fuel into electricity through a chemical reaction of positively charged hydrogen ions with oxygen or another oxidizing agent. Fuel cells are different from primary and secondary batteries in that they require a continuous source of fuel and oxygen or air to sustain the chemical reaction, whereas in a battery the chemicals present in the battery react with each other to generate an electromotive force.

A biologic battery or bio-battery is an energy storing device that is powered by organic compounds. Bio-Battery generates electricity from renewable fuels (glucose, sucrose, fructose, etc) providing a sustained, on-demand portable power source. These types of batteries uses enzymes can convert the sugar into energy similar to the way biological systems use enzymes to convert food into energy. The heart of the device is a nanocomposite anode which contains enzymes capable of oxidizing glucose and other sugars, releasing electrons and generating energy.

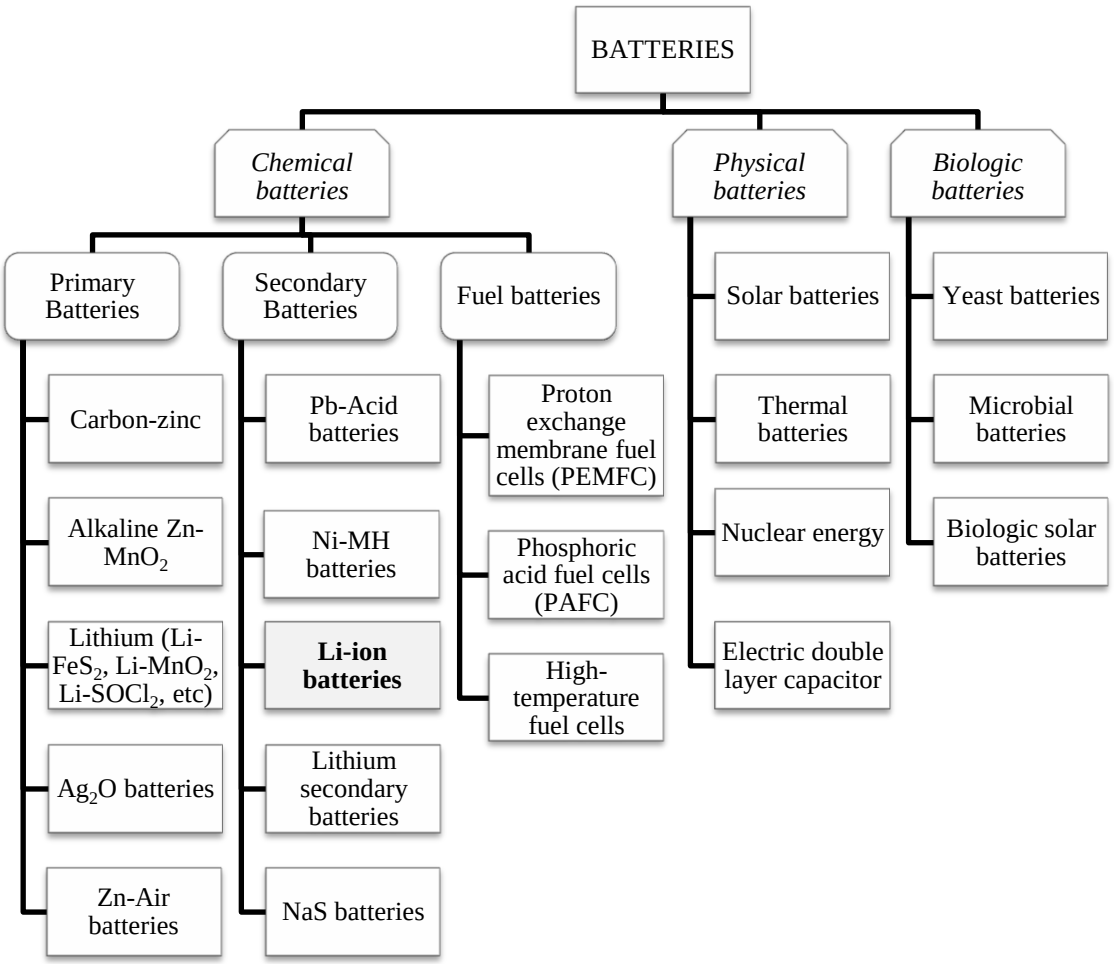

Figure 6.1. Global classification of batteries.

6.1.1. BATTERY PARTS

In a typical chemical battery several parts can always be observed. Two important terminals exist inside every battery: one positive (+) and one negative (−). In addition to other internal parts of a battery work together to help produce electricity. The most important parts can be seen in Figure 6.2.

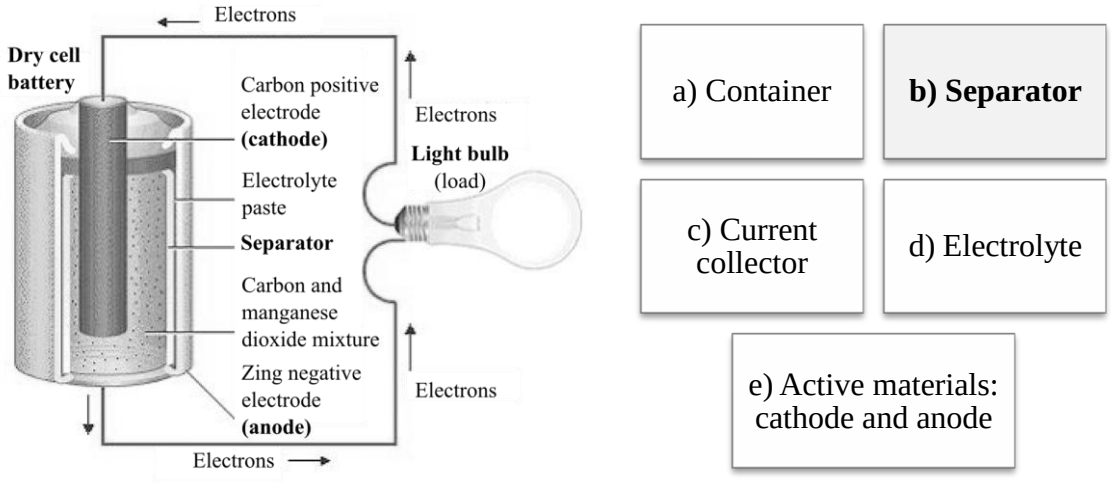

Figure 6.2. Schematic of an alkaline battery (Left) and parts of a typical battery (Right).

a) Container. The battery case must be resistant to corrosion from both inside and outside, and hence it must be stable to chemical attack by the electrolyte, active materials and the environment at the operating temperature. In addition must have the required mechanical strength, be cheap and lightness, and the method of sealing must be simple.

b) Separator. The separator must be chemically stable to the electrolyte and to the active materials at the temperature of operation. It is also necessary for the membrane to have the correct qualities of selectivity, wettability, resistivity and flexibility for the particular battery system.

c) Current collector. In order for the battery to have an acceptable capacity, the active material is normally a thick layer of porous, particulate paste, and the electronic conductivity of this material is very high. Thus, it is necessary to have a current collector, which is usually a metal grid or sheet, to provide a conducting path through the paste and thereby minimize the resistance of the battery. The current collector also acts as a physical support for the active mass which otherwise would be a very brittle structure. The current collector must be stable to chemical attack by both electrolyte and active material, and this limits the choice of material.

d) Electrolyte. The selection of electrolyte is determined by the electrode reactions and its concentration. This will control the plate potentials, the electrolyte resistance and viscosity and, by its effect on the rate of diffusion, the differences in concentrations of species between the inside and the outside of the pores of the active paste.

Temperature has a large effect on electrolyte properties and both viscosity and resistance increase by more an order of magnitude as the temperature drops from room temperature to -30°C. This largely accounts for the poorer performance of the battery at lower temperature.

The weight of the electrolyte is a major contribution to that of the complete battery and hence must be minimized. In any case the electrode spacing should be small to minimize battery resistance.

e) Active materials (cathode and anode). For a battery with a reasonable discharge rate and capacity, the electroactive species must be readily available at the sites of electron transfer and be present in large quantities. In most batteries these necessities are provided by using solid reactants, and at least in secondary batteries the product of the electrode process is also solid; the anion of electrolyte and sometimes the proton are also participants in the chemical change during the charge or discharge process. Hence if the change is to be accomplished at a reasonable rate, intimate contact and a high-area surface between the solid reactants and electrolyte are essential. This is accomplished by using the electroactive materials in the form of a paste on the current collector.

The sizes of the particles and the pores, i.e. the porosity of the paste, are important in determining the performance of the battery. The loading of the paste, the thickness of the porous layer, also affects performance. Thin plates improve capacity particularly at high discharge rates and also give a higher power density.

6.1.2. CHARACTERISTICS OF RECHARGEABLE BATTERIES

Rechargeable batteries work by fully restoring its energy capacity when an electric current is applied to them, because they can reversibly convert electrical energy into chemical energy and store resulting chemical energy in the unit [4]. They are considered to be *electrochemical cells* which produce a finite amount of energy, which once depleted can be recharged by reversing the chemical reaction with the aid of a charging current supplied by the battery charger.

Here are some of the more common chemistries used in rechargeables today: nickel metal hydride (NiMH), lithium ion (Li-ion), nickel cadmium (Ni-Cd), lithium ion polymer (Li-ion polymer), combination of lead and sulfuric acid (Lead-acid). Each technology has its own advantages. These may include: high power delivery for shorter periods of time, longer battery life for low power applications, quicker recharge rates, longer life times or smaller size for the same amount of energy. The designer should pick the most appropriate technology for the application [5].

In the past decades, rechargeable batteries have been most rapidly developed and widely used in numbers of mobile electronic devices, such as laptops, cellular phones, tablets, cameras, and power tools, due to their high energy density, high power capacity, and robust performance. The performances are typically qualified by the energy density, powder capability, cycle life and safety, and the cost by the price of battery materials and engineering.

The cell is the core element of a battery. For many portable electronics, a single cell can satisfy the energy and power requirements. For large scale applications many cells are required to be electrically integrated into modules that are further packed into a battery pack. Thus, the challenges in optimization are remained not only for the designs and engineering of battery packs but also for the materials and process of single cells. In order to overcome the challenges of the performance and cost, new materials and concepts are necessary for the development and commercialization of the next

generation rechargeable battery devices. The performance enhancement is realized by improving the battery materials and design, including the cathode, anode, and electrolyte/separator, and the cost reduction by selecting the low-cost raw materials and process.

Although primary batteries were dominant until the 70s, secondary batteries such as lead-acid and nickel-cadmium (Ni-Cd) eventually took their place. In the 1980s, information technology advanced significantly with the development of portable electronic products such as video cameras, mobile phones and laptops [6], whereby led to a growing need for rechargeable batteries with greater capacity or with reduced size and weight for a given capacity. Conventional rechargeable batteries available at that time such as nickel-cadmium, lead-acid, and nickel-metal hydride batteries used aqueous electrolytes, which posed limitations on increasing the energy density and reducing the size and weight. They energy density reached a limit by the end of the 80s.

Sony Corporation started its battery business in the mid-70s and the development of secondary batteries in 1985, when the choice of the Ni-Cd system was no longer an option. Sony started to study the possibility of cells with lithium-based anodes, and, for the first time, succeeded in the development of lithium-ion secondary battery in 1991. Since then, they have grown to become the dominant power storage solution [6].

The typical features of Li-ion batteries are as follows:

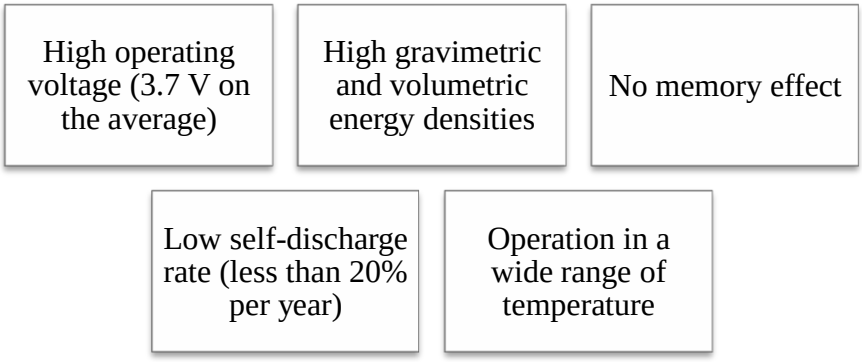

In the same way as other types of batteries, the four major components of the lithium-ion battery are the positive electrode (cathode, +), negative electrode (anode, −),

electrolyte, and separator. In a cell, the cathode and anode are physically isolated by the electrolyte. When a liquid electrolyte is used, a porous membrane must be placed as the separator between the cathode and anode to avoid their electrical contact. The separator allows the liquid electrolyte to penetrate and mechanically isolates the cathode and anode from each other. The electrolyte is ionically conducting and electronically insulating, which enables the redox reaction on each of electrodes.

Rechargeability of a cell is based on a reversible redox reaction between the cathode and anode materials. The open circuit voltage (U_{OCV}) of a cell equals to the difference of chemical potentials between the cathode (E_+) and anode (E_-) as described by (Equation 6.1)

$$U_{OCV} = E_+ - E_- \tag{6.1}$$

where E_+ and E_- vary with the state-of-charge (SOC), more precisely the chemical composition of the electrode materials.

Output voltage *(U)* of the cell depends on the IR polarization, which is described by Equation 6.2.

$$U = U_{OCV} - IR \tag{6.2}$$

where *I* is the current passing through the cell, and *R* is the overall internal resistance of the cell, which is affected by many factors, such as electrode and electrolyte materials, electrode and cell structure, temperature, and cell's SOC or degree-of-discharge (DOD), the other description form of SOC.

A. IMPEDANCE SPECTROSCOPY

Electrochemical Impedance Spectroscopy (EIS) or **impedance spectroscopy** is a powerful diagnostic tool that you can use to characterize limitations and improve the performance of cells. EIS measures dielectric properties of a medium as a function of frequency, permittivity (interaction of an external field with the electric dipole moment of the sample) and impedance (complex electrical resistance). The representation of

complex impedance function (Equation 6.3) is very useful; it replaces the simple concept of resistance/capacitance by impedance, which is a more general circuit parameter. It takes the phase differences between input voltage and output current into account.

$$Z(\omega) = \frac{E_t}{I_t} = \frac{E_0\ exp(j\omega t)}{I_0\ exp(j\omega t - \phi)} = Z_0(\cos\phi + j\sin\phi) \tag{6.3}$$

Among other factors, impedance spectroscopy is an experimental technique that can be used to separate and quantify the sources of polarization. By applying physically-sound equivalent circuit models wherein physicochemical processes occurring within the cell are represented by a network of resistors, capacitors and inductors, it is possible extract meaningful qualitative and quantitative information regarding the sources of impedance. For example, is a powerful tool for investigating the mechanisms of electrochemical reactions, for measuring the dielectric and transport properties of material, for exploring the properties of porous electrodes and for investigating passive surfaces.

Systems can be viewed as linear and non-linear systems. Impedance analysis of linear circuits is much easier. A linear system is one that possesses the important property of superposition: if the input consists of the weighted sum of several signals, then the output is simply the superposition (weighted sum) of the responses of the system to each of the signals. Electrochemical cells (input is potential, output is current) are not linear (doubling voltage ≠ double the current). Therefore, in order to avoid the non-linearity, impedance spectroscopy measurements are made at small ac signals (1 – 10 mV) in order the electrochemical cells to become pseudo-linear. Then, for small excitations a pseudo-linear response results with characteristic phase shifts (Figura 6.3).

The power of the impedance spectroscopy technique arises from: a) is a linear technique and results are interpreted in terms of Linear Systems Theory, b) if measured of an infinite frequency range, the impedance delivers all information from a system by linear electrical perturbation/response techniques, c) high experimental efficiency and d) validation of data is quite easy via integral transform techniques (Kramers-Kronig) that are independent of the physical processes [7].

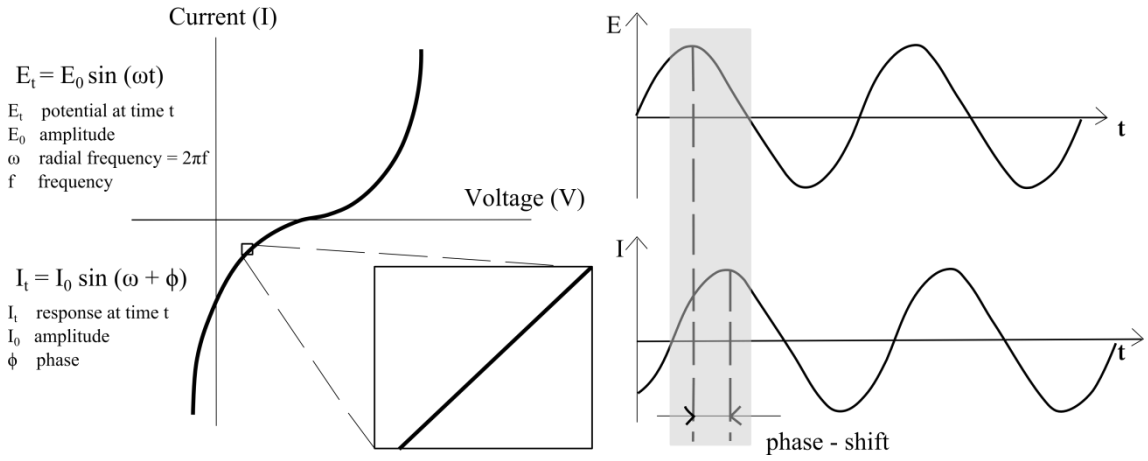

Figure 6.3. Current vs. Voltage curve of an impedance analysis (Left) and characteristic phase shifts for a small excitation with pseudo-linear response (Right).

During an impedance measurement, a frequency response analyzer is used to impose a small amplitude ac signal to the cell. The ac voltage and current response of the cell is analyzed by the response analyzer to determine the resistence, capacitive and inductive behavior – the impedance – of the cell at that particular frequency. Physicochemical processes occurring with the cell have different characteristic time-constants and therefore are exhibited at different ac frequencies, impedance spectroscopy can be used to identify and quantify the impedance associated with these various processes.

Equivalent circuit modeling of impedance spectroscopy data is used to extract physically meaningful properties of the electrochemical system by modeling the impedance data in terms of an electrical circuit composed of ideal resistors *(R)*, capacitors *(C)*, and inductors *(L)* (Table 6.1). Because we are dealing with real systems that do not necessarily behave ideally with processes that occur distributed in time and space, we often use specialized circuit elements. These include the generalized constant phase element *(CPE)* and Warburg element (Z_w). The Warburg element is used to represent the diffusion or mass transport impedances of the cell.

Table 6.1. Summary of the symbols, defining relation of the common circuit elements: resistors, capacitors and inductors.

Defining relation			**Impedance**	*The impedance of elements in series is additive* $Z_{total} = Z_1 + Z_2$
Resistor		$V = I \times R$	$Z_R = R$	
Capacitor		$I = C\frac{dV}{dt}$	$Z_C = \frac{1}{j\omega C} = -\frac{j}{\omega C}$	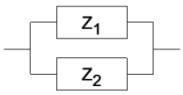 *The impedance of elements in parallel is the inverse of the sum of the inverse of impedance* $\frac{1}{Z_{total}} = \frac{1}{Z_1} + \frac{1}{Z_2}$
Inductor		$V = L\frac{dI}{dt}$	$Z_L = j\omega L$	

Impedance spectroscopy for electrochemical cells is most often represented in Nyquist and Bode plots as shown in Figures 6.4 and 6.5. Bode plots refer to representation of the impedance magnitude (or the real or imaginary components of the impedance) and phase angle as a function of the frequency. Because both the impedance and the frequency often span orders of magnitude, they are frequently plotted on a logarithmic scale [8].

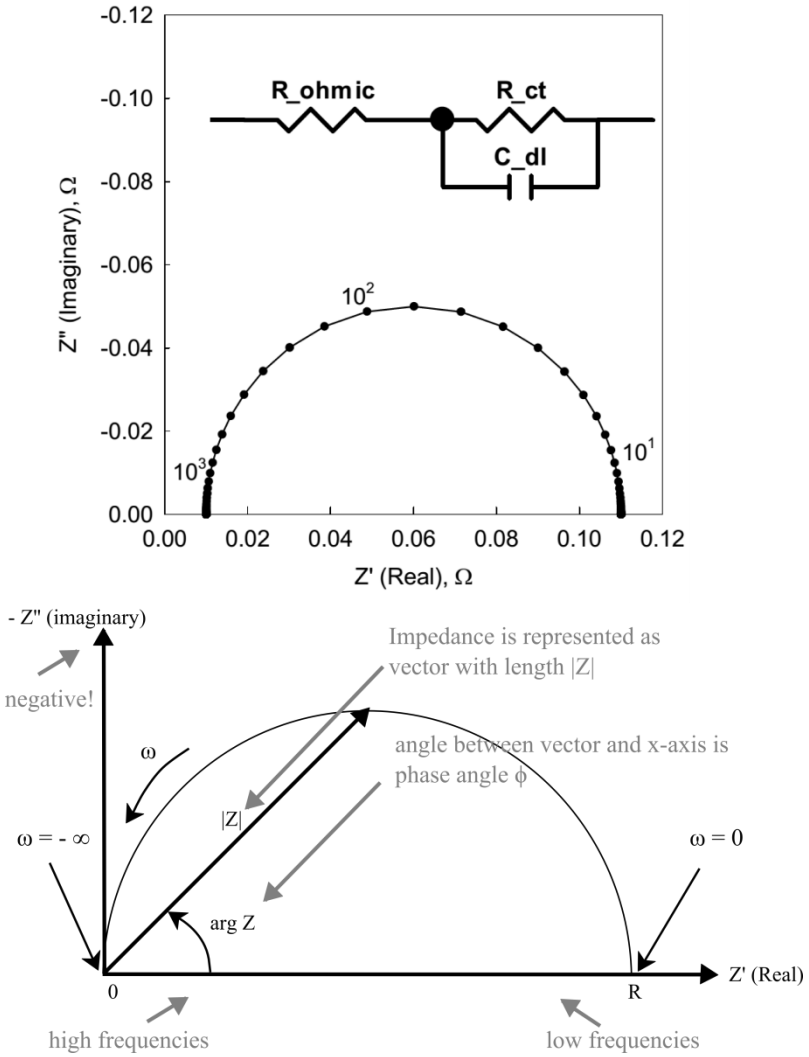

Figure 6.4. Impedance plot (Nyquist plot) for a simple RC circuit where $R_{ohmic} = 0.01\Omega$, $R_{ct} = 0.1\Omega$ and $C_{dl} = 0.02F$. For clarification, 3 frequencies (10^3, 10^2 and 10^1 Hz) are labeled in the complex plane (Up) and schematic of a typical Nyquist plot (Down).

A complex plane or Nyquist plot depicts the imaginary impedance, which is indicative of the capacitive and inductive character of the cell, versus the real impedance of the cell. Nyquist plots have the advantage that activation-controlled processes with distinct time-constants show up as unique impedance arcs and the shape of the curve provides insight into possible mechanism or governing phenomena. Because both data formats have their advantages, it is usually best to present both Bode and Nyquist plots.

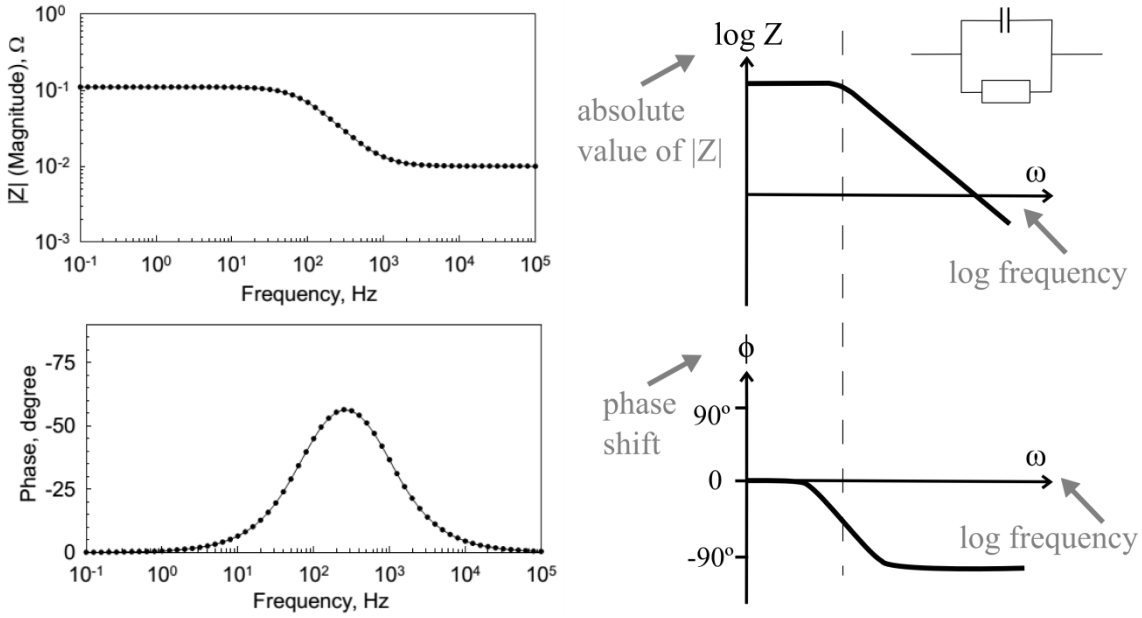

Figure 6.5. Impedance plots (Bode plots) for a simple RC circuit where $R_{ohmic} = 0.01\Omega$, $R_{ct} = 0.1\Omega$ and $C_{dl} = 0.02F$. For clarification, 3 frequencies (10^3, 10^2 and 10^1 Hz) are labeled in the complex plane (Left) and schematic of a typical Bode plot (Right).

In a real Li-ion battery the overall resistance of a cell consists of the ohmic bulk resistance (R_b) contributed by the electronic resistance of cell's hardware and the ionic resistance of the electrolyte, ohmic surface layer resistance (R_{sl}) on two electrodes, Faradic charge-transfer resistance (R_{ct}) relating to the electrochemical reactions occurring in two electrodes and charging with the SOC, and Warburg impedance (Z_w) corresponding to the ionic diffusion on the electrolyte-electrode interface (Figure 6.6). Impedance depends on perturbation frequency: at high frequency a small Warburg impedance results and a low frequency a higher Warburg impedance is generated. It appears in Nyquist plot as diagonal line with slope of 45°. Normally, the R_{ct} remarkably increases near the end of charge or discharge, which hence results in a steep increase in the cell's polarization [9]. This feature has been used to determine the ending point of charging in many battery chargers.

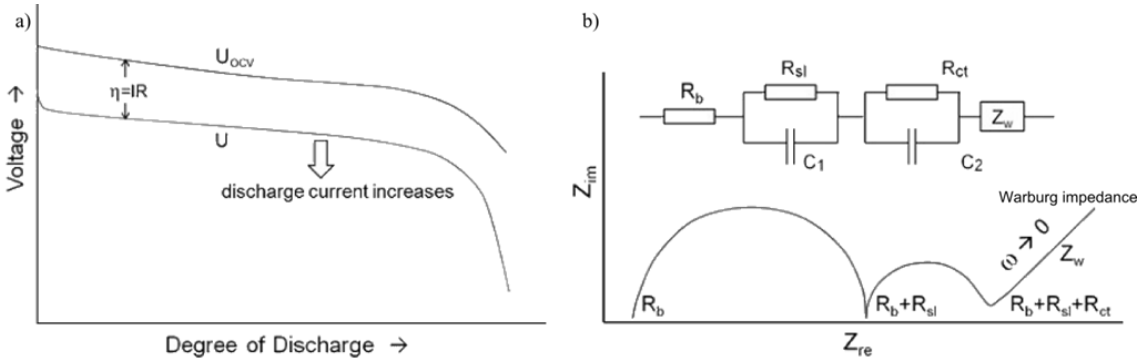

Figure 6.6. Typical characteristics of an electrochemical cell. a) Output voltage versus open-circuit voltage, and b) ac impedance spectrum [4].

B. UPTAKE, POROSITY, TORTUOSITY AND IONIC CONDUCTIVITY

Battery performance is dependent on the separator and its stability with other materials. Main separator parameters include pore diameter (d), porosity (ε), pore tortuosity (τ) and thickness (δ). The ionic conductivity $(\sigma)$of a separator is proportional to the velocity of the solute (υ). In turn, the velocity of an electrolyte is related to the pore diameter, porosity, tortuosity, and thickness of the separator by: $\upsilon \propto d^2 \cdot \varepsilon \cdot \delta^{-1} \cdot \tau^{-2}$.

—Uptake

In batteries, uptake is the absorption and retention of a solvent by a membrane. The uptake from the electrolyte can be obtained by submerging a pristine membrane in a electrolyte solvent. After a certain period of time, the membrane is taken out of the solvent and the excess electrolyte on the surface of the membrane is removed by wiping softly with a tissue paper. The electrolyte uptake of a membrane is often reported in percent and defined on the dry polymer basis and calculated by comparing the dry weight (M_0) and the wet weight (M) of a membrane.

—Porosity

Porosity (ε) or void fraction is a measure of the void spaces (empty spaces) in a material. Porosity is calculated as a fraction of the volume of voids over the total volume (between 0 and 1), or as a percentage between 0 and 100%.

There are different methods to test porosity, such as: direct methods *(pore volume = total volume − material volume)*, optical methods *(the area of the material versus the area of the pores visible under the microscope)*, computer *tomography (method to create a 3D rendering of external and internal geometry, including voids)*, imbibitions methods *(immersion of the porous sample, under vacuum, in a fluid that preferentially wets the pores)*, water saturation method *(pore volume = total volume of water − volume of water left after soaking)*, water evaporation method *(pore volume = (weight of saturated sample − weight of dried sample)/density of water)*, mercury intrusion porosimetry and gas expansion method.

—Tortuosity

Tortuosity (τ) is a property of curve being tortuous (twisted; having many turns) and is a term used to describe diffusion in porous media. There have been several attempts to quantify this property. The objective is to use a simple expression for the tortuosity of porous media as a function of porosity (ε) and of a single parameter characterizing the shape of the porous medium components. It is not possible to discuss the behavior of separators and membranes without considering the effects of tortuosity.

Transport in porous media is a very important issue in a large number of science branches [10,11]. In addition to the specific interactions which may occur between the fluid phase and the solid medium, all the transport phenomena must take into account the decrease of the volume available to fluid transport due to the presence of the solid medium and an increase of the path that the fluid must walk to cross the tortuous medium. These two effects can be described at a macroscopic level using the porosity (ε) and the tortuosity (τ) parameters. ε represents the fraction of free volume, while τ is the reciprocal of the average ratio between the straight distance connecting two points

and the actual path length inside the porous medium. The ratio $f = \varepsilon/\tau$ is known as the structure factor.

Although the porosity of a separator is a major factor in obtaining high conductivity, it is not the only one, since the pores have to be completely filled by the liquid electrolyte. The wetting ability of the electrolyte is a vital factor. Besides, whilst the porosity of a medium can be easily derived from its weight and density, the tortuosity of porous media in general depends on the pore volume fraction, shape and connectivity. However, for some classes of materials, theoretical (or phenomenological) relations exist expressing the tortuosity as a function of the porosity only.

—Ionic conductivity

There are three main factors affecting the performance of lithium-ion batteries: ionic conductivity, electrochemical window, and reactions with the electrodes. Ionic conductivity (σ, the SI unit is Siemens per meter, $\mathrm{S \cdot m^{-1}}$) of an electrolyte solution (a substance that conducts electricity through the movement of ions) is a measure of its ability to conduct electricity. On the one hand, the ionic conductivity of the electrolyte (σ_0) determines the internal resistance and electrochemical behavior at different charge/discharge rates of the battery, which are important parameters for practical applications. In general, ionic conductivity of an electrolyte with lithium salt in an aprotic organic solvent is around $2 \cdot 10^{-2}$ $\mathrm{S \cdot cm^{-1}}$, which is much lower than that of aqueous electrolytes. Moreover, σ_0 is closely related to ion structure of the electrolyte and the salt concentration. On the other hand, the ionic conductivity of the membrane and the electrolyte set (σ_{eff}) is affected by the good teamwork of both components, i.e., σ_{eff} depends on the electrolyte uptake, porosity (ε) and tortuosity (τ) of the membrane.

C. CAPACITY AND C-RATE

Whatever the application, one of the main parameters its **capacity**, which can be defined as the number of Li-based charges that can be reversibly stored in a unit mass (specific capacity, traditionally expressed in ampere-hour per gram, $Ah \cdot g^{-1}$; 1 Ah = 3600 C) or in a unit volume (volumetric capacity, expressed in $Ah \cdot cm^{-3}$) of the active anode material. In other words, the energy density is described by watt-hour per unit weigh or volume and is the product of specific capacity and averaged output voltage. It is mainly affected by the chemical nature of the cathode and anode materials. However, the power density, usually described by watt per unit weigh or volume, is also affected by the design and engineering of the cell in addition to the nature of the electrode materials [12].

For instance, the specific capacity of an anode made of pure lithium is just the number of Li atoms$\cdot g^{-1}$ in the metal multiplied by the elementary charge (since lithium redox reactions involve one electron only), i.e., ~ 3.860 $A \cdot g^{-1}$ or 3860 $mA \cdot g^{-1}$ (corresponding to ~2046 $mAh \cdot cm^{-3}$). For an alloy such as Li_xM_y, the specific capacity can be expressed as:

$$C = \frac{x \times q \times N_{Av}}{y \times M_{at} \times 3600} \ (Ah \cdot g^{-1}) \tag{6.4}$$

where q is the elementary charge (1.602×10^{-19}C), N_{Av} is the Avogadro number and M_{at} is the atomic mass of element M.

It is important to emphasize that the capacity of an electrode is not an absolute parameter, since it varies with the **charge/discharge rate** (or **C-rate**) of the electrode, because is a measure of the rate at which a battery is being discharged. It is defined as the discharge current divided by the theoretical current draw under which the battery would deliver its nominal rated capacity in one hour [13]. Charge/discharge rate is one of the important electrochemical properties of batteries, which ensures a high and stable delivery of batteries, which ensures a high and stable delivery of electrochemical capacity under high current for the batteries. Many factors can affect the rate-capability of electrodes, including active material features (electronic and ionic conductivity,

electrochemical activity, particle size and morphology), electrode recipe, and electrode geometric dimension or structure.

In a battery, electrons are not directly available as they would be in a capacitor. Instead, the availability of electrons results from interface reactions ($Li^+ + e^- \Leftrightarrow Li$), which may be slow. Moreover, Li has to diffuse inside the host material to reach the interface with the electrolyte, which can take time ($t \approx l^2/D$, where t is the diffusion time, l the distance to travel and D the diffusion coefficient of Li in the host material). Finally, Li^+ transport in the electrolyte (which must balance the electron transport in the outside circuit) is generally slower than electron transport in the external circuit.

For all the above reasons, the capacity of the electrode decreases as its charge/discharge rate increases and capacity values are usually specified for low charge/discharge rates, e.g., C/20 or even C/50. A C/N rate corresponds to a complete charge/discharge of the battery in N hours; for instance, a C/20 means charging/discharging the battery in 20h; A 1C discharge rate would deliver the battery's rated capacity in 1 hour, a 2C rate means charging/discharging the battery in $1/2$ h. A 1C discharge rate on a 1.6 Ah battery means a discharge current of 1.6 A. A 2C rate would mean a discharge current of 3.2 A. Standards for rechargeable batteries generally rate the capacity over a 4 hour, 8 hour or longer discharge time. Because of internal resistance loss and the chemical processes inside the cells, a battery rarely delivers rated capacity in only one hour.

Once the capacity of a particular material is known, there are other terms used, such as the electrode capacity per unit area of the current collector, expressed in $mAh \cdot cm^{-2}$. This number incorporates the mass loading of active material per unit area of the current collector, a quantity which is always limited in practice. A second parameter is the potential of the anode (versus Li^+/Li^0), which, for a given cathode material, determines the final voltage delivered by the battery. A higher potential versus $Li/Li^+$of the negative electrode induces a lower cell voltage.

From the thermodynamics of Li-based batteries is known that the open circuit voltage V_{OC} of a lithium cell results from the difference in the chemical potential of lithium between the cathode (μ_{Li-C}) and the anode (μ_{Li-A}). It can be expressed as:

$$V_{OC} = -\frac{\mu_{Li-C} - \mu_{Li-A}}{nF} \tag{6.5}$$

where F is the Faraday constant (96485.33289(59) C·mol^{-1}) and n = 1 for the $Li^+ + e^- \Leftrightarrow Li$ equilibrium. The chemical potential of Li in a host material is related to its thermodynamic activity, a_{Li} (which can be viewed as an effective concentration), so that:

$$\mu_{Li-A,C} = \mu_{Li}^0 + RTLn\left(a_{Li-A,C}\right) \tag{6.6}$$

where R is the gas constant, T the absolute temperature and $a_{Li-A,C}$ is the Li either in the anode *(A)* or the cathode *(C)*; a_{Li} in pure metallic lithium is equal to unity. That is, for a given cathode, in order to maximize the cell voltage, it is necessary to use an anode which the chemical potential of Li in the host structure (which translates into a voltage against Li^+/Li^0, when the host/alloying material is tested as positive electrode in the so-called half-cell configuration using a pure Li anode as the negative electrode) must be as close to that of pure Li as possible [14,15].

If the chemical potential of the anode (or the cathode) lies outside the stability window of the electrolyte, the latter will be reduced (or oxidized in the case of the cathode). In both cases, the unwanted decomposition of the electrolyte will alter the correct functioning of the battery, leading to quick failure after a few charge-discharge cycles if the electrolyte decomposition is not blocked [16]. This means that the electrolyte will be reduced as the battery is charged, i.e., when the voltage is brought below ~ 1 V versus Li^+/Li^0 (all voltage values are expressed with reference to Li^+/Li^0). However, this situation can be avoided by the formation of a passivating film of the electrolyte. This passivating film, also called solid electrolyte interphase (SEI), blocks electron transfer between the anode and the electrolyte (hence preventing further electrolyte reduction), but is permeable to Li^+ ions, thus allowing their reduction at the anode when the battery is charged and their release in the electrolyte when the battery is discharged. The SEI usually forms naturally upon the first battery charge, where electrolyte decomposition is unavoidable. If the SEI is mechanically and chemically stable, there is no more electrolyte decomposition after the first battery charge and the anode is stabilized, even though its chemical potential lies outside the electrolyte stability window. The SEI

composition depends mainly on the particular electrolyte and lithium salt used for battery fabrication and also on the anode material itself.

Figure 6.7 is a schematic of the relative electron energies in the electron energies in the electrodes and the electrolyte of a thermodynamically stable battery cell having an aqueous electrolyte [17]. The difference between the lowest unoccupied molecular orbital (LUMO) and the highest occupied molecular orbital (HOMO) of the electrolyte is the "window" of the electrolyte. The two electrodes are electronic conductors with anode and cathode electrochemical potentials μ_A and μ_C (their Fermi energies ε_F). An anode with a μ_A above the LUMO will reduce the electrolyte unless a passivation layer creates a barrier to electron transfer from the anode to the electrolyte LUMO; a cathode with a μ_C below the HOMO will oxidize the electrolyte unless a passivation layer blocks electron transfer from the electrolyte HOMO to the cathode. Therefore, thermodynamic stability requires locating the electrode electrochemical potentials μ_A and μ_C within the window of the electrolyte, which constrains the open circuit voltage [18].

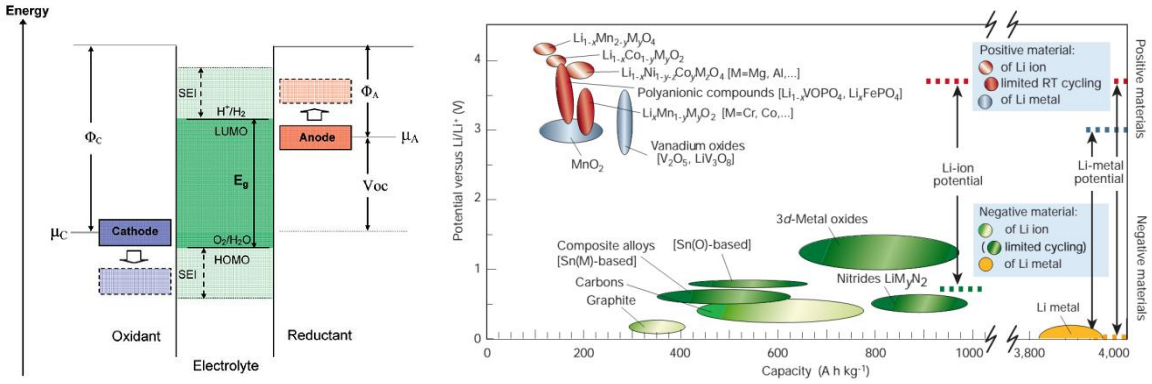

Figure 6.7. Schematic open-circuit energy diagram of an aqueous electrolyte. Φ_A and Φ_C are the anode and cathode work functions. E_g is the window of the electrolyte for thermodynamic stability. A $\mu_A < HOMO$ requires a kinetic stability by the formation of an SEI layer (Left) [17] and voltage versus capacity for positive- and negative-electrode materials used for Li-based cells (Right) [19].

Once the window of the electrolyte has been determined, it is necessary to design electrodes that matched to the LUMO and HOMO of the electrolyte. Elemental Li^0

would be the ideal anode, but $\varepsilon_F = \mu_A$ of Li^0 lies above the LUMO. Therefore, use of Li^0 as an anode is only possible because a passivating SEI layer is formed. The SEI layer allows use of Li^0 as an anode in half-cells used to obtain the μ_A or μ_C of a practical electrode relative to the Li^+/Li^0 energy level; but on repeated charge/discharge cycles, breaking of the SEI layer in selected areas results in the formation of dendrites that can grow across the electrolyte to short-circuit a cell of the battery with dangerous consequences. An important parameter for a good anode is its ability to support/generate a stable SEI. The dimensional stability (small volume change) of the anode upon *Li*, will guaranty the mechanical stability of the SEI on its surface. If the volume variation of the anode is too important (poor mechanical stability), the SEI will tend to locally break.

In this way, other parameter determining the usefulness of an anode is its cycle lifetime: the number of battery charge-discharge cycles it can withstand without significant degradation, i.e., without significant capacity loss.

6.1.3. PARTS OF LI-ION BATTERIES

The basic components of a Li-ion battery are the two metallic collectors, the positive electrode (cathode), negative electrode (anode) and the separator (porous membrane with electrolyte solution), as illustrated in Figures 6.8a and 6.8b for a charging and discharging process. The current collectors are typically metal films placed in each electrode (anode and cathode). Usually, the collector is an aluminum film for the cathode and cupper film for the anode. During the charging process, electrons and lithium ions (positive ions) move from the cathode to the anode and during the discharge process, electrons and positive ions move from the anode to the cathode.

The development of lithium-ion batteries took place as a natural evolution from lithium metal technology (Figure 6.8c). The motivation for using a battery technology based on *Li* metal as anode relied initially on the fact that Li is the most electropositive (-3.04 V versus standard hydrogen electrode) as well as the lightest metal, thus facilitating the

design of storage systems in the 70s. But Li metal has the problem of forming dendrites on the electrode when cycling the cells.

Li-ion batteries technology benefited from the wide knowledge of intercalation chemistry developed in the 1970s and was transformed into a commercialized product in 1991. These first Li-ion batteries generally produced an average cell voltage of around 4 V and operated on the principle of reversible intercalation and deintercalation of *Li* ions (Li^+) in the cathode and anode (Figure 6.8d).

Initially, the most commonly used material for the cathode was lithium cobalt oxide ($LiCoO_2$) and some form of carbon was generally used for the anode. In the completely discharged state, *Li* atoms are only contained as part of the cathode. On charging, *Li* ions are released from the cathode and migrate through the electrolyte into the carbon of the anode. The reverse reaction occurs during discharging, and electric energy is stored or released by repeating these reactions reversibly. This combination marked a new concept of a secondary battery based on the transfer of *Li* ions, because provides stable battery characteristics over a long service life, excellent cycle durability with little degradation by side reactions, and excellent storage characteristics [20,21].

Normally commercial Li-ion batteries use the Li^+ ion intercalation materials for both the cathode and anode, between which the Li^+ ions are shuttled across the electrolyte absorbed in the separator. In order to assemble the battery in discharged state, the cathode materials are lithiated transition metal oxides and the anode materials are carbons or compounds capable of intercalating Li^+ ions or alloying with metallic *Li*.

Another essential constituent for achieving practical Li-ion batteries is the membrane separator. For instance, normally it is used a microporous polyethylene or polypropylene membrane, because provides a “shutdown” function in which the material of the separator melts to close the micropores and shut off battery operation in the case of abnormal heat generation. These were the key technological developments that made the current Li-ion battery possible. Nowadays further technological developments are focused on novel compositions of the cathode, anode, electrolyte, and/or separator.

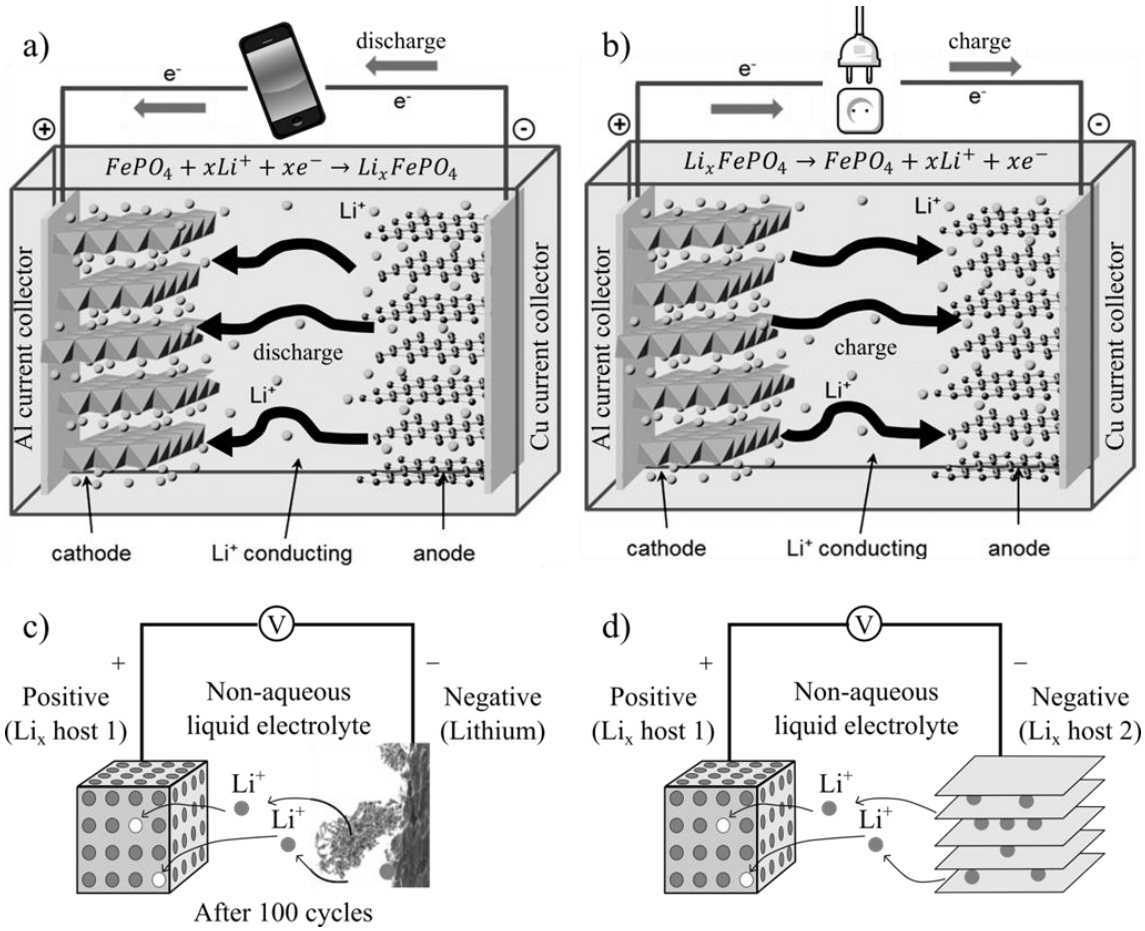

Figure 6.8. Schematic representation of: a) the discharge and b) charge processes of a lithium-ion battery systems, c) Li-metal anode showing the dendrite growth at the Li surface after 100 cycles, and d) reversible intercalation and deintercalation of *Li* ions.

A. CATHODE MATERIAL

Layered $LiMO_2$ (M=Co, Ni, Mn, and their mixture), spinel LiM_2O_4 (M=Mn, and mixture with Co or Ni), and olivine $LiMPO_4$ (M=Fe, Mn, Ni, Co, and their mixture) are three types of major cathode materials.

The lithium insertion compounds built with polyanionic groups such as $(SO_4)^{2-}$, $(PO_4)^{3-}$, $(SO_4)^{2-}$, $(P_2O_7)^{4-}$ or $(MoO_4)^{2-}$ or $(WO_4)^{2-}$ are considered as potential positive electrode materials for use in lithium rechargeable batteries. Yet in this family, olivine phosphate and Nasicon-like frameworks are currently the subject of many

investigations. In particular, lithium iron phosphate ($LiFePO_4$ or LFP) because it realizes the highest capacity at moderate current densities [22]. Olivine $LiFePO_4$, having a one-dimensional Li^+ ion conduction pathway presents several advantages with regard to low cost, non-toxicity, tolerance on abuse, and high safety, which are determinant with respect to cobalt-oxide-based materials for batteries. Typically, $LiFePO_4$ can achieve a ~170 $mAh \cdot g^{-1}$ of specific capacity at 3.4 V versus Li/Li^+, corresponding to a reversible intercalation/deintercalation of one *Li* per $LiFePO_4$ formula unit. The major drawback of $LiFePO_4$ is the intrinsically low electronic and Li^+ ionic conductivities, arising from the one-dimensional Li^+ ion diffusion. Also, the olivine structure is less dense than the layered and spinel structures, resulting in a lower volumetric energy density. To increase the electrochemical performance, it is a common practice in the production of Li-ion battery cathodes to manipulate the active material by a) adding carbon additives to a olivine material [23,24], b) surface coating of particles with thin layers of carbon [25,26] or reducing the particle size [27,28]. However, this significantly increases the processing cost of the $LiFePO_4$ material. In spite of these less favorable properties, the advantages make $LiFePO_4$ a viable cathode material for batteries.

There have been numberous efforts through the years to decrease the size of the particles from a few microns to this "nano" range, for several reasons. One is the increase of the effective contact area of the powder with the electrolyte. A larger effective contact surface with the electrolyte means a greater probability to drain Li^+ ions from the electrode, which increases the power density of the cell. A smaller particle size also reduces the length of the path of *Li* inside the particle, which leads to a greater capacity at higher charge/discharge rates and therefore to a larger power density.

The aspect of tuning the redox potential of an electrode material has been demonstrated by Goodenough et al. [23,29,30]. The use of polyanions $(XO_4)^{n-}$ loweres the redox energy of the 3d-metals to useful levels with respect to the Fermi level of the Li anode. The $X-O$ covalency results in a decrease of the $Fe-O$ covalency. This inductive effect is responsible for a decrease of the redox potential in comparison to the oxides. The polyanion PO_4^{3-} unit stabilizes the olivine structure of $LiFePO_4$ and lowers the

Fermi level of the $Fe^{+2/+3}$ redox couple through the $Fe-O-P$ inductive effect which results in a higher potential for the olivine material.

The electrochemical properties of LFP are known to be sensitive to the mode of preparation and the structural properties [31]. Many synthesis routes can be used, such as solid-state, hydrothermal and jet milling techniques [32–40].

A.1. STRUCTURE OF OLIVINE PHOSPHATE

$LiFePO_4$ crystallizes in the orthorhombic system (No. 62) with *Pnma* space group. It consists of a distorted hexagonal-close-packed oxygen framework containing *Li* and *Fe* located in half the octahedral sites and P ions in one-eighth of the tetrahedral sites [41,42]. The FeO_6 octahedra, however, are distorted, lowering their local cubic-octahedral O_h to the C_s symmetry. Corner-shared FeO_6 octahedra are linked together in the *bc*-plane; the LiO_6 octahedra form edge-sharing chains along the *b*-axis. The tetrahedra PO_4 groups bridge neighboring layers of FeO_6 octahedra by sharing a common edge with one FeO_6 octahedron and two edges with LiO_6 octahedra. Remarkably short $O-O$ bonds at the shared PO_4 and FeO_6 edges help to screen the cation charges from each other. This structure is illustrated in Figure 6.9 showing the 1-D channels via which the lithium ions can be removed. Corner-shared FeO_6 octahedra are linked together in the *bc*-plane, while LiO_6 octahedra from edge-sharing chains along the *b*-axis. The tetrahedral PO_4 groups brige neighboring layers of FeO_6 octahedra.

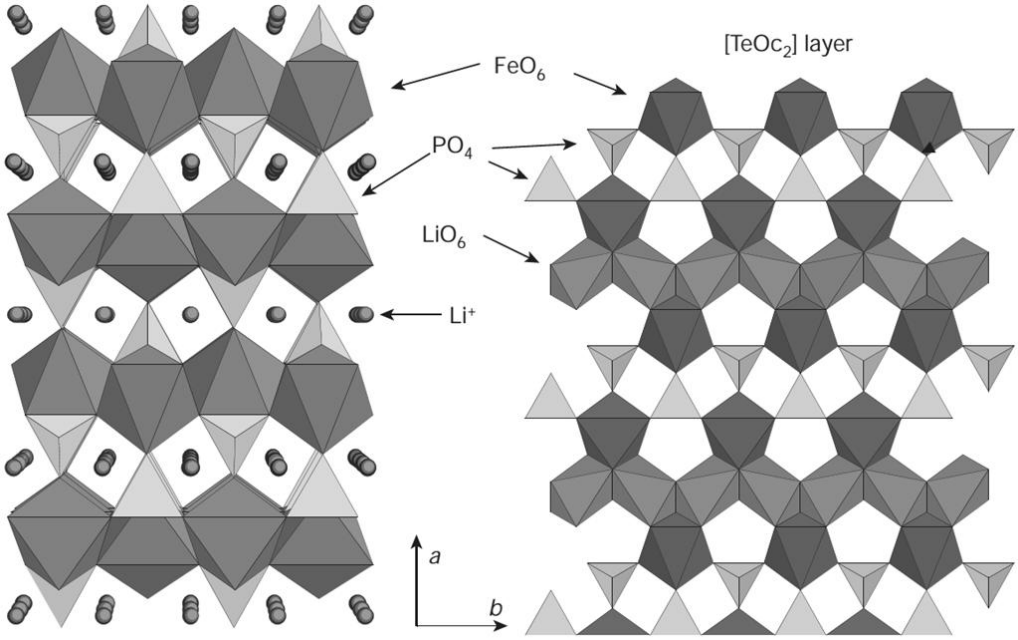

Figure 6.9. The crystal structure of olivine $LiFePO_4$ in projection along [001]. On the left, expanded view of the framework built on FeO_6 octahedra and PO_4 tetrahedra, and Li ions [19]. The FeO_6 octahedra are linked together through corner sharing in the (b,c) plane. On the right view of Li, Fe and P distribution between two distorted, h.c.p. (hexagonal close packed) oxygen-dense layers $(P_{Td}[LiFe]_{Oct}O_4)$. LiO_6 octahedra share edges and Li ions may diffuse along [010] and [001].

The $LiFePO_4$ structure consists in three non-equivalent O sites. Most of the atoms of the olivine structure occupy the *4c* Wyckoff position except O(3) that lies in the general *8d* position and Li^+ ions occupying only the *4a* Wyckoff position (M1 site on an inversion center). The Fe magnetic ions are in the divalent Fe^{+2} state of the FeO_6 units. As a consequence, Fe is distributed so as to form FeO_6 octahedra isolated from each other in $TeOc_2$ layers perpendicular to the (001) hexagonal direction [43]. In addition, the lattice has a strong two-dimensional character, since above a $TeOc_2$ layer comes another one at the vertical of the previous one, to build (100) layers of FeO_6 octahedra sharing corners and mixed layers of LiO_6 octahedra. Nevertheless, these $Fe-O$ planes are strongly linked by the PO_4 bridges, so that the material is truly three-dimensional, which insures the remarkable thermal stability with respect of the lamellar compounds.

B. ANODE MATERIAL

Li can react with elements or compounds in different ways, namely by means of insertion, alloying or conversion reactions [5]. When alloying or conversion reactions take place, they are usually accompanied by a strong electrode volume change and restructuration, including bond breaking and phase transformations. Schematically, the more *Li* can be packed in the host anode material, the larger the volume expansion and the associated mechanical degradation problems upon repeated alloying-dealloying. Moreover, lithium alloys are highly ionic and consequently they are brittle and do not withstand mechanical stresses induced by volume changes. This also contributes to a rapid degradation and pulverization of the electrode as lithiation and delithiation cycles are applied [6,44–46].

B.1. LI METAL AND ALLOY-BASED ANODE MATERIALS

Metallic lithium (*Li*, atomic number 3 and atomic mass 6.94 g) crystallizes in the body centered cubic (bcc) system with a lattice parameter of 351 pm. This corresponds to an atomic density of $\sim 4.597 \times 10^{22}\ \mathrm{at \cdot cm^{-3}}$, yielding a specific weight of $\sim 0.53\ \mathrm{g \cdot cm^{-3}}$, which is the lowest of all metals. *Li* also exhibits the lowest redox potential of the periodic table ($-3.045\ \mathrm{V}$ against a standard hydrogen electrode). Because of those properties, lithium should obviously be a first choice for anodes of rechargeable lithium-based batteries. Unfortunately, *Li* tends to grow in the form of dendrites when re-plated on the anode surface battery charging (Figure 6.10) (even when polymer electrolytes are employed), which after a number of charge-discharge cycles can lead to short circuits between anode and cathode, inducing risks of thermal runaway and fire [47]. Because of the above-mentioned security problems, *Li* metal has been replaced by an insertion-type anode for commercial applications.

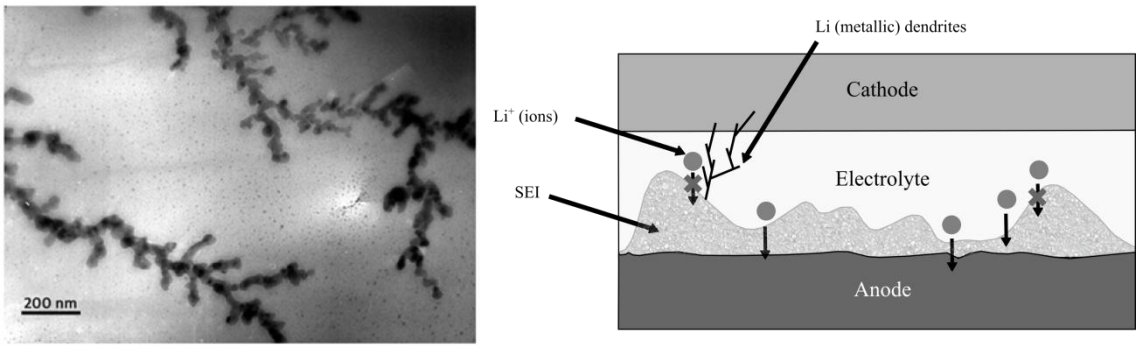

Figure 6.10. An example of Li metal dendritic growth through a polymer electrolyte: picture (Left) and schematic (Right) [4].

Li alloys with elements such as Sn, Si, Ge etc. are appealing because of their superior capacity and suitable operating potentials. Among many *Li* alloy forming elements, *Si* is of particular interest because it offers a specific capacity of as high as 4200 $mAh \cdot g^{-1}$ at a fairly flat potential plateau of 0.4 V versus Li/Li^+ in accordance with the formation of Si_5Li_{22} alloy. Typically, Si is lithiated at potentials from 0.4 to 0 V versus Li/Li^+, which are lower than the reduction potential of electrolyte solvents.

The major challenge with all *Li* alloy materials is the poor cyclability due to the dramatic volume change during the alloying and dealloying processes, which leads to the material pulverization, inter-particle contact loss, and severe capacity fading. The basic strategies to overcome the large volume change are to reduce the material's particle size, and/or further embed the active material particles into a conductive (such as carbon and metal) or a non-conductive (such as stable metal oxide) buffer phase.

B.2. CONVERSION-TYPE ANODE MATERIAL

Conversion-type anode materials are based on a displacement reaction between metallic *Li* and the nanostructured transition metal oxides, sulfides, nitride, phosphides, or halogates [48]. The metal in these compounds can be capable of alloying with *Li* or not. SnO_2 is a typical metal oxide (MO), in which the metal is able to alloy with *Li*. In

operation, SnO_2 is first reduced and combined with Li^+ ions from the electrolyte to form nano-sized Li_2O and *Sn* particles, followed by the *Sn* particles alloying with *Li*.

The MO with the metal unable to alloy with *Li*, such as *Mn*, *Fe*, *Co*, *Ni*, *Cu* etc., operates in entirely different mechanism, which can be described by a reversible displacement reaction, such as $MO + 2Li \rightleftharpoons M + Li_2O$. This kind of reaction generally has higher potential and more potential capacity profile as compared with the Li alloying since the displacement reaction occurs at higher potential profile and undergoes larger structural change than the Li alloying reaction. In a similar way to the MO, metal halogates (MX_n) also have been intensively investigated.

B.3. CARBONACEOUS MATERIAL

Carbon is the standard anode material for the commercial Li-ion batteries used in portable electronics. Well-ordered graphite has a 372 $mAh \cdot g^{-1}$ of theoretical capacity at an operating voltage of ~0.25 V versus Li/Li^+ in accordance with the formation of a LiC_6 graphite intercalation compound. Disordered hard carbon has higher specific capacity and better rate capability, but suffers larger irreversibility, higher voltage hysteresis, lower packing density, and poorer electrical conductivity, as compared with the ordered graphite. Since the intercalation of Li^+ ions into graphite occurs at lower potentials than the organic solvents electrochemically reduce, organic electrolytes are thermodynamically instable with the graphite anode. Therefore, the electrolyte solvents must be first reduced before the Li^+ ions can be intercalated into graphite. The operation of graphite anode can be enabled only when the reduction products of the electrolyte solvents are stably accumulated on the graphite surface to form the SEI film, has proven to be an essential step for the manufacture in affecting the cycling performance, cycle life and safety of the Li-ion batteries.

C. ELECTROLYTE

Electrolyte is an indispensable element of the battery, which enables the electrode reactions and affects the battery's performances. [49]. In Li-ion batteries, many electrolytes are based on mixed solvent systems (**liquid electrolytes**), which can overcome some drawback of a single solvent system. These organic solvents should be relatively stable at low potentials and should not react with metallic lithium Therefore, to obtain high ionic conductivity, polar aprotic solvents are required to dissolve the lithium salt. The melting and boiling points of the solvents affect the working temperature of the electrolyte and the assembled battery, and depend on physical properties. They should have a low melting point, high boiling point, and wide working temperature range (ideally in liquid state between -30 and 60ºC). Other important parameters are the dipole moment as it characterizes the polarity of the molecule and the solvent viscosity, because directly affects the movement of ions.

The standard electrolytes used in the current Li-ion batteries are a solution of Lithium hexafluorophosphate ($LiPF_6$) salt dissolved in a mixture of ethylene carbonate (EC) and other linear carbonates with little variation in the salt concentration (>1 M) and solvent ratio. The salt is generally the lithium conjugate base of a super acid, which makes the anion anodically stable and easily dissociates from Li^+ in organic solvents. For example, the one used in this thesis is the lithium hexafluorophosphate solution – in ethylene carbonate and dimethyl carbonate, 1.0 M $LiPF_6$ in EC:DMC= 50/50 (v/v) (Figure 6.11). The $LiPF_6$ salt is selected because a) it offers high ionic conductivity (~10 $mS \cdot cm^{-1}$ at room temperature), b) it participates in the formation of stable SEI on the graphite surface, c) it passivates aluminium *(Al)* current collector at high potentials, and d) it is stable over a wide electrochemical window. The EC is the indispensable co-solvent because a) its reduction products form dense and stable SEI on the anode surface, and b) its high polarity favors salt dissociation for high ionic conductivity. The formation of this layer is critical, as it prevents other solvent molecules from co-intercalating with lithium within the graphite layers, subsequently inducing exfoliation and disintegration of the electrode. The drawback of EC is that it has high melting point (34-37ºC) and high viscosity (1.90 cP at 40ºC), so it is conventionally used in

combination with linear carbonates. The function of the other linear carbonates is to reduce the viscosity and lower the solution's freezing temperature for the high ionic conductivity and wide operating temperature range. The main drawbacks of these electrolytes are that a) $LiPF_6$ is thermally instable at elevated temperature, especially in the presence of organic solvents, b) EC phase-separates (crystallizes) at low temperatures, depending on the composition of solvent mixture, c) the solution is highly flammable, and 4) carbonate solvents are subject to reduction at <1.2 V and oxidation at >4.5 V.

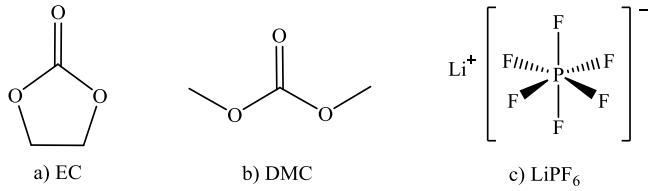

a) EC b) DMC c) $LiPF_6$

Figure 6.11. Structure of the most used molecules in liquid electrolytes for Li-ion batteries. a) Ethylene Carbonate (EC), b) Dimethyl Carbonate (DMC) and c) Lithium hexafluorophosphate ($LiPF_6$).

Other electrolyte components are lithium perchlorate ($LiClO_4$), lithium tetrafluoroborate ($LiBF_4$), lithium hexafluoroarsenate ($LiAsF_6$), lithium trifluoromethanesulfonate ($LiSO_3CF_3$), lihium bis(oxalato)borate (LiBOB), lithium difluoro(oxalate)borate (LiDFOB) and lithium bisfluorosulfonyl imide (LiSFI). But these salts cannot replace $LiPF_6$ to be used as a single salt, only as an additive or a co-salt. Organic electrolytes can be modified to effect improvement of overchargin endurance, flame retardation, SEI film formation, acid conte, ionic conductivity, and low-temperature performance. With respect to the solvent, non-flammable solvents (mainly cointaining phosphorus) and room temperature ionic liquids have been developed to reduce the flammability of the electrolytes. Sulfonates, aliphatic dinitriles and fluorinated carbonates, such as fluoroethylene carbonate (FEC), are the most used [49].

A new promising type of liquid electrolytes are the ionic liquids which consist of an organic cation and an inorganic or organic anion, forming a liquid salt at room temperature. Apart from liquid electrolytes, there are also **solid electroytes** which are ion conductors that should have a high ionic conductivity, low electronic conductivity,

an low activation energy. Solid polymer electrolyte and ceramic solid state electrolyte are possible solutions to the safety of Li-ion batteries. However, their high process cost and relatively low ionic conductivity make them unsuitable for the large size Li-ion batteries. Gel polymer electrolyte offers compromise to bridge the liquid electrolyte and solid polymer electrolyte.

D. SEPARATOR

A separator is a porous membrane that absorbs and retain the required amount of liquid electrolyte, provide channels for ions during electrochemical reactions and physically isolates the cathode and anode frome electrical contact to avoid short circuit [50]. In the operation of batteries the separator does not participate in any electrochemical reactions, however, it strongly affects the battery's performances, especially the power capability and safety. Lithium-ion batteries can be developed using polymer electrolytes where the porous membranes act not only as electrolytes but also as separators.

In practical or commercial applications, the separator should meet the following requirements:

a) **Non-conductor** of electrons.
b) **Good chemical stability**, especially good durability to organic electrolyte and electrode materials.
c) **High mechanical strength** to avoid short-circuiting during the assembly process of the lithium-ion battery.
d) **Suitable porosity and pore size**. It should provide suficient ionic conductivity and also prevent possible micro-short circuiting.
e) As **thin** as possible, because the ionic conductivity of organic electrolytes is about two orders of magnitude lower than that of aqueous ones, and resistance should be as small as possible.
f) **Good retention ability** for or wettability with organic electrolytes. The separator should be fully immersed in the organic electrolyte so that enough organic electrolyte can be retained and enough ions can be provided when they are needed.

g) **Low cost**.

h) Possible shutdown behavior. It is not compulsory.

D.1. "TRADITIONAL" SEPARATORS

The separators currently used in the Li-ion batteries are typically a microporous polyethylene (PE) or polyprolyene (PP) membrane, which may be in a single layer or a multilayer structure with variations in parameters of porosity, pore size, thickness, and mechanical strength. Celgard® is an example of a microporous polyolefin separator, usually between 25 and 35 μm thick [51]. The shutdown function is based on the different melting temperature ranges between the PE (120-130ºC) and PP (>165ºC). When the temperature reaches the PE's melting range, the PE layer melts and closes its pores to shut the current off whereas the PP layers still remain mechanically strong to isolate the electrodes. Since the pore closing is irreversible, the battery will be damaged permanently once the thermal shutdown is initiated [52,53].

Most battery-related accidents are related to the mechanical failure of the separator, such as meltdown and metal penetration. Major energies of an accident are originated from the chemical reactions between the charged cathode and anode material as a result of the separator failure, which makes two electrodes contact together.

All commercial separators so far have been made of polyolefins, but they provide only limited heat resistance. Research is now focusing on separators made of different materials which would offer superior heat resistance. These include heat-resistant rubber such as silicone rubber and fluororubber, aromatic polyamide resin, liquid crystalline polyester resin, heat-resistant resin containing polyoxyalkylene, and resin with crosslinked groups. Separators made of such materials are expected to demonstrate not only high temperature stability and safety but also superior ion transportation for better rate capability at high current discharge.

Normally, separators are obtained by mixing a polymer uniformly with solvent at elevated temperature, and the solvent is then evaporated from the mixture to produce a

porous membrane. After mixing at elevated temperature, cooling, and film formation, the volatile solvent is evaporated to get a porous structure. After evaporation, extension and heat-treatment are applied to adjust thickness, mechanical strength, pore structure, and number of pores. Other components can be added into the mixture of polymer and solvent to change the morphology after phase separation. Nonetheless, electrospinning is another important fabrication technique in innovative separators.

D.2. SOLID ELECTROLYTES: POLYMER ELECTROLYTE MEMBRANES

Solid electrolytes are ion conductors that should have a high ionic conductivity, low electronic conductivity, and low activation energy that can be used as separators in batteries. Currently, solid electrolytes can be divided into inorganic and organic categories. Organic solid electrolytes are also called solid polymer electrolytes, which are regarded as a kind of electrolyte that contains polymeric materials and allows the movement of ions. Gel polymer electrolytes are an intermediate type between liquid and solid electrolyte.

As mentioned earlier, internal short circuits, leaks, corrosive reactions and combustible reaction products at the electrode surface associated with liquid electrolytes can be prevented to a large extent by using polymeric membranes as electrolytes. Polymer electrolytes can be classified as follows:

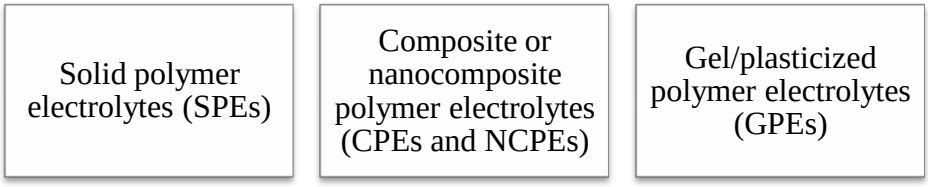

SPEs are neat polymers which serve as both solvents to dissolve lithium salts and mechanical matrices to support processability. GPEs, also called polymer liquid electrolytes, are based on polymer gels where the polymer encages a liquid electrolyte solution and the polymer, swollen by the solvent, mainly provides dimensional stability. In a composite electrolyte, alternatively called “composite polymer electrolytes” high

surface area particulate fillers such as ZrO_2, TiO_2, Al_2O_3 and hydrophobic fumed silica are incorporated into the polymer matrices, eventually obtaining a dispersion at the nanoscale. These organic-inorganic systems can then be used either as all solid electrolytes or as gel electrolytes.

For each class, further groups based on the chemical architecture of the polymer matrix, namely thermoplastic polymers and cross-linked ones can be distinguished (i.e. elastomers or thermoset polymers).

Owing to poor ion conductivities ($\sigma = 10^{-6}\ \mathrm{S \cdot cm^{-1}}$), at present SPEs remain a topic of academic interest, with a remote chance of practical application; on the other hand, GPEs have shown much higher feasibility. The proximity of GPEs to conventional non-aqueous electrolytes, both for physical and electrochemical aspects, including their electrochemical stability on various electrodes and corresponding interfacial chemistry, makes them viable candidates for practical applications.

▪ SOLID POLYMER ELECTROLYTE (SPE) MEMBRANES

Poly(ethylene oxide) (PEO), can dissolve inorganic salts and exhibit ion conduction at room temperature. PEO-based electrolytes offer very low σ values that range from 10^{-8} to 10^{-4} $\mathrm{S \cdot cm^{-1}}$ at temperatures between 30 and 100ºC, which excludes ambient temperature applications.

The advantages that polymer electrolytes can offer are: a) excellent processability and flexibility, b) higher safety owing to the absence of flammable organic solvents and the much lower reactivity of macromolecules toward lithium, c) possible prevention of the growth of Li dendrites upon cycling, d) high dimensional stability, d) improvement in energy density and reduction of manufacturing cost by simplified cell configuration [54].

▪ COMPOSITE AND NANOCOMPOSITE POLYMER ELECTROLYTE MEMBRANES

One of the most promising ways to improve the electrochemical and mechanical properties of polymer electrolytes is the addition of ceramic fillers. It is well established that ceramic filler improve the conductivity of the polymer hosts and enhance their interfacial properties when in contact with the lithium electrode [55].

In general, ceramic particles used in the polymer matrix are broadly classified into two categories: active fillers and passive fillers. The active fillers, such as Li_2N and $LiAl_2O_3$ materials, take part in the conduction process, while inactive materials such as Al_2O_3, SiO_2 and MgO are not involved in the lithium transport process.

The filler content generally influences the ionic conductivity. The dilution effect which tends to depress the conductivity is efficiently contrasted by the specific interactions of the ceramic surface, which can promote fast ion transport. A maximum in the conductivity versus composition curve is expected, generally occurring around 8-10 wt%. There have been many more studies into understanding the effect of solid fillers, quantify of filler, size, type, nature…

—Gel polymer electrolyte (GPE) membranes

Dry polymer electrolyte systems, typically represented by PEO/LiX systems, offer very low ionic conductivity at ambient temperature which excludes this type of membrane from practical applications. Hence, large research efforts have been devoted to expanding the region of operation of the PEO/LiX matrix. The most common approach is the addition of low molecular weight liquid plasticizers.

The plasticized electrolytes are much closer to actual applications than SPEs. They inherit important properties from the bulk liquid electrolytes, including ion conduction, electrochemical stability of the anode and various metal oxide cathode materials. Certainly, the concomitant consequence of the low polymer content in GPEs is their poorer mechanical strength compared to the pure SPEs. So cross-linking is usually

necessary. Since the polymer mainly serves as swollen matrix to provide dimensional integrity, the ether linkage of PEO $(CH_2 - CH_2 - O -)$ with its complexing ability is no longer the sole macromolecular structure of choice. The most used polymers are poly(ethylene oxide) (PEO), poly(propylene oxide) (PPO), poly(acrylonitrile) (PAN), poly(methyl methacrylate) (PMMA), poly(vinyl chloride) (PVC), poly(vinylidene fluoride) (PVDF) or poly(vinylidene fluoride)-hexafluoropropylene) (PVDF-HFP) [56].

While the previous GPE membranes are non-porous and the membrane polymer structure is crucial because transport occurs through the polymer itself, in separator function has also become more demanding and complex; they should be very good electronic insulators and have the capability of conducting ions by soaking electrolyte. The materials should also be soft and flexible enough to be laid between the electrodes. Starting with cedar shingles and sausage casing, separators have been manufactured from many different polymeric materials from cellulosic papers and cellophane to nonwoven fabrics, foams, ion exchange membranes and microporous flat sheet membranes.

6.1.4. POLYIMIDE MEMBRANES

Conventional polyolefin microporous membranes (Celgard©) are usually used as separators for most Li-ion batteries due to their quite suitable chemical stability, thickness, and mechanical strength. However, several intrinsic factors such as low porosity (about 40%), poor thermal stability and large difference of polarity between the highly polar liquid electrolyte and the nonpolar polyolefin separator lead to high cell resistance, low rate capability and even internal short circuits of Li-ion batteries, which severely restricts the electrochemical performance of the Li-ion batteries. Therefore, the development of new separators having high porosity and thermal stability, good wettability toward liquid electrolyte is considered to be of significant importance for fabricating high-performance rechargeable Li-ion batteries [57–60].

Given the low cost and ease in the construction of microstructures (e.g., pore size and porosity), new polymer separators are attractive and promising to replace the

conventional microporous polyolefin membranes. Some novel methods have been applied to fabricate fibrous polymer membranes as the separators of Li-ion batteries, such as the paper-making method, solution extrusion method via a spinning jet, and the melt blowing method. Electrospinning is an interesting and useful technique that produces continuous fibers with diameters in the range of nanometers to a few microns. Electrospun fiber membranes can possess smaller pore size, higher porosity and air permeability compared to the conventional method, making them excellent candidates for separators in rechargeable Li-ion batteries. Different types of polymers are utilized and the most used are poly(ethylene) (PE) [61], poly(propylene) (PP) [62], poly(ethylene oxide (PEO) [63,64], poly(acrylonitrile) (PAN) [63,65], polyimide (PI) [66], poly(vinylidene fluoride) and its copolymers (PVDF-co-trifluoroethylene, PVDF-TrFE and PVDF-co-hexafluoropropene, PVDF-HFP) [67–70] have already been developed and evaluated in Li-ion batteries.

The advantages of polyimide polymer in comparison with other polymers are that exhibit higher thermal stability and chemical resistance [71]. Different works show that some polyimide membranes have higher capacity when compared to Celgard membranes and improve the safety of battery [66,71–73]. In this thesis new amorphous copolyimide containing nitrile groups obtained from a mixture of two aromatic diamines, 1,3-Bis-2-cyano-3-(3-aminophenoxy)phenoxybenzene (diamine 2CN) and 1,3-Bis(3-aminophenoxy)benzene (diamine 0CN) have been synthesized [74]. In this thesis the performance of these electrospun membranes as battery separator is evaluated.

Polyimide (PI), as one kind of high-performance engineering polymers, has been widely used in many advanced technology fields due to their excellent thermal stability, outstanding mechanical properties, low dielectric constants and inertness to solvent and radiation resistance [75–77]. There are many examples of aromatic polyimides in membrane technologies for fuel cells [78], or gas separation membranes [79,80].

Nonetheless, in the beginning polyimides have found application in a limited number of technologies, normally in film form, because their habitual infusible and insoluble nature. But nowadays thanks to the advancements in polymer research and to structural modifications of the polymer backbone these drawbacks can be overcome.

Polyimides (PI) have rigid molecular chains, resulting in poor solubility in common organic solvents and this inevitably affects their synthesis, processing, and application [81]. Therefore, many significant efforts have been made to chemically modify the structure to improve their processability without affecting other properties like thermal stability or mechanical properties by the introduction of flexible groups (–O–, –CO, –SO_2–, –S– and –$C(CF_3)_2$–) into the polyimides backbone, inclusion of bulky side groups or incorporation of a kink in the polyimides backbone through *ortho* or *meta* catenation instead of *para* catenation [82–84].

Traditionally, polyimide processing was carried out with poly(amic acid) intermediate and then converted to polyimide by thermal treatment (two-step method) [85]. However, this process has several inherent problems such as emission of volatile byproducts (e.g., H_2O) and storage instability of poly(amic acid) intermediate [86]. Therefore, alternative synthetic methods were developed in order to obtain directly in a unique step a polyimide. This way, called one-step polycondensation method, is employed for the synthesis of polyimides which are being soluble in organic solvents at polymerization temperatures [87,88]. It involves heating a stoichiometric mixture of monomers in a high boiling solvent or in a mixture of solvents at 180-220ºC. The amic acid group rapidly converts to an imide or reverts back to amine and dianhydride. The imidization proceeds rapidly at these temperatures and the water generated due to the reaction is distilled off continuously as an azeotrope mixture along with the solvent (normally nitrobenzene, m-cresol, or other dipolar aprotic amide solvents) in the presence of a catalyst such as quinoline, tertiary amines, alkali metals and zinc salt of carboxylic acids. An acidic catalyst such as benzoic acid is added to promote the formation of trans-isoimide and later a basic catalyst such as isoquinoline to convert it into a polyimide. The imidization still proceeds via the amic acid route although the concentration of amic acid at any time is very small.

This process is especially useful for polymerization involving unreactive dianhydrides and diamines. The possibility of obtaining directly soluble polyimides has widened the range of applications.

6.1.5. ELECTROSPINNING

In general the processing of polyimides is in film form, but polymers with other forms, such as nanofibers are interesting for some applications. Nanofibers can be processed by a number of techniques such as template synthesis, drawing, self-assembly, phase separation, and electrospinning [89]. Among these techniques, electrospinning is of great interest because of its great potential for industrial-scale processing and repeatability in control of fiber dimension [90]. The production of continuous fibers with diameters ranging from micrometers to nanometers can be a key factor for some high technology applications. This technique creates electrospun structures with unmatchable properties like alignment on the molecule level, high surface area, extremely long length or complex pore structure [91]. Those characteristics enable fibrous structures for potential applications in research field, e.g. fiber and textile, templates, enzyme carriers, surfaces, pharmaceutical, medical applications, electronic industries and battery separators. The combination of high performance polyimides and the facility of electrospinning can give birth to a series of multi-functionalizated PI materials with hierarchical constructions.

A process was patented by Formhals [92], wherein an experimental setup was outlined for the production of polymer filaments using electrostatic force. When used to spin fibers this way, the process is termed as electrospinning. In other words, electrospinning is a process that creates nanofibers through an electrically charged jet of polymer solution or polymer melt. The electrospinning process, in its simplest form, consisted of a syringe to hold the polymer solutions, two electrodes and a dc voltage supply in the kV range. The polymer drop from the syringe tip is drawn into a fiber due to the high voltage. The jet was electrically charged and the charge caused the fibers to bend in such a way that the fiber was collected as a web of fibers on the surface of a grounded target. During the electrospinning an electrical potential is applied between a droplet of polymer solution or melt held at the end of a capillary and a grounded collector. The droplet of the polymer solution is pulled to the capillary tip of the syringe, where is converted into a conical shape jet stream, the so-called Taylor cone (Figure 6.12) [93], due to the influence of the electrostatic forces generated by the applied electric field

[94]. When the surface tension is overcome by the electrostatic forces, a thin charged jet stream is generated and ejected to the counter electrode, evaporating the solvent from the solution. That is, the electrospinning jet will travel towards the region of lower potential, which in most cases, is a grounded collector. Finally, the ultrathin fibers are deposited on the substrate located above the counter electrode, called collector. There are many parameters that will influence the morphology of the resultant electrospun fibers.

Although electrospinning is in theory a very simply process, requiring just simple laboratory equipment to yield fibers down to the nanoscale, the science behind it is not simple at all. Electrospinning process involves the understanding of electrostatics, fluid rheology and polymer solution properties such as rate of solvent evaporation, surface tension and solution conductivity. These fundamental properties are constantly interacting and influencing each other during the electrospinning process.

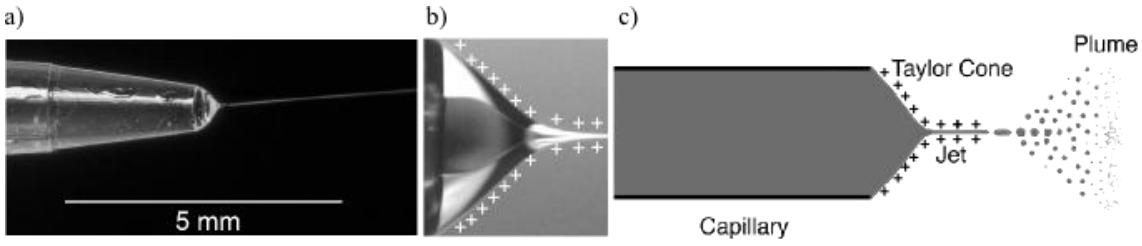

Figure 6.12. a) Picture showing a fiber drawn from a Taylor cone by the process of electrospinning, b) amplified photograph of a Taylor cone, and c) electrospray diagram depicting the Taylor cone, jet and plume.

Important features of electrospinning are: a) suitable solvent should be available for dissolving the polymer, b) the vapor pressure of the solvent should be suitable so that it evaporates quickly enough for the fiber to maintain its integrity when it reaches the target but not too quickly to allow the fiber to harden before it reaches the nanometer range, c) the viscosity and surface tension of the solvent must neither be to large to prevent the jet from forming nor be too small to allow the polymer solution to drain freely from the pipette, d) the power supply should be adequate to overcome the

viscosity and surface tension of the polymer solution to form and sustain the jet from the pipette, and e) the gap between the pipette and grounded surface should not be too small to create sparks between the electrodes but should be large enough for the solvent to evaporate in time for the fibers to form [95].

In order to carry out electrospinning, the polymer must be first in a liquid form, either as molten polymer or as polymer solution. The property of the solution plays a significant part in the electrospinning process, the polymer solution will be drawn from the tip of the needle. The electrical property of the solution, surface tension and viscosity will determine the amount of stretching of the solution. The rate of evaporation will also be influenced by the viscosity of the solution as it is being stretched.

The charges on the polymer solution must be high enough to overcome the surface tension of the solution. As the solution jet accelerates from the tip of the source to the collector, the solution is stretched while **surface tension** of the solution may cause the solution to breakup into droplets. The **solubility** of the polymer in a particular solvent may also affect the resultant fiber morphology. Polymer solubility is more complex than that of low molecular weight compounds due to size difference between polymer and solvent molecules, viscosity of the system, effect of the structure and molecular weight of the polymer. Generally, the **viscosity** of the solution is related to the extent of polymer molecule chains entanglement within the solution. A higher viscosity will means that there is greater interaction between the solvent and polymer molecules thus when the solution is stretched under the influence of the charges, the solvent molecules will tend to spread over the entangled polymer molecules thus reducing the tendency for the solvent molecules to come together [96,97].

During the electrospinning, the solvent will evaporate as the electrospinning jet accelerates towards the collector. If most of the solvent has been evaporated when the jet reaches the collector, individual fibers are formed. However, if the rate of **evaporation** of the solvent is too low such that the solution has not evaporated sufficiently when the electrospinning jet reaches the collector, fibers may not be formed at all and a thin film of polymer solution is deposited on the collector. In addition, during the process the solution must gain sufficient charges such that the repulsive

forces within the solution are able to overcome the surface tension of the solution. Subsequent stretching or drawing of the electrospinning jet is also dependent on the ability of the solution to carry charges.

Generally, the **electric conductivity** of the solvents is very low (typically between 10^{-3} to 10^{-9} $ohm^{-1} \cdot m^{-1}$) as they contain very few free ions, if any, which are responsible for the electric conductivity of the solution. The presence of acids, bases, salts and dissolved carbon dioxide may increase the conductivity of the solvent. The electrical conductivity of the solvent can be increased significantly through mixing chemically non-interacting components. Substances that can be added to the solvent to increase its conductivity includes mineral salts, mineral acids, carboxylic acids, some complexes of acids with amines, stannous chloride and some tetraalkylammonium salts.

Other important parameter that affects the electrospinning process is the various external factors exerting on the electrospinning jet. This includes the voltage supplied, the feed rate, temperature of the solution, type of collector, diameter of needle and distance between the needle tip and collector.

A key element in electrospinning is the application of a high **voltage** to the solution. The high voltage will induce the necessary charges on the solution and together with the external electric field, will initiate the electrospinning process when the electrostatic force in the solution overcomes the surface tension of the solution. Generally, both high negative or positive voltage of more than 6 kV is able to cause the solution drop at the tip of the needle to distort into the shape of a Taylor cone during jet initiation. Depending on the feed rate of the solution, a higher voltage may be required so that the Taylor cone is stable [98].

The **feed rate** will determine the amount of solution available for electrospinning. For a given voltage, there is a corresponding feed rate if a stable Taylor cone is to be maintained. When the feed rate is increased, there is a corresponding increase in the fiber diameter or beads size, because a greater volume of solution that is drawn away from the needle tip. However, there is a limit to the increase in the diameter of the fiber due to higher feed rate. If the feed rate is the same as that at which the solution is carried away by the electrospinning jet, there must be a corresponding increase. Due to the

greater volume of solution drawn from the needle tip, the jet will takes a longer time to dry. As a result, the solvent in the deposited fibers may not have enough time to evaporate given the same flight time [99].

The **temperature** of the solution has both the effect of increasing its evaporation rate and reducing the viscosity of the polymer solution. This may be due to the lower viscosity of the solution and greater solubility of the polymer in the solvent which allows more even stretching of the solution. With a lower viscosity, the Coulombic forces are able to exert a greater stretching force on the solution thus resulting in fibers of smaller diameter.

There must be an electric field between the source and the collector for electrospinning to initiate. The **collector** plate is made out of conductive material such as aluminium foil which is electrically ground so that there is a stable potential difference between the source and the collector. With respect to the **diameter of needle orifice**, a smaller internal diameter was found to reduce the clogging as well as the amount of beads on the electrospun fibers. The reduction in the clogging could be due to less exposure of the solution to the atmosphere during electrospinning. Decrease in the internal diameter of the orifice was also found to cause a reduction in the diameter of the electrospun fibers [100].

The flight time will affect the electrospinning process and the resultant fibers. Varying the **distance between the tip and the collector** will have a direct influence in both the flight time and the electric field strength. The electrospinning jet must be allowed time for most of the solvents to be evaporated. When the distance between the tip and the collector is reduced, the jet will have a shorter distance to travel before it reaches the collector plate. Moreover, the electric field strength will also increase at the same time and this will increase the acceleration of the jet to the collector.

Any interaction between the surrounding (ambient parameters) and the polymer solution may have an effect on the electrospun fiber morphology. High **humidity** for example was found to cause the formation of pores on the surface of the fibers. At high humidity, it is likely that water condenses on the surface of the fiber when electrospinning is carried out under normal atmosphere. The composition of the air (**type of atmosphere**)

in the electrospinning environment will have an effect on the electrospinning process too. Different gases have different behavior under high electrostatic field. Under enclosed condition, it is possible to investigate the effect of **pressure** on the electrospinning jet. Generally, reduction in the pressure surrounding the electrospinning jet does not improve the electrospinning process. When the pressure is below atmospheric pressure, the polymer solution in the syringe will have a greater tendency to flow out of the needle and there causes unstable jet initiation. At very low pressure, electrospinning is not possible due to indirect discharge of the electrical charges [101].

Just by varying those parameters of electrospinning, it is possible to get some variation in the morphology of the nanofibers. Several parameters have been linked to the formation of beaded fibers as covered earlier. There are various possibilities: porous nanofibers, flattened or ribbon-like fibers, branched fibers, helical fibers, hollow nanofibers, and fiber with different compositions (using co-axial electrospinning).

Nevertheless, although the morphology of the nanofibers can be controlled to a certain extent, basic electrospinning can only yield randomly aligned nanofibers. The most basic form of getting aligned fibers rather than random mesh is through the use of a rotating mandrel. This is a simple, mechanical method of aligning the fibers along the circumference of the mandrel. Other possibilities is using a knife edge disk to direct the electrostatic field lines to the knife-edge of the disk, using an auxiliary electrode/electrical field or a parallel conducting collector.

6.2. EXPERIMENTAL DETAILS

6.2.1. SYNTHESIS AND ELECTROSPUN MEMBRANES FABRICATION

A. SYNTHESIS OF POLYIMIDES

The polyimides employed in the study were obtained by a different method to that used in the other chapters. Instead of the two-step method, a polymerization in one step was used.

Two homopolymers and one copolymer have been prepared, a homopolyimide with zero cyano lateral groups in its backbone, a polyimide with two cyano groups, and a random copolyimide which is an equimolar mixture of the two previous ones, i.e, a 50 mole percentage of repetitive unit with zero cyano groups (0CN) and another 50 mole percentage of the two cyanos unit (2CN).

Polycondensation polymerizations start with the reaction between a dianhydride (4,4'-oxydiphtalic anhydride) (ODPA) and a diamine, the 1,3-bis-2-cyano-3-(3-aminophenoxy)phenoxybenzene (Diamine 2CN) [85] or the 1,3-Bis(3-aminophenoxy)benzene (Diamine 0CN), in the case of the homopolymers. For obtaining the copolyimide both diamines are used together.

Polyimides were synthesized via one-step polycondensation with m-cresol as solvent [58,102–105], with a few milliliters of toluene [57] in order to add another component to generate a new lower-boiling azeotrope that the pure m-cresol. In Figure 6.13 can be observed the scheme of the synthesis in the case of the copolyimide 0CN-2CN.

Stoichiometric quantities of dianhydride and diamine were placed in a two-necked flask fitted with a mechanical stirrer and a condenser. The reaction flask was purged with dry N_2 and the solution was progressively heated to 180-190ºC and maintained at that

temperature for 8h. During the heating, water produced by the imidization reaction was removed and continuously simultaneously by azeotropic distillation in an nitrogen stream [87]. The reaction mixture was then cooled to room temperature and poured into excess methanol. The fibrous polymer obtained was washed thoroughly with boiling ethanol using a soxhlet extractor and dried at 80ºC under vacuum overnight.

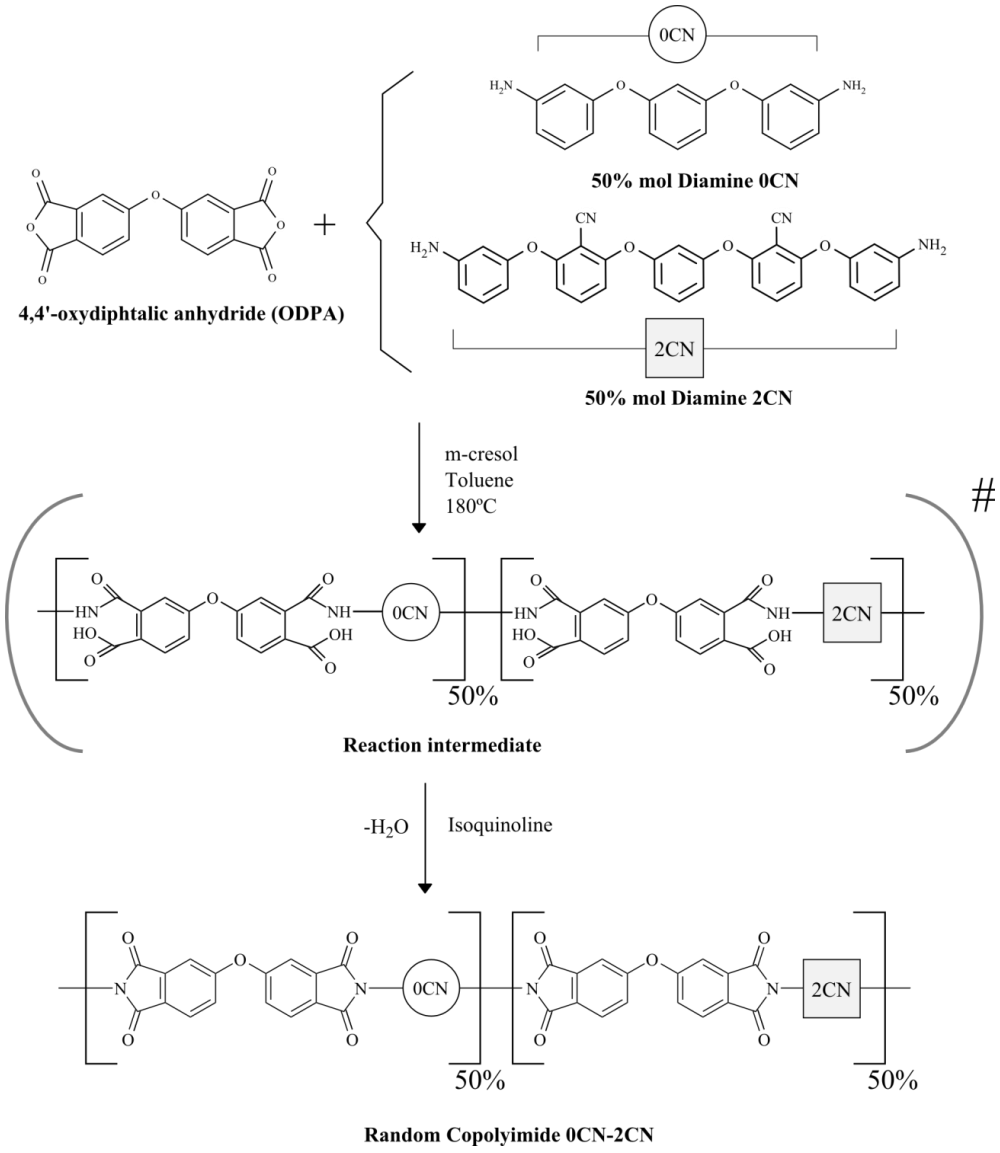

Figure 6.13. Reactive structures and scheme of the one-step method for the copolyimide 0CN-2CN

B. ELECTROSPINNING PROCESS OPTIMIZATION

Electrospinning is a process involving polymer science, applied physics, fluid mechanics, electrical, mechanical, chemical, material engineering and rheology. As indicated above, the fiber morphology is controlled by the experimental parameters and is dependent upon solution conductivity, concentration, viscosity, polymer molecular weight, applied voltage, etc [106,107]. Much work has been done on the effect of parameters on the electrospinning process and morphology of fibers, and the most important parameters are related with the effect of polymer concentration, applied voltage and feed rate [108–111].

In order to optimize the morphology and average fiber diameter of electrospun PI, a series of experiments were designed and employed at ambient conditions (room temperature, humidity, air atmosphere and normal pressure). The total six parameters consisted of:

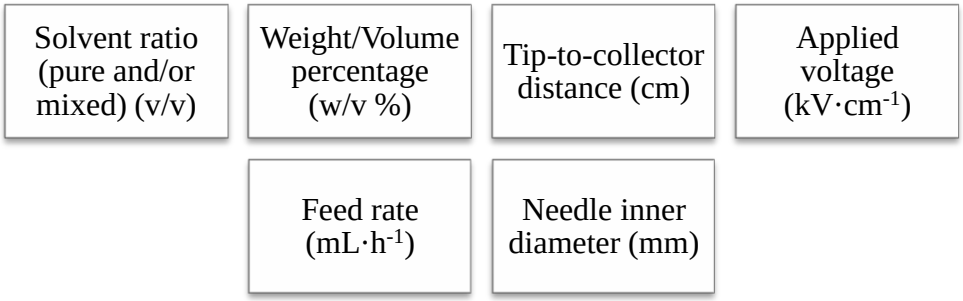

From previous works we have could anticipate some conditions for PI's could be similar with we used for other polymers. For instance, the optimization process was carried out only for the polyimide without cyano groups (Polyimide 0CN), because its behavior in solution is quite similar to the rest of the studied polyimides.

The experimental variables are summarized in Table 6.2.

Mean diameters of the electrospun fibers at different conditions were measured by Image J software and the results appear in Figure 6.14, where it can be noted that the fiber diameter is similar in most of the conditions.

Table 6.2. Electrospinning experiment variables.

Variable description	Conditions
Solvent ratio (DMF and/or DMAc) (v/v)	0/1, 1/1,
Weight/Volume percentage (w/v %)	25, 50
Tip-to-collector distance (cm)	10, 20
Applied voltage ($kV \cdot cm^{-1}$)	0.6, 0.75, 1.0, 1.5,
Feed rate ($mL \cdot h^{-1}$)	0.2, 0.5, 1, 2
Needle inner diameter (mm)	0.2, 0.5, 1, 1.7

It was found that the solvent ratio and polymer concentration affects the formation of particle-to-fiber. Pure DMAc and the lower polymer concentration (25 w/v %) resulted in more beads and polymer particles. But instead when it was employed a solvent ratio 1/1 well defined nanofibers were observed. When the distance between the tip and the collector was reduced to 10 cm, the fibers tended to merge where they contact to form junctions, a situation not desirable for battery separators. Accordingly, only a solvent ratio of 1/1 (DMAc/DMF) and a tip-collector distance of 20 cm was used for the rest of the samples.

C. ELECTROSPINNING SETUP IN THE OPTIMUM CONDITIONS

The three different polymers (polyimide 0CN, copolyimide 0CN-2CN and polyimide 2CN) were dissolved in a mixed solvent of N,N-dimethylformamide and N,N-dimethylacetamide (1/1 volume ratio) to achieve a polymer concentration of 50% (w/v) of the solution. The polymer solution was then dissolved at room temperature using a magnetic stirrer until complete polymer dissolution. Electrospinning was performed on aluminium collector. The polymer solution was placed in a plastic syringe of 10 mL

volume (V) fitted with a steel needle with 0.5 mm of inner diameter (Ø). Electrospinning was conducted at 1.5 kV·cm^{-1} with a high voltage power supply from Glassman (model PS/FC30P04). A syringe pump (from Syringepump) was used to feed the polymer solutions into the needle tip at 0.2 mL·min^{-1} (Q, flux). A schematic of the experimental setup is shown in Figure 6.15a. Polymer 0CN, copolymers 0CN/2CN (50/50) and polymer 2CN were prepared and will be called hereafter 0CN, 0CN/2CN (50/50) and 2CN. In Figure 6.15b is shown a photography of the setup, and in Figure 6.15c, appears one of the samples produced by electrospinning corresponding to a polyimide 0CN.

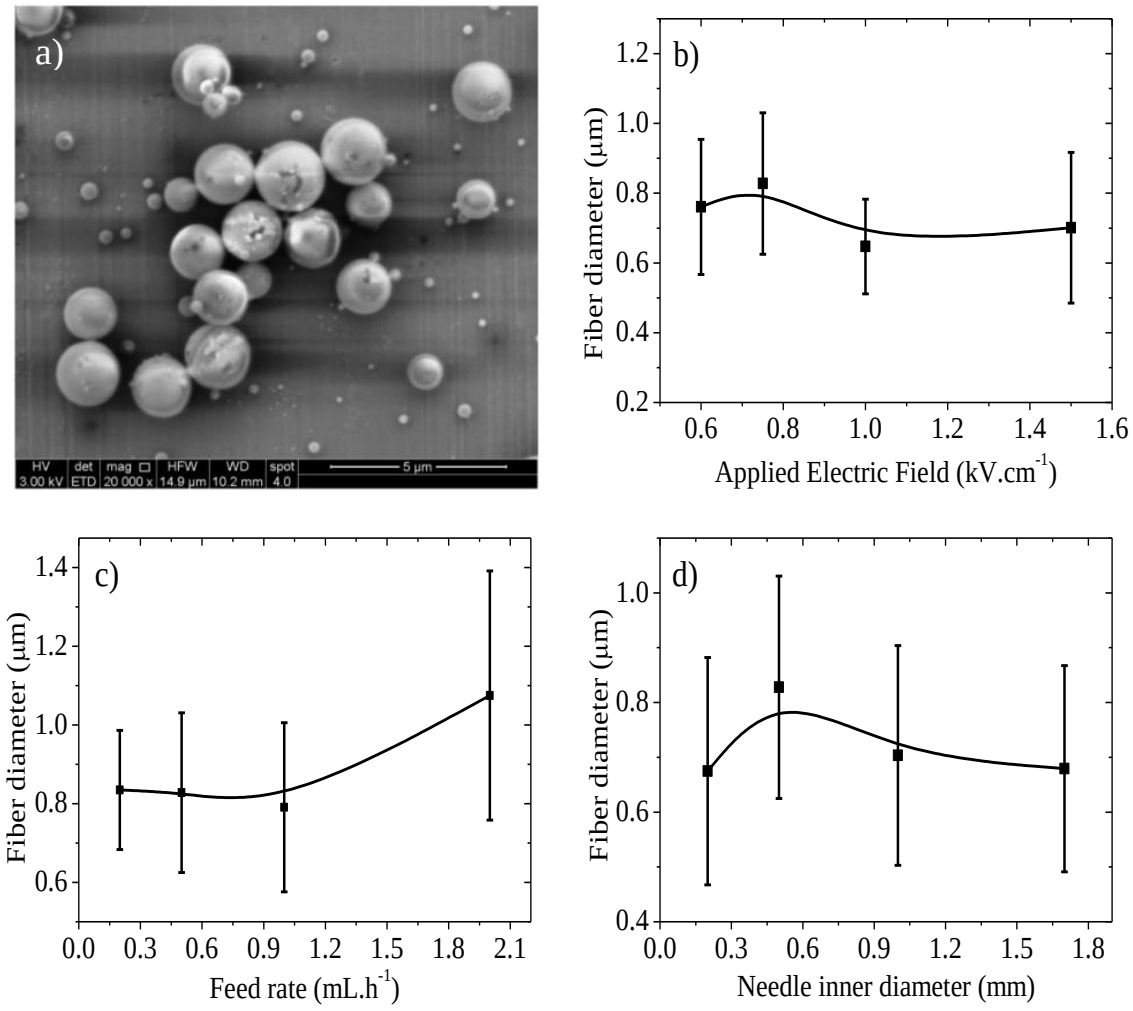

Figure 6.14. a) Polyimide 0CN beads using pure DMAc as solvent. Fiber diameter statistical results for the Polyimide 0CN dissolved in DMF/DMAc (1/1, 50 w/v %), showing the influence of: b) applied electric field (kV cm^{-1}), c) feed rate (mL h^{-1}) and d) needle inner diameter (mm)

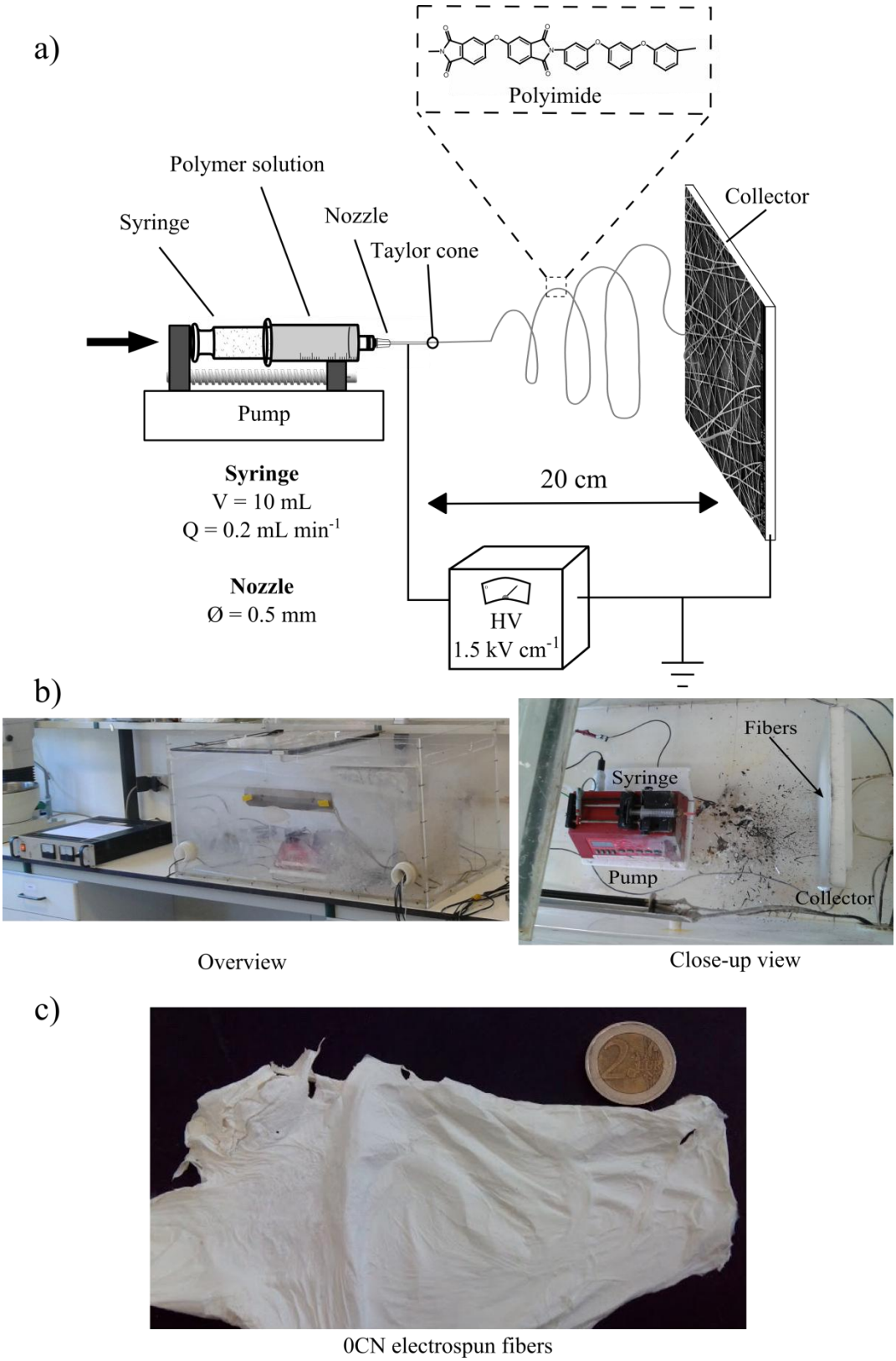

Figure 6.15. a) Schematic of the electrospinning setup in the optimum conditions, b) photographs of the electrospinning setup and c) section of polymer 0CN electrospun fiber mats.

6.2.2. CHARACTERIZATION OF MEMBRANES

A. ELECTROLYTE SOLUTION AND UPTAKE

Electrospun membranes were immersed in a liquid electrolyte consisting of lithium hexafluorophosphate solution – in ethylene carbonate and dimethyl carbonate, 1.0 M $LiPF_6$ in EC:DMC= 50/50 (v/v) (LP30, Merck) and the uptake was evaluated by Equation 6.7:

$$Uptake = \left(\frac{M - M_0}{M_0}\right) \times 100\% \tag{6.7}$$

where M_0 is the mass of the membrane and M is the mass of the membrane after immersion in the electrolyte solution.

B. POROSITY

The porosity of the membranes was determined by the method of dry-wet weight [112]. The wet weight of membrane was measured after wiping the excess water. The dry weight of membrane was measured after drying in freezing dryer. The porosity of membrane was calculated as following:

$$\varepsilon = \frac{W_w - W_d}{\rho_w A\, \delta} \tag{6.8}$$

where ε is the porosity of membrane, W_w (g) is the mass of the wet membrane, W_d (g) is the mass of the dry membrane, ρ_w (g.cm^{-3}) is the water density, A (cm^2) is the membrane area and δ (cm) is the membrane thickness.

C. CELL PREPARATION AND ELECTROCHEMICAL MEASUREMENTS

Electrochemical impedance spectroscopy of electrospun polyimide was evaluated on Biologic VMP3 instrument in a frequency range from 1 MHz to 10 mHz with an amplitude of 10 mV at room temperature. The ionic conductivity was determined by

$$\sigma = \frac{t}{A \times R_b} \tag{6.9}$$

where t is the thickness, A is the area of the samples and $R_b$is the bulk resistance obtained from the intercept of the imaginary impedance (minimum value of Z'') with the slanted line in the real impedance (Z') through the Randles circuit [69].

Li/Separator/C-$LiFePO_4$ half-cells were assembled in an argon-filled homemade glove box using Swagelok-type cells with C-$LiFePO_4$ electrode (8 mm diameter) as cathode material, electrospun polyimide soaked in electrolyte solution as separator (10 mm diameter) and 0.75 mm thick *Li* metal foil (8 mm diameter) as anode material, schematized in Figure 6.16.

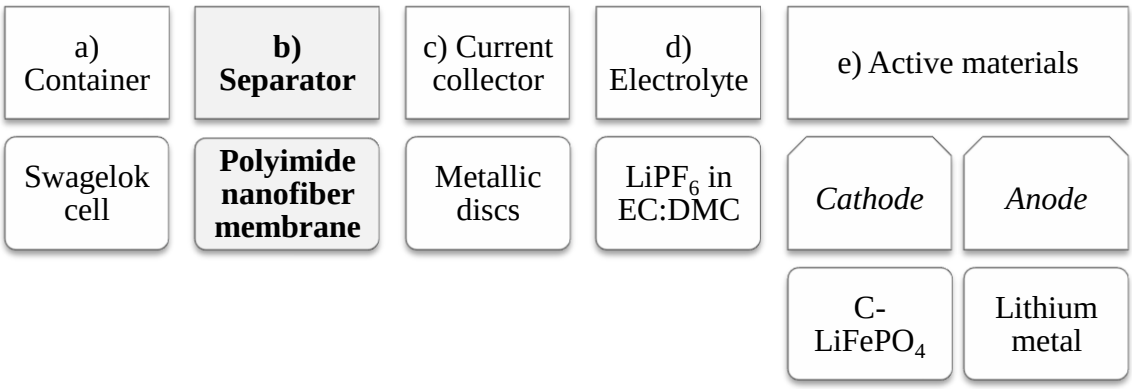

Figure 6.16. Scheme of the different parts of the Li/Separator/C-$LiFePO_4$ half-cells.

The C-$LiFePO_4$ cathode material preparation was described in [113,114]. In order to avoid the largest disadvantage of $LiFePO_4$, its low electrical conductivity, it was

proposed a carbon coating of the cathode. Therefore, the basic constituents of the electrode were the active material ($LiFePO_4$), the conductive additive (carbon) and the binder (PVDF). The preparation occurred in two steps: first, the different components are mixed in the solvent obtaining the electrode slurry; then, casting, drying and calendaring were performed. Electrode films were prepared by casting the slurry on the current collector (Aluminium, Al) by the doctor blade method.

Galvanostatic cycling was carried out, at different C rates (C/20, C/10, and C/5) and at room temperature, between a minimum and a maximum limit of 2.5 and 4.0 V, respectively, using Landt CT2001A Instrument.

6.3. RESULTS AND DISCUSSION

6.3.1. MORPHOLOGY, INFRARED SPECTROSCOPY AND THERMAL PROPERTIES

In section 6.2.1 it was explained that the different electrospinning processing parameters can affect sample morphology, such as applied electric field, solution temperature and viscosity and collection procedure, among others.

In order to obtain uniform electrospun fibres membranes, a stable Taylor cone is required, so preliminary electrospinning experiments were conducted in order to evaluate the best conditions while maintain its stability. It was concluded that a distance between the needle tip and the ground collector of 20 cm, a polymer feed rate of 0.2 $mL \cdot h^{-1}$ and a needle with an inner diameter of 0.5 mm, represent the optimum conditions for the different modified polyimides, and therefore they were kept constant in the different experiments.

The microstructure of the obtained polyimide electrospun samples was analyzed by SEM and is presented in Figure 6.17. Independently of the type of polyimide, smooth and beadless individual fibers were obtained with random alignment and open overall microstructure. The average fiber diameter decreases with the incorporation of dipolar –CN groups in the polymer chain: while neat polyimide presents an average diameter of 1.09 ± 0.24 μm, the modified polymer shows average diameters of 0.50 ± 0.13 μm for the 0CN/2CN and 0.59 ± 0.13 μm for the 2CN sample (Table 6.3). The network structure of the fiber membranes generates a porous structure that is interesting as it facilitates the penetration of the liquid electrolyte (swelling process) through of gelation process.

The average porosity of the polymer membranes was determined according to Equation 6.8 and ranges around 80% for all samples, showing that the modification of the polyimides by incorporation of CN-dipolar groups and even the reduction of the

average fiber diameter does not play any role in the membrane porosity. Table 6.3 summarizes the average fiber diameter and degree of porosity for the different samples.

Table 6.3. Medium diameter fiber and porosity for all electrospun membranes.

Sample	**Medium diameter fiber (μm)**	**Porosity ±15 (%)**
0CN	1.09 ±0.24	82
0CN/2CN (50/50)	0.50 ±0.13	79
2CN	0.59 ±0.13	83

Infrared spectroscopy was used for determining the influence of –CN dipolar groups in the vibration modes of polyimide electrospun membrane. As shown in Figure 6.18, independently of the samples, the vibration modes characteristic of polyimide polymers are detected, that is, at frequencies of 720 cm^{-1} (deformation of the imide ring or of the imide IV carbonyl group, 1028 cm^{-1} (symmetric C-O-C tension), 1117 cm^{-1} (imide III band), 1244 cm^{-1} (asymmetric C-O-C Tension) and 1437-1641 cm^{-1} (C-C Tension) [115,116]. Further, with the incorporation of the –CN dipolar groups, no vibrational modes are totally suppressed and no new modes appear in the spectra (Figure 6.18).

The thermal stability of the electrospun polyimide membranes was evaluated by differential scanning calorimetry (DSC) and thermogravimetric analysis (TGA) and the results are a shown in Figure 6.19. It is observed that the 0CN and 2CN polyimides show a glass transition temperature (T_g) at 176 and 174ºC, respectively, while the copolymer 0CN/2CN (50/50) shows the lowest T_g, at around 157ºC (Table 6.4), which is lower than the one reported in [102] for thermal imidizated polymer films (using the two step method). However, it is important to remember that the synthetic method used in the polyimide fibers was different, chemical imidization was employed (one step method).

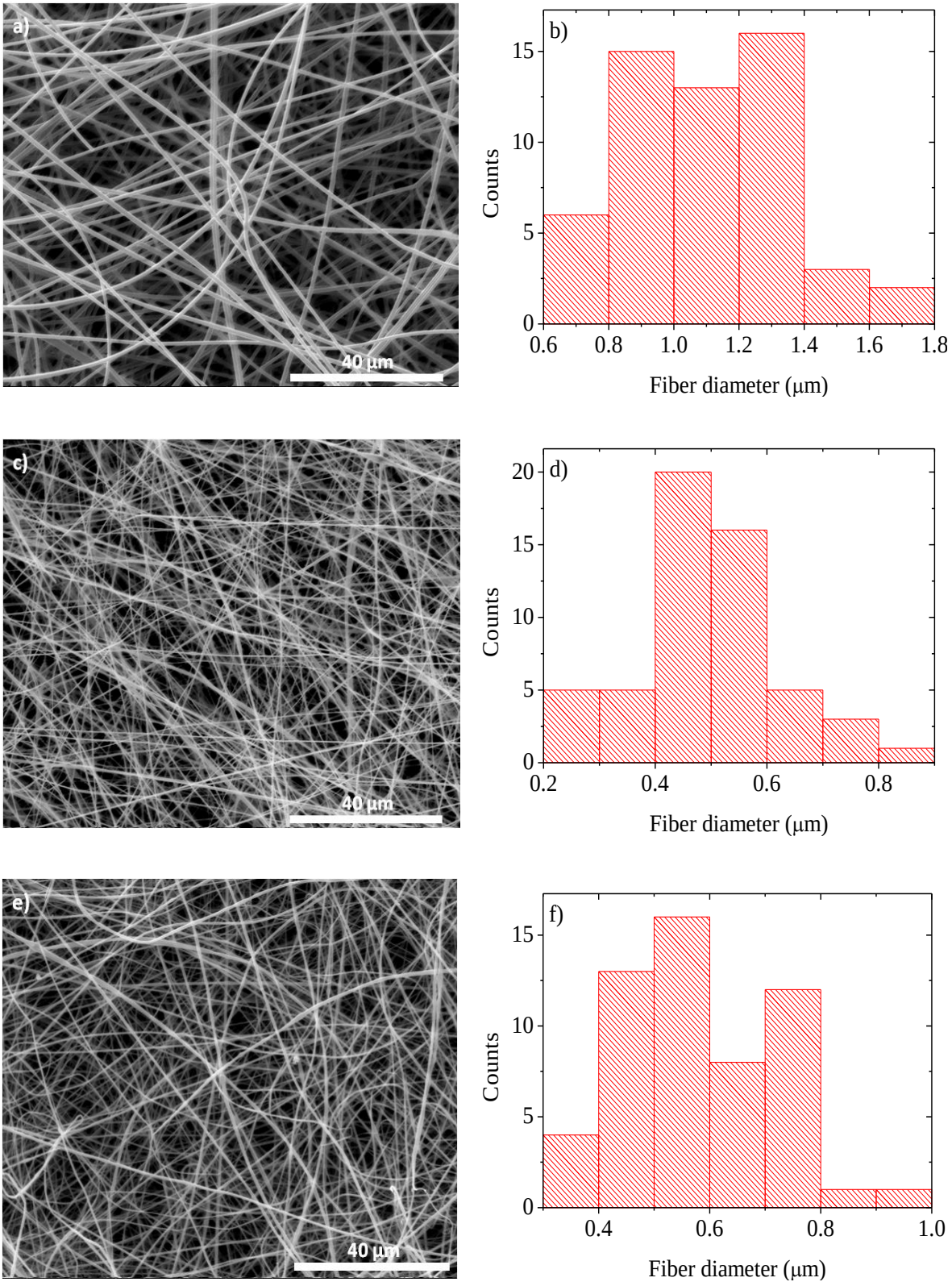

Figure 6.17. SEM images and Size distribution of fibers of polyimide membranes for: a) and b) 0CN, c) and d) 0CN/2CN (50/50), and e) and f) 2CN.

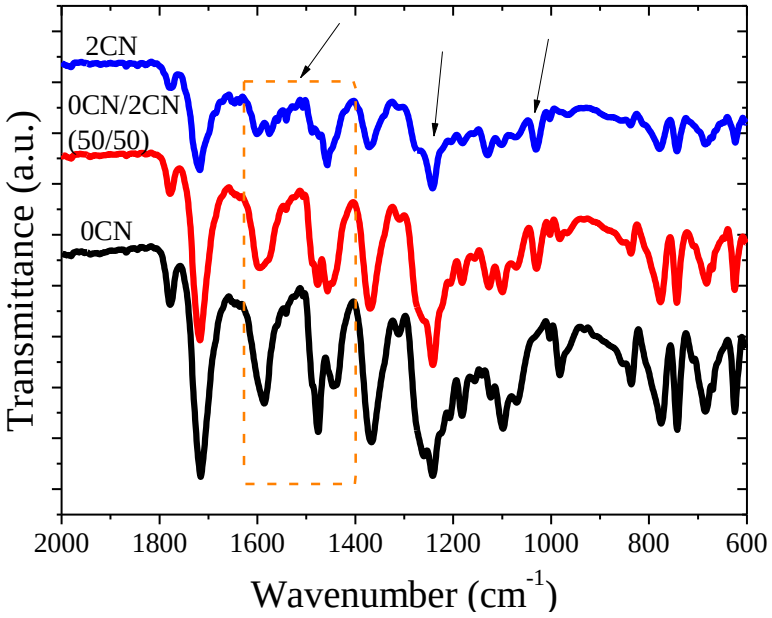

Figure 6.18. FTIR spectra of all electrospun membranes.

In general, in bulk polyimides the thermal properties of polyimides from thermal imidization, including T_g and decomposition temperatures, are superior to those of polyimides from chemical imidization. The difference can be ascribed to morphological changes in the polymers, such as increased ordering from molecular aggregation of the polymer chain segments that occurs during thermal imidization [117]. Moreover, structural modifications are relevant. The incorporation of thermal stable but flexible or unsymmetrical linkages in the backbone, the introduction of large polar or non-polar pendant substituents to the polymer chain, and disruption of symmetry and recurrence of regularity through copolymerization affect the T_g. For instance, the incorporation of flexible linkages, such as –O–, –CH_2–,–SO_2– and hexafluoroisopropylidene groups into the backbone, introduces "kinks" in the main that decrease the rigidity of the polymer backbone and inhibit close packing of the chains.

Apart from the effects of synthetic method or the structural modification, the effect of high electric field must be taking into account. It was reported that the high electric field used to obtain electrospun fibers can lead to polymer chain alignment along the longitudinal direction of the polymer fiber [118], which in turn can influence the glass

transition temperature of the polymer, as demonstrated for poly(vinyl alcohol) (PVA) [119]. Therefore, it might be expected that the alignment of the polymer chains along the longitudinal direction of the polymer fiber would increase T_g, as observed in macroscopic polymer systems [120].

In our case, nevertheless, just a slight change from 178ºC in 0CN and 176ºC in 2CN from bulk polymer [17] down to 176ºC and 174ºC (Table 6.4) in 0CN and 2CN electrospun fibers, respectively, was observed in our samples. On the other hand, a strong decrease of T_g is observed in the 0CN/2CN (50/50) copolymer sample, which can be related to polymer chain [119,121] and amorphous regions confinement [122] in the copolymer due to the different nature of the polymer phases with and without CN-dipolar groups into polyimide polymer.

It was also observed the absence of a cold-crystallization or melting processes, which indicates a complete amorphous polymer with a good thermal stability up to 250ºC (Figure 6.19a).

The TGA results indicate that the 0CN sample and the copolymer 0CN/2CN shows a single step thermal degradation process that starts at ~500 and 403ºC, respectively, while the 2CN sample presents two main degradation steps (Figure 6.19b).

The amount of residue measured at 800ºC is between 57% for the 0CN and 64% for the 2CN sample (Table 6.4). The thermal stability of the polyimide and copolymer are thus dependent on the amount of CN units present in the main chain: increasing the amount of cyano groups (CN) in the polymer chain leads to a decrease in the thermal degradation temperature (Table 6.4).

Thus, it is confirmed the relationship between the initial degradation temperature (T_d) and the presence in the structure of the CN groups, the presence of the two cyano groups (2CN) in the polyimide decreasing the thermal stability of the electrospun membranes.

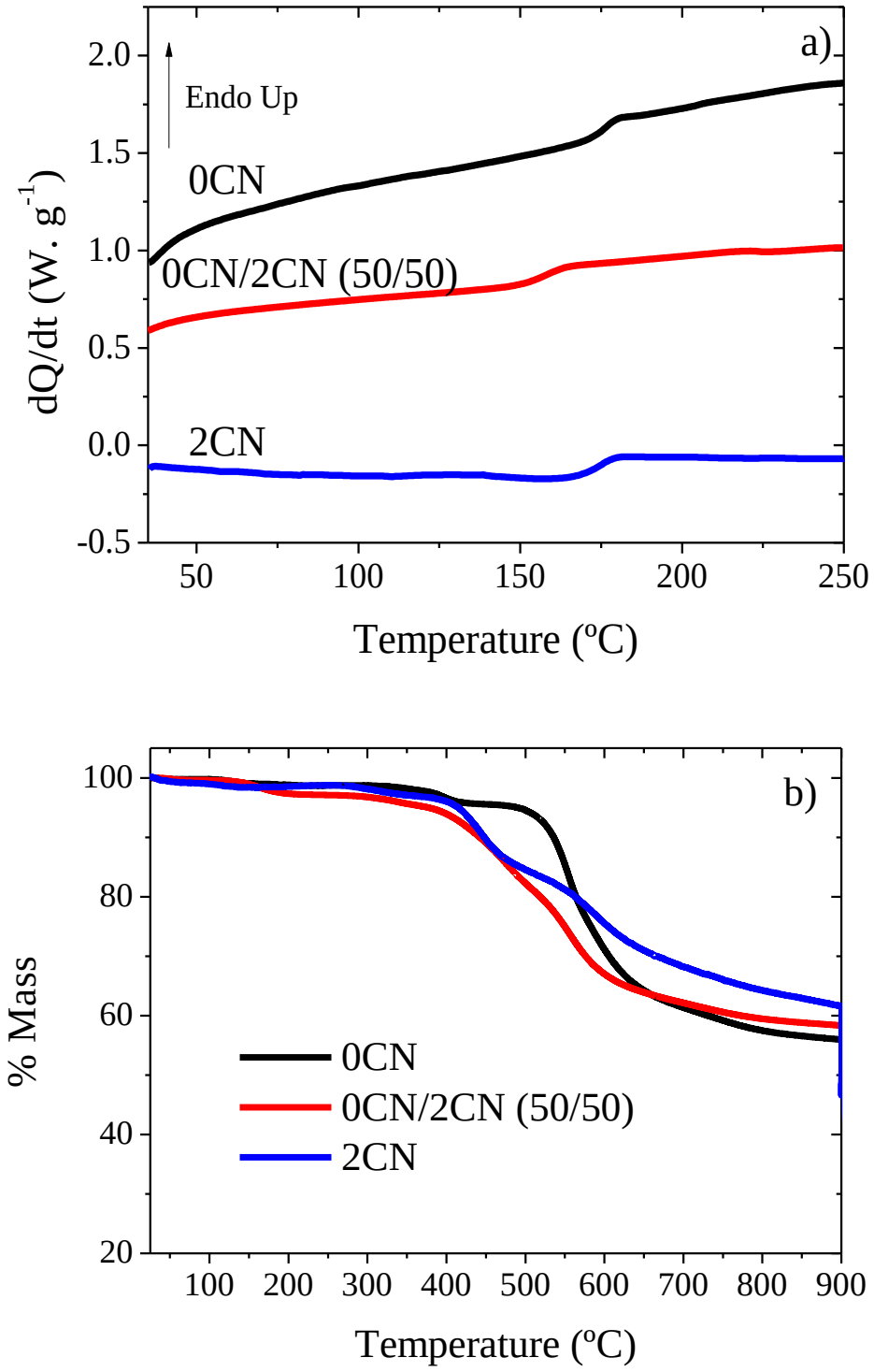

Figure 6.19. a) DSC and b) TGA curves of all electrospun membranes.

Table 6.4. Glass transition temperature (T_g) and onset temperature of degradation (T_d) for all samples.

Sample	$T_g \pm 2$ (ºC)	$T_d \pm 5$ (ºC)	Residue at 800 ºC
0CN	176	500	57
0CN/2CN (50/50)	157	390	60
2CN	174	403	64

6.3.2. ELECTRICAL PROPERTIES

Impedance spectroscopy was used for determination of the ionic conductivity value of all electrospun membranes. Room temperature Nyquist plots of the electrospun membranes after soaked with electrolyte solution are represented in Figure 6.20a. Generally, in the Nyquist plot it is possible to detect two main regions: a semicircle located at the high-frequency range that corresponds to the charge transfer process and a straight line at lower frequencies that is related to the diffusion process [123].

For 0CN and 0CN/2CN (50/50) samples, is not detected the semi-circle at high frequencies where the ionic conductivity value (6.20d) is determined by the intersection of linear relation between the imaginary part axis and the real part axis. For the 2CN sample the semi-circle is observed, its width representing the bulk resistance of the electrospun membrane. Thus, the inclusion of –CN dipolar groups has an effect on the ionic conductivity of the membranes (Figure 6.20d and Table 6.5).

Figure 6.20b shows the impedance modulus as a function of frequency for the electrospun membranes at room temperature. The impedance modulus increases with decreasing frequency, in particular for frequencies below 5 kHz due to the restricted dynamics of ion mobility within the porous membranes.

The phase angle as a function of frequency for all electrospun membranes at room temperature is illustrated in the Figure 6.20c. Independently of the sample, it is observed that maximum phase angle occurs above of -60º, with the existence of multi peaks for the 0CN and 0CN/2CN samples. This behavior can be represented by a constant phase element, which can be modeled as a capacitor with a distribution of relaxation times [124]. Finally, the ionic conductivity value determined through the Nyquist plot (Figure 6.20a) is represented in the Figure 6.20d.

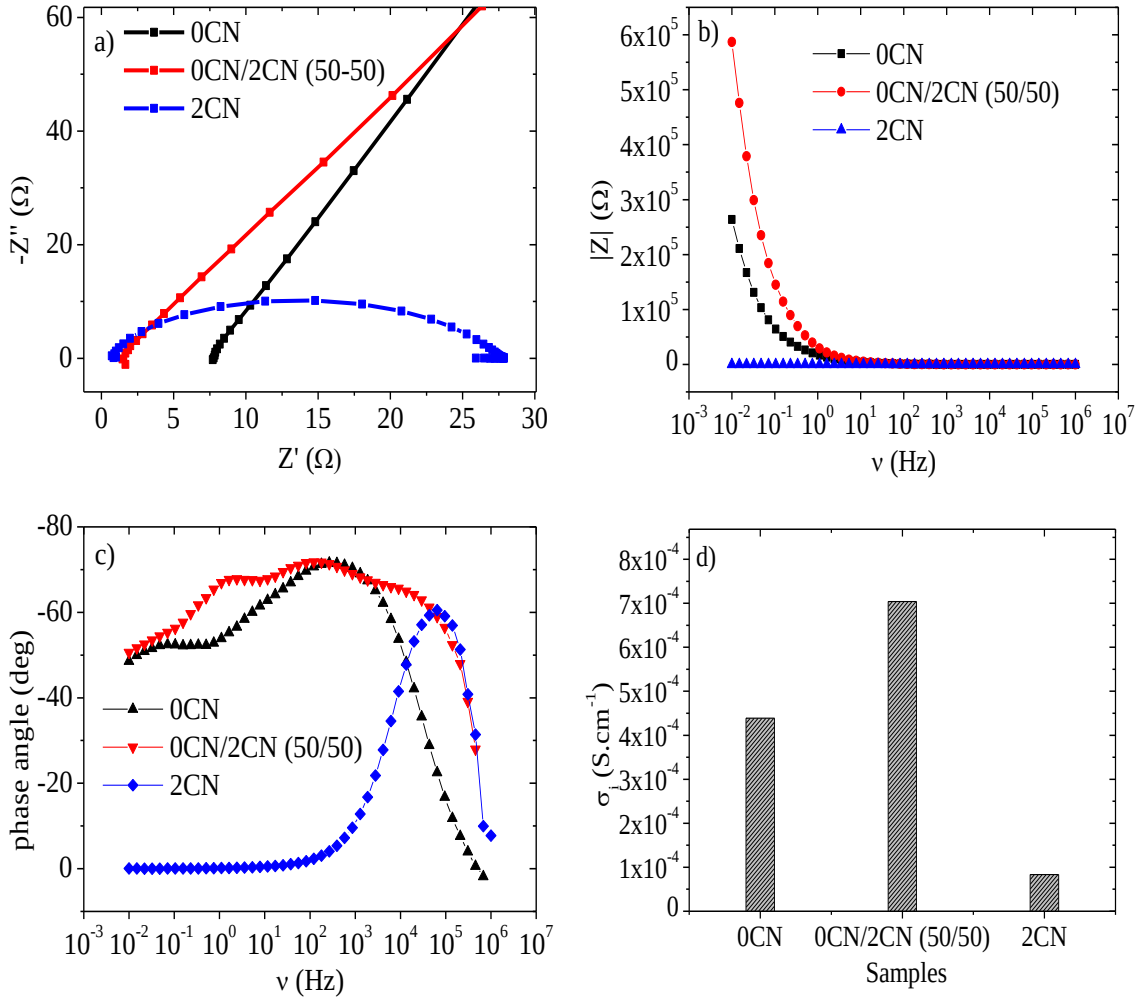

Figure 6.20. a) Nyquist plot, b) impedance modulus, c) phase angle and d) ionic conductivity value for all electrospun membranes at room temperature.

Uptake, tortuosity and ionic conductivity of the samples are summarized in Table 6.5. The tortuosity (τ) represents a measure of how the ionic transport is facilitated by the large pore connectivity, specifically it is the ratio between the effective capillarity to thickness of the sample and was determined through the Equation 6.10 [125]:

$$\sigma_{eff} = \sigma_0 \frac{\varepsilon}{\tau^2} \tag{6.10}$$

where σ_0 is the electrical conductivity of the liquid electrolyte ($\sigma_0 = 11.6\ \mathrm{mS.\,cm^{-1}}$), σ_{eff} is the conductivity of the membrane and the electrolyte set and ε is the porosity of the membrane. The values of the tortuosity range from 4 for the 0CN/2CN copolymer up to 11 for the 2CN sample (Table 6.5). Ideally the tortuosity should be 1, nevertheless these results confirm the good porous interconnectivity, in agreement with the results shown in Figure 6.17, which enhances the ionic transport through the membrane [126].

Table 6.5. Uptake, tortuosity and ionic conductivity value for all samples.

Sample	**Uptake (%)**	$\boldsymbol{\tau}$	$\boldsymbol{\sigma_{eff}}$ **(mS·cm^{-1})**
0CN	1153	5	0.44
0CN/2CN (50/50)	509	4	0.70
2CN	564	11	0.08

Table 6.6 compares the physicochemical properties of the polyimide electrospun membranes developed in this work with related ones in the literature. The ionic conductivity and degree of porosity values determined for the polyimide electrospun membranes are analogous to the values observed for other polyimide separator membranes reported in the literature. The differences can be related to the microstructure and the electrolyte uptake values, as different electrolyte solutions have been used (Table 6.6).

The electrochemical stability window of polyimides for lithium-ion battery separators has been previously determined [66,73], the different polyimides showing excellent electrochemical stability at voltages above 4.0 versus Li/Li^+, *i.e.*, showing compatibility with different cathodes.

Table 6.6. Ionic conductivity value and degree of porosity for the polyimide electrospun membrane produced in this work and comparison with other polyimide separator membranes reported in the literature. The electrolyte solution is also indicated.

Type of membrane	**Electrolyte solution**	**Porosity**	**σ_i (mS.cm^{-1}) at 25ºC**	**Ref.**
Composite	1 M $LiPF_6$ in EC-DMC-EMC	65	0.897	[71]
Nanofiber	0.5M LiBOB/PC	73%-87%	0.89	[66]
Composite	1M $LiPF_6$ in EC-PC-DMC-EA	--------	0.65	[73]
Nanofiber	1M $LiPF_6$ in EC-DMC	82	0.44	This work

6.3.3. BATTERY PERFORMANCE

In order to determinate the battery performance of the electrospun membranes based on polyimide polymer as battery separator in rechargeable lithium-ion batteries, half-swagelok cells (Figure 6.21) were fabricated with C-$LiFePO_4$ as the cathode material and lithium metal as anode material. Lithium hexafluorophosphate solution – in ethylene carbonate and dimethyl carbonate, 1.0 M $LiPF_6$ in EC/DMC= 50/50 (v/v) as electrolyte was used. The results are shown in Figures 6.22, 6.23 and 6.24.

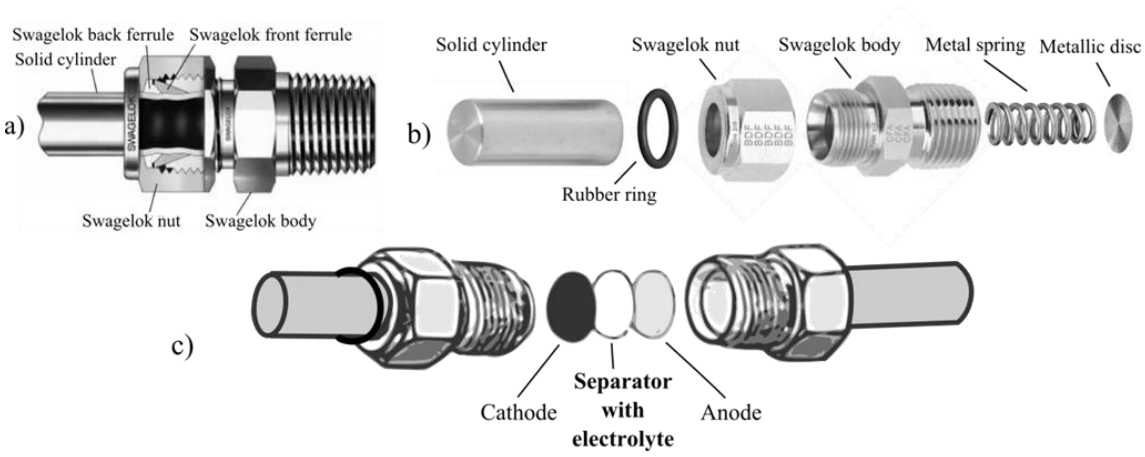

Figure 6.21. a) Cross-section of Swagelok's two-ferrule fitting, b) photography of the Swagelok tube fittings, tube adapters, cylinder, spring and disc used in the cell, and c) schematic representation of the Swagelok-type cell used in the cycling tests.

Taking into account the uptake values and ionic conductivity values presented in Table 6.5, the battery performance is shown for the 0CN and 2CN samples. The polyimide samples with –CN dipolar groups do not show stable mechanical properties after 2 hours in contact with the electrolyte solution.

Figure 6.22 shows the voltage *versus* capacity value at different scan rates from C/20 to C/5 for the 0CN sample (Figure 6.22a) and 2CN sample (Figure 6.22b) where the scan rates are shown at C/20 and C/10 (4º cycle for 0CN and 3º cycle for 2CN). The differences observed in battery performance (Figure 6.22) are related to the ionic conductivity, uptake and mechanical stability of the samples. Independently of the samples, Figure 6.22 shows the typical flat plateau of the C-$LiFePO_4$ cathodes that reflects the reversible charge (lithium removal)-discharge (lithium insertion) behavior.

This flat plateau that corresponds to the Fe^{+2}/Fe^{+3} redox reaction is dependent of the different scan rate [127].

Figure 6.23 shows that the discharge capacity value decreases progressively as the scan rates increase, which is a result of ohmic drop polarization within the electrode material. For the 0CN sample, the discharge capacity value at C/20, C/10 and C/5 is 149.7 $mAh.g^{-1}$, 146.5 $mAh.g^{-1}$ and 124.6 $mAh.g^{-1}$, respectively and for the 2CN sample, the

discharge capacity values at C/20 and C/10 are 98.7 $mAh.g^{-1}$ and 4 $mAh.g^{-1}$, respectively.

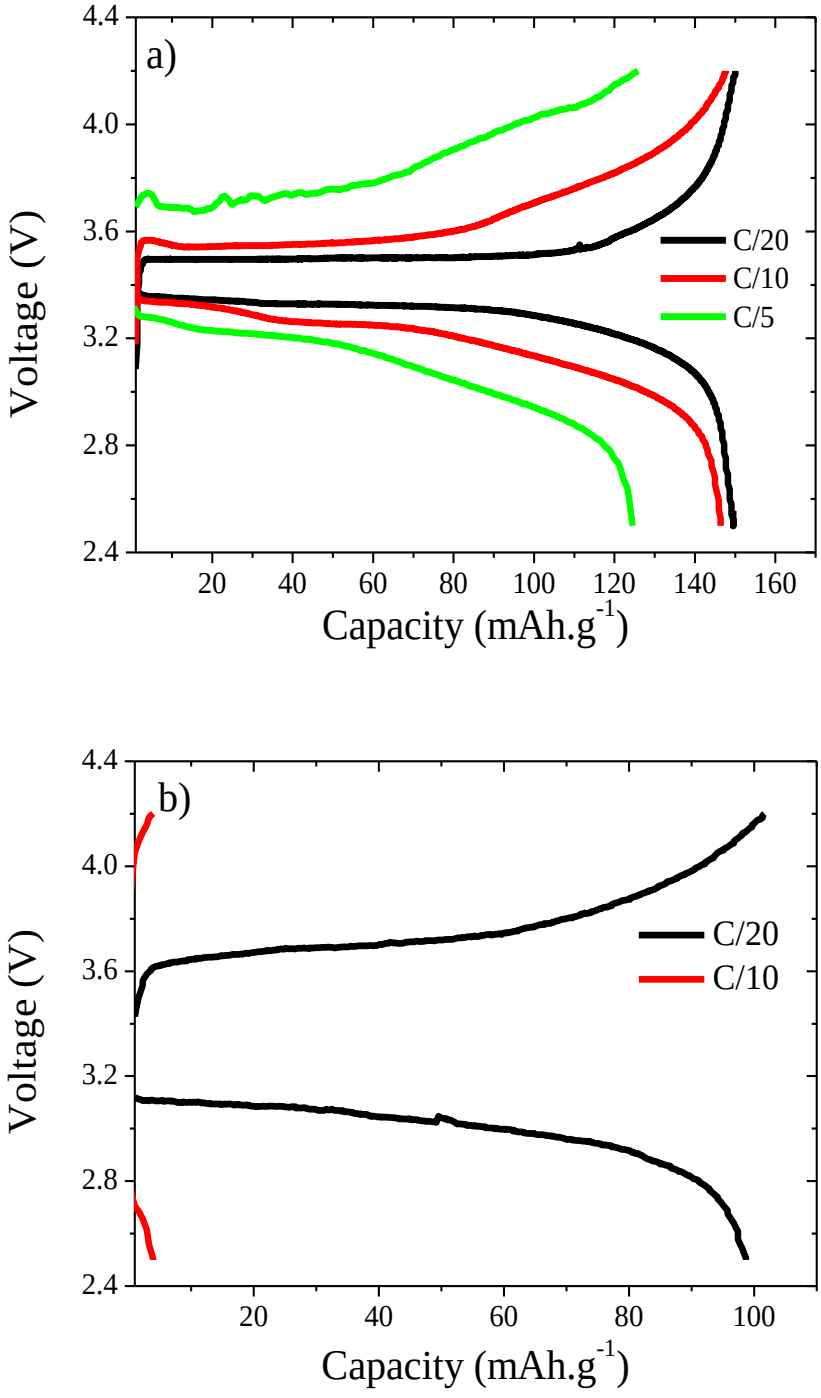

Figure 6.22. Voltage versus capacity value for a) 0CN and b) 2CN samples at different scan rates.

The cyclability behavior of all electrospun membranes (Figure 6.23) was compared in relation to commercial glass fiber separator.

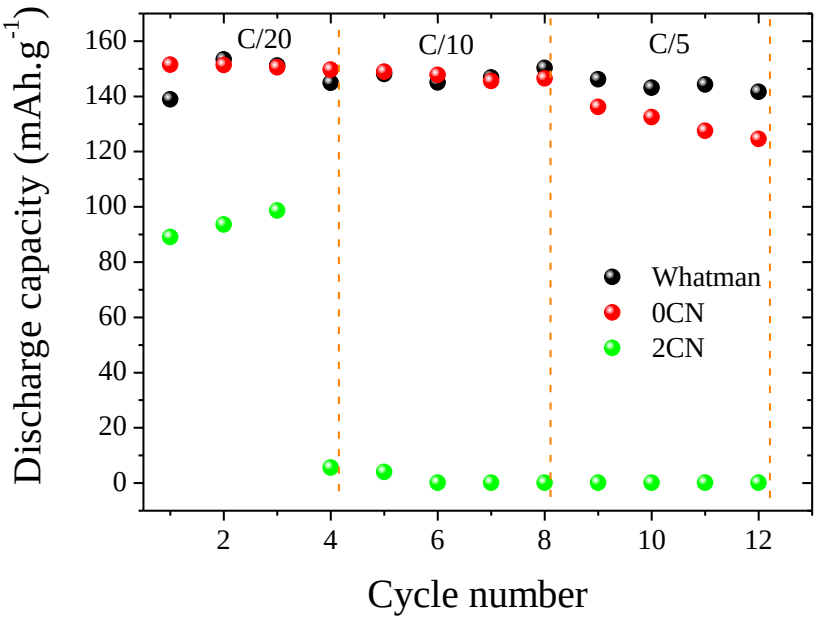

Figure 6.23. Discharge capacity in function of cycle number for different scan rates.

Independently of the scan rate, significant differences are observed in the discharge capacity behavior of the polyimide electrospun membranes. The higher discharge capacity of the lithium-ion battery with 0CN sample is attributed to the higher ionic conductivity which is favorable for the fast transportation of lithium ions between the electrodes. Comparing this sample with the commercial separator, the discharge value of the polyimide samples is similar up to a discharge current rate of C/10.

The cycling performance of the 0CN sample at C/5 is shown in Figure 6.24. The discharge capacity value after 15 cycles is 125 $mAh.g^{-1}$ and corresponds to a capacity retention of 74%. These high values are attributed to the ionic conductivity value and electrolyte uptake value that facilitates the repeated lithium ion insertion/de-insertion. The capacity retention was calculated based on the theoretical capacity of C-$LiFePO_4$ (170 $mAh.g^{-1}$).

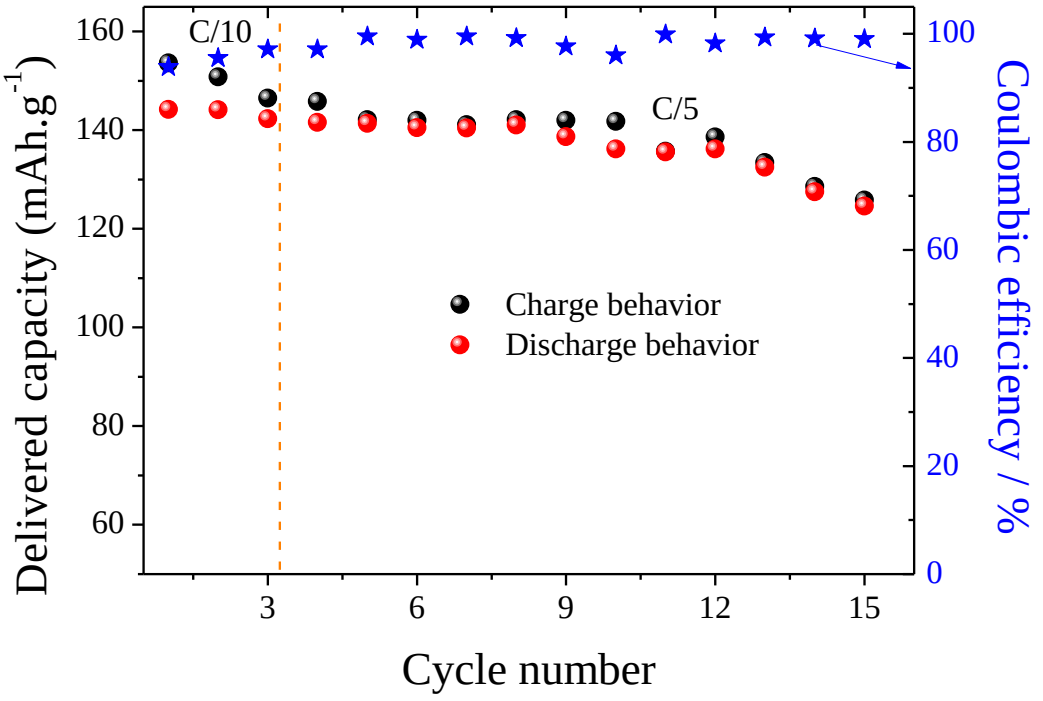

Figure 6.24. Cycling performance of C-LiFePO$_4$ cathodic half cells containing 0CN sample at C/5.

Further, the Coulombic efficiency at C/5 for the 0CN sample is 100% for all cycles, which indicates excellent reversibility and stability upon charge–discharge cycling.

In summary, the 0CN sample shows good cyclability and rate capability in comparison to the commercial separator. Considering also its thermal stability, high wettability and ionic conductivity value, the 0CN sample is the most interesting option as battery separator for high power density lithium-ion batteries.

6.4. CONCLUSIONS

Three types of polyimide membranes (polymer 0CN, copolymers 0CN/2CN (50/50) and polymer 2CN) with different –CN dipolar groups were fabricated by electrospinning. For all samples, the electrospun membranes showed homogeneous morphology made up of uniform fibers. The thermal stability, uptake, tortuosity and ionic conductivity values were investigated. These parameters depend on the presence of –CN dipolar groups in the polyimide. These novel polyimide separators show good wettability, high ionic conductivity and cycling performance for lithium-ion battery application. The cycling performance is also dependent of the cyano groups.

The cathodic half-cell containing the 0CN based separator showed stable cycling performance independently of the scan rate as well as high cycling performance at C/5.

Therefore, the 0CN sample can be a promising sample material as separator for high power lithium-ion battery application.

6.5. REFERENCES

[1] Adamson A. Lead-acid battery technologies: fundamentals, materials, and applications. CRC Press; 2015.

[2] Crompton TR. Battery reference book. Newnes; 2000.

[3] Adamson A. A textbook of physical chemistry. Elsevier Science; 2012.

[4] Zhang Z, Zhang S. Rechargeable batteries: materials, technologies and new trends. Springer; 2015.

[5] Palacín MR. Recent advances in rechargeable battery materials: a chemist's perspective. Chem Soc Rev 2009;38:2565–75.

[6] Pistola G. Lithium-ion batteries: advances and applications. Newnes; 2013.

[7] Macdonald DD. Reflections on the history of electrochemical impedance spectroscopy. Electrochim Acta 2006;51:1376–88.

[8] Barsoukov E, Macdonald JR. Impedance spectroscopy: theory, experiment, and applications. 2005.

[9] Gao F, Tang Z. Kinetic behavior of LiFePO4/C cathode material for lithium-ion batteries. Electrochim Acta 2008;53:5071–5.

[10] Pisani L. Simple expression for the tortuosity of porous media. Transp Porous Media 2011;88:193–203.

[11] Tye FL. Tortuosity. J Power Sources 1983;9:89–100.

[12] Theoretical analysis of the discharge performance of lithium ion and lithium/sulfur cells. ProQuest; 2008.

[13] A guide to understanding battery specifications. MIT Electric Vehicle Team. 2008.

[14] Peled E. The electrochemical behavior of alkali and alkaline earth metals in nonaqueous battery systems—The solid electrolyte interphase model. J Electrochem Soc 1979;126:2047.

[15] Bruce PG, Freunberger SA, Hardwick LJ, Tarascon J-M. Li-O2 and Li-S batteries with high energy storage. Nat Mater 2012;11:19–29.

[16] Christensen J, Albertus P, Sanchez-Carrera RS, Lohmann T, Kozinsky B, Liedtke R, et al. A critical review of Li/Air batteries. J Electrochem Soc 2012;159:R1.

[17] Goodenough JB, Kim Y. Challenges for rechargeable Li batteries. Chem Mater 2010;22:587–603.

[18] Bhatt MD, O'Dwyer C. Recent progress in theoretical and computational investigations of Li-ion battery materials and electrolytes. Phys Chem Chem Phys 2015;17:4799–844.

[19] Tarascon JM, Armand M. Issues and challenges facing rechargeable lithium

batteries. Nature 2001;414:359–67.

[20] Kang B, Ceder G. Battery materials for ultrafast charging and discharging. Nature 2009;458:190–3.

[21] Bruce PG, Scrosati B, Tarascon J-M. Nanomaterials for rechargeable lithium batteries. Angew Chem Int Ed Engl 2008;47:2930–46.

[22] Huang H, Yin S-C, Nazar LF. Approaching theoretical capacity of LiFePO4 at room temperature at high rates. Electrochem Solid-State Lett 2001;4:A170.

[23] Padhi AK. Phospho-olivines as positive-electrode materials for rechargeable lithium batteries. J Electrochem Soc 1997;144:1188.

[24] Dominko R, Gaberšček M, Drofenik J, Bele M, Jamnik J. Influence of carbon black distribution on performance of oxide cathodes for Li ion batteries. Electrochim Acta 2003;48:3709–16.

[25] Ravet N, Chouinard Y, Magnan JF, Besner S, Gauthier M, Armand M. Electroactivity of natural and synthetic triphylite. J Power Sources 2001;97-98:503–7.

[26] Bewlay SL, Konstantinov K, Wang GX, Dou SX, Liu HK. Conductivity improvements to spray-produced LiFePO4 by addition of a carbon source. Mater Lett 2004;58:1788–91.

[27] Wang J, Yang J, Tang Y, Liu J, Zhang Y, Liang G, et al. Size-dependent surface phase change of lithium iron phosphate during carbon coating. Nat Commun 2014;5:3415.

[28] Konarova M, Taniguchi I. Synthesis of carbon-coated LiFePO4 nanoparticles with high rate performance in lithium secondary batteries. J Power Sources 2010;195:3661–7.

[29] Padhi AK. Effect of structure on the Fe 3+⁄Fe2+ redox couple in iron phosphates. J Electrochem Soc 1997;144:1609.

[30] Padhi AK. Tuning the position of the redox couples in materials with NASICON structure by anionic substitution. J Electrochem Soc 1998;145:1518.

[31] Fergus JW. Recent developments in cathode materials for lithium ion batteries. J Power Sources 2010;195:939–54.

[32] Ait Salah A, Mauger A, Zaghib K, Goodenough JB, Ravet N, Gauthier M, et al. Reduction Fe3+ of impurities in LiFePO4 from pyrolysis of organic precursor used for carbon deposition. J Electrochem Soc 2006;153:A1692.

[33] Zaghib K, Charest P, Dontigny M, Guerfi A, Lagacé M, Mauger A, et al. LiFePO4: from molten ingot to nanoparticles with high-rate performance in Li-ion batteries. J Power Sources 2010;195:8280–8.

[34] Brochu F, Guerfi A, Trottier J, Kopeć M, Mauger A, Groult H, et al. Structure and electrochemistry of scaling nano C–LiFePO4 synthesized by hydrothermal route: complexing agent effect. J Power Sources 2012;214:1–6.

[35] Herle PS, Ellis B, Coombs N, Nazar LF. Nano-network electronic conduction in iron and nickel olivine phosphates. Nat Mater 2004;3:147–52.

[36] Ravet N, Gauthier M, Zaghib K, Mauger A, Gendron F. Mechanism of the Fe3+ reduction at low temperature for LiFePO4 synthesis from a polymeric additive. Chem Mater 2007;19:2595–602.

[37] Zaghib K, Mauger A, Gendron F, Julien CM. Surface effects on the physical and electrochemical properties of thin LiFePO4 particles. Chem Mater 2008;20:462–9.

[38] Sato M. Preparation of iron phosphate cathode material of Li3Fe2(PO4)3 by hydrothermal reaction and thermal decomposition processes. Solid State Ionics 2002;152-153:247–51.

[39] Kim D-H, Kim J. Synthesis of LiFePO4 nanoparticles and their electrochemical properties. J Phys Chem Solids 2007;68:734–7.

[40] Lee SB, Jang IC, Lim HH, Aravindan V, Kim HS, Lee YS. Preparation and electrochemical characterization of LiFePO4 nanoparticles with high rate capability by a sol–gel method. J Alloys Compd 2010;491:668–72.

[41] Losey A, Rakovan J, Hughes JM, Francis CA, Dyar MD. Structural variation in the lithiophilite-triphylite series and other olivine-group. Can Mineral 2004;42:1105–15.

[42] Streltsov VA, Belokoneva EL, Tsirelson VG, Hansen NK. Multipole analysis of the electron density in triphylite, LiFePO4, using X-ray diffraction data. Acta Crystallogr Sect B Struct Sci 1993;49:147–53.

[43] Rousse G, Rodriguez-Carvajal J, Patoux S, Masquelier C. Magnetic structures of the triphylite LiFePO4 and of its delithiated form FePO4. Chem Mater 2003;15:4082–90.

[44] Ozawa K. Lithium ion rechargeable batteries: materials, technology, and new applications. John Wiley & Sons; 2012.

[45] Yoshio M, Brodd RJ, Kozawa A. Lithium-ion batteries: science and technologies. Springer Science & Business Media; 2010.

[46] Franco A. Rechargeable lithium batteries: from fundamentals to applications. Elsevier Science; 2015.

[47] Brissot C, Rosso M, Chazalviel J-N, Baudry P, Lascaud S. In situ study of dendritic growth inlithium/PEO-salt/lithium cells. Electrochim Acta 1998;43:1569–74.

[48] Cabana J, Monconduit L, Larcher D, Palacín MR. Beyond intercalation-based Li-ion batteries: the state of the art and challenges of electrode materials reacting through conversion reactions. Adv Mater 2010;22:E170–92.

[49] Jow RT, Xu K, Borodin O, Ue M. Electrolytes for lithium and lithium-ion batteries. Springer; 2014.

[50] Wu Y, editor. Lithium-ion batteries: fundamentals and applications. CRC Press;

2015.

[51] Fenton DE, Parker JM, Wright PV. Complexes of alkali metal ions with poly(ethylene oxide). Polymer (Guildf) 1973;14:589.

[52] Basile A, Pereira Nunes S. Advanced membrane science and technology for sustainable energy and environmental applications. Elsevier Science; 2011.

[53] Zhang SS. A review on the separators of liquid electrolyte Li-ion batteries. J Power Sources 2007;164:351–64.

[54] Agrawal RC, Pandey GP. Solid polymer electrolytes: materials designing and all-solid-state battery applications: an overview. J Phys D Appl Phys 2008;41:223001.

[55] Nunes-Pereira J, Costa CM, Lanceros-Méndez S. Polymer composites and blends for battery separators: State of the art, challenges and future trends. J Power Sources 2015;281:378–98.

[56] Song JY, Wang YY, Wan CC. Review of gel-type polymer electrolytes for lithium-ion batteries. J Power Sources 1999;77:183–97.

[57] Costa CM, Silva MM, Lanceros-Méndez S. Battery separators based on vinylidene fluoride (VDF) polymers and copolymers for lithium ion battery applications. RSC Adv 2013;3:11404.

[58] Scrosati B, Garche J. Lithium batteries: status, prospects and future. J Power Sources 2010;195:2419–30.

[59] Xu K. Nonaqueous liquid electrolytes for lithium-based rechargeable batteries. Chem Rev 2004;104:4303–418.

[60] Arora P, Zhang Z (John). Battery separators. Chem Rev 2004;104:4419–62.

[61] Chung YS, Yoo SH, Kim CK. Enhancement of meltdown temperature of the polyethylene lithium-ion battery separator via surface coating with polymers having high thermal resistance. Ind Eng Chem Res 2009;48:4346–51.

[62] Venugopal G, Moore J, Howard J, Pendalwar S. Characterization of microporous separators for lithium-ion batteries. J Power Sources 1999;77:34–41.

[63] Choi B, Shin KH, Kim YW. Lithium ion conduction in PEO–salt electrolytes gelled with PAN. Solid State Ionics 1998;113-115:123–7.

[64] Kang Y, Kim HJ, Kim E, Oh B, Cho JH. Photocured PEO-based solid polymer electrolyte and its application to lithium–polymer batteries. J Power Sources 2001;92:255–9.

[65] Huang B. Lithium ion conduction in polymer electrolytes based on PAN. Solid State Ionics 1996;85:79–84.

[66] Jiang W, Liu Z, Kong Q, Yao J, Zhang C, Han P, et al. A high temperature operating nanofibrous polyimide separator in Li-ion battery. Solid State Ionics 2013;232:44–8.

[67] Djian D, Alloin F, Martinet S, Lignier H. Macroporous poly(vinylidene fluoride)

membrane as a separator for lithium-ion batteries with high charge rate capacity. J Power Sources 2009;187:575–80.

[68] Costa CM, California A, Cardoso VF, Sencadas V, Rodrigues LC, Silva MM, et al. Electroactive poly(vinylidene fluoride-trifluorethylene) (PVDF-TrFE) microporous membranes for lithium-ion battery applications. Ferroelectrics 2012;430:103–7.

[69] Costa CM, Rodrigues LC, Sencadas V, Silva MM, Lanceros-Méndez S. Effect of the microsctructure and lithium-ion content in poly[(vinylidene fluoride)-co-trifluoroethylene]/lithium perchlorate trihydrate composite membranes for battery applications. Solid State Ionics 2012;217:19–26.

[70] Costa CM, Rodrigues LC, Sencadas V, Silva MM, Rocha JG, Lanceros-Méndez S. Effect of degree of porosity on the properties of poly(vinylidene fluoride–trifluorethylene) for Li-ion battery separators. J Memb Sci 2012;407-408:193–201.

[71] Ding J, Kong Y, Li P, Yang J. Polyimide/poly(ethylene terephthalate) composite membrane by electrospinning for nonwoven separator for lithium-ion battery. J Electrochem Soc 2012;159:A1474–80.

[72] Miao Y-E, Zhu G-N, Hou H, Xia Y-Y, Liu T. Electrospun polyimide nanofiber-based nonwoven separators for lithium-ion batteries. J Power Sources 2013;226:82–6.

[73] Shi J, Hu H, Xia Y, Liu Y, Liu Z. Polyimide matrix-enhanced cross-linked gel separator with three-dimensional heat-resistance skeleton for high-safety and high-power lithium ion batteries. J Mater Chem A 2014;2:9134.

[74] Maceiras A, Costa CM, Lopes AC, San Sebastián M, Laza JM, Vilas JL, et al. Dielectric relaxation dynamics of high-temperature piezoelectric polyimide copolymers. Appl Phys A 2015;120:731–43.

[75] Yen H-J, Chen C-J, Liou G-S. Flexible multi-colored electrochromic and volatile polymer memory devices derived from starburst triarylamine-based electroactive polyimide. Adv Funct Mater 2013;23:5307–16.

[76] Popovici D, Hulubei C, Cozan V, Lisa G, Bruma M. Polyimides containing cycloaliphatic segments for low dielectric material. High Perform Polym 2012;24:194–9.

[77] Ghosh M. Polyimides: fundamentals and applications. New York: CRC Press; 1996.

[78] Pan H, Zhang Y, Pu H, Chang Z. Organic–inorganic hybrid proton exchange membrane based on polyhedral oligomeric silsesquioxanes and sulfonated polyimides containing benzimidazole. J Power Sources 2014;263:195–202.

[79] Ohya H, Kudryavsev V V, Semenova SI. Polyimide membranes: applications, fabrications and properties. CRC Press; 1997.

[80] Wiegand JR, Smith ZP, Liu Q, Patterson CT, Freeman BD, Guo R. Synthesis and characterization of triptycene-based polyimides with tunable high fractional free

volume for gas separation membranes. J Mater Chem A 2014;2:13309.

[81] Jiang G-MM, Jiang X, Zhu Y-FF, Huang D, Jing X-HH, Gao W-DD. Synthesis and characterization of organo-soluble polyimides derived from a new spirobifluorene diamine. Polym Int 2010;59:896–900.

[82] Thiruvasagam P. Synthesis and characterization of new unsymmetrical diamine monomer and polyimides. Des Monomers Polym 2014;17:166–75.

[83] Yan S, Chen W, Yan W, Huang M, Chen C, Xu Z, et al. Optical transparency and light colour of highly soluble fluorinated polyimides derived from a novel pyridine-containing diamine m, p-3FPAPP and various aromatic dianhydrides. Des Monomers Polym 2011;14:579–92.

[84] Huang M, Wang L, Li X, Yan S, Yeung KWK, Chu PK, et al. Design and preparation of novel fluorescent polyimides containing ortho -linked units and pyridine moieties. Des Monomers Polym 2012;15:389–404.

[85] Dine-Hart RA, Wright WW. Preparation and fabrication of aromatic polyimides. J Appl Polym Sci 1967;11:609–27.

[86] Baise AI. Optimizing polyimide cure using infrared spectroscopy and a factorial design. J Appl Polym Sci 1986;32:4043–8.

[87] Zuo HJ, Chen JS, Yang HX, Hu AJ, Fan L, Yang SY. Synthesis and characterization of melt-processable polyimides derived from 1,4-bis(4-amino-2-trifluoromethylphenoxy)benzene. J Appl Polym Sci 2008;107:755–65.

[88] Chen J-C, Wu J-A, Chang H-W, Lee C-Y, Li S-W, Chou S-C. Organosoluble polyimides derived from asymmetric 2-substituted-and 2,2′,6-trisubstituted-4,4′-oxydianilines. Polym Int 2014;63:352–62.

[89] Li D, Xia Y. Electrospinning of nanofibers: reinventing the wheel? Adv Mater 2004;16:1151–70.

[90] Li YX, Lu XF, Liu XC, Zhang CC, Li XA, Zhang WJ, et al. Ultra-low dielectric performance of polymer electrospun nanofiber mats. Appl Phys A Mater Sci Process 2010;100:207–12.

[91] Gong G, Wu J, Jiang L. Novel polyimide materials produced by electrospinning. Prog Chem 2011;23:750–9.

[92] Anton F. Process and apparatus for preparing artificial threads. US50028330A, 1934.

[93] Taylor G. Disintegration of water drops in an electric field. Proc R Soc A Math Phys Eng Sci 1964;280:383–97.

[94] Reneker DHH, Yarin ALL, Fong H, Koombhongse S. Bending instability of electrically charged liquid jets of polymer solutions in electrospinning. J Appl Phys 2000;87:4531.

[95] Ramakrishna S. An introduction to electrospinning and nanofibers. World Scientific; 2005.

[96] Morozov V, Morozova T, Kallenbach N. Atomic force microscopy of structures produced by electrospraying polymer solutions. Int J Mass Spectrom 1998;178:143–59.

[97] Shenoy SL, Bates WD, Frisch HL, Wnek GE. Role of chain entanglements on fiber formation during electrospinning of polymer solutions: good solvent, non-specific polymer–polymer interaction limit. Polymer (Guildf) 2005;46:3372–84.

[98] Lee JS, Choi KH, Ghim H Do, Kim SS, Chun DH, Kim HY, et al. Role of molecular weight of atactic poly(vinyl alcohol) (PVA) in the structure and properties of PVA nanofabric prepared by electrospinning. J Appl Polym Sci 2004;93:1638–46.

[99] Zong X, Ran S, Fang D, Hsiao BS, Chu B. Control of structure, morphology and property in electrospun poly(glycolide-co-lactide) non-woven membranes via post-draw treatments. Polymer (Guildf) 2003;44:4959–67.

[100] Kessick R, Fenn J, Tepper G. The use of AC potentials in electrospraying and electrospinning processes. Polymer (Guildf) 2004;45:2981–4.

[101] Mo X., Xu C., Kotaki M, Ramakrishna S. Electrospun P(LLA-CL) nanofiber: a biomimetic extracellular matrix for smooth muscle cell and endothelial cell proliferation. Biomaterials 2004;25:1883–90.

[102] Maceiras A, Martins P, San Sebastián M, Lasheras A, Silva M, Laza JM, et al. Synthesis and characterization of novel piezoelectric nitrile copolyimide films for high temperature sensor applications. Smart Mater Struct 2014;23:105015.

[103] Gonzalo B, Vilas JL, Breczewski T, Pérez-Jubindo MA, De La Fuente MR, Rodriguez M, et al. Synthesis, characterization, and thermal properties of piezoelectric polyimides. J Polym Sci Part A Polym Chem 2009;47:722–30.

[104] Gonzalo B, Vilas JL, San Sebastian M, Breczewski T, Perez-Jubindo MA, de la Fuente MR, et al. Electric modulus and polarization studies on piezoelectric polyimides. J Appl Polym Sci 2012;125:67–76.

[105] Gutierrez J, Lasheras A, Barandiaran JM, Vilas JL, Maceiras A, Leon LM. Improving the performance of high temperature piezopolymers for magnetoelectric applications. Mater Appl Sensors Transducers II 2013;543:439–42.

[106] Fong H, Chun I, Reneker D. Beaded nanofibers formed during electrospinning. Polymer (Guildf) 1999;40:4585–92.

[107] Demir M., Yilgor I, Yilgor E, Erman B. Electrospinning of polyurethane fibers. Polymer (Guildf) 2002;43:3303–9.

[108] Gu SY, Ren J, Vancso GJ. Process optimization and empirical modeling for electrospun polyacrylonitrile (PAN) nanofiber precursor of carbon nanofibers. Eur Polym J 2005;41:2559–68.

[109] Liu M, Cheng Z, Jin Y, Ru X, Ding D, Li J. Optimization and investigation of the governing parameters in electrospinning the home-made poly(l -lactide-co-ε-caprolactone-diOH). J Appl Polym Sci 2013;130:3600–10.

[110] Verma R, Creager S, Ballato J, Smith DW. Optimized statically non-wetting hydrophobic electrospun surface of perfluorocyclobutyl aryl ether polymer. Polym Int 2013:n/a – n/a.

[111] Kong L, Ziegler GR. Quantitative relationship between electrospinning parameters and starch fiber diameter. Carbohydr Polym 2013;92:1416–22.

[112] Liu Y, Su Y, Li Y, Zhao X, Jiang Z. Improved antifouling property of PVDF membranes by incorporating an amphiphilic block-like copolymer for oil/water emulsion separation. RSC Adv 2015;5:21349–59.

[113] Gören A, Costa CM, Ferdov S, Cíntora-Juárez D, Tirado JL, Silva MM, et al. Effect of drying temperature on poly(vinylidene fluoride) polymer binder for C-LiFePO4 cathode slurry preparation. 2015.

[114] Gören A, Costa CM, Silva MM, Lanceros-Méndez S. State of the art and open questions on cathode preparation based on carbon coated lithium iron phosphate. Compos Part B Eng 2015;83:333–45.

[115] Chen XY, Kaliaguine S. Mixed gas and pure gas transport properties of copolyimide membranes. J Appl Polym Sci 2013;128:380–9.

[116] Pramoda KP, Liu S, Chung T-S. Thermal imidization of the precursor of a liquid crystalline polyimide. Macromol Mater Eng 2002;287:931–7.

[117] Liaw D-JJ, Wang K-LL, Huang Y-CC, Lee K-RR, Lai J-YY, Ha C-SS. Advanced polyimide materials: Syntheses, physical properties and applications. Prog Polym Sci 2012;37:907–74.

[118] Kakade M V, Givens S, Gardner K, Lee KH, Chase DB, Rabolt JF. Electric field induced orientation of polymer chains in macroscopically aligned electrospun polymer nanofibers. J Am Chem Soc 2007;129:2777–82.

[119] Wang W, Barber AH. Measurement of size-dependent glass transition temperature in electrospun polymer fibers using AFM nanomechanical testing. J Polym Sci Part B Polym Phys 2012;50:546–51.

[120] Aharoni SM. Increased glass transition temperature in motionally constrained semicrystalline polymers. Polym Adv Technol 1998;9:169–201.

[121] Curgul S, Van Vliet KJ, Rutledge GC. Molecular dynamics simulation of size-dependent structural and thermal properties of polymer nanofibers. Macromolecules 2007;40:8483–9.

[122] Arinstein A, Burman M, Gendelman O, Zussman E. Effect of supramolecular structure on polymer nanofibre elasticity. Nat Nanotechnol 2007;2:59–62.

[123] Chang B-Y, Park S-M. Electrochemical impedance spectroscopy. Annu Rev Anal Chem (Palo Alto Calif) 2010;3:207–29.

[124] Costa CM, Nunes-Pereira J, Sencadas V, Silva MM, Lanceros-Méndez S. Effect of fiber orientation in gelled poly(vinylidene fluoride) electrospun membranes for Li-ion battery applications. J Mater Sci 2013;48:6833–40.

[125] Karabelli D, Leprêtre J-C, Alloin F, Sanchez J-Y. Poly(vinylidene fluoride)-

based macroporous separators for supercapacitors. Electrochim Acta 2011;57:98–103.

[126] Quartarone E, Mustarelli P, Magistris A. Transport properties of porous PVDF membranes. J Phys Chem B 2002;106:10828–33.

[127] Wu H-C, Su C-Y, Shieh D-T, Yang M-H, Wu N-L. Enhanced high-temperature cycle life of LiFePO4-based Li-ion batteries by vinylene carbonate as electrolyte additive. Electrochem Solid-State Lett 2006;9:A537.

Chapter 7.

Conclusions and final considerations

Since the corresponding conclusions were explained in each chapter, in this section only the general considerations will be outlined with reference to the initial objectives derived from the work. Besides, possible future work in the field will be outlined.

In conclusion, we believe that the goals outlined in this thesis have been fulfilled since polyimides have been tested in the applications proposed in the section General objectives and working plan.

A series of nitrile containing polyimide polymers and copolymers have been synthesized and studied its piezoelectric response. In order to achieve it the corona poling conditions were optimized to maximize the value of the d_{33} coefficient, showing the d_{33} coefficient thermal stability and over time. Moreover, the influence of the repeating unit with two cyano groups in the piezoelectric properties was studied, being observed that a progressive increase in the content of 2CN in the film improves the piezoelectric response. The high thermal stability of polymer films was demonstrated by means of DSC and TGA, allowing their use at temperatures higher than 100ºC.

Dielectric properties of the samples were determined by means of dielectric spectroscopy in order to understand the dielectric behaviour of our polyimide films. The contribution of nitrile groups in the dielectric relaxations and the types of polarization involved were analyzed. Different functions and parameters were employed for a better understanding of the conduction or relaxation mechanisms, determining that the spectrum is dominated by high conductivity contribution and interfacial polarization (Maxwell-Wagner-Sillars polarization).

The use of polyimides in magnetoelectric (ME) nanocomposites was demonstrated for the first time. Magnetoelectric voltage coefficient was measured in a 0–3 nanocomposite film, prepared via in-situ polymerization method, using spherical cobalt ferrite nanoparticles ($CoFe_2O_4$) as fillers and an amorphous copolyimide, (β-CN)APB/ODPA, as matrix. The amorphous copolyimide was used as an alternative to the semicrystalline polyvinylidene fluoride (PVDF) to increase the temperature range of application above 100ºC. This achievement is an important step in applications where the PVDF do not meet the requirement of working under extreme conditions, thanks to the great dielectric, thermal stability, chemical and radiation resistance of polyimides.

Lithium-ion batteries have been widely used in numbers of mobile electronic devices. An essential constituent for achieving practical Li-ion batteries is the membrane separator. Different polyimide fibers have been prepared by electrospinning,

characterized and tested as separators for Li-ion batteries. Despite gel polymer electrolyte (GPE) membranes are in general characterized by poorer stability and mechanical properties when compared with other types of separators, they are promising materials. In our case, we made the first and promising approach in the development of gel polymer separators based in cyano containing polyimides.

—Possible future work

In this thesis we proceeded with the first step in the development of new applications of nitrile containing polyimides. In our opinion there is still room to improve their characteristics and qualities.

For instance, we believe that since piezoelectricity in amorphous polymers is mainly due to the frozen-in dipolar orientation, if we could increase the number of pendant dipole permanent groups, the d_{33}-coefficient would also increase. If we could increase the number of pendant dipole permanent groups, the d_{33}-coefficient would also increase. Thanks to the chemistry of polyimides is a vast field, and it includes a large variety of available monomers and different synthetic methodologies, their properties can be easily modified for specific applications by using different monomers. In principle, we consider as first option to replace the dianhydride employed up to now, the 4,4'-oxydiphthalic anhydride (dianhydride ODPA), by the 4,4'-(hexafluoroisopropylidene)diphthalic anhydride (dianhydride 6FDA). The reason is that the dianhydride 6FDA contains a hexafluoroisopropylidene group (6 bonds C–F) instead of a group –O– linking the two phthalimide isomeric parts. Therefore, in theory the piezoelectric capacity would increase because of the addition of new extra C–F dipoles. Moreover, this structural modification could also modify the solubility and thermal characteristics of the material, being of interest for future applications.

New polymers with new structures involve different glass transition temperatures. Hence, corona poling method should be optimized again for the new characteristics of the materials. Moreover, to understand the dielectric behavior of the new polyimide

films and to study the contribution of Fluor groups in the dielectric relaxations and the types of polarization, it would be recommended the use of dielectric spectroscopy.

In polyimide based magnetoelectric nanocomposites we observed a stable but low value of ME. We can think of several options to increase that effect. One possibility is clearly by means of varying the magnetostrictive element and/or the piezoelectric material. In this way, there are different types of magnetostrictive nanoparticles, such as other ferrites or also Terfenol-D; and about the topic of new polyimides, it was already explained. Other choice is by increasing the coupling between the piezoelectric and the magnetic phase, because ME effect in composites is a product tensor property that results from the cross elastic interaction between different orderings of the two phases in the composite. In polymer composites is typical the use of coupling agents for that purpose, which are chemicals which improve the interfacial properties of fillers and polymers.

In general "gelled polymer electrolytes" are characterized by higher ambient ionic conductivity but poorer mechanical properties when compared with pure Solid Polymer Electrolytes. The key point is that the polymer matrix must be capable of forming a stable gel with the polymer host structure, and because of the incorporation of large quantities of liquid plasticizer and (or) solvent(s) to a polymer matrix can be problematic. Therefore, in order to improve the mechanical properties of the gel polymer electrolytes, components which can be cross-linked and/or thermoset may also be added to the gel electrolyte formulation. Apart from that, we might consider to test the hexafluoroisopropylidene group (6FDA) containing polyimides as battery separators, and to study the effect of these new Fluor dipolar groups on the performance of lithium-ion battery electrospun polyimide gel electrolyte membranes.

Curriculum vitae & contributions

Alberto Maceiras Martínez

Departamento de Química Física

Facultad de Ciencia y Tecnología

Universidad del País Vasco/Euskal Herriko Unibertsitatea (UPV/EHU)

Campus de Leioa, Bº Sarriena s/n

48940, Leioa, Spain

email: *alberto.maceiras@ehu.eus*

Personal Information:

Gender: Male

Date of Birth: May 1st, 1984

Language skills: English, Spanish

RESEARCH TOPICS

Polyimides, piezoelectric polymers, magnetoelectric nanocomposites and battery polymer separators.

Polymer synthesis, DSC, TGA, IR, poling, dielectric spectroscopy, ME measurements, battery testing.

EDUCATION

PhD	University of the Basque Country UPV/EHU (2011-Present)
Thesis Title	Polyimides for piezoelectric materials, magnetoelectric nanocomposites and battery separators: synthesis and characterization
Advisors	Prof. Luis Manuel León Isidro (UPV/EHU) Dr. María San Sebastián (BCmaterials)
M.Sc. New Materials	University of the Basque Country UPV/EHU (2010)
B.Sc Chemistry	University of the Basque Country UPV/EHU (2009)

FELLOWSHIPS OR SCHOLARSHIPS

Recipient of UPV/EHU Predoctoral Fellowship, 2011

Advisor: Prof. Luis Manuel León Isidro (UPV/EHU)

RESEARCH STAYS ABROAD

Universidade do Minho, Braga, Portugal (Three months)

Advisor: Prof. Senentxu Lanceros-Mendez

SCIENTIFIC PUBLICATIONS

Part of the thesis

1) Maceiras A, Martins P, San Sebastián M, Lasheras A, Silva M, Laza JM, et al. Synthesis and characterization of novel piezoelectric nitrile copolyimide films for high temperature sensor applications. Smart Mater Struct 2014;23:105015.
2) Maceiras A, Martins P, Gonçalves R, Botelho G, Venkata Ramana E, Mendiratta SK, et al. High-temperature polymer based magnetoelectric nanocomposites. Eur Polym J 2015;64:224–8.
3) Maceiras A, Costa CM, Lopes AC, San Sebastián M, Laza JM, Vilas JL, et al. Dielectric relaxation dynamics of high-temperature piezoelectric polyimide copolymers. Appl Phys A 2015;120:731–43.
4) Maceiras A, Gören A., Sencadas V, Costa CM, Vilas JL, Lanceros-Méndez S, León LM. Effect of cyano dipolar groups on the performance of lithium-ion battery electrospun polyimide gel electrolyte membranes. J Energy Storage *(Submitted)*

Other articles

1) Gutierrez J, Lasheras A, Barandiaran JM, Vilas JL, Maceiras A, Leon LM. Improving the performance of high temperature piezopolymers for magnetoelectric applications. Mater Appl Sensors Transducers II 2013;543:439–42.

2) Lasheras A, Gutierrez Echevarria J, Maceiras A, San Sebastian M, Barandiaran JM, Vilas JL, et al. Radio-frequency magnetoelectric effect measured at high temperature. IEEE Trans Magn 2015;51:1–1.
3) San Sebastian M, Martinez-Martinez V, Maceiras A, Vilas JL, Lopez-Arbeloa I, Leon LM. Enhanced charge-transfer emission in polyimides by cyano-groups doping. J Phys Chem B 2015;119:5685–92.
4) Mejri R, Dias JC, Lopes AC, Bebes Hentati S, Silva MM, Botelho G, et al. Effect of ionic liquid anion and cation on the physico-chemical properties of poly(vinylidene fluoride)/ionic liquid blends. Eur Polym J 2015;71:304–13.

BOOK CHAPTER

Maceiras A, Vilas JL, Luis Manuel León LM. High temperature polymers for ME applications. Wiley-VCH *(Submitted)*

CONTRIBUTIONS TO MEETINGS

1) San Sebastián M, Maceiras A, Vilas JL, Breczewski T, Pérez-Jubindo MA, de la Fuente MR. Enhancing properties of piezoelectric polyimides by copolymerization. *European Polymer Congress 2011*. (Granada, Spain, 2011). Poster contribution.
2) Gutiérrez J, Lasheras A, Barandiarán JM, Vilas JL, Maceiras A, León LM. Improving the performance of high temperature piezopolymers for magnetoelectric applications. *2nd International Conference on Materials and Applications for Sensors and Transducers*. (Budapest, Hungary, 2012). Poster contribution.
3) Maceiras A, San Sebastián M, Martíns P, Lasheras A, Silva M, Laza JM, Vilas JL, Gutiérrez J, Lanceros-Mendez s, Barandiarán JM, León LM. Nitrile containing copolyimides for sensor applications. *3rd International Conference on Materials and Applications for Sensors and Transducers.* (Praque, Czech Republic, 2013). Poster contribution.
4) Lasheras A, Gutiérrez J, Barandiarán JM, Maceiras A, Vilas JL, León LM. Radio-frequency range magnetoelectric effect measured at high temperature. *The 10th*

European Conference on Magnetic Sensors and Actuators (EMSA 2014). (Vienna, Austria, 2014). Oral contribution.

5) Maceiras A. IV Piezoelectric polyimides for high temperature applications. Jornadas de Investigación de la Facultad de Ciencia y Tecnología. Oral contribution. (Leioa, Spain, 2016).
6) Maceiras A, San Sebastián M, Laza JM, Mijangos F, Rodriguez M, Vilas JL, León LM. Nuevas poliimidas piezoeléctricas sintetizadas a partir del dianhídrido 4,4'-(hexafluorosiopropilideno) diftálico (6FDA). XIII Reunión del Grupo Especializado de Polímeros GEP (RSEQ, RSEF). (Girona, Spain, 2016). Poster contribution.